Mesoscopic modeling of active matter : Explicit model for the propulsion of an isotropic colloid

Jeanne Decayeux

Thèse de doctorat

Pour l'obtention du grade de

Docteure de Sorbonne Université

École doctorale Chimie Physique et Chimie Analytique de Paris Centre (ED 388)

Mesoscopic simulation of active matter: Explicit model for the propulsion of an isotropic colloid

---

présentée par

Jeanne DECAYEUX

Sous la direction de Marie JARDAT

et le co-encadrement de Vincent DAHIREL et de Pierre ILLIEN

Soutenue le 27 septembre 2022 devant un jury composé de :

M. François DETCHEVERRY ..... Rapporteur

M. Ignacio PAGONABARRAGA ..... Rapporteur

Mme Maria BARBI ..... Présidente

M. Jean-François DUFRÊCHE ..... Examinateur

Mme Marie JARDAT ..... Directrice de thèse

M. Vincent DAHIREL ..... Invité

M. Pierre ILLIEN ..... Invité

Contents

Introduction

The context of this PhD work is the mesoscopic modeling of active matter. One of the challenges related to this topic is to understand how activity emerges from microscopic considerations. The basic identified ingredient in most experimental systems is the presence of anisotropy. The body of literature related to the theoretical study of anisotropic active particles is impressive. Yet, it is possible for an isotropic system to exhibit activity, and a few theoretical studies concern isotropic objects. Moreover, it usually lacks in microscopic descriptions of the medium in which active particles are moving. The propulsion of isotropic particles requires a spontaneous symmetry breaking of the environment of the particle, which leads to an anisotropic situation. The aim of this PhD work is to propose and to study a novel type of propulsion mechanism for an isotropic colloid.

The proposed model takes its origin in the identified hollow parts of the literature on the topic, which are the study of isotropic active particles in general, and the explicit description of the environment. The presented results in this work rely on numerical simulations using Brownian dynamics. Initially, the topic of this PhD project was the modeling of active polymers containing both active and passive monomers, with an explicit description of the environment. This reflects the ambitious aim for the applications of the proposed model, which is to be used to describe complex situations which often lack in microscopic insight. The present PhD work is devoted to the construction of the model, to the development of a Brownian dynamics code, and to the thorough understanding of the propulsion mechanism based on the analysis of the simulated trajectories. Also, the obtained results using an explicit description of the colloid environment are linked to those obtained with standard theoretical descriptions of active matter via effective Langevin equations.

The manuscript is organized as follows. Chapter 1 presents a panorama of existing

experimental and theoretical studies of active matter that allows one to understand the genesis of the proposed model and its pertinence. In Chapter 2, the model is introduced, and the numerical method used to simulate it is presented. First, the simplest system is investigated in Chapter 3, where only one isotropic colloid is surrounded by explicit solute particles. The influence of the parameters of the model on the dynamics of the colloid is thoroughly investigated, and the mechanism at the origin of activity is unraveled. In Chapter 4, the more complex situation of a suspension of active colloids is studied. Preliminary work on an extension of the model, where different types of active monomers are mixed together, is proposed in Chapter 5.

CHAPTER 1

Context

Contents

1.1 Brownian motion

1.1.1 Definition

In 1827, the botanist Robert Brown reported the erratic motion of organic as well as inorganic particles in water. It was found that in a solvent, the motion of particles originates from the collision with solvent molecules. The latter are agitated due to the effect of the temperature T of the system. As it was later understood, more generally, a particle of diameter σ in a fluid undergoes what is called Brownian motion, providing that its size is:

- small enough so that thermal energy ($k_{\mathrm{B}}T$) dominates the gravitational potential energy ($g\rho\sigma^4$), i.e :

$$g\rho\sigma^4 < k_{\mathrm{B}}T \Longrightarrow \sigma < \left(\frac{k_{\mathrm{B}}T}{\rho g}\right)^{1/4} \sim 10^{-6}\ \mathrm{m} \tag{1.1}$$

  where $g \sim 10\ \mathrm{m/s^2}$ is the gravity constant, ρ is the effective particle mass density, which has the same order of magnitude than the mass density of water, then $\rho \sim 10^3\ \mathrm{kg/m^3}$, and $k_{\mathrm{B}}T \sim 4\cdot 10^{-21}\ \mathrm{m^2 kg/s^2}$ is the thermal energy at room temperature.

- large enough, because the particle must be more massive than solvent particles, which implies $\sigma > 10^{-9}$ m.

This indicates that a colloid or a solute particle whose typical size is between a few nanometers to a few micrometers can be sensitive to Brownian motion. This is at least one order of magnitude larger than solvent molecules, which have usually a typical size $\sim 10^{-1}$ nm, for example water. Consequently, solvent molecules move much faster than the colloid or the solute particles and collide relentlessly with them. The solvent molecules in the solvent are densely packed. Therefore, the distance travelled between two collisions is comparable to their radius R. The time between two collisions τ_{C} is thus estimated by $\tau_{\mathrm{C}} \sim R/\sqrt{\langle v^2\rangle}$, where the velocity v is linked to the kinetic energy of a molecule $E_{\mathrm{kin}} = \frac{3}{2}k_{\mathrm{B}}T = \frac{1}{2}m\langle v^2\rangle$, with m its mass. The resulting force vector applied on a solute is thus changing with time, at a very small characteristic time $\tau_{\mathrm{C}} \sim 10^{-13}$ s, leading to the erratic motion of solutes.

1.1.2 A simple model to describe Brownian motion

Several scientists, such as Einstein or Smoluchowski, have contributed to build a framework for Brownian motion, whose theories have later been confirmed in experiments carried by Jean Perrin in 1910 [1]. Among them, Langevin has constructed an equation of

motion to describe a colloidal particle in a solvent. Due to the timescales separation between the dynamics of the solvent and that of solute particles, the solvent can be seen as a continuous medium. Derived from Newton's second law: $m\boldsymbol{a} = \sum \boldsymbol{F}_{\text{ext}}$, the Langevin equation proposes to describe the solvent implicitly and to account for its influence on the solute particle dynamics via two contributions: a friction force and a random force. The equation reads:

$$m\frac{\mathrm{d}}{\mathrm{d}t}\boldsymbol{v}(t) = -m\gamma\boldsymbol{v}(t) + \boldsymbol{\mathcal{R}}(t), \tag{1.2}$$

where m is the mass of the particle, $\boldsymbol{v}$ its velocity, and γ its friction coefficient. Langevin's equation takes into account the effect of the solvent by two terms:

- a friction force $-m\gamma\boldsymbol{v}(t)$, which slows down the solute particles.
- a random force $\boldsymbol{\mathcal{R}}$ called Langevin force, which represents the impacts with the solvent molecules randomizing the particles orientation. The Langevin force is a statistical description of the effect of the solvent. $\boldsymbol{\mathcal{R}}$ is a Gaussian white noise and satisfies :
  - $\langle\boldsymbol{\mathcal{R}}(t)\rangle = 0$, as the collisions are random with, in average, no preferred orientation.
  - $\langle\boldsymbol{\mathcal{R}}(t')\cdot\boldsymbol{\mathcal{R}}(t'')\rangle = 2dm\gamma k_{\mathrm{B}}T\delta(t'-t'')$, where d is the number of dimensions. The time between two collisions being very small in comparison to the other timescales of the problem, the correlation function of the noise is assumed to be a delta function. The friction coefficient γ also appears in the correlation function as both friction and random terms have the same origin: the solvent.

The relaxation time τ_{R} is the time needed by a colloid with an initial velocity v to be slowed down by a factor e. At $t \gg \tau_{\mathrm{R}}$ the particle velocity is zero. At the considered scale (between a few micrometers to a few nanometers), viscous effects dominate, which is characterized by a low Reynolds number, so that for a colloidal particle $\tau_{\mathrm{R}} \sim 10^{-9}$ s is very small. A usual approximation is to consider the overdamped limit of the Langevin equation, where inertial effects are neglected. In this case, $\frac{\mathrm{d}\boldsymbol{v}}{\mathrm{d}t} = 0$, and from (1.2) the equation becomes:

$$\boldsymbol{v}(t) = \frac{1}{m\gamma}\boldsymbol{\mathcal{R}}(t). \tag{1.3}$$

The overdamped Langevin equation is the starting point of Brownian dynamics simulations that are described in Chapter 2.

1.1.3 Transport properties of a Brownian particle

Transport properties of Brownian particles can be characterized by the translational diffusion coefficient D_t, which quantifies the space explored during a unit of time, and the rotational diffusion coefficient D_r, which quantifies the frequency of reorientation of the particle. The diffusion is affected by temperature: when T increases, the solvent molecules become more agitated, there are then more collisions, and the transport of colloids is enhanced. Conversely, due to the collisions, the solvent also slows down the movement of colloids. The Stokes-Einstein equation precises how the transport is dependent on the solvent property, namely its viscosity η, the particle size $R = \sigma/2$ and temperature. For a spherical particle in a Newtonian fluid (e.g.: water), the translational diffusion coefficient reads:

$$D_\mathrm{t} = \frac{k_\mathrm{B}T}{6\pi\eta R}. \tag{1.4}$$

The fluctuation-dissipation theorem links the transport due to the thermal energy $k_\mathrm{B}T$ to the friction γ through the following relation:

$$D_\mathrm{t} = \frac{k_\mathrm{B}T}{\gamma m}. \tag{1.5}$$

The rotational diffusion coefficient is:

$$D_\mathrm{r} = \frac{k_\mathrm{B}T}{8\pi\eta R^3}. \tag{1.6}$$

The mean squared displacement of the particle, which characterizes the size of the explored region, increases linearly with time and is proportional to the translational diffusion coefficient.

1.2 Active systems

1.2.1 What is activity?

In contrast to Brownian particles, which are passive, active particles are able to overcome thermal fluctuations. Active particles take energy from their environment and convert it into directed motion. Such a system is out of equilibrium. The difference can be easily understood by comparing trajectories of active and passive particles. On Figure 1.1, the trajectories obtained on a time window of equal duration from an experiment done by Howse et al. are shown [2]. On the top, the particles are passive, whereas on the bottom, the particles are active. The particles used in this experiment are Janus particles. Similarly as the Roman god, Janus particles possess two faces. One hemisphere catalyzes

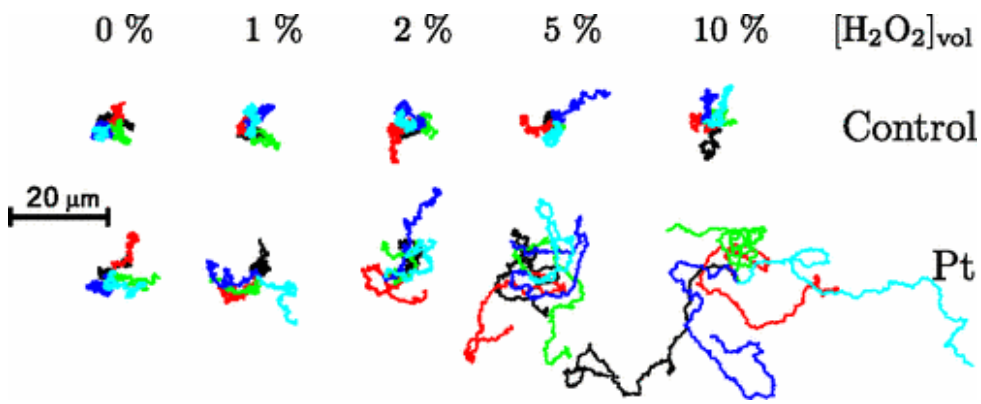

Figure 1.1: Example of trajectories from experimental data for a passive particle (top) and for an active particle (bottom). From left to right, the activity intensity of the active particles is enhanced. Extracted from [2].

H_2O_2, which serves as a fuel for propulsion. The activity intensity is thus proportional to the concentration of H_2O_2, increased from left to right. For the most active case (last column on the right) the difference is striking: while the motion of the passive particle on the top exhibits the characteristics of erratic motion, the active particle, on the bottom, clearly exhibits a persistent motion. This results in enhanced space exploration. The mean squared displacement of the particle is proportional to an effective diffusion coefficient, which is higher than the one of passive particles predicted by the Stokes-Einstein equation (Eq. (1.4)).

In the light of this example, an active colloid can be characterized by its mean squared displacement which is different from its equilibrium counterpart. Particularly, its diffusion coefficient at long time is higher.

1.2.2 Examples of active systems

In nature, activity is ubiquitous and exists at all scales. In the biological world, cells are overflowed with proteins or macromolecules which use activity to achieve various tasks: find nutrients, carry molecular cargo, avoid toxins etc. This metabolism is at the origin of the cell motion itself. One of the main source of energy involved in biological processes is ATP. An example of an ATP-based molecular motor is depicted on Figure 1.2a. ATP is hydrolyzed in ADP, which generates the rotation of the top basis of the motor. This motor can be linked to a flagellum, which produces the motion of bacteria such as *E. Coli* [3]. Other examples of living microorganisms that self-propel are shown on Figure 1.2b. Their swimming strategies have been detailed from a hydrodynamic perspective in [4].

Although progress has been made in the characterization of the mechanism at the origin of the propulsion in living systems, numerous questions remain unanswered. Bi-

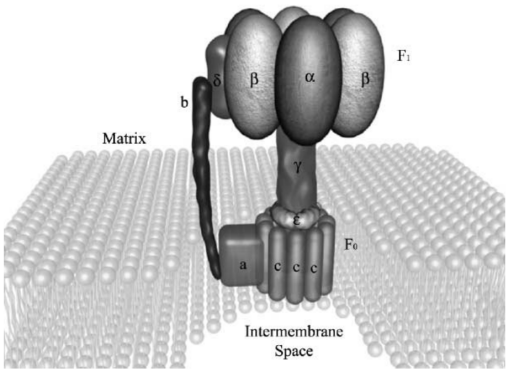

(a) ATP based molecular motor, named F_0F_1-ATP synthase, extracted from [3].

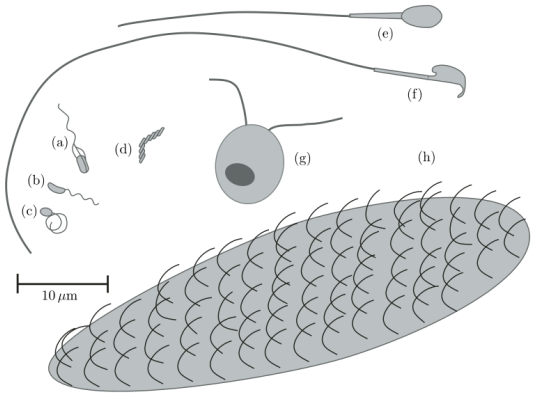

(b) Different biological micro-swimmers extracted from [4]. (a)-(d) bacteria, (e)-(f) spermatozoa, (g) alga, and (h) unicellular organism.

Figure 1.2: Examples of living organisms and artificial microswimmers.

ological swimmers evolve in complex environments, which makes the understanding and the characterization of activity difficult. Inspired by nature and taking advantages of the current knowledge, researchers have created man-made micro or nanoswimmers. On the one hand, the study of artificial swimmers in a controlled environment can bring a new insight on the analysis of activity in living systems. On the other hand, these artificial objects can be designed and tuned for the purpose of diverse applications. The latter has received a growing interest for biological applications such as drug delivery [5] or for the industry and soil cleaning [6] to name just a few examples. Experimental work has succeeded to create artificial swimmers of various shapes: spherical particles, rods, L-shape like particles [7]. Successful experiments of a nanomotor carrying cargos have also been reported [8].

The diversity of existing systems is displayed on Figure 1.3 which shows living (yellow diamonds) as well as artifical (orange circles) microswimmers of different sizes, shapes and propulsion speeds.

1.2.3 Propulsion mechanisms

Mechanism based on phoretic effects

Several mechanisms have been identified as leading to the propulsion. One of the promising route is phoretic motion, which refers to a particle driven by a gradient of an external field Φ. The motion of the colloid is caused by the interaction of the ambient fluid, namely the solvent, with the solute particles. Due to the colloid-solute particles interaction at the colloid surface, there is an interfacial layer where the solute particles

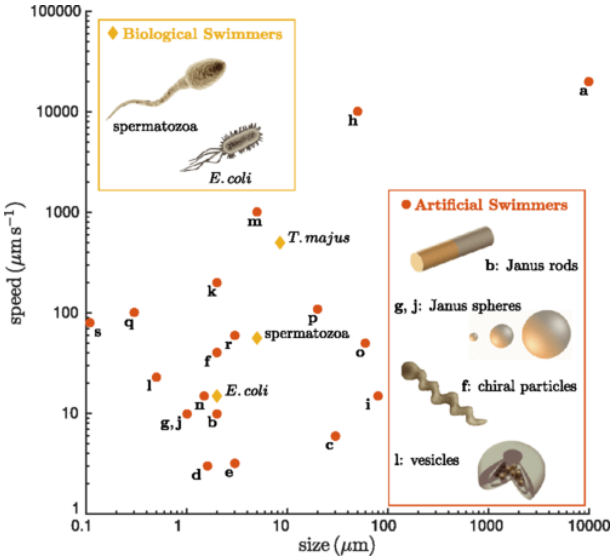

Figure 1.3: A map which summarizes the main active systems studied in the literature and sorts them according to their propulsion speed and size. Examples of living microswimmers are represented by yellow diamonds and artificial particles by orange circles. Extracted from [9].

structure is modified. This induces a tangential slip velocity v_s of the solvent in the interfacial region. The system is force free, which set the colloid in motion. This has been demonstrated by Anderson, who has predicted that the velocity of a colloid is linked to the slip velocity. He demonstrated that v_s is proportional to the gradient at the surface of the particle [10]:

$$v_s = \mathcal{M} \nabla_s \Phi. \tag{1.7}$$

This is derived from the low-Reynolds limit of the Navier-Stokes equation, namely the Stokes equation. The mobility $\mathcal{M}$ depends on the type of the considered phoretic effect. In the case of diffusiophoresis, when a particle is in a gradient of concentration c, the Stokes equation for the solvent velocity $\boldsymbol{v}$ is written:

$$-\eta \nabla^2 \boldsymbol{v} = -\nabla p - c \nabla U, \tag{1.8}$$

where p is the pressure field, and U is the interaction potential between the solute particles and the colloid. In order to find $\mathcal{M}$, some approximations are made:

- The concentration of solute particles follows a Boltzmann-like distribution, i.e. $c \propto \mathrm{e}^{-\frac{U}{k_\mathrm{B} T}}$.
- The interaction potential is short-ranged and the interaction layer is much smaller than the colloid size.
- The velocity and the potential are functions of the radial component only.

- In the most simple approach, the advection is neglected as small Péclet numbers are considered. The Péclet number is the ratio between advection over diffusion, and is denoted by Pe.

This leads to:

$$\mathcal{M} = \frac{k_B T}{\eta} \lambda^2,$$

where $\lambda^2 = \int_0^\infty \left(1 - e^{-U(r)/(k_B T)}\right) r dr$ is the Derjaguin length which include the effect of the interactions between the solute particles and the colloid. λ^2 can either be positive or negative depending on the nature of the interactions (repulsive or attractive) [11]. Other derivations were made considering a temperature gradient (thermophoresis) and an electric gradient (electrophoresis). In the original work of Anderson, the gradient was imposed in the colloid environment by an external source.

Recently, a more interesting perspective has been exploited: a gradient generated by the particle itself, what is referred to as self-phoretic effects. To do so, the particle needs to have some built-in asymmetry. Particularly, particles with asymmetric surface properties have been designed and studied, such as Janus particles. An example of a rod-like and of a sphere-like Janus particle is shown on Fig. 1.4. Self-phoretic effects have been observed in numerous experiments that are reviewed in [9]. Here are listed a few examples where Janus particles generate a gradient:

- Self-electrophoresis: an example is depicted Fig. 1.4-top. A bimetallic nanorod, half coated with platinum and half coated with gold, in a hydrogen peroxide solution shows propulsion. The hydrogen peroxide is oxidized at the platinum end : $H_2O_2 \rightarrow 2H^+ + 2e^- + O_2$. The protons and electrons are then consumed at the gold end with the reduction of the hydrogen peroxide : $H_2O_2 + 2H^+ + 2e^- \rightarrow 2H_2O$. The two reactions create an ionic flux, producing the propulsion of the nanorod [12]. This experiment corresponds to the letter **b** on the graphic shown in Figure 1.3.

- Self-thermophoresis: a Janus particle, half coated with silica and half coated with gold, is considered. A laser beam irradiates the solutions in which the particles are placed. Only the golden cap of the particle heats up, generating a gradient of temperature around it, which makes the particle self-propel [13]. This experiment is represented by the point labelled **g** on Figure 1.3.

- Self-diffusiophoresis: the mechanism is illustrated on Fig. 1.4-bottom. A polystyrene sphere, half coated with platinum, is in a hydrogen peroxide solution. The platinum side catalyzes the reaction : $H_2O_2 \rightarrow H_2O + 1/2O_2$ creating a gradient of concentration which leads to the self-propulsion of the particle [2]. This experiment

corresponds to the point labelled **d** on Figure 1.3. The trajectories reproduced on Fig. 1.1 were extracted from the same article.

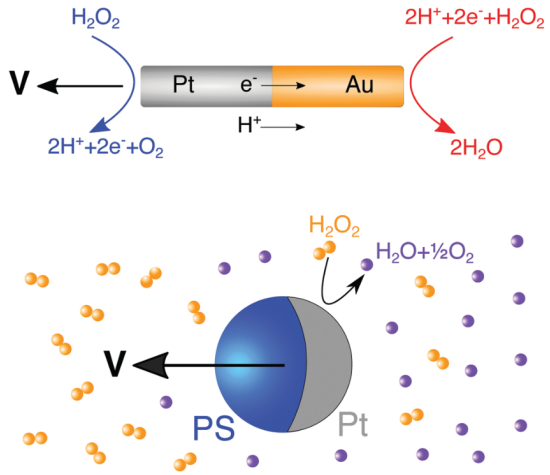

Figure 1.4: Top: Example of self-electrophoresis. A Janus nanorod, half coated with platinum and half coated with gold, self-propels in a hydrogen peroxide solution. At the platinum end, the hydrogen peroxide is oxidized and at the other end it is reduced. Bottom: Example of self-diffusiophoresis. A Janus polystyrene sphere, half coated with platinum, is in a hydrogen peroxide solution. The hydrogen peroxide is decomposed at the platinum end. Extracted from [14].

Mechanism based on a phase separation

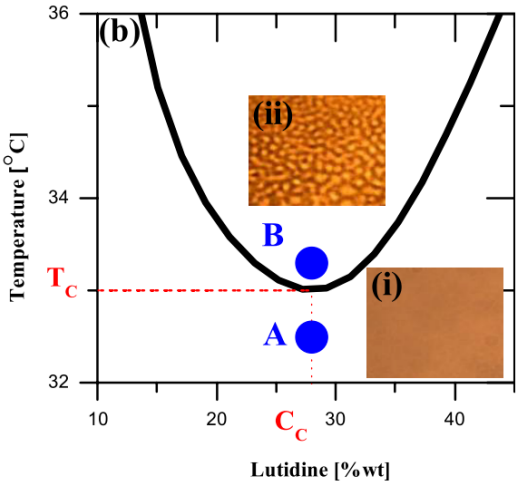

Figure 1.5: Phase diagram of a water lutidine mixture, the demixing curve is represented in the plane (temperature; concentration of lutidine in the mixture). Extracted from [15].

An alternative route for locomotion has been explored: propulsion caused by a phase separation. In contrast to experiments involving a one-way reaction, such as the decom-

position of hydrogen peroxide, the mechanism described here is not fuel-limited. The set-up is the following: a Janus particle half coated with gold is in a binary mixture of water lutidine. The gold cap is either made hydrophobic or hydrophilic. The mixture is at the critical concentration and just below the critical temperature of demixing as illustrated on the water lutidine phase diagram by the A point on Figure 1.5. The system is illuminated, the light is absorbed by the gold cap. The gold cap heats up, which raises the local temperature up to above the critical temperature, represented by the B point on Fig. 1.5. Therefore, the binary mixture phase separates. If the golden cap is hydrophilic (resp. hydrophobic), a water (resp. lutidine) rich phase forms on this side. The gradient of concentration leads to self-propulsion, which have been observed in [16, 15] in a quasi-2D experiment and in 3D in [17, 18, 19].

1.3 Characterization of the physical principles at the origin of self-propulsion

1.3.1 Continuum description theories

Theoretical descriptions have been proposed to decipher the origin of propulsion of anisotropic particles. Anderson has shown that a particle in a gradient will self-propel due to interfacial effects. On this basis, analytical derivations have been proposed to predict what would be the propulsion speed in a system where the particle itself generates the gradient. In these calculations, the solute particles are described in a continuous limit considering the concentration field $c(\boldsymbol{r}, t)$. Most often, the concentration is supposed to be stationary: $c(\boldsymbol{r}, t) = c(\boldsymbol{r})$. A simple model, considering a colloid with an active site at its surface, is investigated in [20]. Solute particles are emitted from the active site. The concentration field can be found using a diffusion equation and its value is substituted in Eq. (1.7) to find the propulsion velocity. In another article [21], the authors find that the velocity depends on the surface properties through: the mobility and the activity mechanism. The conditions for an optimized propulsion are discussed. Such model has also been studied under confinement [22] or in an active medium [23]. In [24], a squirmer model is used to study the optimal propulsion of cells that is linked to their feeding strategy. The computations are done under some hypothesis: the interaction layer where the solute particles interact with the colloid is assumed to be much smaller than the colloid size, the advective effects are neglected which decouples the Stokes equation from the diffusion equation.

More recently, these usual approximations have been challenged in [25]. A more general phoretic framework, which includes advective effects and arbitrary surface chemical

properties, have been considered. It has been shown that advective effects enhanced the swimming velocity, while the reactive effects penalize the propulsion. An analogous derivation has been done in [26] for a Janus particle which self-propels due to thermophoresis. The authors characterize the flow pattern and point out the limit of the model. Still based on the slip velocity defined by Anderson, in [27] the authors derive the mobility in a case of phase separation due to a local increase of the temperature. The calculations of [28] include the effects of advection and complete the theoretical description. The authors find that conversely to the work of [27] the propulsion does not arise from a slip velocity but from perpendicular forces to the surface. An alternative approach to study this system suggests that the motion is not simply due to an asymmetric concentration of solute particles, but also to an asymmetric dissipation [29].

1.3.2 Particle-based numerical simulations

In order to be more precise than continuous descriptions, which do not take into account microscopic details, the use of numerical simulations have brought new insights to the understanding of the problem. In particle-based simulations, the solute particles are described explicitly and the solvent is implicit. However, though their interactions with the colloidal particles are modeled, the interactions between solute particles are usually not taken into account. The chemical reaction, which is supposed to occur at the colloid surface, is also modeled and it is shown that the type of considered reaction is important. In [30], the authors demonstrate that an exothermic reaction will lead to propulsion due to self-thermophoresis while a dissociation reaction leads to self-diffusiophoresis. In [31], the authors consider a dimer: one of the sphere catalyzes a reaction, the other does not. The gradient of concentration generated by this asymmetric reaction results in self-propulsion. The propulsion of a dimer has been investigated thoroughly: the parameters which have an influence on the self-propulsion are characterized [32], the motion of the active dimer is studied in an active medium [33] and in an external chemical gradient [34].

1.4 Is anisotropy necessary to achieve self-propulsion?

1.4.1 Symmetric contributions

So far, all the examples I mentioned were systems where the colloid is anisotropic. In the case of an isotropic colloid releasing isotropically a solute, the fluctuations of the solute concentration due to thermal effects would lead to a transiently anomalous diffusion before reaching the diffusive regime. The measured diffusion coefficient is however larger than the one predicted by Eq. (1.4), and is shown to be an increasing function of the

release rate k of solute particles [35]. This prediction was then tested in Monte Carlo simulations of an isotropic "chucker" which emits isotropically solute particles [36]. The authors have not captured the anomalous diffusion but have observed a larger diffusion coefficient. D_t is however a non-monotonic function of the rate k. For large values of k, the crowding induced by the solute particles slows the colloid down and D_t decreases with k. Nevertheless, these effects are transitory. The fluctuations perturbate the short-time dynamics, at long times the system returns to an isotropic state.

1.4.2 Isotropic systems

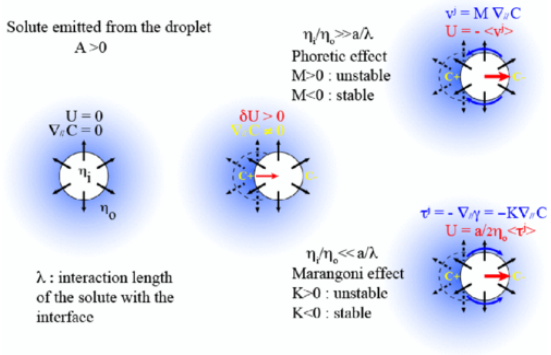

(a) Schematic representation of the mechanism leading to the self-propulsion of water droplets extracted from [37].

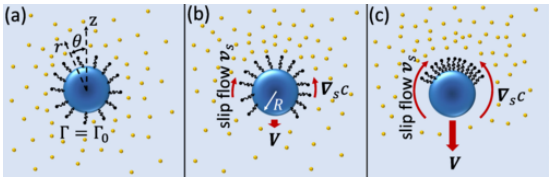

(b) Schematic representation of the mechanism leading to the self-propulsion of colloid on which mobile enzymes that emit a solute particles are attached, extracted from [38].

Figure 1.6: Examples of spontaneous symmetry breaking mechanisms.

Recently, it was demonstrated that anisotropy is not necessary to achieve self-propulsion. In contrast to the previous examples, it is shown that in an unstable isotropic system, the fluctuations are amplified. The symmetry is spontaneously broken, generating at long time an anisotropic situation where the propulsion velocity is higher than the predicted equilibrium velocity and a transient ballistic behavior is observed. A more elaborated description of the problem is required, in order to understand the origin of the symmetry breaking. In particular, the equations must include the interplay between the colloid motion and the advection of the solute particles. In [39], the authors demonstrate that the non-linear coupling between the Stokes and the advection-diffusion equations leads to instabilities. A small perturbation of the system, such as the position of the colloid which fluctuates, creates a concentration gradient in its vicinity. Under suitable conditions, the fluctuations are amplified and maintained, leading to long-time self-propulsion. Unstable swimming modes exist above a critical Péclet value for repulsive interactions combined with a surface which emits solute particles, or for attractive interactions combined with absorption of solute particles at the colloid surface. The critical Péclet number implies

a critical particle radius. The mechanism was observed in a simulation where a colloid catalyzes a reaction isotropically. The product particles interact with the colloid more repulsively than the reactant particles. Density fluctuations lead to the self-propulsion of the colloid [40]. On the ground of the phoretic description, in [41], the authors have derived a simple point source model also valid for interfacial swimmers. An experimental set-up using camphor disks confirms the predictions. Numerous experiments have also reported the self-propulsion of pure water droplets [42, 37]. A link was made with the observations of [39], with Marangoni effects, which denote a flow induced by a gradient of surface tension, in addition to the phoretic effects. The droplets isotropically emit solute particles. Under suitable conditions, fluctuations of the solute concentration are amplified and the anisotropy is self-sustained leading to long-time propulsion as depicted on Figure 1.6a. The conditions for the self-propulsion of droplets are reviewed in [43]. Again, spontaneous symmetry breaking was also reported in [38] due to a non-linear coupling in the equations. A colloid has mobile enzymes attached to its surface. The enzymes catalyze a reaction releasing small solute particles which leads to a phoretic flow. The enzymes distribution equation is thus coupled to the solute concentration due to advection effects. A small perturbation generates an imbalance of product around the colloid. For some parameters, the inhomogeneities are maintained and the colloid self-propels as depicted on Figure 1.6b.

1.5 Descriptions of activity at the mesoscale

1.5.1 Coarse-grained descriptions for a single active particle

For the study of long-time effects, the microscopic description of the origin of the propulsion may not be necessary [44]. The dynamics can be coarse-grained by describing only the colloid and not considering the solute particles. In these models, the activity is postulated and added as an external force on the particle. The persistent motion is characterized by a propulsion speed v_0 along an orientation vector $\boldsymbol{n}$. Most studies consider simple problems where v_0 is a constant and the dynamics is two-dimensional. These models are particularly relevant to study collective motion of active particles. Indeed, the study of collective properties requires a large number of particles in the system, which is numerically very expensive.

The run-and-tumble particle (RTP) model captures well the motion of motile bacteria, such as *E. Coli*. Such organism perform a run-and-tumble dynamics, which consists of a succession of straight trajectory at a constant speed v_0 followed by an abrupt reorientation event which occurs at Poisson-distributed times [45].

In contrast, artificial swimmers such as Janus particles exhibit another type of motion which is well described by the active Brownian particle (ABP) model. The activity term $v_0\boldsymbol{n}$ is added to the overdamped Langevin equation. The ABP particles reorient smoothly due to rotational diffusion [46].

A more elaborated model has recently received attention, the active Ornstein-Uhlenbeck particle (AOUP) model. The equation of motion bears the same structure as for the ABP model, but the velocity fluctuates as an Ornstein-Uhlenbeck process. This model is particularly relevant to take into account a complex environment such as a bacterial bath in which the interactions with a colloidal particle would lead to a change in the amplitude and orientation of the velocity [47, 48].

1.5.2 Collective effects

Interacting active particles exhibit a wide variety of collective behaviors. It is interesting to see how the propulsion mechanisms evidenced in the previous paragraphs are affected in this context. For instance, isotropic particles, whose characteristics are not suitable for spontaneous symmetry breaking, will not self-propel by themselves. However, an assembly of such particles is shown to form a propelling cluster [49]. Agglomerates of Janus particles also exhibit a rich variety of trajectories such as spiraling [50]. The rich phenomenology of collective motions is exemplified in biological systems. For instance, active turbulence has been observed in a dense suspension of bacteria [51], or actine filaments driven by molecular motors show polar patterns [52]. In particular, clusters formation are detected in bacterial suspensions [53].

Experimental setups of artificial active colloids also exhibit clustering [54, 55, 56, 57]. A colloidal suspension of Janus particles is studied under gravity by Palacci et al. [58]. The self-propulsion is achieved by adding H_2O_2 in the system. At the Pt-coated side of the particle, the chemical reaction decomposing the hydrogen peroxide occur, creating a gradient of concentration. In the absence of H_2O_2, the colloids are passive and form a dense phase at the bottom. In contrast, when activity is triggered, in addition to the dense phase, different density regimes are realized. At low and intermediate densities, there is a phase separation between a gaslike phase and clusters. The clusters are dynamical, as particles leave, new ones enter the cluster. Clustering and motility induced phase separation seems to be a generic feature of active systems [59].

Using the RTP or the ABP model, which are found to be in this case equivalent [60], a self-trapping mechanism is discussed. The authors point out the role played by the propulsion speed v_0 relatively to the rotational diffusion D_r. Due to the persistent motion, the particles block each other when colliding, until being freed by rotational diffusion. The simplicity of the model underlines that the mechanism is athermal and

does not need effective attraction between particles [45]. The effective forces exerted by the other particles on a tagged particle can be described by a mean force, which can be decomposed into a contribution along the particle orientation and along the density gradient. This evidences an instability region in which particles tend to swim towards high density region, hence the phase separation [61].

Numerical simulations of ABP particles are employed to characterize the phase transition between the different states observed experimentally. A freezing transition is evidenced as in equilibrium systems but the shift occurs at a lower density [62]. Using the relevant parameters in this context: the surface fraction ϕ and the Péclet number Pe, a phase diagram is drawn [63, 64]. In this context, the Péclet number quantifies the activity intensity over the noise strength. Simulation reveals that eventually the clusters condense in a unique large one. In experiments where the self-propulsion is achieved by the demixing of water-lutidine, the dynamics of the system can be studied on larger timescales as the experiment is not limited by the fuel. Under those conditions, the condensation state has been observed [65]. 3D simulations also exhibit clustering [66, 67].

More elaborated theoretical work includes hydrodynamic and phoretic effects. Indeed, each particle generates a flow field as well as a concentration gradient in case of diffusiophoresis. This perturbs their neighbors near-field, which has been shown to play a significant role in determining pattern formation [68]. A polar ordering has for example been observed in the collective motion of self-propelling liquid droplets. Moreover, two phoretic swimmers can either attract or repel each others [69, 49, 70]. Including the phoretic effects, a rich phenomenology of structure formations is found [71, 72, 73]. Simulation using particle-based methods include both phoretic and hydrodynamic effects have been carried [74, 75] which complete the framework.

1.6 A new route for locomotion?

Despite the impressive body of literature on active colloids, the isotropic case has received less attention. Moreover, from the literature review, the lack of microscopic description stands out. The solute particles are either described in a continuous limit or, if described explicitly, their interactions are not taken into account. The role of interactions on the dynamics at a microscopic scale is a typical questioning in the chemical physics community. It is at the heart of the research thematics in the PHENIX laboratory, where I carried out my PhD work. The arrival of a new member, Pierre Illien, who has a background in active matter, has led to a new research direction between my three supervisors. The technics of multiscale modeling are already well established in the laboratory. Especially, Marie Jardat and Vincent Dahirel have an expertise on mesoscopic simulation

methods such as multi-particle collision dynamics (MPCD) or Brownian dynamics (BD). The idea of exploring an isotropic system where the symmetry breaking would emerge from the interaction between solute particles have then naturally emerged and is at the heart of my PhD work.

The goal of this PhD work is to construct a minimal model in which activity would emerge from interactions within the environment of an isotropic colloid. The developed strategy during this work in order to break the symmetry relies on the interactions between solute particles: under suitable conditions, a phase separation can occur near the colloid, which creates density fluctuations. First, the model has been designed, the interactions have been carefully chosen, and the relevant parameters defining the phase separation have been identified. I have developed a home-made code to match the specificities of the designed model. The analysis of the simulations revealed that activity emerges. The mechanism has been then characterized and compared to the literature. Secondly, simulations show that activity still persists when there are many self-propelling colloids in the system. The results have been compared to usual coarse-grained simulations that do not account for solute particles explicitly as an attempt to link explicit and implicit models.

CHAPTER 2

Model and simulation methods

Contents

Summary

In this chapter, the model and the methods are presented. First, the general principle of the design of the model is explained, and the involved parameters are defined (the geometry of studied systems, the choice of the interaction potentials, and the modeling of the reaction). The model is simulated using Brownian dynamics (BD). This numerical method is based on the integration of an overdamped Langevin equation. A home-made BD code was developed, whose numerical implementation is detailed in this chapter. BD results will be confronted to simulations of active Brownian particles, denoted by BD-ABP in what follows. The equations used for the ABP model, as well as the numerical implementation of the BD-ABP code, are also explained in this chapter. Both codes are validated by running simulations of simple systems, for which results exist in the literature. Finally, the simulation procedure is described.

2.1 Introduction

In this chapter, I will introduce the model I studied and present the simulation method used, called Brownian dynamics (BD). This numerical method is based on the integration of coupled overdamped Langevin equations (see Chap. 1). In contrast, a common approach in the literature to model active particles relies on a Langevin equation that contains an additional force or noise generating activity and is known as the active Brownian particle model (ABP) (see Chap. 1). In the ABP model, solute particles are modeled implicitly. In following chapters BD results will be confronted to simulations of active Brownian particles, denoted by BD-ABP in what follows. The chapter is organized as follows: In Section 2.2, the model is presented, from a general perspective to a detailed description of the parameters of the system. Section 2.3 describes the overdamped Langevin equation used for the Brownian Dynamics code. The Langevin equation of the ABP model is described in Section 2.4. Section 2.5 explains the numerical implementation of the BD and BD-ABP algorithm, as well as the quantities computed during the simulation. I choose the appropriate parameters to simulate the model in Section 2.6. In Sections 2.7 and 2.8, I validate my code comparing some results with the literature. Last, in Section 2.9, I describe the simulation procedure.

2.2 Model of an isotropic colloid in a phase-separating environment

2.2.1 General considerations to design the model

In the case of an isotropic colloid, it has been shown that a symmetry breaking is necessary so that activity emerges [39]. This occurs when fluctuations near the colloid are maintained, leading to a spontaneous polarization of the environment of the colloid. As a result, the colloid self-propels. The idea of this PhD work, based on the literature review given in the preceding chapter, is to study a model where the symmetry breaking would arise from the interactions between solute particles. The effect of the latter have indeed always been left aside. That is why we choose to describe solute particles explicitly. Therefore, the model consists of one or several isotropic colloids in a bath of smaller particles, denoted by solute particles in what follows, embedded in an implicit solvent. The model is mainly studied in two dimensions (2D). The three-dimensional case is briefly studied in order to confirm that the results obtained in 2D still hold in 3D.

How can interactions create strong fluctuations around the colloidal particle? According to the nature of the interaction potential between particles, they organize as a gas,

a liquid or a solid. Typically, with a purely repulsive interaction potential, particles that are not closely packed form a gas, but can separate into low and high density phases if short-range attractions exist. The most used interaction potential to describe liquids is the Lennard-Jones (LJ) potential. It involves two parameters: the particles diameter σ and the depth of the minimum ε. According to these parameters and to the density of particles, a liquid-gas phase separation can arise. At low $\varepsilon/k_{\mathrm{B}}T$, the fluid is a gas. At sufficiently high $\varepsilon/k_{\mathrm{B}}T$, the fluid can separate into two phases: one dilute, typical of a gas, and one dense, typical of a solid or a liquid. Based on this knowledge of the role of interactions, our main research hypothesis is that strong density fluctuations of a phase separating LJ fluid can be a source of symmetry breaking, leading to activity. To test this hypothesis, we must design a model where the colloid is surrounded by a phase separating LJ fluid. The situation of a colloid in a LJ fluid close to a phase separation has already been studied by simulation [76, 77]. In this situation, the dynamics of the colloid is affected, but it does not present activity. We think that in such models, the colloidal particle may not feel the fluctuations, since the latter may be located far from the colloid surface. Therefore, in the proposed model, the LJ fluid is confined near the colloid. I will denote by B the solute particles forming the LJ fluid. Far away from it, solute particles would interact purely repulsively forming a gas phase, denoted by A in what follows. In this case, a LJ fluid confined in the vicinity of a colloid, the behavior is expected to be different.

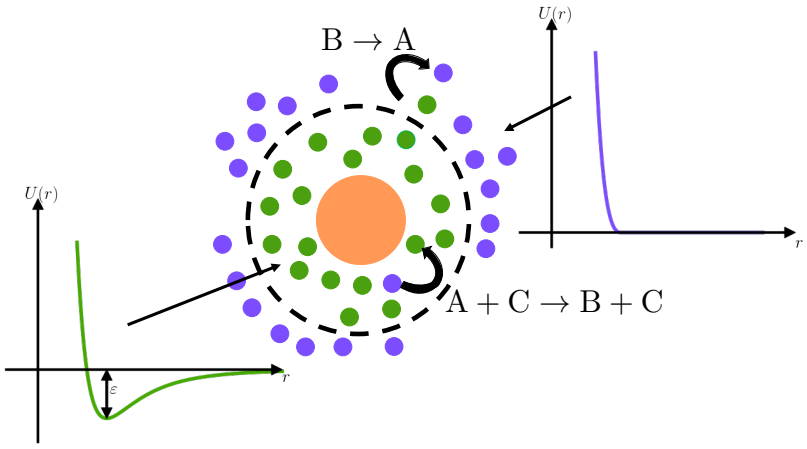

Figure 2.1: Drawing of the designed model. The sketch describes what typically occurs in the vicinity of a colloid: the isotropic colloid catalyzes the reaction $\mathrm{A} + \mathrm{C} \rightarrow \mathrm{B} + \mathrm{C}$. Farther, in the bulk, the reverse reaction $\mathrm{B} \rightarrow \mathrm{A}$ takes place. The solute particles A, in violet, interact with each other through a purely repulsive potential. Conversely, the solute particles B, in green, interact with each other through a LJ potential where short-range interactions are controlled by ε.

How can one design a simple model where a LJ fluid is confined close to a colloidal particle? Based on the idea that, in literature, the surface of active colloids often plays the role of a catalyst [14], we have considered the simplest route, where the LJ fluid would originate from the colloid. To this end, the colloids catalyze the reaction A+C $\rightarrow$ B+C in their vicinity. Once the LJ fluid formed, in order to maintain the fluid close to the surface of the colloid, the reverse reaction B $\rightarrow$ A takes place in the bulk. This also mimics a real system in which solute particles diffuse. The ones near a colloid, of type B, would displace and disperse in the repulsive bath, while the one far away would come closer. There is then a LJ fluid near the colloid in the reaction area, and a gas further away from the colloid. This describes an out-of-equilibrium situation, which is maintained by the reverse reaction, as the latter ensures a constant supply of reactant for each colloid to catalyze the reaction. The model is schematically represented on the Figure 2.1.

2.2.2 Presentation of the key parameters of the model

Geometric considerations

The system is two-dimensional and is constituted of N_{C} colloids, N_{A} solute particles of type A and N_{B} solute particles of type B embedded in a solvent bath. In total, there are $N = N_{\mathrm{A}}+N_{\mathrm{B}}$ solute particles of the same diameter σ_{A} and N_{C} colloids of diameter σ_{C}. The $N+N_{\mathrm{C}}$ particles are in a square simulation box of size l_{box}. Periodic boundary conditions are used to model a bulk situation. The solute density of the system is $\rho = N/l_{\mathrm{box}}^2$ and is one of the parameters determining the state of the LJ fluid.

Interaction potentials

As previously stated there are two types of interaction between the solute particles. Consequently, there are two interaction potentials used: the Lennard-Jones potential to model interactions between solute particles of type B, and the Weeks-Chandler-Anderson (WCA) potential to model purely repulsive interactions between solute particles of type A [78]. The LJ potential contains an attractive part as well as a repulsive part. The attraction intensity, adjusted by the parameter ε, controls the phase of the LJ fluid. Therefore, ε is a key parameter of the model along with the solute density ρ. The LJ potential is a function of the distance between two particles $r_{ij} = |\boldsymbol{r}_i - \boldsymbol{r}_j|$, where $\boldsymbol{r}_i$ (resp. $\boldsymbol{r}_j$) is the position of the particle i (resp. j), and is described by the following equation:

$$U_{\mathrm{LJ}}(r_{ij}) = \begin{cases} 4\varepsilon \left[\left(\frac{\sigma_{\mathrm{A}}}{r_{ij}}\right)^{12} - \left(\frac{\sigma_{\mathrm{A}}}{r_{ij}}\right)^{6} \right] & \text{if } r_{ij} \leq 2.5\sigma_{\mathrm{A}}, \\ 0 & \text{otherwise.} \end{cases} \tag{2.1}$$

A cutoff is set for $r_{ij} \geq 2.5\sigma_{\mathrm{A}}$ to reduce computational costs, since the long-range effects are here negligible [79]. The WCA potential is a truncated and shifted version of the Lennard-Jones potential to keep only the repulsive part, which yields:

$$U_{\mathrm{WCA}}(r_{ij}) = \begin{cases} 4\varepsilon' \left[\left(\frac{d_{ij}}{r_{ij}}\right)^{12} - \left(\frac{d_{ij}}{r_{ij}}\right)^{6} \right] + \varepsilon' & \text{if } r_{ij} \leq 2^{1/6} d_{ij}, \\ 0 & \text{otherwise.} \end{cases} \tag{2.2}$$

In the WCA potential, ε' adjusts the repulsive intensity, and is a constant in the model. d_{ij} represents the minimum interparticle distance to avoid interpenetration: $d_{ij} = (\sigma_{\mathrm{A}}+\sigma_{\mathrm{C}})/2$ if i or j is the colloid, and $d_{ij} = \sigma_{\mathrm{A}}$ otherwise. The interaction between solute particles of type A and solute particles of type B as well as the interactions between the colloid and all the solute particles are modeled with the WCA potential. To sum up: A-A, A-B, A-C and B-C are purely repulsive interactions modeled using the WCA potential, while B-B interactions are modeled using the LJ potential.

Modeling of the reaction

The colloid isotropically catalyzes the reaction $\mathrm{A} + \mathrm{C} \rightarrow \mathrm{B} + \mathrm{C}$. The reaction takes places in a reaction area of radius r_{cut} centered around the colloid. Particles of type A are transformed into particles of type B after an average time τ_{AB}, when at a distance smaller than r_{cut}. Conversely, outside this reactive area, B is transformed back into A after an average time τ_{BA}. The rates are $k_{\mathrm{AB}} = 1/\tau_{\mathrm{AB}}$ for the $\mathrm{A} \rightarrow \mathrm{B}$ reaction and $k_{\mathrm{BA}} = 1/\tau_{\mathrm{BA}}$ for the $\mathrm{B} \rightarrow \mathrm{A}$ reaction. In the model, the rates are chosen so that the reactions are almost instantaneous in comparison to the other timescales of the problem. The radius of the reaction area is another key parameter of the model. Indeed, contrary to a bulk situation, the phase diagram depends on the geometry of the reaction area, controlled here by r_{cut}.

Conclusion on the key parameters

To conclude, the constructed model leads to the typical situation represented Fig. 2.2. Close to the colloid, the solute particles of type B, in green on the figure, form a LJ fluid. Further, the solute particles interact with each other purely repulsively and are of type A, represented in violet on the figure. From this model, three parameters emerge, which will influence the phase of the LJ fluid: ρ, ε and r_{cut}. Their effects are analyzed in the next chapter.

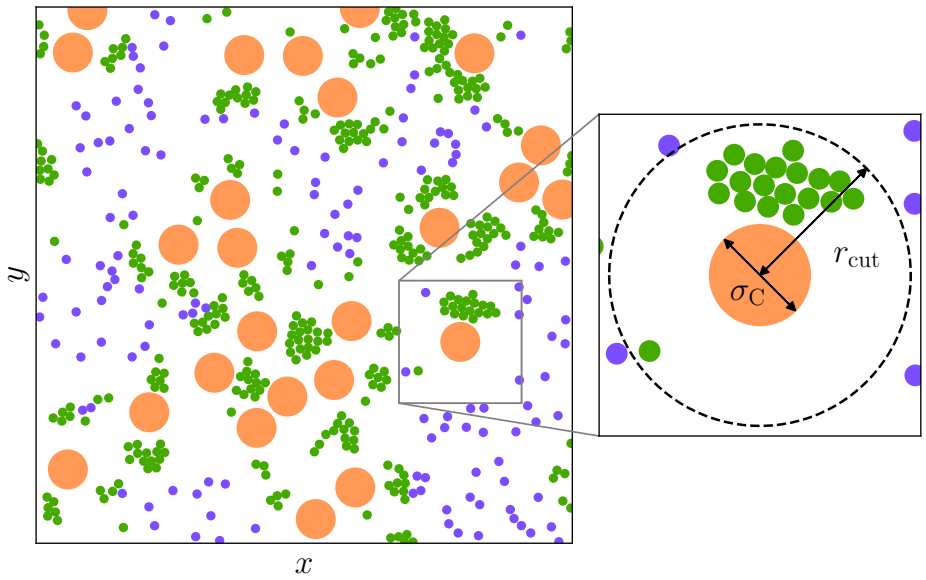

Figure 2.2: Snapshot of the system where solute particles of type A (violet) and B (green), and colloids C (orange) are in a periodic square box. Zoom on one colloid, where the reaction $\text{A} + \text{C} \to \text{B} + \text{A}$ takes place in the reaction area of radius r_{cut}.

2.3 Langevin equation for Brownian motion

In this section I will present the equations used to simulate the dynamics of the model, beginning with the general framework of the Langevin equation to its overdamped limit, then presenting the numerical integration of the equations and concluding with the dimensionless version.

2.3.1 The Langevin equation

For each of the $N + N_{\text{C}}$ particles of the system, the Langevin equation reads as follows:

$$m_\alpha \frac{\mathrm{d}}{\mathrm{d}t}\boldsymbol{v}_i(t) = -m_\alpha \gamma_\alpha \boldsymbol{v}_i(t) + \sum_{i \neq j} \boldsymbol{F}_{j \to i}(t) + \boldsymbol{\mathcal{R}}_i(t), \tag{2.3}$$

where $\boldsymbol{v}_i$ is the velocity of the considered particle, m_α is the mass and γ_α the friction coefficient of the particle of type α. $\boldsymbol{F}_{j \to i}$ is the interparticle force. The displacement of each particle is measured by the distance traveled by the particle from its initial position $\boldsymbol{r}(0)$ and is defined as $\Delta\boldsymbol{r}(t) = \boldsymbol{r}(t) - \boldsymbol{r}(0)$. Calculations to characterize its dynamics considering only one particle are detailed in Appendix C and lead to the following results:

- The mean displacement is shown to be zero as the motion of the particles is random, $\langle \Delta\boldsymbol{r}(t) \rangle = 0$, where $\langle . \rangle$ denotes the average over the noise realizations.

- The mean squared displacement (MSD) represents the size of the region explored by the particles. $\mathrm{MSD}(t) = \langle \Delta \boldsymbol{r}^2(t) \rangle - \langle \Delta \boldsymbol{r}(t) \rangle^2 = \langle \Delta \boldsymbol{r}^2(t) \rangle$. The MSD is shown to be:

$$\left\langle \Delta \boldsymbol{r}^2(t) \right\rangle = \frac{2dk_{\mathrm{B}}T}{\gamma^2 m} \left(\gamma t + \mathrm{e}^{-\gamma t} - 1 \right).$$

At short times, $t \ll \gamma^{-1}$, the MSD becomes:

$$\left\langle \Delta \boldsymbol{r}^2(t) \right\rangle = \frac{dk_{\mathrm{B}}T}{m} t^2.$$

The MSD is proportional to t^2 indicating a ballistic motion. Indeed, during this time window, the friction has no effect, the particle motion is unhindered since it has not yet collided with the solvent.

At long times, $t \to \infty$, the MSD yields:

$$\left\langle \Delta \boldsymbol{r}^2(t) \right\rangle = \frac{2dk_{\mathrm{B}}T}{\gamma m} t.$$

Using the fluctuation-dissipation theorem (Eq. (1.5)), the long-time MSD is also related to the translational diffusion coefficient of the particle D_{t} by:

$$\left\langle \Delta \boldsymbol{r}^2(t) \right\rangle = 2dD_{\mathrm{t}}t. \tag{2.4}$$

At long times, the motion is diffusive with a MSD proportional to the time t with a slope proportional to the translational diffusion coefficient D_{t}. The translational diffusion coefficient D_{t} is the only relevant transport coefficient for isotropic particles. Hence, unless explicit notation is necessary, I will refer to the translational diffusion coefficient by the term diffusion coefficient and drop the subscript t in what follows.

2.3.2 The overdamped Langevin equation

The overdamped limit of the Langevin equation is considered here, since as discussed in Chapter 1, inertial effects are neglected. In this case, $\frac{\mathrm{d}\boldsymbol{v}_i}{\mathrm{d}t} = 0$, and from (2.3) the equation becomes:

$$\boldsymbol{v}_i(t) = \frac{1}{m_\alpha \gamma_\alpha} \sum_{i \neq j} \boldsymbol{F}_{j \to i}(t) + \frac{1}{m_\alpha \gamma_\alpha} \boldsymbol{\mathcal{R}}_i(t). \tag{2.5}$$

Using the definition of the diffusion coefficient (Eq. (1.5)), the equation yields:

$$\boldsymbol{v}_i(t) = \frac{D_\alpha}{k_\mathrm{B}T} \sum \boldsymbol{F}_{j\to i}(t) + \frac{D_\alpha}{k_\mathrm{B}T} \boldsymbol{\mathcal{R}}_i(t). \tag{2.6}$$

The correlation of the noise can also be expressed with the diffusion coefficient D_α:

$$\langle \boldsymbol{\mathcal{R}}_i(t') \cdot \boldsymbol{\mathcal{R}}_j(t'') \rangle = \frac{2d(k_\mathrm{B}T)^2}{D_\alpha} \delta_{ij} \delta(t' - t''),$$

where δ_{ij} is the Kronecker symbol. Again the motion is characterized by considering only one particle. Under this condition, the overdamped Langevin equation becomes:

$$\boldsymbol{v}(t) = \frac{D}{k_\mathrm{B}T} \boldsymbol{\mathcal{R}}(t)$$

From which the position $\boldsymbol{r}(t)$ can be obtained:

$$\boldsymbol{r}(t) = \frac{D}{k_\mathrm{B}T} \int_0^t \boldsymbol{\mathcal{R}}(t')\, \mathrm{d}t' + \boldsymbol{r}(0)$$

The calculations of the mean displacement and of the mean squared displacement are detailed in Appendix D and the results are:

- The mean displacement of the particle is null $\langle \Delta \boldsymbol{r}(t) \rangle = 0$.
- The mean squared displacement is $\langle \Delta \boldsymbol{r}^2(t) \rangle = 2dDt$. In two dimensions, it becomes:

$$\mathrm{MSD}(t) = \left\langle \Delta \boldsymbol{r}^2(t) \right\rangle = 4Dt \tag{2.7}$$

In the overdamped limit, since the inertial effects have been neglected, the MSD is linear at all times, and its slope is proportional to the diffusion coefficient D.

2.3.3 Numerical integration of the overdamped Langevin equation

In the model of interest, there are $N + N_\mathrm{C}$ colloids. Therefore, $N + N_\mathrm{C}$ equations are necessary to describe the dynamics of the system. The particles interact with each other, coupling all the equations together. This N-body problem cannot be solved analytically, so the equations are discretized with an Euler scheme and then numerically integrated. In Cartesian coordinates, the position vector is $\boldsymbol{r} = (x, y)$, which can be projected in the

base $(\boldsymbol{e}_x, \boldsymbol{e}_y)$. For each dimension, the derivative of the position can be approximated by:

$$\dot{x}_i(t) = \frac{x_i(t+\Delta t) - x_i(t)}{\Delta t},$$

where Δt is the discretization time step. Consequently, knowing the position of a particle i at time t, its positions at $t + \Delta t$ can be computed with:

$$x_i(t+\Delta t) = x_i(t) + \Delta t \frac{D_\alpha}{k_\mathrm{B}T} \sum_{i \neq j} F_{x,j\to i}(t) + \frac{D_\alpha}{k_\mathrm{B}T} \underbrace{\int_t^{t+\Delta t} \mathcal{R}_{x,i}(t')\mathrm{d}t'}_{\mathcal{B}(\Delta t)},$$

where $F_{x,j\to i}$ and $\mathcal{R}_{x,i}$ are the element along the vector $\boldsymbol{e}_x$ of the vector $\boldsymbol{F}_{j\to i}$ and $\boldsymbol{\mathcal{R}}$, respectively. $\mathcal{B}(\Delta t)$ is a random variable which follows a Gaussian distribution according to the central limit theorem, since the integration of $\mathcal{R}_{x,i}$ can be seen as the sum of random variables. In Appendix E, the mean of $\mathcal{B}$ is shown to be null and the mean standard deviation to be:

$$\sqrt{\langle \mathcal{B}^2(\Delta t) \rangle} = \frac{k_\mathrm{B}T}{D_\alpha} \sqrt{2D_\alpha \Delta t}.$$

The discretized equations become:

$$x_i(t+\Delta t) = x_i(t) + \Delta t \frac{D_\alpha}{k_\mathrm{B}T} \sum_{i \neq j} F_{x,j\to i}(t) + \sqrt{2D_\alpha \Delta t}\ \eta_{x,i}(t).$$

In d dimensions, and considering that the forces are derived from a potential which describes the interaction between a particle of type α and a particle of type β, $\boldsymbol{F} = -\boldsymbol{\nabla} U_{\alpha\beta}$, the discretized equations are:

$$\boldsymbol{r}_i(t+\Delta t) = \boldsymbol{r}_i(t) - \Delta t \frac{D_\alpha}{k_\mathrm{B}T} \sum_{i \neq j} \boldsymbol{\nabla} U_{\alpha\beta}(r_{ij}) + \sqrt{2D_\alpha \Delta t}\ \boldsymbol{\eta}_i(t), \tag{2.8}$$

where $\boldsymbol{\eta}_i$ follows a normal distribution of mean 0 and variance 1.

2.3.4 Dimensionless overdamped Langevin equation

The equations to simulate the motion of particles are set. As announced in Section 2.2.2, the parameters of the model are those related to the interaction potential, d_{ij} and ε' for WCA, σ_A and ε for LJ, the density ρ, and the size of the reaction area r_cut. An extra parameter is the diffusion coefficient of each particle D_α which characterizes the motion of each particle of type α. The diffusion coefficient is assumed to follow the Stokes-Einstein relation (Eq. (1.4)), thus is inversely proportional to the particle radius

R_α. This represents the diffusion coefficient at infinite dilution, i.e. for a unique particle in an infinite solvent, which is denoted in what follows by D_α^0. All the solute particles have the same diffusion coefficient $D_\mathrm{A}^0 \propto 1/R_\mathrm{A}$. The diffusion coefficient of the colloid is $D_\mathrm{C}^0 \propto 1/R_\mathrm{C}$. It is common to use dimensionless quantities in order to simplify the interpretation of the relevant physical measures of the problem. Here, the chosen quantities to make the equations dimensionless are: the size of the solute particles σ_A as a unit of length, the typical time taken by a solute particle to diffuse over its own size $\sigma_\mathrm{A}^2/D_\mathrm{A}^0$ as a unit time, and the thermal energy $k_\mathrm{B}T$ as a unit of the energy. The dimensionless quantities are represented with a $*$. The following quantities: $\boldsymbol{r}_i = \boldsymbol{r}_i^* \sigma_\mathrm{A}$, $\Delta t = \frac{\Delta t^* \sigma_\mathrm{A}^2}{D_\mathrm{A}^0}$, $U_{\alpha\beta} = U_{\alpha\beta}^* k_\mathrm{B}T$ are replaced in Eq. (2.8):

$$\sigma_\mathrm{A}\boldsymbol{r}_i^*(t^*+\Delta t^*) = \sigma_\mathrm{A}\boldsymbol{r}_i^*(t^*) - \frac{\Delta t^*\sigma_\mathrm{A}^2}{D_\mathrm{A}^0}\frac{D_\alpha^0}{k_\mathrm{B}T\sigma_\mathrm{A}}\sum_{i\neq j}\boldsymbol{\nabla}^* U_{\alpha\beta}^*(r_{ij}^*)k_\mathrm{B}T + \sqrt{2D_\alpha^0\Delta t^*\frac{\sigma_\mathrm{A}^2}{D_\mathrm{A}^0}}\,\boldsymbol{\eta}_i(t)$$

$$\boldsymbol{r}_i^*(t^*+\Delta t^*) = \boldsymbol{r}_i^*(t^*) - \Delta t^*(D_\alpha^0)^*\sum_{i\neq j}\boldsymbol{\nabla}^* U_{\alpha\beta}^*(r_{ij}^*) + \sqrt{2(D_\alpha^0)^*\Delta t^*}\,\boldsymbol{\eta}_i(t)$$

$\boldsymbol{\eta}_i(t)$ is already dimensionless, $(D_\alpha^0)^* = \frac{D_\alpha^0}{D_\mathrm{A}^0}$ is the dimensionless diffusion coefficient, which results in the ratio of their sizes $(D_\alpha^0)^* = \frac{R_\mathrm{A}}{R_\alpha}$. In what follows, each quantity is dimensionless, the $*$ is removed for clarity.

To finish, the gradient of the potential is computed. In two dimensions with Cartesian coordinates, the gradient is:

$$\boldsymbol{\nabla}U_{\alpha\beta}(r_{ij}) = \begin{pmatrix} \frac{\partial}{\partial x_i}U_{\alpha\beta} \\ \frac{\partial}{\partial y_i}U_{\alpha\beta} \end{pmatrix} = \begin{pmatrix} \frac{\partial r_{ij}}{\partial x_i}\frac{\partial U_{\alpha\beta}}{\partial r_{ij}} \\ \frac{\partial r_{ij}}{\partial y_i}\frac{\partial U_{\alpha\beta}}{\partial r_{ij}} \end{pmatrix},$$

with $\frac{\partial r_{ij}}{\partial x_i} = \frac{x_i - x_j}{r_{ij}}$ and $\frac{\partial r_{ij}}{\partial y_i} = \frac{y_i - y_j}{r_{ij}}$. The partial derivative $\frac{\partial U_{\alpha\beta}}{\partial r_{ij}}$ depends on the potential considered:

$$\frac{\partial U_{\alpha\beta}}{\partial r_{ij}} = \begin{cases} -\frac{4\varepsilon'}{r_{ij}}\left[12\left(\frac{d_{ij}}{r_{ij}}\right)^{12} - 6\left(\frac{d_{ij}}{r_{ij}}\right)^{6}\right] & \text{if } U_{\alpha\beta} = U_\mathrm{WCA}, \\ -\frac{4\varepsilon}{r_{ij}}\left[12\left(\frac{\sigma_\mathrm{A}}{r_{ij}}\right)^{12} - 6\left(\frac{\sigma_\mathrm{A}}{r_{ij}}\right)^{6}\right] & \text{if } U_{\alpha\beta} = U_\mathrm{LJ}, \end{cases} . \tag{2.9}$$

Consequently, the final equation used in the code I have developed during my PhD thesis is:

$$\boldsymbol{r}_i(t+\Delta t) = \boldsymbol{r}_i(t) - \Delta t D_\alpha^0 \sum_{i\neq j}(\boldsymbol{r}_i - \boldsymbol{r}_j)\frac{1}{r_{ij}}\frac{\partial U_{\alpha\beta}}{\partial r_{ij}} + \sqrt{2D_\alpha^0\Delta t}\,\boldsymbol{\eta}_i(t). \tag{2.10}$$

In the Section 2.5, the numerical implementation is explained.

2.4 Langevin equation of the Active Brownian Particle model

In recent years, the overdamped Langevin equation has been adapted in order to model active particles by adding a bias in the equation of motion [46]. ABP is a minimal model that successfully captures the basic features of microswimmers and of synthetic self-propelled particles [2]. The simplicity of this model makes the computation fast, so that collective effects of large systems containing numerous active particles can be studied [61, 65, 80, 64]. This PhD work aims at studying a system in which the activity is not postulated, but emerges from the explicit description of the interactions between solute particles. Nevertheless, some results will be confronted to the ABP model, as it provides an interesting point of comparison. Therefore, I have also developed a BD-ABP code that is based on the Langevin equation for the ABP model. In this section, the equations of motion for this model are presented, from which the MSD can be computed. Then, just as for the Brownian model, the equations are integrated with the Euler scheme and are made dimensionless. Less details are given as the derivations are similar to the ones for Brownian model.

2.4.1 Equation of motion

In this model, an extra degree of freedom appears, namely the rotation of particle propulsion axis. Therefore, in this model, the translational diffusion coefficient is denoted $D_{\mathrm{t},\alpha}$, to differentiate it from $D_{\mathrm{r},\alpha}$ the rotational diffusion coefficient. Again, the motion of particles is restricted to two dimensions. Each particle obeys the following equation of motion:

$$\frac{\mathrm{d}\boldsymbol{r}_i(t)}{\mathrm{d}t} = -\frac{D_{\mathrm{t},\alpha}}{k_{\mathrm{B}}T}\sum_{i\neq j}\boldsymbol{\nabla}U_{\alpha\beta}(r_{ij}) + v_0\boldsymbol{n}_i(t) + \frac{D_{\mathrm{t},\alpha}}{k_{\mathrm{B}}T}\boldsymbol{\mathcal{R}}_i(t), \tag{2.11}$$

where the vector $\boldsymbol{n}_i = (\cos\theta_i, \sin\theta_i)$ is normal to the colloid surface. The angle θ_i denotes the orientation of particle i regarding the axis $\boldsymbol{e}_x$, and v_0, the self-propulsion speed, is a parameter of the model. The dynamics of the orientation angle θ_i is also described by a stochastic equation:

$$\frac{\mathrm{d}\theta_i(t)}{\mathrm{d}t} = \sqrt{2D_{\mathrm{r},\alpha}}\,\eta_{\theta,i}, \tag{2.12}$$

where $\eta_{\theta,i}$ is a random variable following a normal distribution of mean 0 and variance 1. Particles have a persistent motion in the direction of $\boldsymbol{n}_i$ at a velocity v_0. The correlation function of the orientation vector decays exponentially:

$$\langle \boldsymbol{n}_i(t') \cdot \boldsymbol{n}_i(t'') \rangle = \mathrm{e}^{-|t'-t''|/\tau_{\mathrm{r},\alpha}}, \tag{2.13}$$

where $\tau_{r,\alpha} = 1/D_{\mathrm{r},\alpha}$ is the characteristic time during which the orientation persists. $\tau_{\mathrm{r},\alpha}$ is called persistence time in what follows.

2.4.2 Analysis of the MSD for the ABP model

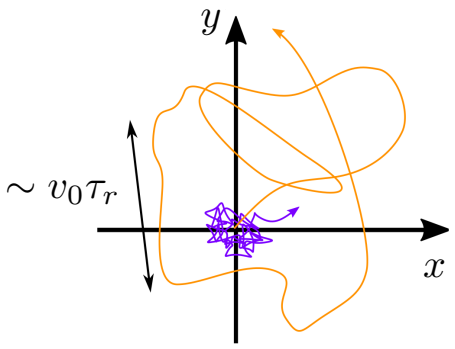

(a) Schematic comparison between the trajectory of a passive particle (purple) and that of an active particle (orange).

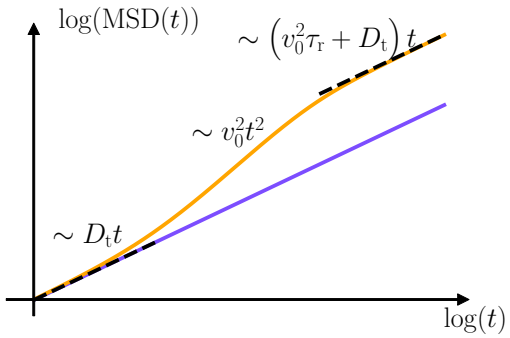

(b) Comparison of the MSD. The dashed black lines represent the short-time and long-time asymptotes. The different regimes are indicated.

Figure 2.3: Comparison of the characteristics of a passive particle (in purple) and an active particle (in orange).

The dynamics of an active particle differs from its passive counterpart due to the persistent motion in a given direction for a significant time $\sim \tau_\mathrm{r}$. Figure 2.3a represents a schematic comparison between the trajectory of a passive and that of an active particle. The active particle has a persistent motion over a distance $\sim v_0\tau_\mathrm{r}$. For a single active particle with no external force applied on it, the MSD can be calculated. First, the position of the particle is deduced from Eq.(2.11) and is:

$$\boldsymbol{r}(t) = \int_0^t \left(v_0 \boldsymbol{n}(t') + \frac{D_\mathrm{t}}{k_\mathrm{B}T} \boldsymbol{\mathcal{R}}(t') \right) \mathrm{d}t' + \boldsymbol{r}(0),$$

and the displacement is:

$$\Delta\boldsymbol{r}(t) = \boldsymbol{r}(t) - \boldsymbol{r}(0) = \int_0^t \left(v_0 \boldsymbol{n}(t') + \frac{D_\mathrm{t}}{k_\mathrm{B}T} \boldsymbol{\mathcal{R}}(t') \right) \mathrm{d}t'.$$

Then, the MSD is calculated:

$$\begin{aligned}\left\langle \Delta \boldsymbol{r}^2(t) \right\rangle &= v_0^2 \int_0^t \mathrm{d}t' \int_0^t \mathrm{d}t'' \left\langle \boldsymbol{n}(t') \cdot \boldsymbol{n}(t'') \right\rangle + \left(\frac{D_\mathrm{t}}{k_\mathrm{B}T} \right)^2 \int_0^t \mathrm{d}t' \int_0^t \mathrm{d}t'' \left\langle \boldsymbol{\mathcal{R}}(t') \cdot \boldsymbol{\mathcal{R}}(t'') \right\rangle \\ &+ \frac{v_0 D_\mathrm{t}}{k_\mathrm{B}T} \int_0^t \mathrm{d}t' \int_0^t \mathrm{d}t'' \underbrace{\left\langle \boldsymbol{\mathcal{R}}(t') \cdot \boldsymbol{n}(t'') \right\rangle}_{=0} + \frac{v_0 D_\mathrm{t}}{k_\mathrm{B}T} \int_0^t \mathrm{d}t' \int_0^t \mathrm{d}t'' \underbrace{\left\langle \boldsymbol{n}(t') \cdot \boldsymbol{\mathcal{R}}(t'') \right\rangle}_{=0} \\ &= v_0^2 \int_0^t \mathrm{d}t' \int_0^t \mathrm{d}t'' \, \mathrm{e}^{-D_\mathrm{r}|t'-t''|} + \left(\frac{D_\mathrm{t}}{k_\mathrm{B}T} \right)^2 \int_0^t \mathrm{d}t' \int_0^t \mathrm{d}t'' \left\langle \mathcal{R}_x(t') \mathcal{R}_x(t'') + \mathcal{R}_y(t') \mathcal{R}_y(t'') \right\rangle\end{aligned}$$

For convenience, the double integral is reduced to a simple integral, details are given in Appendix B. The MSD becomes:

$$\begin{aligned}\left\langle \Delta \boldsymbol{r}^2(t) \right\rangle &= 2v_0^2 \int_0^t \mathrm{d}u (t-u) \, \mathrm{e}^{-D_\mathrm{r}u} + 2 \left(\frac{D_\mathrm{t}}{k_\mathrm{B}T} \right)^2 \int_0^t \mathrm{d}t' \int_0^t \mathrm{d}t'' 2 \frac{(k_\mathrm{B}T)^2}{D_\mathrm{t}} \delta(t'-t'') \\ &= 2v_0^2 \left(\left[-\frac{t}{D_\mathrm{r}} \, \mathrm{e}^{-D_\mathrm{r}u} \right]_0^t + \left[\frac{u}{D_\mathrm{r}} \, \mathrm{e}^{-D_\mathrm{r}u} \right]_0^t - \int_0^t \mathrm{d}u \frac{1}{D_\mathrm{r}} \, \mathrm{e}^{-D_\mathrm{r}u} \right) + 4D_\mathrm{t}t \\ &= 2v_0^2 \left(-\frac{t}{D_\mathrm{r}} \, \mathrm{e}^{-D_\mathrm{r}t} + \frac{t}{D_\mathrm{r}} + \frac{t}{D_\mathrm{r}} \, \mathrm{e}^{-D_\mathrm{r}t} - \left[-\frac{1}{D_\mathrm{r}^2} \, \mathrm{e}^{-D_\mathrm{r}u} \right]_0^t \right) + 4D_\mathrm{t}t \\ &= 2v_0^2 \left(\frac{t}{D_\mathrm{r}} + \frac{1}{D_\mathrm{r}^2} \, \mathrm{e}^{-D_\mathrm{r}t} - \frac{1}{D_\mathrm{r}^2} \right) + 4D_\mathrm{t}t\end{aligned}$$

Finally, the computation leads to this expression for the MSD:

$$\left\langle \Delta \boldsymbol{r}^2(t) \right\rangle = 2 \frac{v_0^2}{D_\mathrm{r}^2} \left(tD_\mathrm{r} + \mathrm{e}^{-D_\mathrm{r}t} - 1 \right) + 4D_\mathrm{t}t \tag{2.14}$$

The MSD of the active particle exhibits a more complex behavior than the passive particle one. As it is shown on Figure 2.3b, where the MSD is represented as a function of time in a log-log scale, the MSD of an active particle (in orange) exhibits three distinct regimes whereas the MSD of a passive particle (in purple) only has one.

For times small compared to the persistence time $t \ll \tau_\mathrm{r}$, the MSD becomes:

$$\begin{aligned}\left\langle \Delta \boldsymbol{r}^2(t) \right\rangle &= 2 \frac{v_0^2}{D_\mathrm{r}^2} \left(tD_\mathrm{r} + 1 - D_\mathrm{r}t + D_\mathrm{r}^2 \frac{t^2}{2} - 1 \right) + 4D_\mathrm{t}t \\ &= v_0^2 t^2 + 4D_\mathrm{t}t\end{aligned}$$

Two regimes emerge, separated by a characteristic time $\frac{4D_\mathrm{t}}{v_0^2}$. For times smaller than this characteristic time, the particle has a usual Brownian motion characterized by the translational diffusion coefficient D_t. For $\frac{4D_\mathrm{t}}{v_0^2} < t < \tau_\mathrm{r}$ the motion is ballistic.

For times larger than the orientation persistence time $t \gg \tau_\mathrm{r}$, the MSD becomes:

$$\left\langle \Delta \boldsymbol{r}^2(t) \right\rangle = \left(2\frac{v_0^2}{D_\mathrm{r}} + 4D_\mathrm{t} \right) t. \tag{2.15}$$

The motion is diffusive with an effective translational diffusion coefficient $D'_\mathrm{t} = \frac{v_0^2}{2D_r} + D_t$. The different regimes are schematically represented on Figure 2.3b.

2.4.3 Numerical integration of the Langevin equation for the ABP model

The equations Eq. (2.11) and Eq. (2.12) are integrated using the Euler scheme to be solved numerically:

$$\begin{cases} \boldsymbol{r}_i(t+\Delta t) = \boldsymbol{r}_i(t) - \dfrac{D_{\mathrm{t},\alpha}}{k_\mathrm{B}T} \displaystyle\sum_{i \neq j} \boldsymbol{\nabla} U_{\alpha\beta}(r_{ij}) \Delta t + v_0 \boldsymbol{n}_i(t) \Delta t + \sqrt{2D_{\mathrm{t},\alpha}\Delta t}\, \boldsymbol{\eta}_i(t) \\ \theta(t+\Delta t) = \theta(t) + \sqrt{2D_{\mathrm{r},\alpha}\Delta t}\, \eta_{\theta,i}(t) \end{cases} \tag{2.16}$$

The random variables $\boldsymbol{\eta}_i$ and $\eta_{\theta,i}$ are independent.

2.4.4 Dimensionless equations

In the ABP model, there are no solute particles, consequently the quantities are made dimensionless in relation to the colloid: $\boldsymbol{r}_i = \tilde{\boldsymbol{r}}_i \sigma_\mathrm{C}$, $\Delta t = \frac{\Delta\tilde{t}\sigma_\mathrm{C}^2}{D_{\mathrm{t,C}}}$, and $U_{\alpha\beta} = \tilde{U}_{\alpha\beta} k_\mathrm{B}T$. The equations become:

$$\sigma_\mathrm{C}\tilde{\boldsymbol{r}}_i(\tilde{t}+\Delta\tilde{t}) = \sigma_\mathrm{C}\tilde{\boldsymbol{r}}_i(\tilde{t}) - \frac{\Delta\tilde{t}\sigma_\mathrm{C}^2}{D_{\mathrm{t,C}}} \frac{D_{\mathrm{t},\alpha}}{\sigma_\mathrm{C} k_\mathrm{B}T} \sum_{i\neq j} \tilde{\boldsymbol{\nabla}} \tilde{U}_{\alpha\beta}(\tilde{r}_{ij}) k_\mathrm{B}T + v_0 \Delta\tilde{t} \frac{\sigma_\mathrm{C}^2}{D_{\mathrm{t,C}}} \boldsymbol{n}_i + \sqrt{2D_{\mathrm{t},\alpha}\Delta\tilde{t}\frac{\sigma_\mathrm{C}^2}{D_{\mathrm{t,C}}}}\, \boldsymbol{\eta}_i(t)$$

$$\tilde{\boldsymbol{r}}_i(\tilde{t}+\Delta\tilde{t}) = \tilde{\boldsymbol{r}}_i(\tilde{t}) - \Delta\tilde{t}\tilde{D}_{\mathrm{t},\alpha} \sum_{i\neq j} \tilde{\boldsymbol{\nabla}} \tilde{U}_{\alpha\beta}(\tilde{r}_{ij}) + \tilde{v}_0 \Delta\tilde{t} \boldsymbol{n}_i(t) + \sqrt{2\tilde{D}_{\mathrm{t},\alpha}\Delta\tilde{t}}\, \boldsymbol{\eta}_i(\tilde{t}) \tag{2.17}$$

and

$$\theta(\tilde{t}+\Delta\tilde{t}) = \theta(\tilde{t}) + \sqrt{2D_{\mathrm{r},\alpha}\Delta\tilde{t}\frac{\sigma_\mathrm{C}^2}{D_{\mathrm{t,C}}}}\, \eta_{\theta,i}(t)$$

$$\theta(\tilde{t}+\Delta\tilde{t}) = \theta(\tilde{t}) + \sqrt{2\tilde{D}_{\mathrm{r},\alpha}\Delta\tilde{t}}\, \eta_{\theta,i}(\tilde{t}) \tag{2.18}$$

$\boldsymbol{\eta}_i$, $\eta_{\theta,i}$ and θ are already dimensionless. Other dimensionless quantities emerge: the translational diffusion coefficient $\tilde{D}_{\mathrm{t},\alpha} = \frac{D_{\mathrm{t},\alpha}}{D_{\mathrm{t,C}}}$, the rotational diffusion coefficient $\tilde{D}_{\mathrm{r},\alpha} = \frac{\sigma_{\mathrm{C}}^2 D_{\mathrm{r},\alpha}}{D_{\mathrm{t,C}}}$, the velocity $\tilde{v}_0 = \frac{v_0 \sigma_{\mathrm{C}}}{D_{\mathrm{t,C}}}$. In what follows, all the quantities are dimensionless, the $\tilde{}$ is removed for clarity.

2.5 Numerical implementation of BD and BD-ABP simulations

In this section, I explain the technical details and the particularities of the Brownian dynamics and of the active Brownian particles codes I have developed. Firstly, the simulation parameters are introduced. Secondly, the general algorithm is presented on the one hand for the BD code and on the other hand for the ABP code. Then the cell list algorithm, a numerical trick making the code more efficient, is explained. Afterwards, the numerical implementation to model the reactions is described. Finally, I will give an overview of the quantities computed during the simulation.

2.5.1 Simulation parameters

New parameters of the problem appear when creating the code. In the model, the solvent is represented using a statistical description. The particles, which are initially randomly placed in the simulation box, follow a trajectory which contains a random part. This corresponds to a realization of the noise. The different quantities computed to characterize the system must then be averaged over different trajectories starting from different initial positions that were produced by different noise realizations. The parameter $n_{\mathrm{realizations}}$ indicates the number of noise realizations to perform. The overdamped Langevin equations are discretized with the Euler scheme to be solved, which introduces a new parameter: the time step Δt. Its choice is discussed in Section 2.6 since its value must be carefully chosen in order to have an efficient numerical integration. The number of time steps, n_{run}, the simulation runs, defines, with the time step, the length in time of the simulation.

2.5.2 Brownian dynamics algorithm

All the needed parameters are written in an input file, which is read at the very beginning of the simulation. For each realization, the time is initialized to 0 and the particle positions are initialized randomly. Then, at each time step the code loops over

each particle i, forces exerted by particles j are computed by looping for each particle i over the other particles $j \neq i$. Once the resultant force is known, the new position $\boldsymbol{r}_i(t+\Delta t)$ is computed. When the loop over the particles i is done, the positions $\boldsymbol{r}_i(t)$ are updated with $\boldsymbol{r}_i(t+\Delta t)$. The reaction occurs at this stage of the algorithm, after that a new time step begins. Periodic boundary conditions are implemented, which consist of copying the simulation box in every dimension infinitely in order to model a bulk system. The distances are computed by taking, for each pair (i, j), the minimum distance between the particle i and all the representations of the particle j. When the particle is displaced, if the new position is outside the box, its image is replaced inside the simulation box. The code I have written consists of one main code and about 30 routines, the whole containing approximately 3700 lines. The routines for the cell list algorithm and the reaction will be presented in the next paragraphs. The main code algorithm is presented here:

```
Initialization of parameters using the input file.
Loop i_realizations over n_realizations realizations:
  Time initialization t = 0.
  Set initial configuration r_i(t = 0) for each particle.
  Loop t over n_run time steps:
    Loop i over N particles:
      Loop j ≠ i over N − 1 particles or loop j using cell list algorithm:
        Compute and sum forces exert on particle i by all particles j.
      End loop particles j.
      Compute the new position of particle i, r_i(t + Δt).
      Apply the periodic boundary conditions.
    End loop particles i.
    Update positions r_i(t) = r_i(t + Δt).
    Do reaction routine.
  End loop time steps t.
End loop realizations i_realizations.
```

The code has been implemented to be as general as possible. Flags in the input file indicate whether the colloid catalyzes the reaction and whether the reverse reaction takes place. Flags are also used to indicate which quantities are computed during the simulation. Each flag is associated with a saving frequency. The code works in two or three dimensions, a flag is used to define the number of dimensions d.

2.5.3 BD-ABP algorithm

Another code has been implemented in order to carry BD-ABP simulations for comparison purposes. The code is much simpler as it does not necessitate the implementation

of a chemical reaction. The same implementation as for Brownian dynamics has been done, replacing the equation of motion by Eq. (2.11), and adding the equation on the orientation Eq. (2.12). The code I have written for this case also consists of one main code and about 30 routines, the whole containing approximately 2300 lines. The choice of the dynamic parameters v_0 and D_r as well as the potential used in order to make a valid comparison with the BD results are presented in Chapter 4.

2.5.4 Computation of interactions with the cell algorithm

The basic method to compute interactions between particles is to loop over all particles i, and for each i to loop over all particles $j \neq i$. Hence, the algorithm scales as N^2, where N the number of particles. The cell list algorithm is a clever way to compute interactions for a system involving short-range interactions, and it reduces the algorithm order to N. For instance, the intensity of the Lennard-Jones potential decays with $(1/r)^6$. Therefore, if the system is large enough, particles are far from each other and a cutoff is generally implemented, typically 2.5σ for LJ. Only the computation of the interactions between a particle and its nearest neighbors is necessary. The cell list algorithm implemented comes from [79] and is described here.

The idea is to divide the system into square (2D) or cubic (3D) cells numbered from 1 to n_cells, whose size is chosen to be of the same size as the LJ cutoff, i.e. 2.5σ. Each particle belongs to a cell, and two arrays are used to record the distribution of particles in cells. One represents the cells, each index of this array represents the corresponding cell. The other one represents the particles indexes. Only one loop over the particles is necessary to build these tables. The cells array stores the index of the particle which was found last inside the cell, empty cells are filled with 0. In the particles array, for each particle, the index of another particle in the same cell is saved. For the first particle found inside the cell, the number is 0. Both arrays are constructed at each time step. The construction algorithm is the following:

```
Initialization of the cells array to 0.
Initialization of the particles array to 0.
Loop i over N particles:
   Compute the cell number x_cell in which the particle i is.
   In the particles array, replace the value at the position i with the value of
the cells array at x_cell.
   In the cells array update the value at x_cell with the particle index i.
End loop particles i.
```

During the computation of interactions, for each particle i, the algorithm loops over all particles j inside the same cell and in the neighboring cells instead of in the whole simulation box. There is for a 2D simulation $n_{\text{neighbors}} = 8$ and for a 3D simulation $n_{\text{neighbors}} = 26$. For each cell, the reverse procedure is done. The last particle found during the construction is the first one to be extracted using the cells array. Then, using the particles array, the other particles of the same cell can be found. The algorithm for the forces computation becomes:

```
Loop i over N particles:
   Compute the cell number x_cell in which the particle i is.
   Find the n_neighbors neighbors of the cell x_cell.
   Loop i_cell over the n_neighbors + 1 neighboring cells and its own cell:
      Collect the index j of the particle in the cells array at i_cell.
      While j is not 0, do:
         Compute and sum forces that particle j exert on particle i.
         Find the next particle in the cell, j is updated with the value of the
particles array at j.
   End loop neighboring cells i_cell.
End loop particles i.
```

An example is shown on Fig. 2.4 for a simulation box divided into $n_{\text{cells}} = 36$, which contains $N = 20$ particles. The drawing represents how both particles and cells arrays would be filled by the algorithm for the particles 5, 13, 15, found in cell 26.

A flag must be set in the input file in order to use the cell list algorithm. This trick is used in the simulation only if the system is large enough to have $n_{\text{cells}} > n_{\text{neighbors}}$. If this condition is not fulfilled, the flag is unset and the basic double loop is carried.

2.5.5 Implementation of the chemical reaction

Two reactions are defined in the system: $\text{A} + \text{C} \rightarrow \text{B} + \text{C}$ and $\text{B} \rightarrow \text{A}$. The localization of the species A or B regarding the colloid determines which reaction will occur. Close to the colloid, the first one takes place while far away from the colloid, it is the other one. The colloid is then the reference point around which a reaction area of radius r_{cut} is defined. The implementation of the reactions in this code performs more generally any reaction which transforms a solute particle of type α into a solute particle of type β catalyzed by a colloid C, i.e. the reaction $\alpha + C \rightarrow \beta + C$, inside a reaction area. For reactions far away from the colloid, which occur outside the reaction area, the general reaction $\alpha \rightarrow \beta$ is implemented. Flags are set to indicate the type of reaction which will be simulated. The probability for the reaction to occur is $p_{\alpha\beta} = \Delta t / \tau_{\alpha\beta}$, where $\tau_{\alpha\beta}$ is

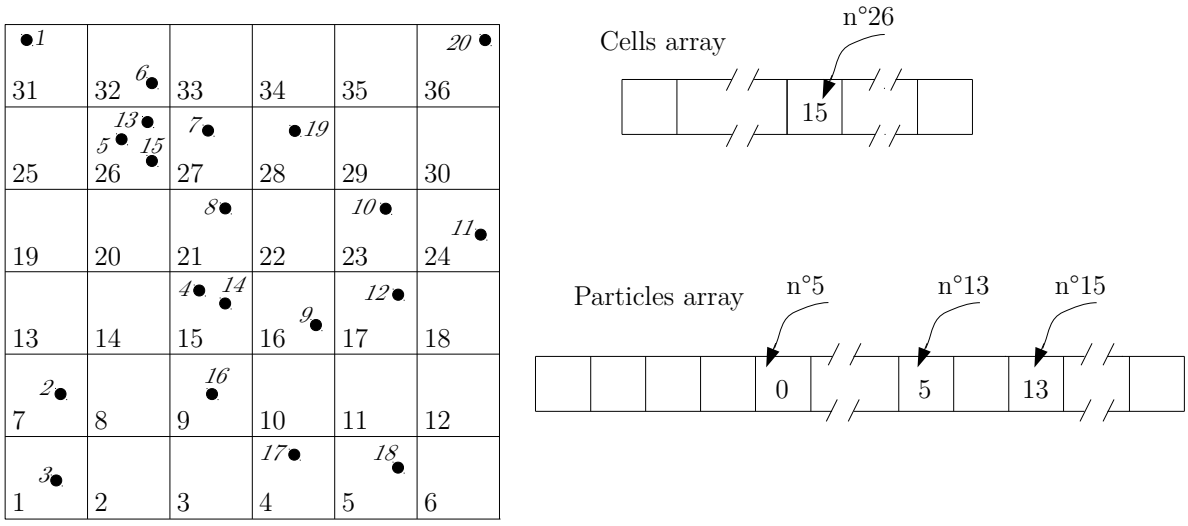

Figure 2.4: Drawing of a simulation box divided into $n_{\text{cells}} = 36$, containing $N = 20$ particles. Cells numbers are in regular font, particles numbers are in italic. The example illustrate how both particles and cells arrays would be filled with the algorithm for particles found in cell 26.

the average time after which a particle α is transformed into a particle β. This is correct if the time step is much smaller than $\tau_{\alpha\beta}$. In the limit $\Delta t \to 0$, $\tau_{\alpha\beta}$ are exponentially distributed. Here, $n_{\text{reactions}} = 2$ reactions occur in the system, one inside the reaction area and one outside. Two routines have been written: one for inside reactions and one for outside reactions. To implement the reactions, the type of each particle is stored and updated at each time step. The types are initialized at the beginning of the simulation from the input file. At the end of each time step, after the positions have been updated, there is a loop over the $n_{\text{reactions}}$ reactions, according to the place of the reaction (inside or outside) the corresponding routine is called. For each reaction the code loops over N_α, all solute particles of type α and for each particle of type α over N_{C}, all the colloids C. The distance r between the colloid and the considered solute particle is computed. If $r < r_{\text{cut}}$, a random number is drawn and compared to the reaction probability $p_{\alpha\beta}$. If the probability is higher than the random number, the reaction occurs and the solute particle type is updated. The algorithm for the inside routine is detailed here:

```
Loop k over N_α solute particles:
  Loop c over N_C colloids:
    Compute the distance r between k and c.
    If r < r_cut:
      Draw a random number x.
      If x < p_αβ:
        Type of the particle k is updated to β.
```

```
   End loop colloids c.
End loop solute particles k.
```

When there are several colloids in the system, the reaction outside must be done only if the considered solute particle is outside all the reaction areas. The routine for the outside reaction is then slightly different, introducing a new flag is_inside in order to take into account this subtlety. The routine is the following:

```
Loop k over N_α solute particles:
   Initialize the flag is_inside to FALSE.
   Loop c over N_C colloids:
      Compute the distance r between k and c.
      If r < r_cut:
         Set the flag is_inside to TRUE.
   End loop colloids c.
   If is_inside is FALSE:
      Draw a random number x.
         If x < p_αβ:
            Type of the particle k is updated to β.
End loop solute particles k.
```

2.5.6 Detailed version of the algorithm

```
Initialization of parameters using the input file.
Loop i_realizations over n_realizations realizations:
   Time initialization t = 0.
   Set initial configuration r_i(t = 0) for each particle.
   Set initial type α for each particle.
   Loop t over n_run time steps:
      Construct the cells and particles arrays.
      Loop i over N particles:
         Loop j ≠ i over N − 1 particles or loop j using cell list algorithm:
            Compute and sum forces exert on particle i by all particles j.
            If i is a colloid and j a solute particle:  compute their respective
distance to compute polarity contact data.
               If reaction:  compute number of particles in the reaction area.
         End loop particles j.
         If flag save_MSD set and saving frequency ok:  Save Δr.
         If flag save_gr and saving frequency ok:  Compute g_αβ(r).
         If flag save_cr and saving frequency ok:  Compute c_α(r).
         Compute the new position of particle i, r_i(t + Δt).
```

```
        Apply the periodic boundary conditions.
      End loop particles i.
      Update positions r_i(t) = r_i(t + Δt).
      If reaction flag set:
        Loop i_reaction over n_reactions:
          If the inside reaction flag set:  Do inside reaction routine.
          If the outside reaction flag set:  Do outside reaction routine.
          Update the types.
        End loop reactions i_reaction.
    End loop time steps t.
End loop realizations i_realizations.
```

2.6 Choice of the simulation parameters

In this section, the different parameters are adjusted: the time step Δt, and the size of the simulation box l_{box}. To this end, I consider a simple system which consists of only one type of solute particles. Simulations of N solute particles of type A interacting through a WCA interaction potential are run at a fixed solute density $\rho = 0.25$. Values for the time step Δt, and the size of the simulation box l_{box} vary to find the appropriate ones. The value of one parameter at a time is varied, keeping the others fixed. The radial distribution function $g_{\alpha\beta}$ indicates the probability to find a particle of type α at a distance r from a particle of type β. This quantity is computed during the simulation. Here, the radial distribution function between solute particles of type A, g_{AA}, is used as an indicator to guide the choice of the simulation parameters.

2.6.1 Choice of the time step

To investigate the system dynamics, simulations must be as long as possible. Therefore, to reduce the computational cost, the time step Δt must be as large as possible. However, a time step too large can induce numerical errors or a simulation which does not represent a physical state. The time step must then be chosen carefully. Fig. 2.5a shows the effect of the time step on the radial distribution function g_{AA}. For the largest time step $\Delta t = 0.001$, the function g_{AA} slightly differs from the other time steps tested. Besides, another test was done at a higher solute density and the simulation crashed. A suitable value for the time step is then $\Delta t = 0.0001$, which is found to be reliable also for higher solute density. This value is chosen to be the reference value. As the solute density ρ is increased, the time step is adapted and decreased. As well, when increasing the value of ε, which increases the attraction between solute particles, hence their local

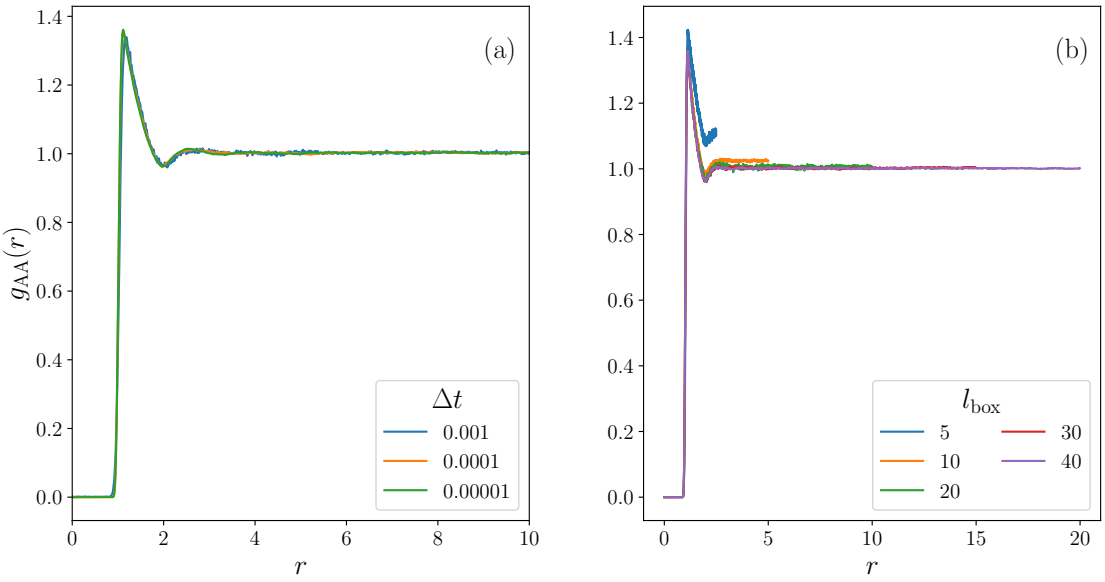

Figure 2.5: The radial distribution function g_{AA} between solute particles of type A of a system containing N solute particles of type A. The figure shows the effect of (a) the time step Δt and (b) the size of the box l_{box}.

density, Δt is decreased. The numerical values of Δt for each system investigated are given in Section 3.2.

2.6.2 Choice of the size of the system

Using periodic boundary conditions to model a bulk system makes computation faster, as a smaller system suffices to represent a much larger one. Nevertheless, the system can not be too small in order to represent the bulk correctly and avoid finite size effects. Fig. 2.5b illustrates the effect of the size of the simulation box l_{box} on the radial distribution function g_{AA}. In order to keep a fixed value for the solute density ρ, the number of solute particles N in the system was adjusted. For $l_{box} = 5$ or $l_{box} = 10$, g_{AA} has not converged, the simulation box is too small. Moreover, each colloid is surrounded by a LJ fluid in its reaction area. The reaction area can be up to 20 times larger than solute particles. Both colloids and their reaction areas must be modeled in a bulk. Therefore, the minimum box size $l_{box} = 40$ is chosen as it is at least twice larger than the colloids and their reaction areas. For a lower value of the solute density l_{box} will be increased.

2.7 Validation of the BD code

In this section, I present the tests performed to ensure the correct modeling of physical properties of the system. Initially, the validations are carried out on a simple system which

has been well studied: a monodisperse suspension of passive particles interacting with a WCA potential. Numerous analytical results have been derived for hard spheres in which $U_{\alpha\beta} = \infty$ if the particles are in contact and is null otherwise. There is no simple expression for the WCA potential, consequently the results from the simulation will be compared qualitatively to the literature. For this system, I will compare the radial distribution functions g_{AA}, the MSDs and the diffusion coefficients obtained with the simulation to analytical predictions found in the literature. Finally, I carry out tests with one colloid in a bath of N solute particles. The dynamic behavior of the colloid is in the latter case first investigated in the absence of reaction, and then with it.

2.7.1 Solution of WCA particles

For the comparison purpose, I introduce a new parameter: the surface (resp. volume) fraction of the particles ϕ, which is related to the solute density by $\phi = \pi R^2 \rho$ in 2D (resp. $\phi = \frac{4\pi R^3 \rho}{3}$ in 3D). For the validation process, several ϕ are investigated. To do so, the size of the box is fixed $l_{\mathrm{box}} = 10$ and $l_{\mathrm{box}} = 40$ for 3D and 2D simulations, respectively. The number of particles is adjusted to have the desired surface or volume fraction.

Radial distribution function between solute particles of type A

For a monodisperse suspension, analytical expression for the radial distribution function have been found in 3D [81] modeling the colloid as hard objects. Fig. 2.6 shows simulation results compared to theoretical results for different volume fractions in 3D. An excellent agreement is found between the theory and the simulation. Only a very small difference appears near the peaks of g_{AA}, due to the difference between the interaction potentials: g_{AA} between hard spheres contains a vertical line at the minimal distance of approach due to the discontinuity of the interaction potential. The code implementation is validated from a static insight.

Diffusion coefficient of solute particles

The dynamics of the system is verified by computing the mean squared displacements of solute particles. Simulations are run in 2D for various values of the surface fraction ϕ at a fixed simulation box size $l_{\mathrm{box}} = 40$. Fig. 2.7a shows the MSDs for different values of ϕ. As expected, the MSDs are linear in time. Fitting each with Eq. (2.7) the diffusion coefficients of solute particles D_{A} are extracted. The computed values of D_{A} are normalized by the diffusion coefficient at infinite dilution D^0_{A} and are plotted as a function of ϕ on Figure 2.7b. The diffusion coefficient is expected to decrease as the surface fraction ϕ increases. Thorneywork et al. have demonstrated that the diffusion coefficient of hard

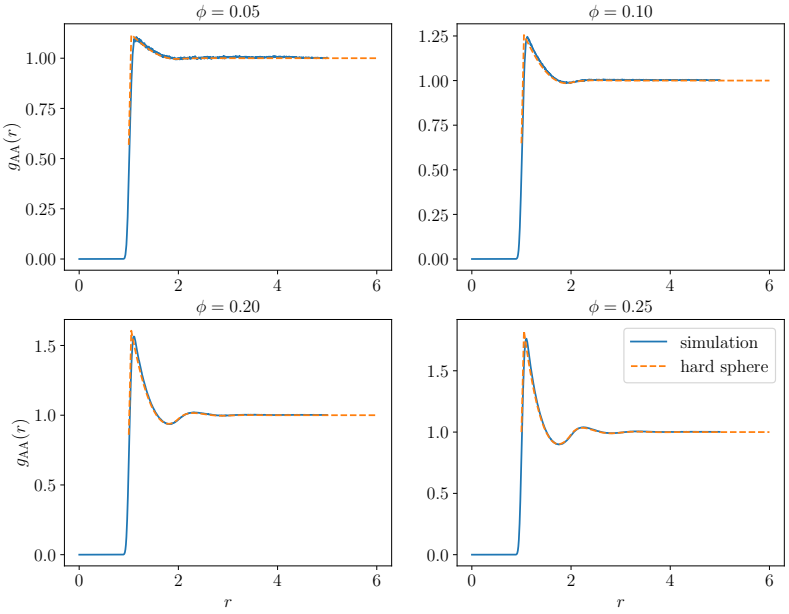

Figure 2.6: In a three-dimensional system with only N solute particles of type A. The radial distribution functions g_{AA} between solute particles of type A are computed using simulation of my code (blue lines) and using analytic results from [81] (orange lines) for different volume fractions ϕ.

disks has a linear dependence with the surface fraction given by $\frac{D_{\mathrm{A}}}{D_{\mathrm{A}}^0}(\phi) = 1 - a\phi$ where $a \approx 1.74$ in 2D for low fraction area [82]. Good agreements are found with this analytical prediction, see Fig. 2.7b where $a = 1.79$.

2.7.2 One colloid in the presence of solute particles

Similarly, a system with one colloid in a bath of solute particles is explored in order to validate the code. First the colloid does not catalyze a reaction, in this case the radial distribution function g_{CA} between the solute particles A and the colloid C, and the MSD of the colloid can be analyzed as some features are expected. Then, the reaction is added, but the interaction between solute particles are removed in order to compare concentration profiles computed in the simulation to analytical derivations.

System without reaction

Simulations are in 2D, and the colloid is surrounded by N solute particles of type A. Various solute densities ρ are investigated, to do so the number of particles is fixed ($N = 500$) and the size of the box varies accordingly. Radial distribution functions between solute particles and the colloid g_{CA} are displayed Fig. 2.8a. The plot emphasizes

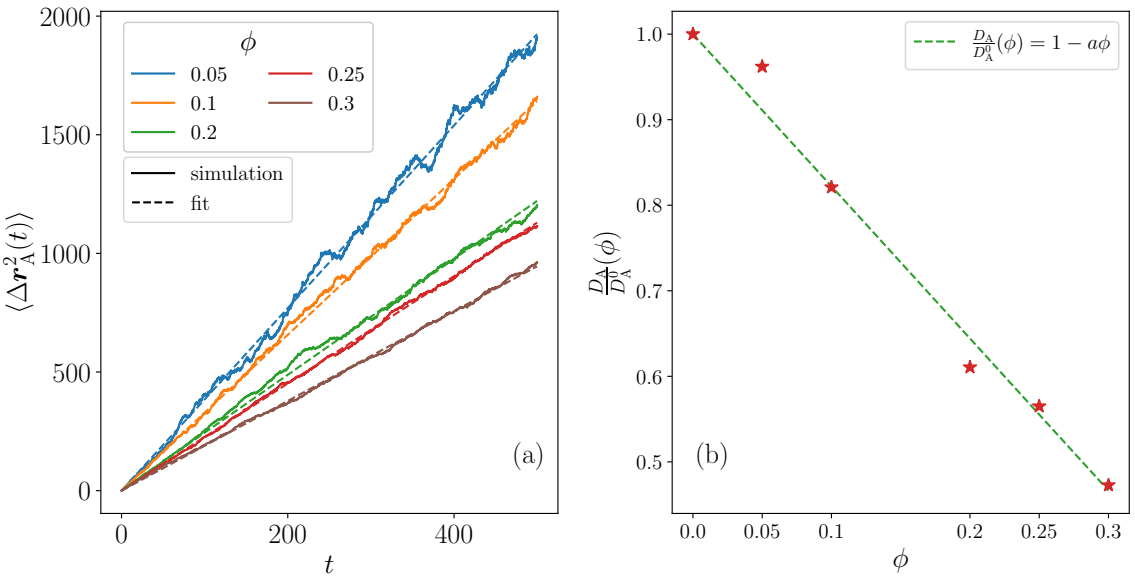

Figure 2.7: Results from simulations of a system composed of N solute particles of type A only. (a) Mean squared displacements of the solute particles as a function of time for different values of ϕ, linear fit are done using Eq. (2.7). (b) Diffusion coefficients of solute particles of type A, D_A, normalized by the diffusion coefficient at infinite dilution D_A^0 as a function of the surface fraction ϕ. Values measured in simulations are represented by the red stars. The dashed line represents the linear fit with $a = 1.79$

that there is an increasing structuration around the colloid due to the increasing crowding induced by the solute particles with the increase of ρ. This behavior is confirmed when analyzing the plot showing the MSDs on Figure 2.8b. First, the MSDs are linear in time, indicating that the colloid has typical Brownian motion. For each solute density, the diffusion coefficient of the colloid D_C is extracted by fitting the curves with Eq. (2.7). The fits, represented by the dashed lines on the plot, are in good agreement with the simulation data. The values found for the diffusion coefficient are normalized by the diffusion coefficient at infinite dilution D_C^0 and are plotted as a function of ρ in the inset of Figure 2.8b. The diffusion coefficient decreases as ρ increases as expected. Indeed, the denser is the bath of solute particles, the slower is the colloid.

System with reaction

The concentration profiles of the solute particles around the colloid which catalyzes the reaction around itself can be analytically determined, assuming the particles do not interact with each others. The reaction $\mathrm{A} + \mathrm{C} \rightarrow \mathrm{B} + \mathrm{C}$ takes place in a reaction area r_cut centered around the colloid of diameter σ_C. In this domain, labelled 1 in the calculations to come, the reaction occurs at a rate k_AB. Under these conditions, the concentration of solute particles A, $c_\mathrm{A}^{(1)}$, and the concentration of solute particles B, $c_\mathrm{B}^{(1)}$, obey the following

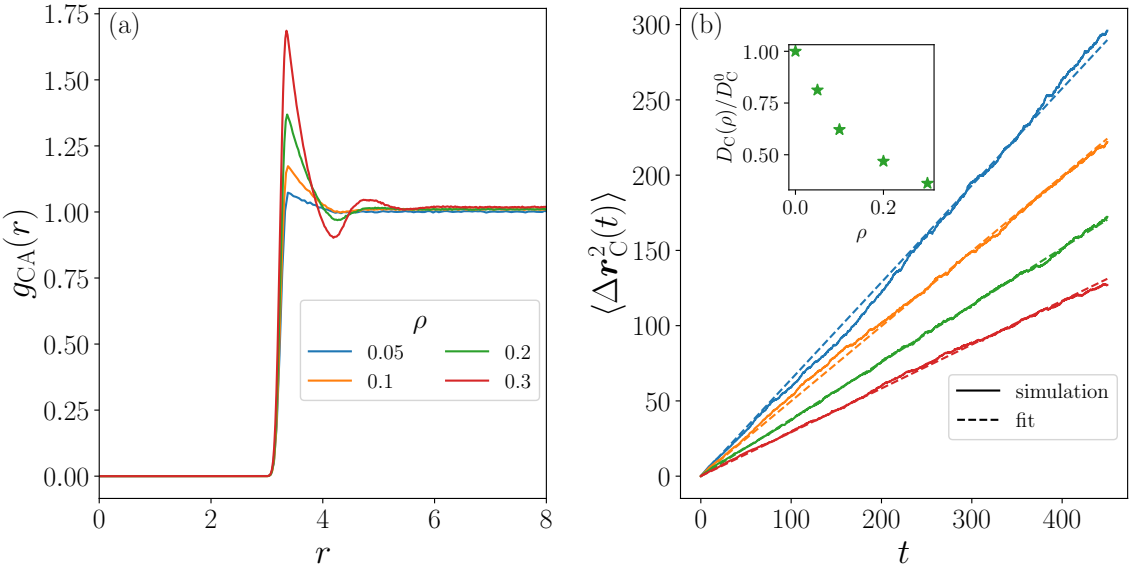

Figure 2.8: (a) Radial distribution functions g_{CA} between the colloid and the solute particles of type A as a function of r, the plot shows distances for $r < 8$ to zoom on the interesting part, and (b) MSDs of a colloid in a bath of N solute particles of type A with no reaction. Various solute densities ρ are investigated. Inset: the measured diffusion coefficient D_C normalized by the diffusion coefficient of the colloid at infinite dilution D_C^0 as a function of the solute density ρ.

reaction-diffusion equations:

$$\begin{cases} \frac{\partial}{\partial t} c_A^{(1)}(\boldsymbol{r},t) &= D_A^0 \nabla^2 c_A^{(1)}(\boldsymbol{r},t) - k_{AB} c_A^{(1)}(\boldsymbol{r},t) \\ \frac{\partial}{\partial t} c_B^{(1)}(\boldsymbol{r},t) &= D_A^0 \nabla^2 c_B^{(1)}(\boldsymbol{r},t) + k_{AB} c_A^{(1)}(\boldsymbol{r},t) \end{cases},$$

where D_A^0 is the diffusion coefficient of solute particles A and B at infinite dilution. Outside the reaction area, the reverse reaction B $\rightarrow$ A takes place at a rate k_{BA}. In this domain, labelled 2, the reaction-diffusion equations for the concentration of solute particles A, $c_A^{(2)}$, and B, $c_B^{(2)}$, are:

$$\begin{cases} \frac{\partial}{\partial t} c_A^{(2)}(\boldsymbol{r},t) &= D_A^0 \nabla^2 c_A^{(2)}(\boldsymbol{r},t) + k_{BA} c_B^{(2)}(\boldsymbol{r},t) \\ \frac{\partial}{\partial t} c_B^{(2)}(\boldsymbol{r},t) &= D_A^0 \nabla^2 c_B^{(2)}(\boldsymbol{r},t) - k_{BA} c_B^{(2)}(\boldsymbol{r},t) \end{cases}$$

The resolution of the concentration profiles for each type of solute particles in each domain is explained in Appendix F. The radial concentration profile of solute particles of type α around the colloid $c_\alpha(r)$, is also computed during the simulation. Fig. 2.9 shows that the concentration profiles of solute particles inside and outside the reaction area, as well as the transitions between the two domains obtained with simulations are in good agreements

with the results from theory, which validates the correct implementation of the reaction.

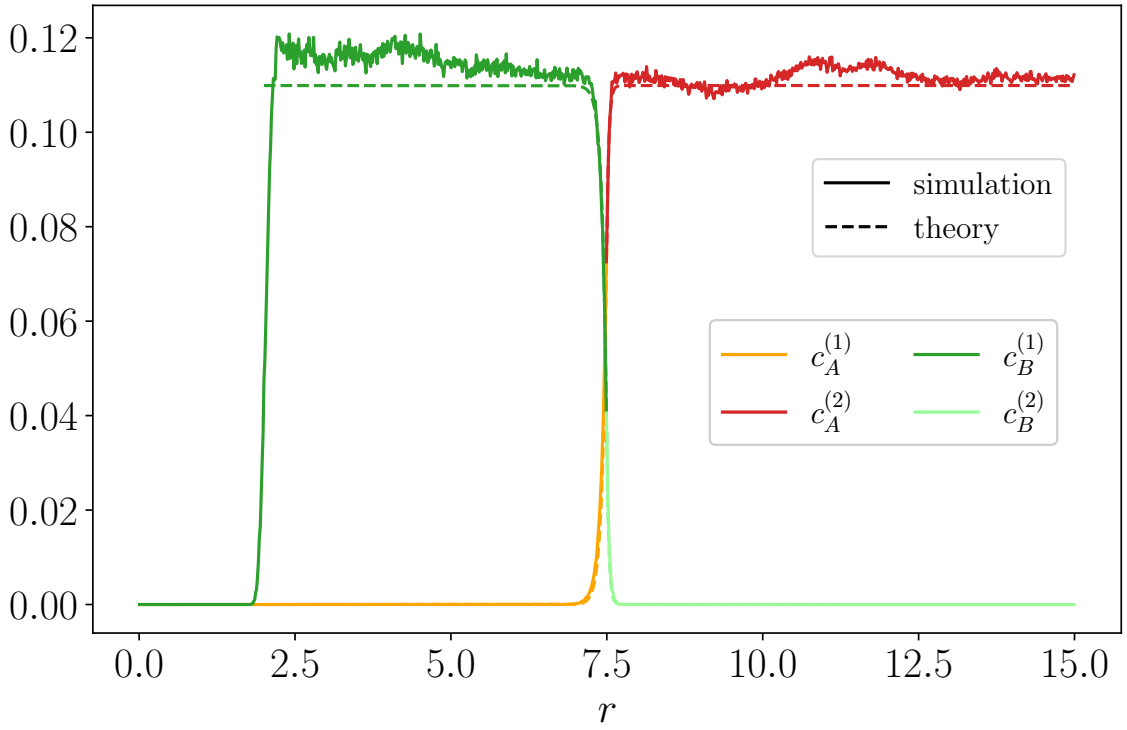

Figure 2.9: The colloid of diameter σ_{C} catalyzes the reaction $\mathrm{A} + \mathrm{C} \rightarrow \mathrm{B} + \mathrm{C}$ at a rate k_{AB} in a reaction area of radius r_{cut}, labelled 1. Outside, in the domain labelled 2, the reverse reaction $\mathrm{B} \rightarrow \mathrm{A}$ takes place at a rate k_{BA}. The concentration profiles of the solute particles A, $c_{\mathrm{A}}^{(\gamma)}(r)$, and of solute particles B, $c_{\mathrm{B}}^{(\gamma)}(r)$, in each domain γ are shown. r being the distance between the solutes and the colloid. The dashed lines represent the analytical results, solid lines the simulation results.

2.8 Validation of the BD-ABP code

In this section, I present the tests performed to ensure the correct modeling of physical properties of the system using the BD-ABP code. In the simulations of the ABP model, only colloids are modelled. For the validation process, $N_{\mathrm{C}} = 1$. Figure 2.10a shows the mean squared displacement of the colloid as a function of time. The data from simulation are in good agreements with the analytical expression for the MSD of the ABP model for one particle given by Eq. (2.14). The autocorrelation function of the orientation vector $\boldsymbol{n}$ is shown as a function of time, $\langle \boldsymbol{n}(t') \cdot \boldsymbol{n}(t'+t) \rangle_{t'}$, on Figure 2.10b. Again, simulation data are in good agreements with the analytical prediction given by Eq. (2.13).

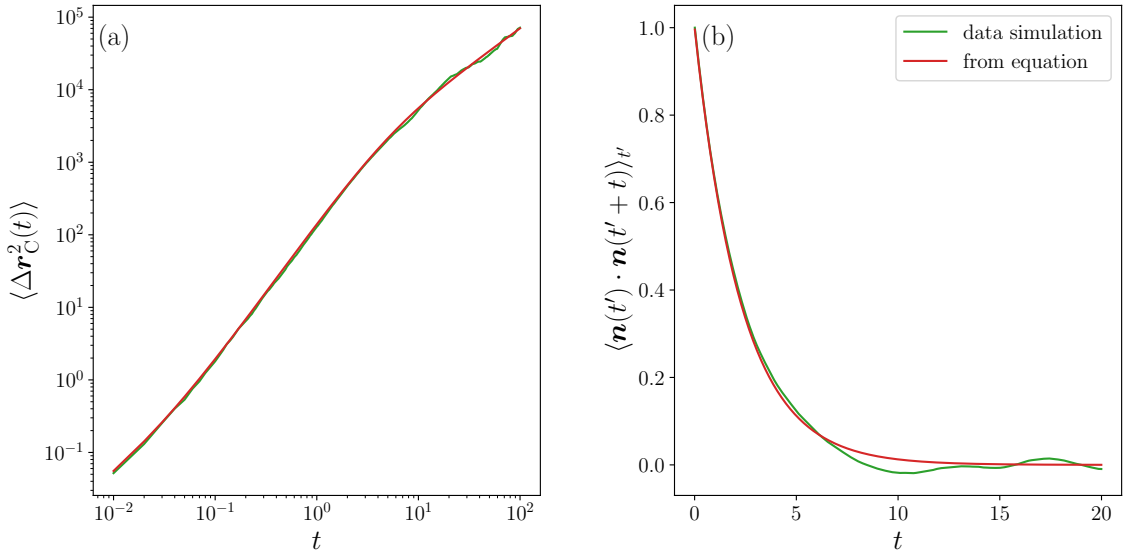

Figure 2.10: Comparison between simulation and theory with $N_C = 1$. (a) The MSD as a function of time from simulation data is confronted to Eq. (2.14). (b) The autocorrelation function of the orientation vector $\boldsymbol{n}$ as a function of time from simulation data is confronted to Eq. (2.13)

2.9 Simulation procedure

In this section, the procedure executed for each system studied, whose results are presented in this manuscript, is explained.

First, a system without reaction is simulated. One or several colloids are surrounded by N solute particles of type A and do not catalyze a reaction. The solute density ρ is fixed. The particles are randomly positioned in the simulation box, therefore equilibrium steps need to be run. The time t_{eq} needed to equilibriate the system, is determined by looking at the radial distribution function g_{AA} between solute particles at different times. The WCA fluid around the colloid has reached the equilibrium when the radial distribution function has converged. It takes $t_{\text{eq}} = 10$. The positions of the particles at equilibrium are saved in order to be the initial random equilibrated configuration for the next simulations. From the equilibrium state, the simulation continues in order to produce several independent configurations, each separated by t_{eq}. In total, a set of $n_{\text{realizations}}$ configurations are saved and will serve as a starting point for each noise realization of the studied systems. The procedure is schematically represented on Figure 2.11.

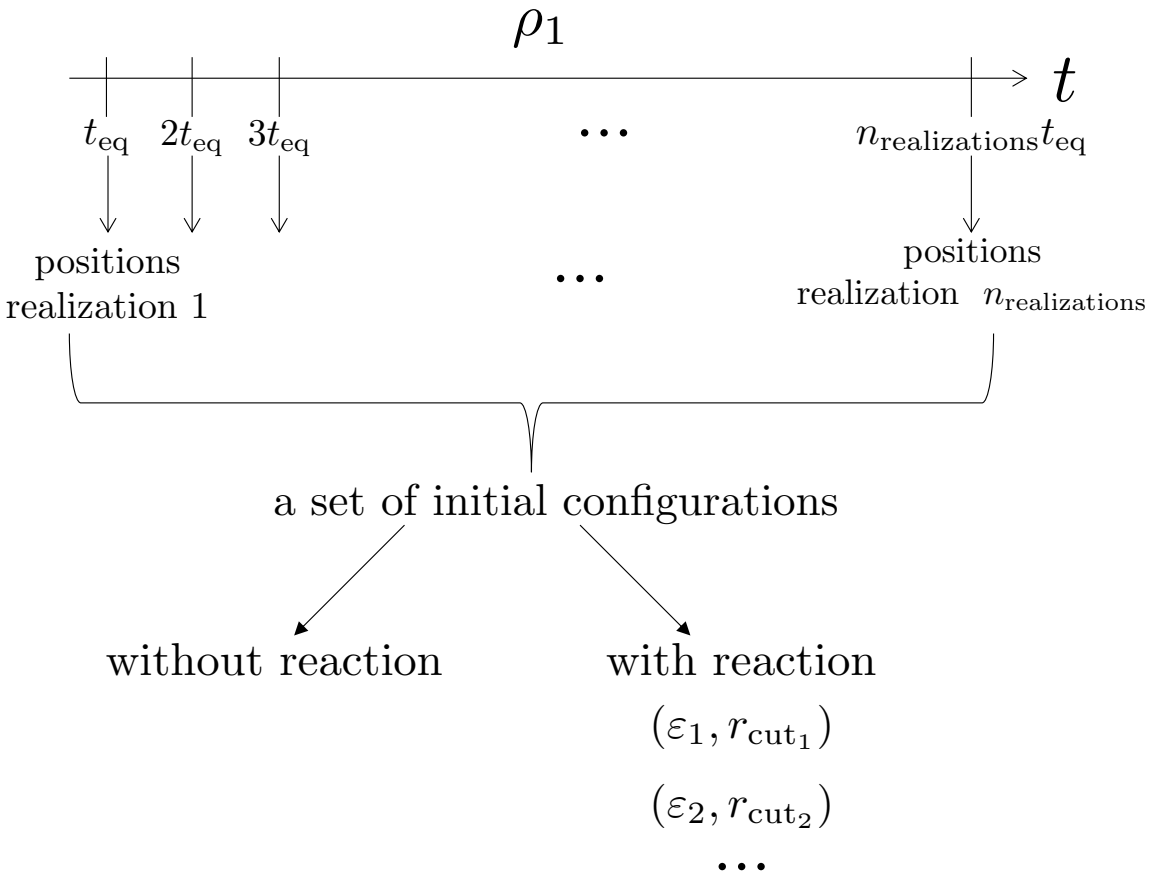

Figure 2.11: A drawing representing the preparation of the set of $n_{\mathrm{realizations}}$ independent initial configurations. The set corresponds to a fixed value of the solute density ρ_1 and will serve as the starting point of all the simulations at this density in order to average over the noise realizations.

CHAPTER 3

Dynamics of an isotropic colloid in a phase-separating environment

Contents

Summary

In this chapter, the dynamics of one colloid in a bath of solute particles is studied. This colloid catalyzes a reaction in its vicinity, which transforms purely repulsive solute particles into Lennard-Jones (LJ) ones. The key parameters of the model are varied: the solute density ρ, the intensity of the attraction between LJ solute particles ε, and the reaction area radius r_{cut}. First, the mean squared displacement of the colloid is computed and exhibits characteristics of activity: the diffusion coefficient at long times is enhanced compared to the reference one in a system at equilibrium. A state diagram gathers the results for all the parameters studied, which clarifies for which set of parameters activity emerges. Second, the microscopic mechanism is unveiled: the LJ fluid demixes for suitable parameters, solute particles can aggregate and form droplets. This leads to strong density fluctuations in the vicinity of the colloid, which are quantified with the polarization vector $\boldsymbol{p}$ of solute particles around the colloid introduced in this chapter. The autocorrelation function of $\boldsymbol{p}$ is analyzed and shows that the fluctuations of orientation can persist during a characteristic persistence time τ_p. On the basis of the ABP model, a coarse-grained equation to model the dynamics of the colloid is proposed, where the polarization vector $\boldsymbol{p}$ plays the role of the source of the biased motion. A thorough analysis of the MSD derived from this equation confirms the identified mechanism: the persistence of the density fluctuations generates the self-propulsion. A key parameter that controls whether there is activity and its intensity emerges, namely the filling fraction of the reaction area. Indeed, at a low filling fraction, the LJ fluid around colloids is in a gaseous state, droplets cannot form, consequently there are no density fluctuations. In contrast, at high filling fractions, the reaction area is densely filled, which hinders the colloid motion. At intermediate filling fractions, all the conditions are met for self-propulsion and enhanced diffusion at long times. Finally, the robustness of the model is challenged in this chapter by varying: the size ratio between the colloid and the solute particles, the reverse reaction rate, and the location of the reverse reaction. These modifications alter the geometry of the reaction area, but the mechanism identified still holds and activity still emerges. A 3D simulation is also performed, where the colloid also self-propels due to the demixing of the LJ fluid.

3.1 Introduction

In this chapter, the case of the dynamics of a unique colloid in a phase separating environment is investigated. The colloid is in a bath of N solute particles and catalyzes the reaction $A + C \rightarrow B + C$. The reverse reaction $B \rightarrow A$ also takes place far away from it. Different systems are studied, varying the key parameters identified as controlling the phase of the LJ fluid: the solute density ρ, the intensity of the attraction ε and the reaction area radius r_{cut}. The results obtained from the simulations of these reactive systems are compared to a reference system, without reaction. For each solute density ρ, the corresponding reference system is simulated and analyzed. The confrontation of the mean squared displacement of the colloid between the reactive system and the reference one, shows that activity emerges for some parameters when the reaction is triggered, which can be explained from a microscopic insight. The mechanism leading to self-propulsion is then shown to be robust. Besides, a quantity to interpret the data steps out from this investigation. The chapter is organized as follows: in Section 3.2, the numerical values of the parameters defining the system are given, as well as the range of the studied parameters: ρ, ε and r_{cut}. Section 3.3 describes the procedure to characterize the colloid dynamics, which is then analyzed. In Section 3.4, the mechanism at the origin of the self-propulsion is unveiled. A coarse-grained equation to describe the colloid dynamics is proposed and analyzed in Section 3.5, which confirms the proposed intuitive mechanism. In Section 3.6, some parameters, considered so far as fixed, are varied to challenge the robustness of the identified mechanism.

3.2 Numerical values of the parameters of the system

In this chapter, the dynamics of only one colloid is investigated, $N_{\text{C}} = 1$. The colloid catalyzes the reaction $A + C \rightarrow B + C$ and the reverse reaction $B \rightarrow A$ takes place far from it. Initially, the colloid is placed in a bath of $N = N_{\text{A}}$ solute particles of type A. N_{A} and N_{B} evolves with time when the reaction is triggered, but N remains constant. The effects of the key parameters, identified in the preceding chapter as controlling the phase of the LJ fluid, are investigated. Consequently, the solute density ρ, the intensity of the attraction ε, and the size of the reaction area r_{cut} vary.

The number of solute particles in the system is fixed to $N = 500$. Various solute densities ρ are investigated: N remains unchanged, while the size of the simulation box l_{box} varies. The values are recorded in Table III.1.

The solute particles are of diameter $\sigma_{\text{A}} = 1$ and the colloid diameter is $\sigma_{\text{C}} = 5$. Therefore, diffusion coefficients at infinite dilution used as input for the overdamped

ρ	0.05	0.1	0.2	0.3
l_{box}	100	70	50	40

Table III.1: Size of the simulation box l_{box} for the corresponding solute density $\rho = N/l_{\text{box}}^2$.

Langevin equation are $D_{\text{A}}^0 = 1$ and $D_{\text{C}}^0 = 0.2$ for the solute particles and the colloid, respectively. In Sect. 3.6, where the effect of the colloid size is investigated, σ_{C} changes.

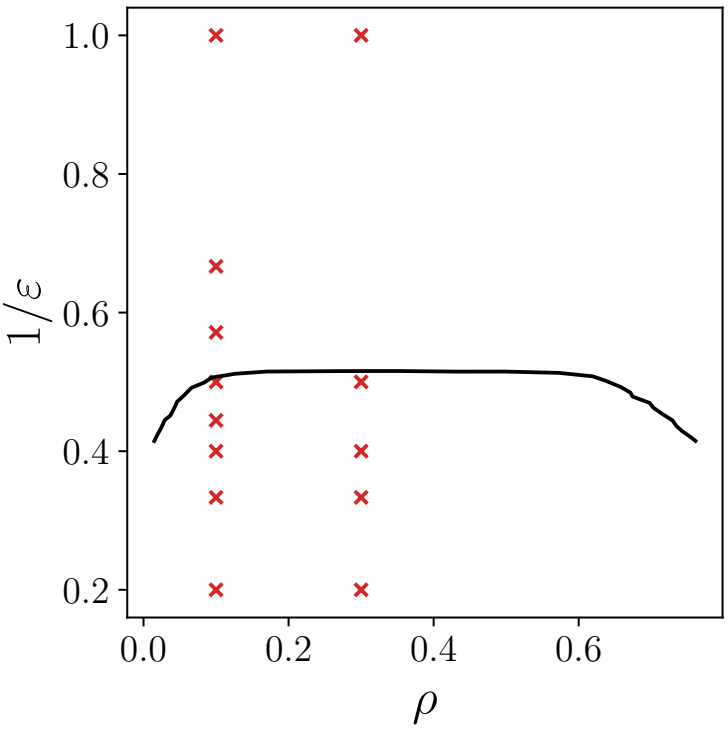

Figure 3.1: Phase diagram of a (full) Lennard-Jones fluid in two dimensions. The black line represents the coexistence curve in the plane $(1/\varepsilon, \rho)$. Below the curve, there is a gas phase and a liquid phase. Above the curve, the fluid is in a gaseous state. The curve was drawn using values extracted from [83]. The red crosses correspond to the simulations carried out in this PhD work.

The purely repulsive interactions of the system modeled using the WCA potential are controlled by ε' which remains the same in every case: $\varepsilon' = 10$. For the LJ potential, the choice of the attraction intensity, controlled by ε, is crucial in order to create a phase separation. The range was chosen based on the phase diagram of a bulk LJ fluid in 2D, as the equivalent for the particular confined geometry of our system does not exist. The phase diagram is displayed on Figure 3.1. The black line symbolizes the coexistence curve in the plane $(1/\varepsilon, \rho)$. Below, the fluid exhibits both gas and liquid phases, above, the fluid is in a gaseous state. Varying the attraction intensity ε amounts to change the temperature T, as both quantities are linked through the relation $T = 1/\varepsilon$. Data comes from [83], in which the authors have carried out simulations using the full LJ potential,

and not the truncated LJ potential. This still gives a correct estimation, as the phase diagram was used in order to have a qualitative idea of which values to target. The red crosses indicate the parameters values for ε and ρ tested in the simulations. Two solute densities ρ were investigated, $\rho = 0.1$ and $\rho = 0.3$, for which ε takes values between 1 and 5. Indeed, at these solute densities, at $\varepsilon = 1$ the LJ fluid is in a gaseous phase. When ε increases, the coexistence curve is crossed, and a phase separation might occur.

The radius of the reaction area r_{cut}, centered on the colloid, varies from 5.5 to 15. This defines reaction areas, whose shape is a shell, of thickness between 3 and 12.5. The averaged time for the reaction to occur, τ_{AB}, and the one for the reverse reaction to occur, τ_{BA}, are fixed and equal: $\tau_{\text{AB}} = \tau_{\text{BA}} = 0.1$. This value is chosen so that the reactions are instantaneous in comparison to the other timescales of the problem. In Sect. 3.6, the reverse reaction characteristic time τ_{BA} is modified to slow it down in order to prove the robustness of the model.

For a system without reaction, at the chosen solute densities, the maximum time step accepted has been shown to be $\Delta t = 0.0001$. As highlighted in what precedes, this value must be adapted when the reaction is triggered. The solute particles B, which interact with each other with attraction, will agglomerate, increasing the local solute density. This attraction is enhanced with ε, therefore the time step depends on ε. The chosen values are summarized in Table III.2.

$\rho = 0.05$	
ε	Δt
3	0.00006

$\rho = 0.1$	
ε	Δt
1, 1.5, 1.75, 2, 2.25	0.0001
2.5, 3, 5	0.00006

$\rho = 0.2$	
ε	Δt
3	0.00005

$\rho = 0.3$	
ε	Δt
1	0.00006
2	0.00005
2.5, 3	0.00003
5	0.00001

Table III.2: Values of the time step Δt as a function of ρ and ε in the systems investigated.

3.3 Characterization of the colloid dynamics

For each studied solute density, a set of initial configurations at equilibrium has been extracted from simulations without reaction. From then, either simulations without reaction are carried on longer timescales, or the reaction is set. The former simulations will serve as references. For the latter, for each solute density, various values of the intensity of the attraction ε, and of the size of the reaction area r_{cut} are investigated. After the reaction is triggered, the reactive system rapidly reaches a steady state, during which quantities to characterize the colloid dynamics are computed. In this section, I describe

the procedure established to analyze the results from simulations. First, the steady state is defined. Next, the dynamics of the system at steady state is presented. I explain how I compute the diffusion coefficient in both reference and reactive systems, and I compare the obtained results. Finally, all the examined combinations of parameters are assembled on a state diagram, which clarifies how the emergence of self-propulsion depends on the key parameters ρ, ε and r_{cut}. A key observable is unraveled which controls the existence and the intensity of activity: the filling fraction of the reaction area.

3.3.1 Definition of the steady state of the system

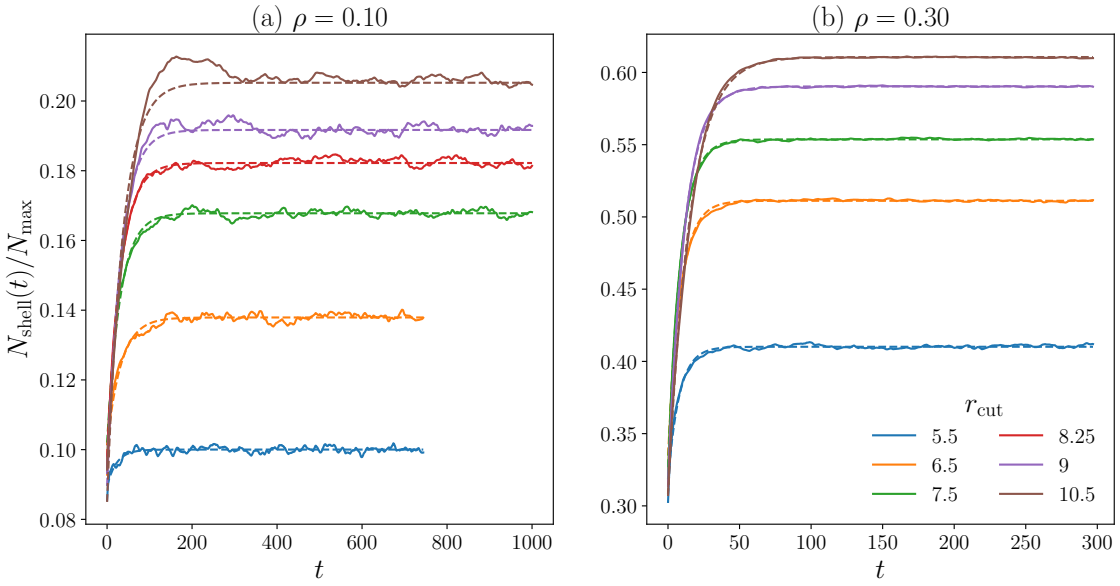

Figure 3.2: The number of particles inside the reaction area normalized by N_{max} as a function of time, $N_{\text{shell}}(t)/N_{\text{max}}$, at $\varepsilon = 3$ and various r_{cut} for (a) $\rho = 0.1$ and (b) $\rho = 0.3$. The dashed lines represent the exponential fits using Equation (3.2). Note that the time is shown for (a) $t < 1000$ and (b) $t < 300$ to emphasize the interesting part.

The number of particles inside the reaction area, which is a circular shell, is denoted by N_{shell}. This quantity is actually an average over the noise realizations, $N_{\text{shell}} = \langle N_{\text{shell}} \rangle_{n_{\text{realizations}}}$. In order to compare the various systems with each other, the number of particles inside the reaction area is normalized by the maximum number of particles which would fill the reaction area at the maximum packing fraction, denoted by N_{max}. N_{max} is defined by Equation (3.1) where ϕ_{max} is the maximum surface packing fraction.

$$N_{\text{max}} = \phi_{\text{max}} \frac{r_{\text{cut}}^2 - (\sigma_{\text{C}}/2)^2}{(\sigma_{\text{A}}/2)^2} \tag{3.1}$$

For hard disks in 2D, $\phi_{\text{max}} = \pi\sqrt{3}/6 \simeq 0.91$. Figure 3.2 represents N_{shell} normalized by

$N_{\max}$ as a function of time for a fixed value of the interaction strength between LJ particles ($\varepsilon = 3$), at $\rho = 0.1$ (Fig. 3.2a), and at $\rho = 0.3$ (Fig. 3.2b). These examples of the kinetics of filling of the reaction area show that the number of particles inside the reaction area increases, before reaching a plateau. Thus, this quantity is a relevant indicator to define the steady state. Initially, $N_{\text{shell},0} = N_{\text{shell}}(0)$ solute particles A are inside the reaction area. The reaction disrupts the established solute equilibrium as a LJ fluid forms inside the reaction area. Due to attractive interactions, more solute particles than the initial number of solute particles agglomerate, N_{shell} increases. At some point, the number of particles inside the shell saturates at the value $N_{\text{shell},\infty}$. Indeed, as the colloid moves, it accumulates as much as it loses particles: a steady state is established. The curves can be modeled by the following exponential behavior:

$$N_{\text{shell}}(t) = N_{\text{shell},\infty} - (N_{\text{shell},\infty} - N_{\text{shell},0})\, \mathrm{e}^{-t/\tau_N} \tag{3.2}$$

The corresponding exponential fits, normalized by $N_{\max}$, are represented by the dashed lines on Fig. 3.2 and are in good agreement with computed data. The steady state is reached when the number of particles inside the reaction area is constant, at about $t = \tau_{\text{N}}$.

The filling fraction of the reaction area at steady state, measured here by $N_{\text{shell},\infty}/N_{\max}$, is represented for the various systems on Figure 3.3. The values of $N_{\text{shell},\infty}$ are reported in Appendix H for all the studied systems. As a comparison, the equivalent ratio in the simulation box is $N/N_{\text{box,max}}$, where the maximum number of particles that would fill the simulation box is $N_{\text{box,max}} = \phi_{\max} \frac{l_{\text{box}}^2 - \pi(\sigma_{\text{C}}/2)^2}{\pi(\sigma_{\text{A}}/2)^2}$. $N/N_{\text{box,max}}$ is equal to 0.08 and 0.27 for the solute densities $\rho = 0.1$ and 0.3, respectively. $N_{\text{shell},\infty}/N_{\max}$ increases with ε as it is expected: the stronger are the attractive interactions between solute particles, the more they agglomerate, attracting increasingly new particles. Moreover, $N_{\text{shell},\infty}/N_{\max}$ increases with r_{cut}, before reaching a maximum. This draws attention to the limits of the simulations in which the system is finite. Indeed, as r_{cut} increases, the filling fraction at steady state of the reaction area is limited by the amount of available solute particles in the bulk. The situation where the reaction area would absorb all the particles due to finite size effect should be avoided. For instance, at $\rho = 0.1$, $\varepsilon = 3$, and $r_{\text{cut}} = 15$, a simulation was carried in a system containing twice as more particles ($N = 1000$ and $l_{\text{box}} = 100$). The filling fraction at steady state is found to be in this case $N_{\text{shell},\infty}/N_{\max} = 0.18$ instead of 0.17 in the smaller system. Similary, for the system at $\rho = 0.3$, $\varepsilon = 5$, and $r_{\text{cut}} = 10.5$, in simulations with twice more particles ($N = 1000$ and $l_{\text{box}} = 57.7$) $N_{\text{shell},\infty}/N_{\max} = 0.66$ instead of 0.65. These larger systems are represented on Figure 3.3 by the empty symbols. To conclude, for some values of the parameters, a phase forms inside the reaction area

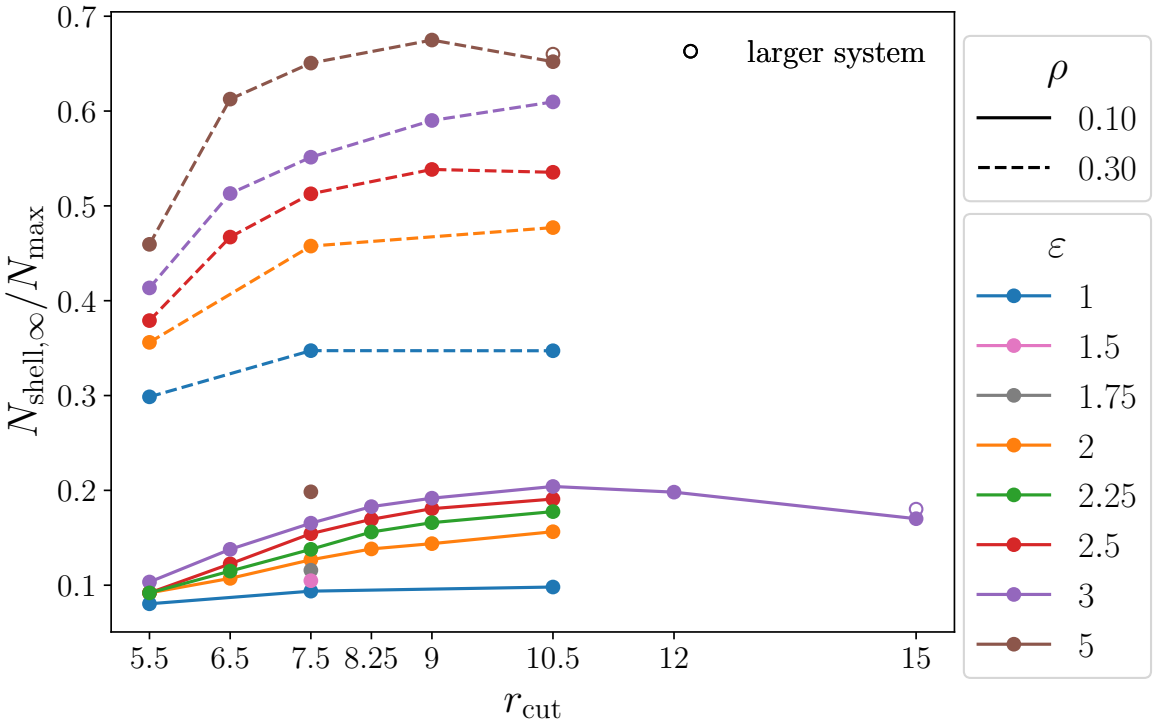

Figure 3.3: The filling fraction of the reaction area, measured by the stationary number of particles in the reaction area normalized by the maximum number of particles, $N_{\text{shell},\infty}/N_{\text{max}}$, as a function of r_{cut} for various ρ and ε. Empty symbols correspond to simulations of larger systems.

which is denser than in the bulk as $N_{\text{shell},\infty}/N_{\text{max}} > N/N_{\text{box,max}}$. Yet, the reaction area is not entirely filled, as $N_{\text{shell},\infty}/N_{\text{max}} < 1$. This observation underlines that the model successfully gathers the conditions for a phase separation to occur.

3.3.2 Dynamics of the colloid at steady state

The mean squared displacement of the colloid $\langle \Delta \boldsymbol{r}_{\text{C}}^2(t) \rangle$ is computed from simulations at steady state, for each set of parameters (ρ, ε, r_{cut}). The MSD is averaged over the noise realizations, $\langle \Delta \boldsymbol{r}_{\text{C}}^2(t) \rangle = \langle \Delta \boldsymbol{r}_{\text{C}}^2(t) \rangle_{n_{\text{realizations}}}$. The time is rescaled for these calculations so that the initial simulation time t_{init} is $t_{\text{init}} = 3\tau_{\text{N}}$, where τ_{N} is the time needed by the system to reach the steady state. From then, all the other quantities are computed. The MSDs for various systems at $\rho = 0.1$ are represented on Figure 3.4. On each plot, the MSD of the reference system is in black. At a first glance, it is straightforward that for some parameters presented on these plots, the diffusion of the colloid is enhanced, as the MSDs are much larger than for the reference. For a fixed value of r_{cut} ($r_{\text{cut}} = 7.5$), it appears on Figure 3.4a that the enhancement is amplified when ε increases. For a fixed value of ε ($\varepsilon = 3$), on Figure 3.4b, it is amplified with r_{cut}. In other words, for large values

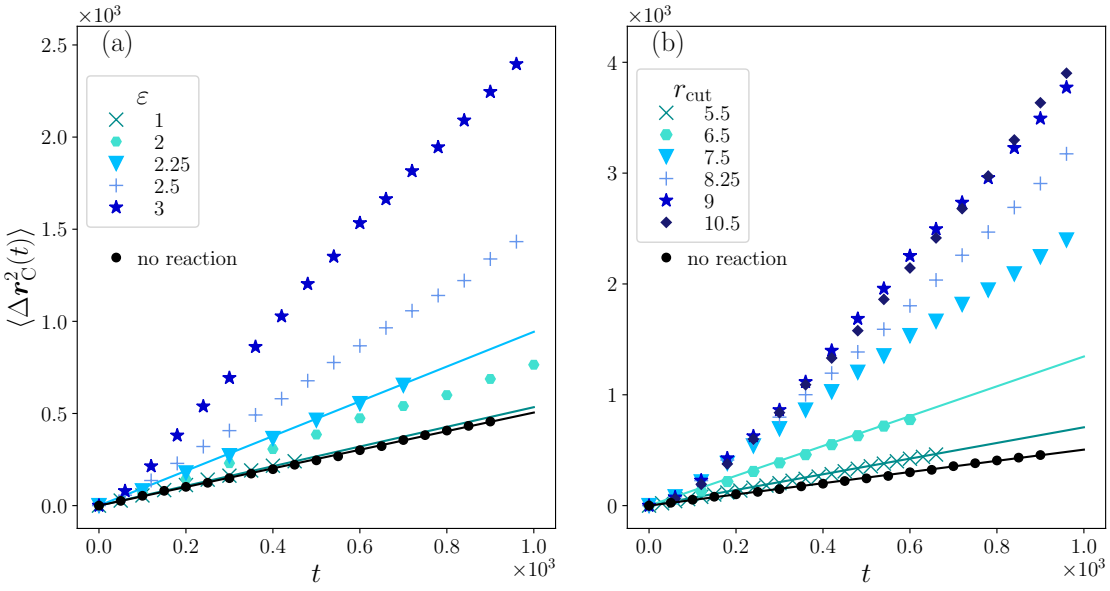

Figure 3.4: Mean squared displacements of the colloid as a function of time, for (a) a fixed value of r_{cut} ($r_{\text{cut}} = 7.5$) and various values of ε, and for (b) a fixed value of ε ($\varepsilon = 3$) and various values of r_{cut}. Solid lines are guides for the eye. The time is rescaled in order to compute the MSD at steady state. So the initial time t_{init}, here and in what follows, corresponds to $t_{\text{init}} = 3\tau_{\text{N}}$, where τ_{N} is the time needed to reach the steady state.

of ε and/or r_{cut}, the diffusion of the colloid is greatly enhanced.

A closer look at the MSD, represented for one set of parameters ($\rho = 0.1$, $\varepsilon = 3$ and $r_{\text{cut}} = 10.5$) in a log-log scale on Figure 3.5, evidences three distinct regimes, whereas the reference MSD on the same plot has only one. Interestingly, the MSD bears the same structure as the MSD of an ABP model (Eq. (2.14)), although the propulsion is not postulated in the constructed model. The three regimes are the following:

- On small timescales, both reference and reactive systems display a diffusive behavior characterized by approximately the same diffusion coefficient, i.e. the same intercept on the plot. Indeed, although the reaction triggered by the colloid creates a LJ fluid of solute particles B, the interactions between B solute particles and the colloid are the same as the interactions between solute particles A and the colloid. At these timescales, the colloid has encountered at most its first neighbors. In some cases, the diffusion coefficient of the reactive systems slightly deviates from the reference value, since the local density is affected by r_{cut} and ε as shown on Figure 3.3.

- At intermediate times, the trajectory of the colloid is ballistic. The MSD is proportional to t^2. This is the signature of activity. Surprisingly, despite the crowding induced by the solute particles, the colloid self-propels. Density fluctuations arise in the LJ fluid, which transiently favors a direction for the colloid displacement, hence

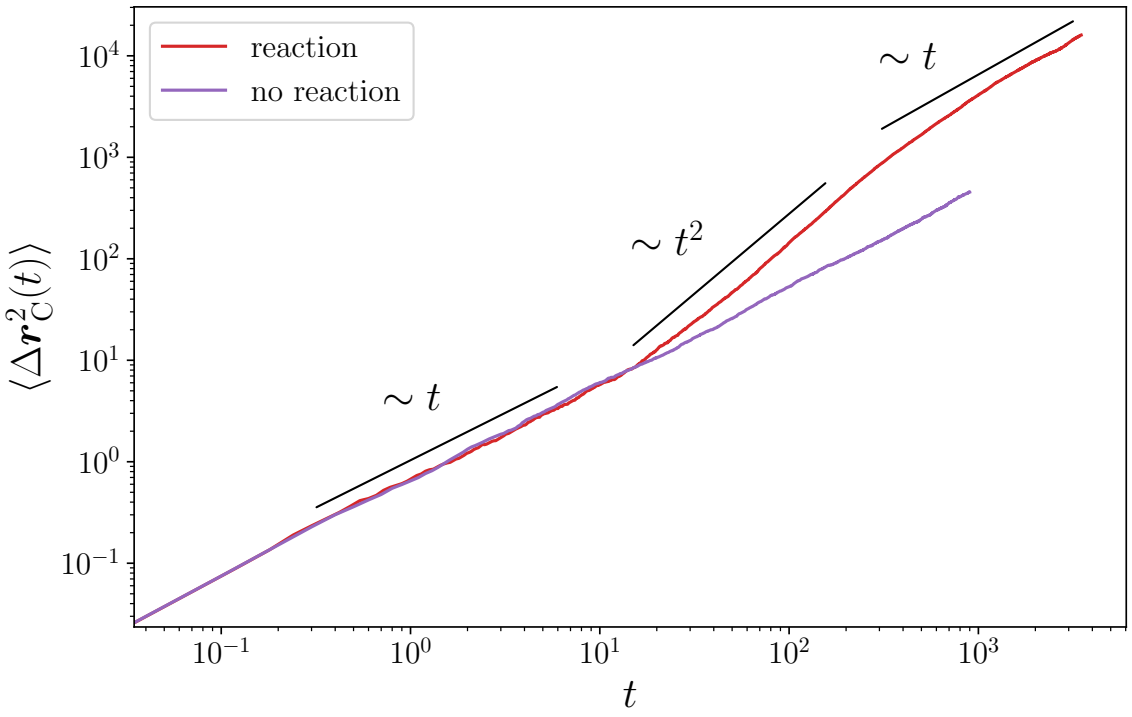

Figure 3.5: MSDs of the colloid as a function of time in a log-log scale. Comparison between the reference system without reaction at $\rho = 0.1$, and a system with reaction where $\rho = 0.1$, $\varepsilon = 3$ and $r_{\mathrm{cut}} = 10.5$.

the ballistic intermediate behavior.

- On longer timescales, the colloid has a diffusive regime again, with a MSD which is again linear in time. Indeed, at these timescales, the density fluctuations are randomized, modifying the preferred direction. The enhanced diffusion is characterized by an effective diffusion coefficient denoted by D_{eff}, and whose definition is given in the next paragraph.

3.3.3 Definition of activity

As underlined before, the presence of activity in the system can be noticed on the MSD by the intermediate ballistic trajectory. However, this criterion is qualitative rather than quantitative. Moreover, for some systems, the intermediate regime is not easily identifiable. Therefore, the activity of the system is quantified by comparing the effective diffusion coefficient at long times D_{eff} to the reference one denoted by $D_{\mathrm{no\_reac}}$. A systematic procedure is done to measure the diffusion coefficient. For the systems with reaction, it is first important that the last linear regime has been reached in order to determine the effective diffusion coefficient. Simulations must be run long enough, which

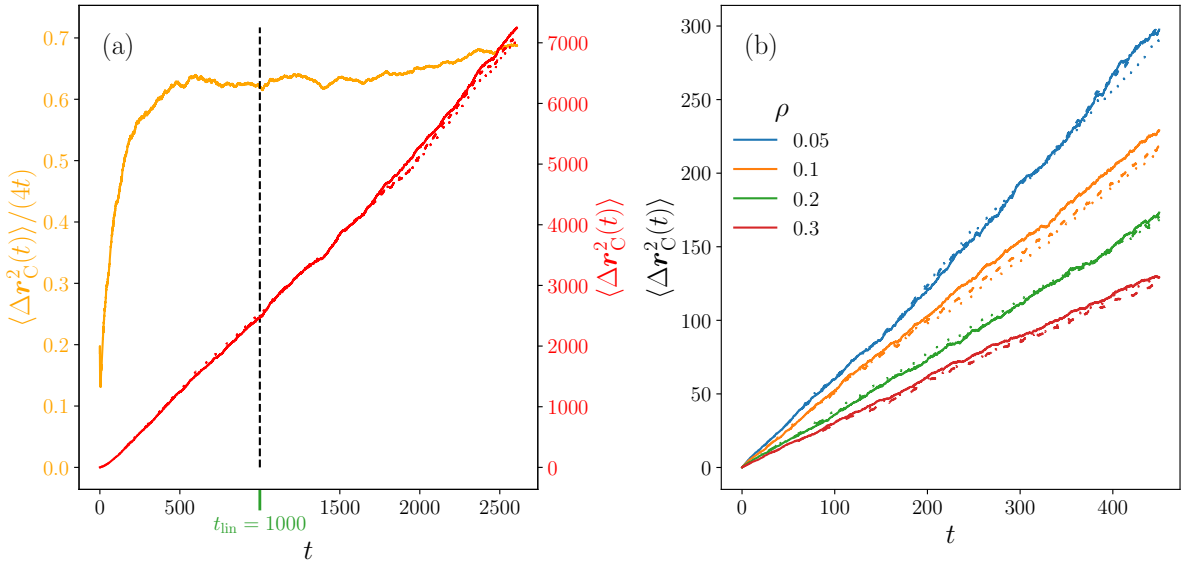

Figure 3.6: (a) In orange: $\frac{\langle \Delta \boldsymbol{r}_C^2(t) \rangle}{4t}$. In red: mean squared displacements of the colloid as a function of time, $\langle \Delta \boldsymbol{r}_C^2(t) \rangle$. The type of line: dotted, dashed or plain differentiates the subset from which each MSD comes. The vertical line indicates the time from which the orange curve reaches a plateau, t_{lin}. The plot corresponds to a system with reaction for the parameters $(\rho, \varepsilon, r_{\text{cut}}) = (0.1, 3, 7.5)$. Graphically, $t_{\text{lin}} = 1000$. (b) In this plot, there is no reaction in the system. MSDs for each subset, differentiated as in (a) by the line styles, are displayed as function of time. The colors indicate the solute density ρ of the system.

can be verified by plotting $\frac{1}{4t} \langle \Delta \boldsymbol{r}_C^2(t) \rangle$ as a function of time. From this plot, the time from which the MSD enters the last diffusive regime, t_{lin}, is defined graphically. An example is shown on Figure 3.6a in orange for the parameters $(\rho, \varepsilon, r_{\text{cut}}) = (0.1, 3, 7.5)$. The linear time is obtained choosing the time from which the curve presents a plateau, which yields $t_{\text{lin}} = 1000$ for this example. Afterwards, for $t > t_{\text{lin}}$, the MSD is fitted using Eq. (2.7) and a diffusion coefficient can be extracted. The effective diffusion coefficient is thus the long time slope of the MSD and is defined by:

$$D_{\text{eff}} \equiv \lim_{\substack{t \to \infty \\ t > t_{\text{lin}}}} \frac{1}{4t} \left\langle [\boldsymbol{r}_C(t) - \boldsymbol{r}_C(0)]^2 \right\rangle \tag{3.3}$$

Values for t_{lin} are reported in Appendix H for all the studied systems.

For both systems, with and without reaction, the accuracy of the computation of the diffusion coefficient depends on the average made over the noise realizations. There must be enough repetitions for the results to be representative of the physical state. Therefore, for each system $n_{\text{realizations}}$ noise realizations are made. For a system containing a single colloid at $\rho = 0.1$, the number of noise realizations is typically $n_{\text{realizations}} = 1000$. For each

realization, it takes about 8 hours to run until $t = 1000$. The simulations are run in series, i.e they are distributed on several processors. The number of processors being limited, the noise realizations are grouped and are launched one at a time. Typically, the 1000 noise realizations are split on 10 processors, and on each processor 100 noise realizations are run. In total, to reach t_{lin} in the case presented here takes about 800 hours, which corresponds to a month.

$D_{\text{no\_reac}}$ and D_{eff}, the diffusion coefficient of the colloid in the reference system and in the reactive system, respectively, as well as the associated errors, denoted by $\delta D_{\text{no\_reac}}$ and δD_{eff}, are computed by the means of the following method. I took three subsets of realizations which contains typically $0.7 n_{\text{realizations}}$ realizations each, and computed the corresponding MSDs. An example is shown on Figure 3.6b which displays the MSDs of a colloid in a passive system for various solute densities. Another example for a reactive system is shown in red on Fig. 3.6a, for the parameters $(\rho, \varepsilon, r_{\text{cut}}) = (0.1, 3, 7.5)$. The type of line (plain, dashed or dotted) represents the subset from which the MSD comes. I extracted the diffusion coefficient of the colloid fitting each MSD using Eq. (2.7) at all times for the reference system, and using Eq. (3.3) for the reactive system. $D_{\text{no\_reac}}$ or D_{eff} is then the average of the three values, and the associated error is the standard deviation of this sample. The values for both the diffusion coefficient and the associated error for the reference system are displayed in Table III.3, for each solute density ρ investigated in this PhD work. The error is very small, indicating enough noise realizations have been done.

The reactive systems showing activity will be referred to as active systems, whereas systems where the colloid does not self-propel will be referred to as passive systems. In order to discriminate between passive and active systems, I have decided to use the following criterion:

$$\begin{cases} \text{if } D_{\text{eff}} - \delta D_{\text{eff}} > D_{\text{no\_reac}} + \delta D_{\text{no\_reac}}, & \text{the system is active} \\ \text{otherwise,} & \text{the system is passive.} \end{cases} \tag{3.4}$$

ρ	0.05	0.1	0.2	0.3
$D_{\text{no\_reac}}$	0.163	0.124	0.094	0.072
$\delta D_{\text{no\_reac}}$	0.002	0.004	0.001	0.001

Table III.3: Values of the diffusion coefficient of the colloid and of the associated error for the reference systems. The colloid is in a bath of solute particles at a density ρ, and does not catalyze a reaction.

3.3.4 State diagram of the studied systems

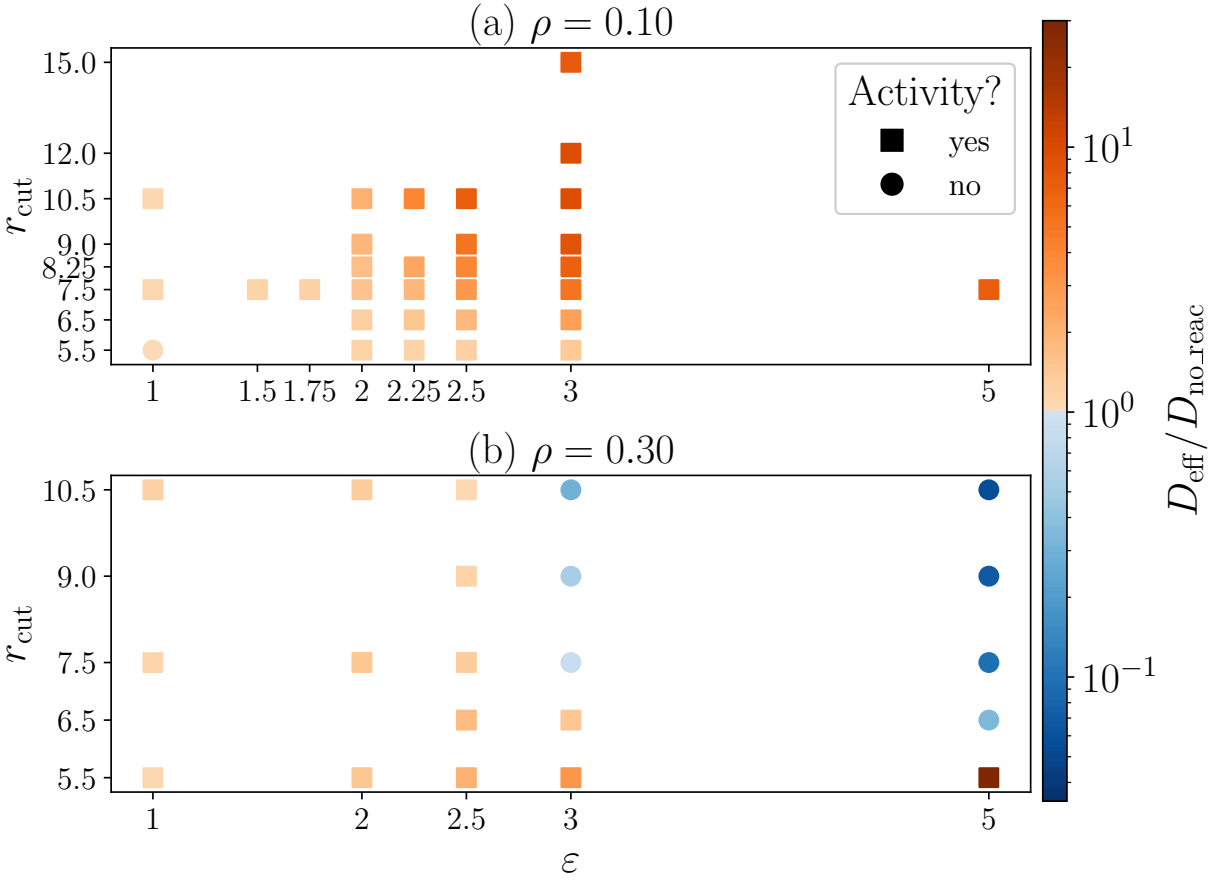

Figure 3.7: State diagram of the studied systems at $\rho = 0.1$ (top) and $\rho = 0.3$ (bottom). Colors indicate the value of $D_{\text{eff}}/D_{\text{no\_reac}}$, where D_{eff} is the long-time diffusion coefficient of the colloid (defined in Eq. (3.3)) and $D_{\text{no\_reac}}$ its value in the absence of reaction. From lower values (blue) to higher ones (dark orange). Square symbols indicate systems where activity was reported, circles systems without activity. Colloid displays activity if $D_{\text{eff}} - \delta D_{\text{eff}} > D_{\text{no\_reac}} + \delta D_{\text{no\_reac}}$.

A wide range of parameters is investigated for both solute densities $\rho = 0.1$ and $\rho = 0.3$, varying the attraction intensity ε and the size of the reaction area r_{cut}. For each system, the effective diffusion coefficient D_{eff} is computed from the MSD. Values are recorded in Appendix H. As previously stated, for some systems the presence of activity is obvious and can be affirmed after a quick overview of the MSD. For other systems, the ballistic part is small and the enhanced diffusion limited, so that whether the system is active or not is less obvious. By the means of the criterion previously defined (Eq. (3.4)), I have constructed a state diagram, represented on Figure 3.7, which summarizes the influence of the parameters for $\rho = 0.1$ (Fig. 3.7a) and $\rho = 0.3$ (Fig. 3.7b). The color represents the relative value of the effective diffusion coefficient compared to its equilibrium value,

$D_{\text{no\_reac}}$. Symbols indicate if activity is observed (squares where activity occurs, circles if not). Colors are ranging from blue for passive systems to dark orange for $D_{\text{eff}} \gg D_{\text{no\_reac}}$.

As it appears on Fig. 3.7a, at a relatively low solute density ($\rho = 0.1$), activity occurs for all the parameters tested (except at $\varepsilon = 1$ and $r_{\text{cut}} = 5.5$), and is increased when ε or r_{cut} increases. The results obtained at a higher density of solute, $\rho = 0.3$, are displayed on Fig. 3.7b. At this solute density, the propulsion is more difficult to achieve, as the range of parameters where D_{eff} is significantly higher than $D_{\text{no\_reac}}$ is more restricted. For example, activity occurs for all values of r_{cut} investigated here at $\varepsilon = 2.5$, but disappears for large reaction areas ($r_{\text{cut}} \geq 7.5$) at $\varepsilon = 3$. Indeed, at a solute density $\rho = 0.3$, the reaction area is more likely to be densely filled with B particles than when $\rho = 0.1$. The dense fluid, which occupies the reaction area, tends to hinder the motion of the colloid.

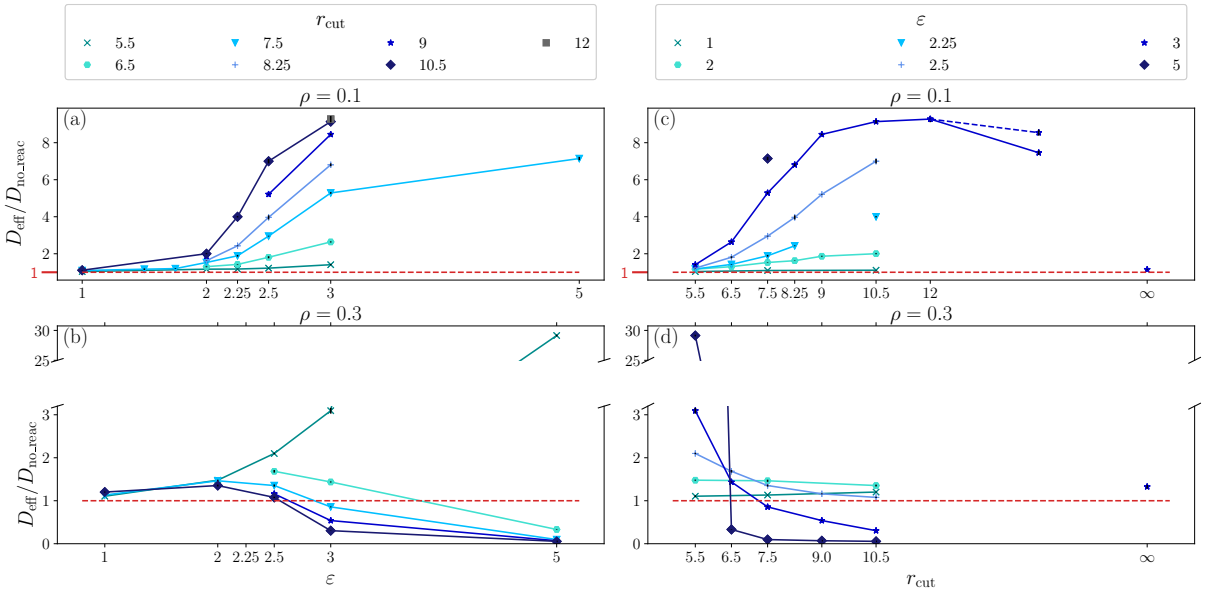

Figure 3.8: Intensity of the activity measured by $D_{\text{eff}}/D_{\text{no\_reac}}$ as a function of the attraction strength ε, for various reaction area radii r_{cut}, at $\rho = 0.1$ (a) and $\rho = 0.3$ (b). $D_{\text{eff}}/D_{\text{no\_reac}}$ is also presented as a function of r_{cut} for various ε, at $\rho = 0.1$ (c) and at $\rho = 0.3$ (d). On these plots, the values at $r_{\text{cut}} = \infty$ correspond to simulations where the reaction area is larger than the simulation box. The colloid is then in a bulk of a LJ fluid. On all the plots, the dashed red line marks the limit between active systems $D_{\text{eff}}/D_{\text{no\_reac}} > 1$ and passive systems $D_{\text{eff}}/D_{\text{no\_reac}} < 1$. The estimated errors on the diffusion coefficients are represented by the black error bars.

Figure 3.8 brings another perspective to the state diagram. The intensity of the self-propulsion is measured by the ratio $D_{\text{eff}}/D_{\text{no\_reac}}$ and is represented as a function of the key parameters ε and r_{cut} in another way. On the left part, the plots show the evolution of $D_{\text{eff}}/D_{\text{no\_reac}}$ as a function of ε for various r_{cut}, at $\rho = 0.1$ on Figure 3.8a and $\rho = 0.3$ on Figure 3.8b. Note that on Figure 3.8a, $r_{\text{cut}} = 12$ and $r_{\text{cut}} = 15$ are not shown since

these radii have only been studied at $\varepsilon = 3$. On the right part, the plots show the evolution of $D_{\text{eff}}/D_{\text{no\_reac}}$ as a function of r_{cut} for various ε, at $\rho = 0.1$ on Figure 3.8c and $\rho = 0.3$ on Figure 3.8d. On all the plots, the dashed red line delimits passive systems, $D_{\text{eff}}/D_{\text{no\_reac}} < 1$ (corresponding to the circle points on Figure 3.7), from active systems, $D_{\text{eff}}/D_{\text{no\_reac}} > 1$, (corresponding to the square points on Figure 3.7). Fig. 3.8a and 3.8b depict two different behaviors of the activity as a function of ε:

- At all the reaction area radii considered at $\rho = 0.1$ on Fig. 3.8a and for $r_{\text{cut}} = 5.5$ at $\rho = 0.3$ on Fig. 3.8b, $D_{\text{eff}}/D_{\text{no\_reac}}$ increases with ε. At first, the ratio increases slowly, and its value indicates that the self-propulsion of the colloid is limited. Indeed, the effective diffusion coefficient is of the same order as the reference one: the ratio $D_{\text{eff}}/D_{\text{no\_reac}}$ is on the dashed line or just above. Then, from a threshold value of ε, $D_{\text{eff}}/D_{\text{no\_reac}}$ increases sharply with ε. The threshold value for ε seems to vary as a function of r_{cut}. For instance on Fig. 3.8a, $D_{\text{eff}}/D_{\text{no\_reac}}$ is noticeably increased from $\varepsilon = 2$ at $r_{\text{cut}} = 10.5$, while the change seems to occur around $\varepsilon = 2.5$ at $r_{\text{cut}} = 6.5$. From the data exposed here, the threshold value of ε seems to be in the interval $[2, 3]$. For higher ε, the diffusion of the colloid is significantly increased and the effective diffusion coefficient reaches values up to ten times the reference value. The threshold value for ε can be interpretated as a crossover between a gaseous state of the LJ fluid in the reaction area to a state of liquid-gas coexistence, which induces large fluctuations, hence a significant self-propulsion.

- The results for values of $r_{\text{cut}} > 5.5$ at $\rho = 0.3$ shown on Figure 3.8b, evidence another behavior of the effective diffusion coefficient with ε: the activity is a non-monotonic function of ε. Initially, the systems present activity, although it is limited ($D_{\text{eff}}/D_{\text{no\_reac}} \sim 1$), and the intensity of the activity increases with ε. $D_{\text{eff}}/D_{\text{no\_reac}}$ reaches a maximum, whose value depends on r_{cut}, after which the self-propulsion decreases until crossing $D_{\text{eff}}/D_{\text{no\_reac}} = 1$. This indicates that there is no activity anymore, the colloid is even slower than in the system without reaction. The maximum is located around $\varepsilon = 2$ for the systems considered here.

Fig. 3.8c and 3.8d show how the activity is influenced by r_{cut}. On both plots, the points at $r_{\text{cut}} = \infty$ for $\varepsilon = 3$ correspond to a system where the reaction area is larger than the simulation box. This leads to a situation where the colloid is in a bulk fluid of LJ particles. In a world with infinite computational resources, the real case $r_{\text{cut}} = \infty$ would be to simulate an infinitely huge system at the chosen solute density with a very large reaction area regarding the colloid size. By this means, the LJ fluid in this infinite reaction area would not be at the same solute density as in the bulk. Indeed, the reaction area is in principle more densely filled than the bulk due to the attractive interactions. The

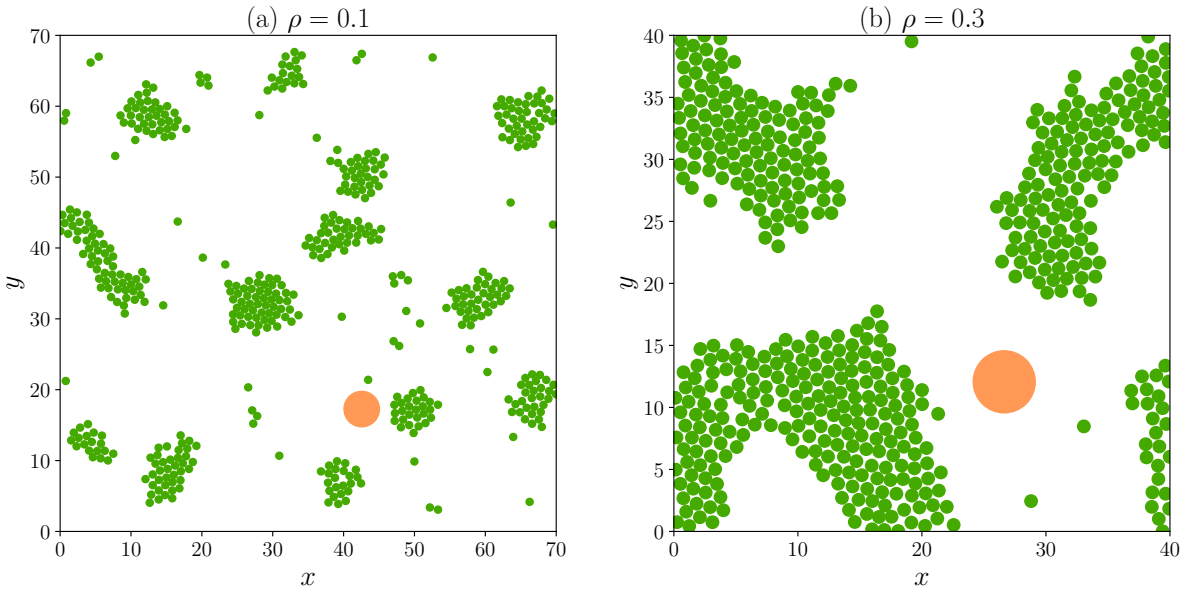

Figure 3.9: Snapshots of systems at $\varepsilon = 3$ and at a solute density (a) $\rho = 0.1$ and (b) $\rho = 0.3$. Here, $r_{\text{cut}} = \infty$ corresponds to systems where the reaction area is larger than the simulation box. This leads to a situation where the colloid is in a bulk of LJ solute particles.

two systems with a bulk of LJ solute particles aim at giving an idea of what would be the diffusion of the colloid in an infinitely large reaction area. The investigation at both solute densities shows that the diffusion of the colloid is comparable to the diffusion in the reference system. Snapshots of these systems are shown on Figure 3.9. There are two phases which coexist in the bulk of LJ solute particles: a dense liquid phase and a gas phase. However, the density fluctuations are not confined near the colloid, which is free to move. Now that I have discussed the case $r_{\text{cut}} = \infty$, I come back to the study of the activity as a function of r_{cut} shown on Figure 3.8 which also brings to light two different behaviors:

- At $\rho = 0.1$ (Fig. 3.8c), $D_{\text{eff}}/D_{\text{no\_reac}}$ is a non-monotonic function of r_{cut} at $\varepsilon = 3$. It increases as a function of r_{cut} before reaching a maximum between $r_{\text{cut}} = 12$ and $r_{\text{cut}} = 15$. The point at $r_{\text{cut}} = \infty$ for $\varepsilon = 3$ confirms that an optimum value for r_{cut} exists. As discussed in a previous paragraph, for $r_{\text{cut}} > 10.5$, there is finite size effect due to the large size of the reaction area regarding the simulation box size. Nevertheless, a simulation under the same conditions at $r_{\text{cut}} = 15$ in a larger system is shown by the empty symbol linked at $r_{\text{cut}} = 12$ by the dashed line. Qualitatively, the results are unchanged: there is a decrease of activity, and an optimum value for r_{cut} exists. Although large values of r_{cut} have not been investigated for other values of ε, a similar behavior is expected.

- Results at $\rho = 0.3$ (Fig. 3.8d) show an opposite behavior, $D_{\text{eff}}/D_{\text{no\_reac}}$ decreases with r_{cut}. The point $r_{\text{cut}} = \infty$ for $\varepsilon = 3$ suggests the existence of a minimum value for the diffusion coefficient, which seems to be around $r_{\text{cut}} = 10.5$. The larger system investigated at $r_{\text{cut}} = 10.5$, $\varepsilon = 5$ is not shown as the same effective diffusion coefficient than in the smaller system was found. Although the case $r_{\text{cut}} = \infty$ was not investigated for other values of ε, a similar behavior is expected.

From this analysis, the dependence of the effective diffusion coefficient D_{eff} on the key parameters becomes clearer. The systems can be classified in three categories: passive systems for which $D_{\text{eff}}/D_{\text{no\_reac}} < 1$, active systems where the self-propulsion is limited characterized by $D_{\text{eff}}/D_{\text{no\_reac}} \sim 1$, and active systems with a significant enhanced diffusion for which $D_{\text{eff}}/D_{\text{no\_reac}} > 1$.

3.3.5 A normalized local density as a key parameter to predict activity

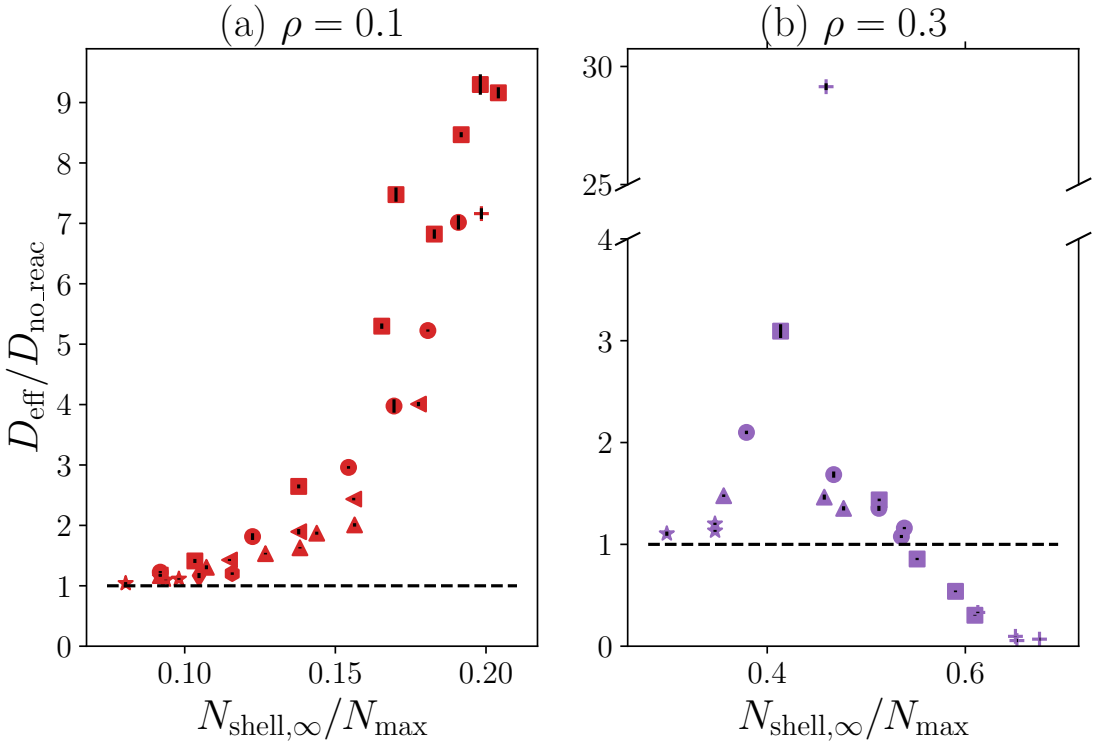

Figure 3.10: Long-time diffusion coefficient of the colloid D_{eff} divided by the value without reaction $D_{\text{no\_reac}}$ as a function of the filling fraction of the reaction area, measured by the stationary number of particles in the reaction area normalized by the maximum number of particles, $N_{\text{shell},\infty}/N_{\text{max}}$. Results obtained with a solute density (a) $\rho = 0.1$ and (b) $\rho = 0.3$. All data, corresponding to different sets of parameters ε, and r_{cut}, are collected here. Each symbol corresponds to a value of the Lennard-Jones parameter ε.

Figure 3.10 shows the long-time diffusion coefficient of the colloid divided by its value in the absence of reaction, $D_{\text{eff}}/D_{\text{no\_reac}}$ as a function of the number of particles inside the reaction area, normalized by the maximum number of particles which would fill the reaction area, $N_{\text{shell},\infty}/N_{\text{max}}$. The dashed line represents the threshold ($D_{\text{eff}}/D_{\text{no\_reac}} = 1$) above which the colloid is active. All the data obtained for different values of r_{cut}, ε and ρ are shown here.

Interestingly, it appears that using the filling fraction of the reaction area at steady state, $N_{\text{shell},\infty}/N_{\text{max}}$, all the data can be collapsed on a single line, at a given solute density. This representation underlines that the filling fraction is a key parameter that controls whether there is activity, and its intensity. The influence of the filling fraction of the reaction area is subtle, and three situations can be distinguished, as already mentionned. The first regime can be seen on Fig. 3.10a for $N_{\text{shell},\infty}/N_{\text{max}} < 0.12$ and on Fig. 3.10b for $N_{\text{shell},\infty}/N_{\text{max}} < 0.35$. At small filling fractions, solute density fluctuations in the vicinity of the colloid are very small, as only a gas phase is present. Thus, the relative increase of the diffusion coefficient is limited. A second regime is observed at intermediate values of the filling fraction, where propulsion appears. In this range, a phase separation can occur, resulting in a highly enhanced diffusion. In this regime, $D_{\text{eff}}/D_{\text{no\_reac}}$ is an increasing function of the filling fraction. At relatively low bath concentration ($\rho = 0.1$, Figure 3.10a), only these two regimes are observed and the second regime corresponds to $N_{\text{shell},\infty}/N_{\text{max}} > 0.12$. At a larger bath concentration ($\rho = 0.3$, Figure 3.10b), the second regime appears in the range $0.35 < N_{\text{shell},\infty}/N_{\text{max}} < 0.45$. Interestingly, at $\rho = 0.3$, a non-monotonous behavior is observed, revealing a third regime for $N_{\text{shell},\infty}/N_{\text{max}} > 0.45$. When the filling fraction reaches the critical value of 0.45, the activity starts to decrease. Actually, for high filling fractions, activity is suppressed due to the formation of a dense crystal around the colloid, as shown on the snapshot on Fig. 3.11. A special case occurs for $\rho = 0.3$, $\varepsilon = 5$ and $r_{\text{cut}} = 5.5$, for which a huge propulsion is observed, due to an artifact of the model. Under these conditions, the reaction area is not large enough to form a closed crystal which leads to a particular geometry of the shell of B particles, which favors an enhanced diffusion.

3.4 Analysis of the propulsion mechanism

3.4.1 Qualitative analysis of the mechanism

A microscopic analysis of the mechanism at the origin of activity is proposed and is schematically represented on Figure 3.12. The LJ fluid undergoes local phase transition in the vicinity of the colloid, creating density fluctuations. Solute particles polarize,

forming one or several droplets which push the colloid in the opposite direction. The persistence time of the droplets orientation is denoted by τ_p. If τ_p is large enough, the motion of the colloid is transiently ballistic. On longer timescales, the droplets orientation is randomized. The motion of the colloid is diffusive again characterized by an effective diffusion coefficient, D_{eff}, higher than the reference one, $D_{\text{no\_reac}}$.

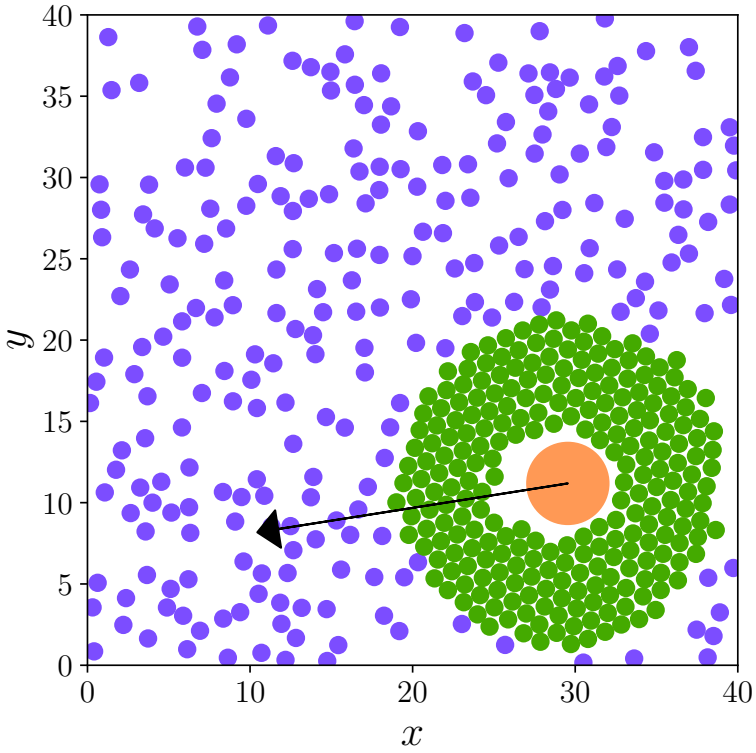

Figure 3.11: Snapshot of the system at $\rho = 0.3$, $\varepsilon = 5$ and $r_{\text{cut}} = 10.5$. A dense crystal forms in the reaction area, which is not centered around the colloid. The asymmetric filling propels the colloid, yet, activity is not observed for this system. Indeed, the shell is closed, and the side in the opposite direction from the propulsion of the colloid hinders its movement. The polarity vector $-\boldsymbol{p}$, defined in Section 3.4, is represented by the black arrow.

3.4.2 Polarization vector of the solute density around the colloid

The phase separation in the vicinity of the colloid polarizes its local environment. Solute density fluctuations arise, which breaks the symmetry of the system and leads to the self-propulsion of the colloid. A polarization vector $\boldsymbol{p}$ is introduced in order to quantify the polarization of solute particles in the colloid environment:

$$\boldsymbol{p}(t) = \sum_{i \in \mathcal{P}} \left[\boldsymbol{r}_i(t) - \boldsymbol{r}_{\text{C}}(t) \right], \tag{3.5}$$

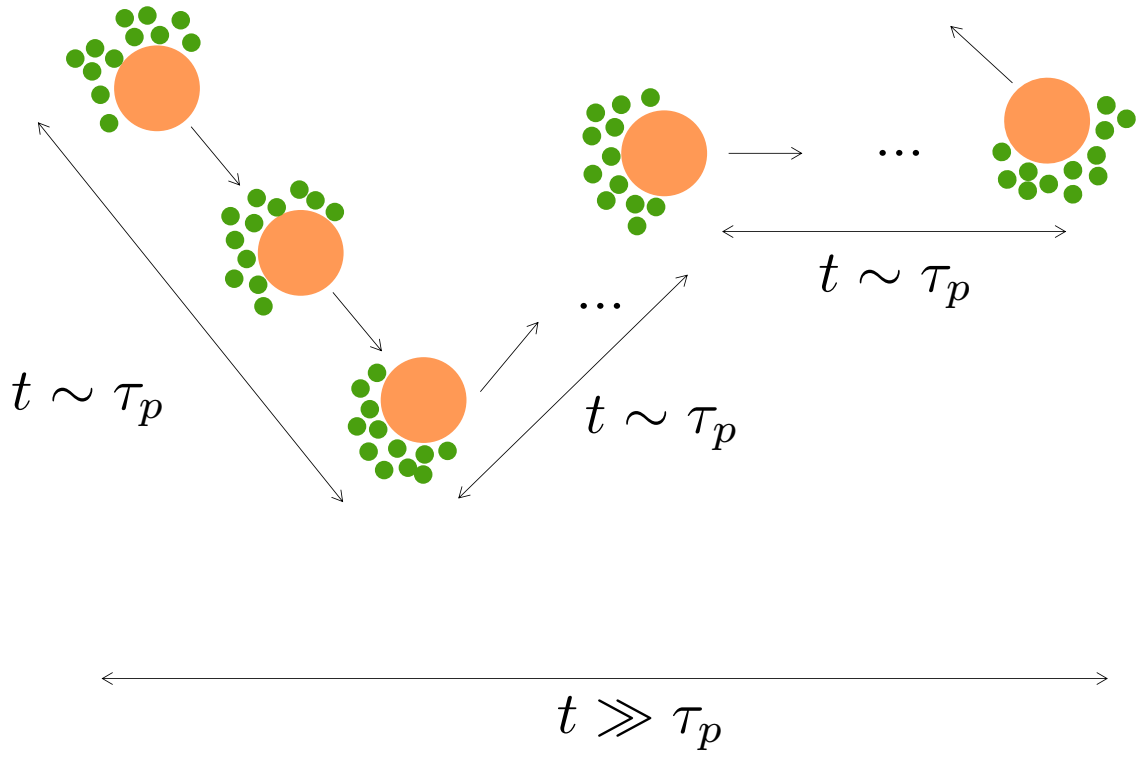

Figure 3.12: Sketch of the identified mechanism as being at the origin of the self-propulsion of the colloid. Droplets form in the vicinity of the colloid, which push it away in the opposite direction. The droplets orientation is characterized by a persistence time τ_p. For $t < \tau_p$, the motion of the colloid is ballistic. On longer timescales, the droplets orientation is randomized, leading to a diffusive motion with enhanced diffusion.

where $\mathcal{P}$ defines a proximal circular area around the colloid C, where the solute particles i interact directly with it. The solute particles interact purely repulsively with the colloid, however, the potential used here is softer than a hard sphere potential. In order to capture the solute particles interacting directly with the colloid, the proximal area must be larger than $(\sigma_\mathrm{A} + \sigma_C)/2$. Several trials have led to the conclusion that a suitable value for the area radius is $(3\sigma_\mathrm{A} + \sigma_\mathrm{C})/2$. To estimate the persistence time of the droplets orientation, the autocorrelation function of the polarization vector $\langle \boldsymbol{p}(t) \cdot \boldsymbol{p}(t+t') \rangle_{t'}$ is computed. The average runs over the noise realizations $n_\mathrm{realizations}$ and the initial time t', $\langle \boldsymbol{p}(t') \cdot \boldsymbol{p}(t'+t) \rangle_{t'} = \langle \boldsymbol{p}(t') \cdot \boldsymbol{p}(t'+t) \rangle_{n_\mathrm{realizations}, t'}$. This autocorrelation function is plotted on Figure 3.13 for various systems where activity is observed, and for the reference system for comparison. The study of the effective diffusion coefficient as a function of the filling fraction of the reaction area, $N_{\mathrm{shell},\infty}/N_\mathrm{max}$, has highlighted that two categories emerge among active cases. In the first one, for low values of $N_{\mathrm{shell},\infty}/N_\mathrm{max}$, the activity

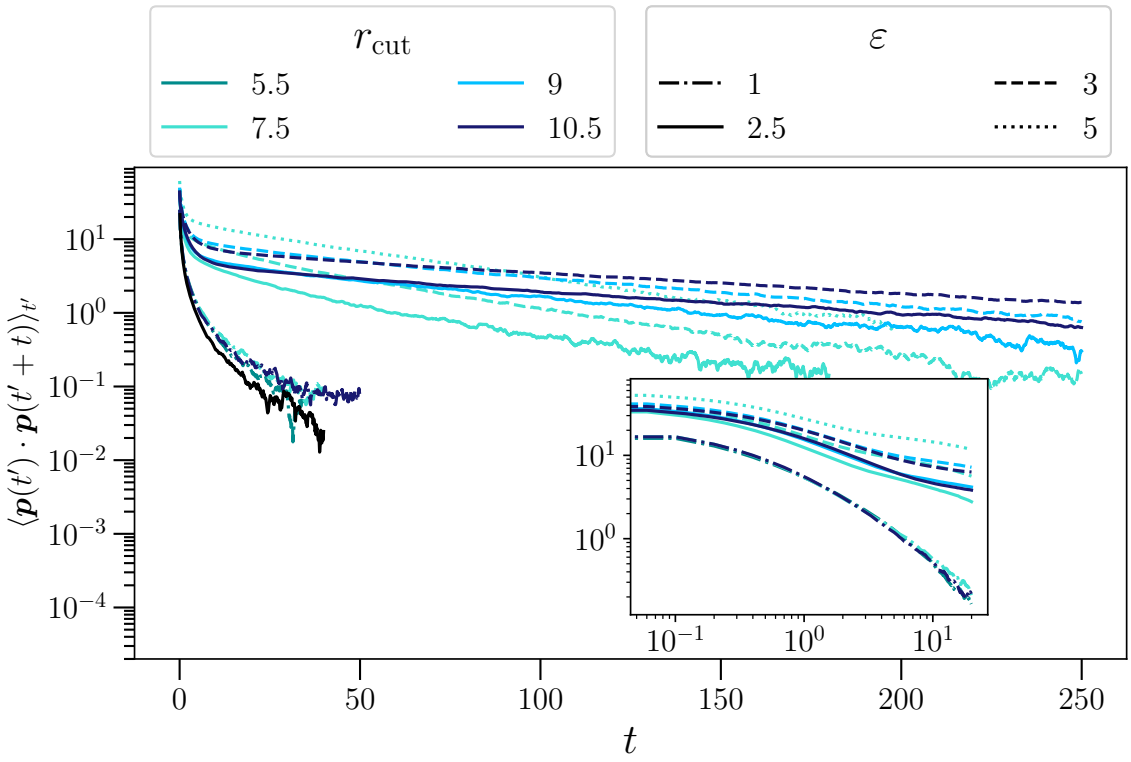

Figure 3.13: Autocorrelation functions of the polarization vector as a function of time $\langle \boldsymbol{p}(t') \cdot \boldsymbol{p}(t'+t) \rangle_{t'}$ for various parameters where activity is observed. The black curve represents the reference system. Inset: the log-log representation of the autocorrelation functions.

is limited and D_{eff} is hardly larger than $D_{\mathrm{no\_reac}}$. In constrast, active systems belonging to the second category present a significantly enhanced diffusion, $D_{\mathrm{eff}} \gg D_{\mathrm{no\_reac}}$. The analysis of the autocorrelation function of the polarization vector confirms this separation. Figure 3.13 represents the autocorrelation functions as a function of the time for various active systems. The parameters $\rho = 0.1$, $\varepsilon = 1$ and $r_{\mathrm{cut}} \in \{5.5, 7.5, 10.5\}$, correspond to systems belonging to this first category. For these cases, $\langle \boldsymbol{p}(t') \cdot \boldsymbol{p}(t'+t) \rangle_{t'}$ exhibits the same characteristics as the reference system: it decays as a power law at all times, as shown in the inset. This fast decrease comes from the fluctuations of the positions of the solute particles in the vicinity of the colloid due to Brownian motion, thus the absence of correlation of the polarization vector. For the parameters $\rho = 0.1$, $\varepsilon \in \{2.5, 3, 5\}$ and all the r_{cut} values, corresponding to systems belonging to the second category, the autocorrelation functions display two regimes: a power law decay at short times and an exponential decay at longer timescales. The crossover between the two regimes occurs at a characteristic time denoted by t_0. The second regime appears at longer times in active systems where the solute particles have merged in droplets. The droplets diffuse much slower than a single solute particle, consequently the droplets orientation is persistent

regarding the other timescales at stake, as indicated by the exponential tail of the autocorrelation function. For active systems of the first category, small density fluctuations appear, but the parameters are not favorable to droplets formation, hence the absence of exponential regime. The characteristic time of decay of the exponential behavior represents the persistence time τ_p of the droplets orientation, and can be found by fitting the autocorrelation function with an exponential function. The autocorrelation function is entirely described by:

$$\langle \boldsymbol{p}(t') \cdot \boldsymbol{p}(t'+t) \rangle_{t'} = \begin{cases} \frac{A}{(t+c)^{\alpha}} & \text{if } t \leq t_0, \\ B \exp\left(\frac{-t}{\tau_p}\right) & \text{else.} \end{cases}$$

The autocorrelation function is continuous in t_0, hence:

$$\frac{A}{(t_0+c)^{\alpha}} = B\,\mathrm{e}^{-t_0/\tau_p} \Longleftrightarrow B = \frac{A}{(t_0+c)^{\alpha}}\,\mathrm{e}^{t_0/\tau_p}\,.$$

The autocorrelation function can also be written:

$$\langle \boldsymbol{p}(t') \cdot \boldsymbol{p}(t'+t) \rangle_{t'} = \begin{cases} \frac{A}{(t+c)^{\alpha}} & \text{if } t \leq t_0, \\ \frac{A}{(t_0+c)^{\alpha}} \exp\left(\frac{-(t-t_0)}{\tau_p}\right) & \text{else.} \end{cases} \tag{3.6}$$

The autocorrelation function is fitted at all times by the power law in systems where only one regime is present. In any case presenting the two regimes, t_0 is obtained graphically. A fit is then performed on the autocorrelation function using the short-time equation for $t < t_0$ and using the long-time equation, for $t \geq t_0$. The following parameters can be extracted from the fits: A, c, α and τ_p. Examples of fits are shown Fig. 3.14, which are in good agreements with the simulation data. The polarization vector was not computed for all the systems investigated in this PhD work. The values of the fitted parameters for all the systems where $\boldsymbol{p}$ exists are summed up in Table III.4. If τ_p can not be extracted, no value is indicated. It is difficult to draw conclusions on the values found for the parameters of the power law regime. The interpretation will focus on the persistence time of orientation τ_p for which a physical meaning is associated and is detailed in a next paragraph.

3.4.3 Situations without activity

The autocorrelation function, $\langle \boldsymbol{p}(t') \cdot \boldsymbol{p}(t'+t) \rangle_{t'}$, for various passive systems is plotted on Figure 3.15. Its analysis surprisingly reveals two behaviors. As expected for some parameters, the autocorrelation functions display only the first power law regime (for

ρ	ε	r_{cut}	t_0	A	c	α	τ_p	Activity?
	1	5.5	10	6.3	0.2	0.9	-	No
	1	7.5	10	6.4	0.2	1.0	-	Yes
	1	10.5	10	6.8	0.3	1.0	-	Yes
	1.5	7.5	10	7.5	0.2	0.9	-	Yes
	1.75	7.5	10	8.2	0.2	0.9	-	Yes
	2.5	6.5	10	10.7	0.1	0.6	16.4	Yes
0.1	2.5	7.5	25	13.2	0.1	0.5	43.6	Yes
	2.5	9	10	16.7	0.2	0.6	88.7	Yes
	2.5	10.5	15	17.3	0.2	0.6	142.9	Yes
	3	7.5	20	18.0	0.1	0.4	48.0	Yes
	3	9	10	21.2	0.1	0.4	99.6	Yes
	3	10.5	15	21.0	0.2	0.5	161.9	Yes
	5	7.5	10	28.5	0.1	0.3	60.8	Yes
	1	7.5	5	6.0	0.2	1.4	-	Yes
	1	10.5	5	7.4	0.2	1.4	-	Yes
	2	7.5	5	6.2	0.2	1.3	18.7	Yes
	2	10.5	5	12.4	0.4	1.7	-	Yes
	2.5	6.5	5	5.7	0.1	1.1	-	Yes
	2.5	7.5	5	6.3	0.3	1.7	-	Yes
0.3	2.5	9	3.3	10.0	0.4	1.8	-	Yes
	2.5	10.5	2	13.0	0.3	1.6	-	Yes
	5	5.5	2	56.9	0.0	0.1	19.2	Yes
	5	6.5	15	2.2	0.0	0.5	16.1	No
	5	7.5	5	3.8	0.0	0.2	25.8	No
	5	9	5	20.8	0.0	0.1	371.0	No
	5	10.5	10	43.7	0.0	0.3	521.3	No

Table III.4: Parameters found using Eq. (3.6) to fit the computed autocorrelation function of the polarization vector $\langle \boldsymbol{p}(t') \cdot \boldsymbol{p}(t'+t) \rangle_{t'}$. τ_p is found with an exponential fit on systems where the second regime is observed. If not applicable, no value is indicated.

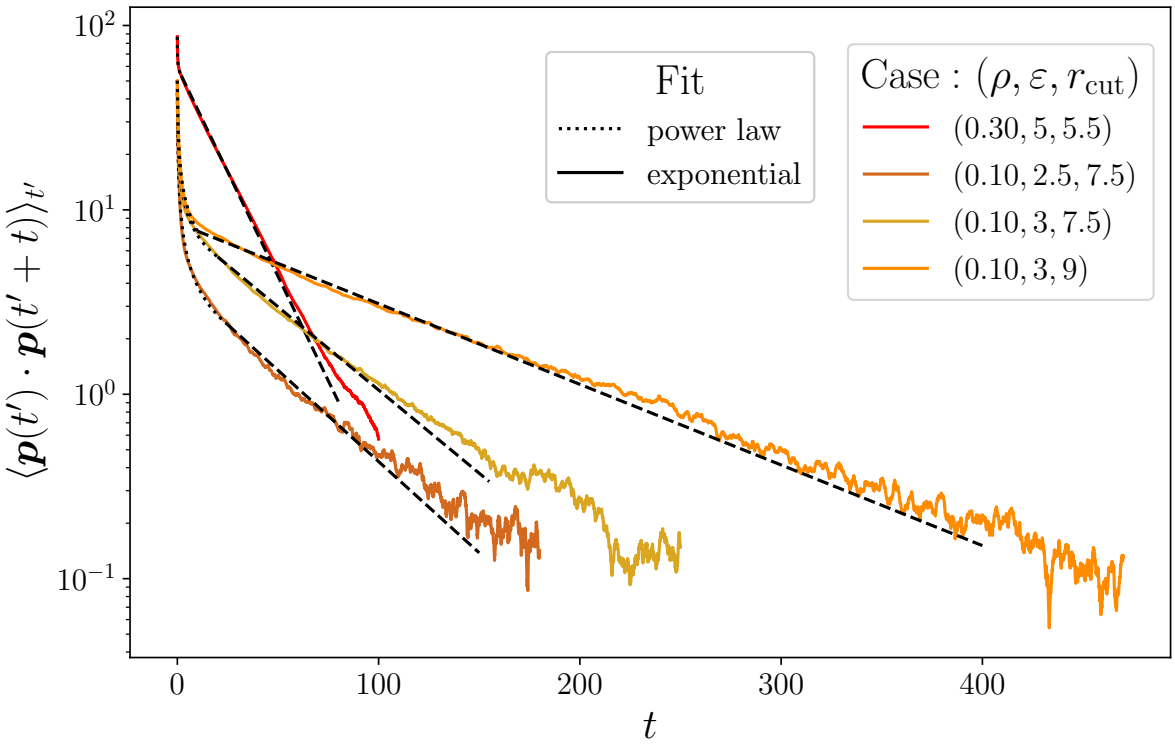

Figure 3.14: Examples using Eq. (3.6) to fit the autocorrelation functions of the polarization vector as a function of time $\langle \boldsymbol{p}(t') \cdot \boldsymbol{p}(t'+t) \rangle$ when activity is observed.

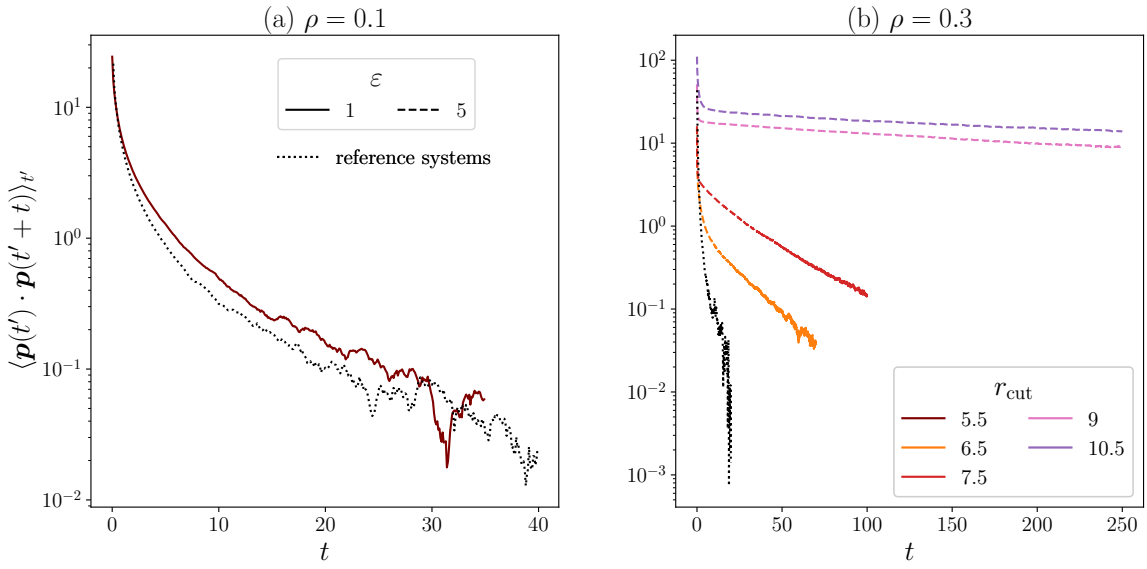

Figure 3.15: Autocorrelation functions of the polarization vector as a function of time $\langle \boldsymbol{p}(t') \cdot \boldsymbol{p}(t'+t) \rangle_{t'}$ for various passive systems. The solute density is (a) $\rho = 0.1$ and (b) $\rho = 0.3$.

instance $\rho = 0.1$, $\varepsilon = 1$, and $r_{\text{cut}} = 5.5$ on Fig. 3.15a, or $\rho = 0.3$, $\varepsilon = 5$, and $r_{\text{cut}} \in \{6.5, 7.5\}$ on Fig. 3.15b). This shows that no droplets form, or on the contrary, the

droplet forms a closed shell around the colloid. Thus, there is no longer persistence of the density fluctuations which results in the absence of activity. However, the autocorrelation functions of some passive systems exhibit an exponential tail, and their fitting reveals large values for τ_p. This can be explained by looking at the snapshot on Fig. 3.11, where the polarity vector is represented by a black arrow. There are still density fluctuations as the crystal is not centered on the colloid. The formed shell is very large, leading to a very slow diffusion, hence large orientation persistence times. But, the side of the crystal situated in the same direction as the polarization vector hinders the motion of the colloid and suppresses the activity. This occurs at large values of ε and/or r_{cut} at a rather high solute density, for instance on Fig. 3.15b $\rho = 0.3$, $\varepsilon = 3$ and $r_{\text{cut}} \in \{9, 10.5\}$.

3.4.4 The persistence orientation time in light of the normalized local density

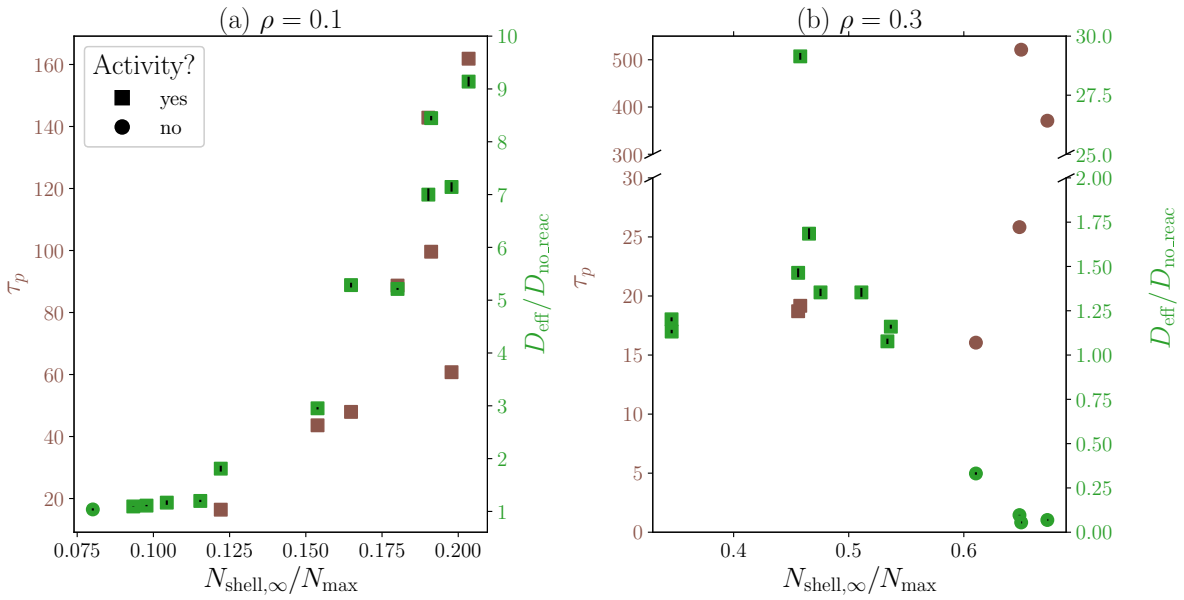

Figure 3.16: The persistence time of the polarization vector orientation τ_p as a function of the filling fraction at steady state of the reaction area $N_{\text{shell},\infty}/N_{\text{max}}$ is represented by the brown points. $D_{\text{eff}}/D_{\text{no\_reac}}$ as a function of $N_{\text{shell},\infty}/N_{\text{max}}$ is represented by the green points. The estimated errors on the diffusion coefficients are represented by the black error bars, which are smaller than the size of the symbols. All the data for which the polarization vector was computed for different values of r_{cut}, ε and ρ are shown here.

Figure 3.16 shows the long-time diffusion coefficient of the colloid divided by its value in the absence of reaction as a function of $N_{\text{shell},\infty}/N_{\text{max}}$ in green and the persistence orientation time τ_p as a function of $N_{\text{shell},\infty}/N_{\text{max}}$ in brown. The estimated errors on the diffusion coefficients are represented by the black error bars, which are smaller than

the size of the symbols. The circles represent passive systems, while the squares indicate systems where activity occurs. All the data for which the polarization vector was computed for different values of r_{cut}, ε and ρ are shown here. For systems with no exponential regime, τ_p can not be extracted. That is the case at small filling fractions. Solute density fluctuations in the vicinity of the colloid are very small, the polarization vector fluctuates and its autocorrelation function does not present an exponential tail. This is typically represented on Fig. 3.16a for $N_{\text{shell},\infty}/N_{\max} < 0.12$. The activity is limited as $D_{\text{eff}}/D_{\text{no\_reac}} < 1.5$ and there is no associated value for τ_p. In the second regime, there are enough particles in the vicinity of the colloid to form persistent droplets. τ_p is an increasing function of $N_{\text{shell},\infty}/N_{\max}$. As the filling fraction of the reaction area increases, the size of the droplets grows. The latter diffuse then more slowly raising τ_p. The increase of τ_p is correlated to the increase of $D_{\text{eff}}/D_{\text{no\_reac}}$ which is also an increasing function of $N_{\text{shell},\infty}/N_{\max}$ in this regime. This corresponds to values of $N_{\text{shell},\infty}/N_{\max} > 0.12$ on Fig. 3.16a. At higher filling fractions at $\rho = 0.3$ (Fig. 3.16b), the first regime is represented by the two green points with no associated values for τ_p at $N_{\text{shell},\infty}/N_{\max} \approx 0.35$. Less data are available for the second regime. In the third regime, only visible at $\rho = 0.3$, corresponding to data where $N_{\text{shell},\infty}/N_{\max} > 0.46$, $D_{\text{eff}}/D_{\text{no\_reac}}$ and τ_p are not correlated anymore. Indeed, at this filling fraction of the reaction area, a close shell has formed. As evidenced in the previous paragraph, some closed shells are not centered on the colloid. This results in density fluctuations characterized by a large persistence time τ_p, as it can be observed on Fig. 3.16b for $N_{\text{shell},\infty}/N_{\max} > 0.6$ where $\tau_p = 500$ at its highest. For $0.46 < N_{\text{shell},\infty}/N_{\max} < 0.6$, the reaction area is densely filled and a closed shell has probably formed. The absence of exponential tail for these cases indicates that if a shell has formed, it is probably centered on the colloid.

3.5 Effective description of the colloid dynamics

3.5.1 Effective Langevin equation

The analysis of the polarization vector reveals that the features of the model share similarities with the classical ABP description I have presented in Section 2.4. Although the dynamics of the polarization vector is more complex than in ABP model, as it presents two regimes, the long-time behavior is exponential with a characteristic time τ_p analogous to τ_r in Eq. (2.13). On the basis of the ABP model, a coarse-grained equation to model the dynamics of the colloid is proposed, where the polarization vector $\boldsymbol{p}$ plays the role of

the source of the biased motion:

$$\frac{\mathrm{d}\boldsymbol{r}_{\mathrm{C}}(t)}{\mathrm{d}t} = -K\boldsymbol{p}(t) + \boldsymbol{\xi}(t). \tag{3.7}$$

The effective Langevin equation written here bears the same structure as the ABP Langevin equation (Eq. (2.11)). The term $K\boldsymbol{p}(t)$ results from an effective active force, and the noise $\boldsymbol{\xi}(t)$ represents the fluctuations of the bath. K is a propulsion coefficient which links the velocity to the polarization vector.

The idea is to analyze the dynamics of a colloid whose motion is controlled by Eq. (3.7) by computing its MSD. The position of the colloid is obtained by integrating the equation of motion: $\boldsymbol{r}_{\mathrm{C}}(t) = -K\int_0^t \mathrm{d}t'\boldsymbol{p}(t') + \int_0^t \mathrm{d}t'\boldsymbol{\xi}(t') + \boldsymbol{r}(0)$, from which the MSD yields:

$$\begin{aligned}\left\langle \Delta\boldsymbol{r}_{\mathrm{C}}^2(t)\right\rangle = K^2\int_0^t \mathrm{d}t'\int_0^t \mathrm{d}t''\left\langle \boldsymbol{p}(t')\cdot\boldsymbol{p}(t'')\right\rangle + \int_0^t \mathrm{d}t'\int_0^t \mathrm{d}t''\left\langle \boldsymbol{\xi}(t')\cdot\boldsymbol{\xi}(t'')\right\rangle \\ - K\int_0^t \mathrm{d}t'\int_0^t \mathrm{d}t''\left(\left\langle \boldsymbol{p}(t')\cdot\boldsymbol{\xi}(t'')\right\rangle + \left\langle \boldsymbol{\xi}(t')\cdot\boldsymbol{p}(t'')\right\rangle\right).\end{aligned}$$

I define $\Delta_{\boldsymbol{ab}}(t) \equiv \int_0^t \mathrm{d}t'\int_0^t \mathrm{d}t''\left\langle \boldsymbol{a}(t')\cdot\boldsymbol{b}(t'')\right\rangle$ and I write the MSD as the sum of three contributions:

$$\left\langle \Delta\boldsymbol{r}_{\mathrm{C}}^2(t)\right\rangle = K^2\Delta_{\boldsymbol{pp}}(t) + \Delta_{\boldsymbol{\xi\xi}}(t) - K\left(\Delta_{\boldsymbol{p\xi}}(t) + \Delta_{\boldsymbol{\xi p}}(t)\right). \tag{3.8}$$

$K^2\Delta_{\boldsymbol{pp}}(t)$ is the contribution of the polarization vector, $\Delta_{\boldsymbol{\xi\xi}}(t)$ of the noise and $-K\left(\Delta_{\boldsymbol{p\xi}}(t) + \Delta_{\boldsymbol{\xi p}}(t)\right)$ of the cross-correlation between the noise and the polarization. The computation of the different contributions can be done either analytically or using the simulation data. Both approach are presented in what follows. In this section, the discussion will focus on a smaller set of parameters: the solute density is $\rho = 0.1$, $\varepsilon \in \{2.5, 3, 5\}$, and $r_{\mathrm{cut}} \in \{7.5, 9, 10.5\}$.

3.5.2 Analysis of the MSD for the effective model

In contrast to the ABP model, the autocorrelation function of the orientation vector is not purely exponential. Therefore, in this part, the goal is to compute analytically the MSD and to analyze the consequences of the power law regime on the short times of the autocorrelation function of $\boldsymbol{p}$. Under some hypotheses listed below, the MSD can be computed from Eq. (3.8):

1. The autocorrelation function of the polarization vector is supposed to be defined by Eq. (3.6).

2. The autocorrelation function of the noise, which represents uncorrelated fluctuations of the bath, is approximated by a delta function:

$$\langle \boldsymbol{\xi}(t') \cdot \boldsymbol{\xi}(t'') \rangle = \delta(t' - t''). \tag{3.9}$$

3. The contribution of the cross-correlation between the noise and the polarization is assumed to vanish.

$$-K \left(\Delta_{\boldsymbol{p}\boldsymbol{\xi}}(t) + \Delta_{\boldsymbol{\xi}\boldsymbol{p}}(t) \right) = 0. \tag{3.10}$$

The MSD is calculated (see details in Appendix G) and results in:

$$\left\langle \Delta \boldsymbol{r}_{\mathrm{C}}^2(t) \right\rangle = \begin{cases} 4D_{\mathrm{C}}t + \frac{2AK^2}{(1-\alpha)(2-\alpha)} \left[(t+c)^{2-\alpha} - t(2-\alpha)c^{1-\alpha} - c^{2-\alpha} \right] & \text{if } t \leq t_0, \\ 4D_{\mathrm{C}}t \\ + \frac{2AK^2}{1-\alpha} \left[(t-t_0)(t_0+c)^{1-\alpha} - tc^{1-\alpha} \right] + \frac{2AK^2}{(1-\alpha)(2-\alpha)} \left[(t_0+c)^{2-\alpha} - c^{2-\alpha} \right] \\ + \frac{2AK^2\tau_p}{(t_0+c)^{\alpha}} \left[(t-t_0) + \tau_p \left(\mathrm{e}^{-(t-t_0)/\tau_p} - 1 \right) \right] & \text{else.} \end{cases} \tag{3.11}$$

D_{C} represents the diffusion coefficient of the colloid (the choice of its numerical value is discussed in a next paragraph). The different regimes of the analytical MSD are also computed in appendix G. The analysis reveals five regimes separated by four characteristic times, which are:

- $t_1 = \frac{4D_{\mathrm{C}}c^{\alpha}}{K^2 A}$
- t_0, which is the time from which the autocorrelation function of the polarization vector becomes exponential.
- $t_2 = \frac{4D_{\mathrm{C}}(t_0+c)^{\alpha}}{AK^2} + \frac{2(t_0+c)}{1-\alpha} \left[1 - \left(\frac{t_0+c}{c} \right)^{\alpha-1} \right] - 2t_0$
- τ_p the characteristic re-orientation time of the droplets in the shell.

The different regimes are:

- At $t < t_1$, the MSD is linear, indicating a diffusive motion:

$$\left\langle \Delta \boldsymbol{r}_{\mathrm{C}}^2(t) \right\rangle \sim 4D_{\mathrm{C}}t \tag{3.12}$$

- At $t_1 < t < t_0$, the MSD is proportional to t^2, indicating a ballistic motion:

$$\left\langle \Delta \boldsymbol{r}_{\mathrm{C}}^2(t) \right\rangle \sim AK^2 c^{-\alpha} t^2 \tag{3.13}$$

- At $t_0 < t < t_2$, the MSD is linear again, indicating a diffusive motion:

$$\left\langle \Delta \boldsymbol{r}_{\mathrm{C}}^2(t) \right\rangle \sim \left[4D_{\mathrm{C}} + \frac{2AK^2}{1-\alpha} \left((t_0 + c)^{1-\alpha} - c^{1-\alpha} \right) - \frac{2t_0 AK^2}{(t_0 + c)^{\alpha}} \right] t \tag{3.14}$$

- At $t_2 < t < \tau_p$, the MSD is proportional again to t^2, indicating a ballistic motion:

$$\left\langle \Delta \boldsymbol{r}_{\mathrm{C}}^2(t) \right\rangle \sim \frac{AK^2}{(t_0 + c)^{\alpha}} t^2 \tag{3.15}$$

- At $t > \tau_p$, the MSD is linear again, indicating a diffusive motion:

$$\left\langle \Delta \boldsymbol{r}_{\mathrm{C}}^2(t) \right\rangle \sim \left(4D_{\mathrm{C}} + \frac{2AK^2}{1-\alpha} \left[(t_0 + c)^{1-\alpha} - c^{1-\alpha} \right] + \frac{2AK^2 \tau_p}{(t_0 + c)^{\alpha}} \right) t \tag{3.16}$$

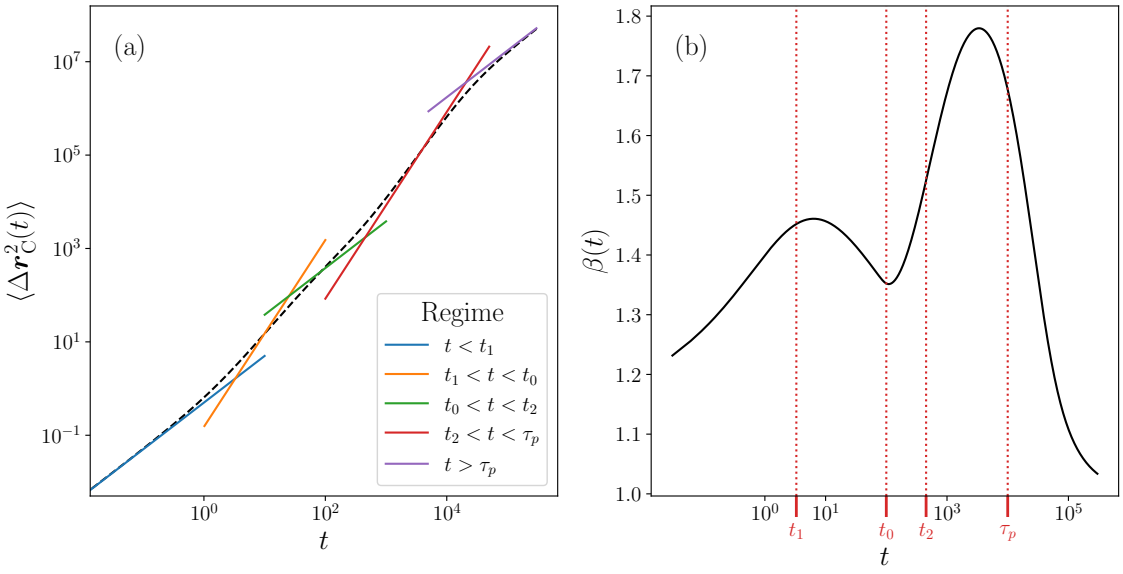

Figure 3.17: (a) Analytical MSD using Eq. (3.11) as a function of time $\langle \Delta \boldsymbol{r}_{\mathrm{C}}^2(t) \rangle$, the parameters D_{C}, K, c, t_0, τ_p, α, and A are chosen arbitrarily in order to observe the different predicted regimes. (b) Exponent of the MSD as a function of time, with $\beta(t) = \log \langle \Delta \boldsymbol{r}_{\mathrm{C}}^2(t) \rangle / \log t$.

The analysis of the MSD derived from the effective Langevin equation emphasizes that the dynamics is much richer than the one from the ABP model. First, the simulation results are left aside. The analytical MSD is computed using parameters, which are chosen so that the five regimes are well separated in order to visualize them. To determine the suitable values, the crossover times must be approximately: $t_1 \sim 10$, $t_0 \sim 100$, $t_2 \sim 1000$, and $\tau_p \sim 10000$. t_0 and τ_p are fixed to the expected values, thus $t_0 = 100$ and $\tau_p = 10000$. t_1 and t_2 depends on the other parameters: D_{C}, K, c, α, and A. The following parameters

are fixed: $D_C = 0.125$, $K = 0.0374$, $c = 5$, $\alpha = 0.95$ $D_C = 0.125$, while A remains a free parameter and is adjusted to obtain the correct time separation between the different regimes. A suitable value is found to be $A = 500$, which yields $t_1 = 3.3$ and $t_2 = 452.5$. The MSD as well as the different regimes are computed and are shown on Figure 3.17a. The 5 regimes are observed.

Writing out that $\langle \Delta \boldsymbol{r}_C^2(t) \rangle \propto t^\beta$, the exponent is computed and plotted on Figure 3.17b. The crossover times are indicated by the red dotted lines. Interestingly, the exponent does not reach the value of 2, which would be expected in the ABP model, provided that τ_r is large enough. Here, there is an alternation of $\beta = 1$ regimes, which corresponds to the minima at the beginning, the middle ($t_0 < t < t_2$), and the end, and $\beta = 2$ regimes, which corresponds to the maxima between t_1 and t_0, and between t_2 and τ_p. Yet, the different regimes are not totally separated, consequently the exponent never reaches 1 nor 2. This figure underlines that for more than one intermediate regime, there is an overlap, yielding a more complex behavior of the MSD.

Then, the exponent β is computed with the simulation data, and is plotted as a function of time on Figure 3.18 for the systems investigated in this section. In contrast with Fig. 3.17b, the figure emphasizes that there is a superposition of the various regimes as there is only one maximum around 10^2. In order to go further, I will compute and plot the analytical MSD to compare it with the simulation data.

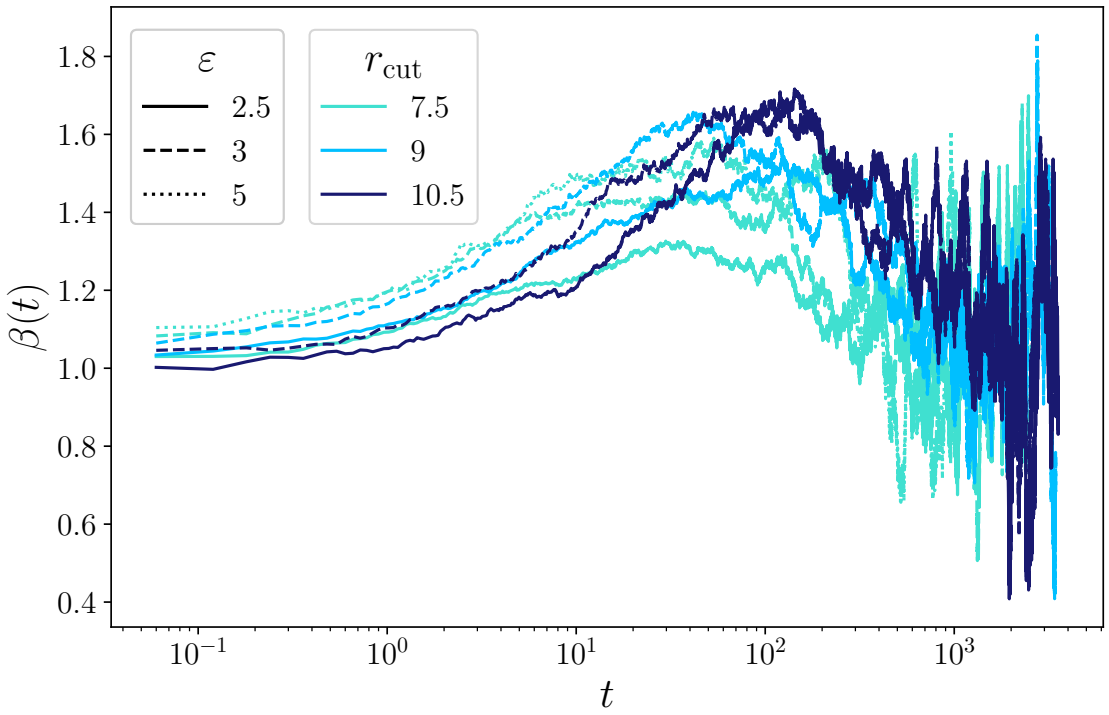

Figure 3.18: Exponent of the MSD as a function of time, with $\beta(t) = \log \langle \Delta \boldsymbol{r}_C^2(t) \rangle / \log t$.

3.5.3 Reconstruction of the MSD from semi-analytical calculations

All the parameters involved in the effective Langevin equation, defined by Eq. (3.7), are known, using values extracted from the autocorrelation functions of $\boldsymbol{p}$ in Table III.4. The only unknown quantity is the propulsion coefficient K which is here determined analytically from simple considerations.

The droplets, which form inside the reaction area, push the colloid in the same orientation. Consequently, the velocity of the colloid $\boldsymbol{v}_{\mathrm{C}}$ is, during a time window, denoted in what follows τ_0, smaller than τ_p, proportional to the polarization vector: $\boldsymbol{v}_{\mathrm{C}} = -K\boldsymbol{p}$. The velocity of the colloid, in Brownian dynamics using Eq. (2.6) and neglecting the noise, is $\boldsymbol{v}_{\mathrm{C}}(t) \propto -D_{\mathrm{C}}^0 \sum_{i=1}^{N} \boldsymbol{\nabla} U(r_{\mathrm{C},i}(t))$, with U the interaction potential between the colloid C and the solute particles i. D_{C}^0 is the diffusion coefficient at infinite dilution of the colloid, used as an input in the Brownian dynamics code. The polarization vector is given by Eq. (3.5). Both vectors, $\boldsymbol{v}_{\mathrm{C}}$ and $\boldsymbol{p}$, can be written in the continuous limit and computed. To do so, polar coordinates $\boldsymbol{r} = (r, \theta)$ are used in the coordinate system $(\boldsymbol{e}_r, \boldsymbol{e}_\theta)$, where $\boldsymbol{e}_r$ is the normal vector at the surface of the colloid and $\boldsymbol{e}_\theta$ is the tangential vector. The following usual assumptions are made:

- The solute particles are described using a continuous concentration field $c(\boldsymbol{r}, t)$.
- The concentration of solute particles is assumed to be time independent $c(\boldsymbol{r}, t) = c(\boldsymbol{r})$.
- The concentration follows a Boltzmann distribution along the radial axis: $c(\boldsymbol{r}) = \mathcal{C}(\theta)\, \mathrm{e}^{-U(r)}$, where U is the interaction potential between solute particles and the colloid.
- The potential, U, is invariant along the axial axis, i.e $U(\boldsymbol{r}) = U(r)$. Consequently: $\boldsymbol{\nabla} U(r) = \frac{\partial U(r)}{\partial r}\boldsymbol{e}_r + \frac{1}{r}\frac{\partial U(r)}{\partial \theta}\boldsymbol{e}_\theta = \frac{\partial U(r)}{\partial r}\boldsymbol{e}_r$.

Using this, the velocity of the colloid in a continuous limit becomes:

$$\begin{aligned}\boldsymbol{v}_{\mathrm{C}}(t) &= D_{\mathrm{C}}^0 \int c(\boldsymbol{r}) \boldsymbol{\nabla} U(\boldsymbol{r}) \mathrm{d}\boldsymbol{r} \\ &= D_{\mathrm{C}}^0 \int_0^{2\pi} \mathcal{C}(\theta) \mathrm{d}\theta \int_0^{\infty} r \frac{\partial U(r)}{\partial r}\, \mathrm{e}^{-U(r)}\, \mathrm{d}r\, \boldsymbol{e}_r\end{aligned}$$

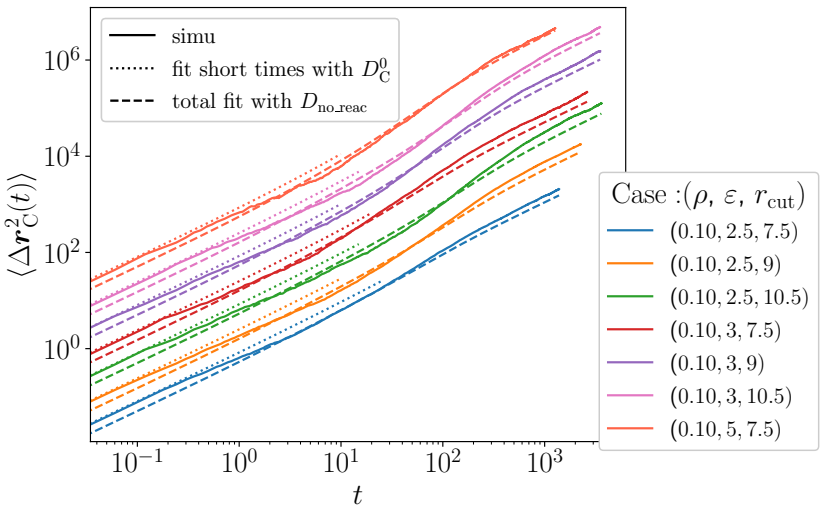

Figure 3.19: MSDs from simulations (plain lines) compared to the analytical results given by Eq. (3.11). The dashed lines represent the analytical MSDs computed with $D_C = D_{no\_reac}$. The dotted lines show the short times using $D_C = D_C^0$. Results obtained for the various systems investigated in this section are presented. The curves are vertically shifted for more clarity.

Similarly, the continuous form of the polarization vector yields:

$$\begin{aligned} \boldsymbol{p}(t) &= \int_{\mathcal{P}} \boldsymbol{r} c(\boldsymbol{r}) \, \mathrm{d}\boldsymbol{r} \\ &= \int_0^{2\pi} \mathcal{C}(\theta) \mathrm{d}\theta \int_{\sigma_C/2}^{(3\sigma_A+\sigma_C)/2} r^2 \, \mathrm{e}^{-U(r)} \, \mathrm{d}r \, \boldsymbol{e}_r \end{aligned}$$

The velocity and the polarization vectors are linked through the relation $\boldsymbol{v}_C = -K\boldsymbol{p}$, from which K can be deduced:

$$K = \frac{D_C^0 \int_0^{2^{1/6}(\sigma_A+\sigma_C)/2} (1 - \mathrm{e}^{-U(r)}) \mathrm{d}r}{\int_{\sigma_C/2}^{(3\sigma_A+\sigma_C)/2} r^2 \, \mathrm{e}^{-U(r)} \, \mathrm{d}r} \tag{3.17}$$

The integrals can be numerically solved taking the WCA potential, and doing so, $K = 0.0374$.

All the parameters of the effective Langevin equation (Eq. (3.11)) are now known. For the diffusion coefficient of the colloid, D_C, two options are possible. The first one is to take the diffusion coefficient at infinite dilution, D_C^0, and the other one is to take the value of the reference system, D_{no_reac}. In order to take into account the effect of the solute particles in this coarse-grained description, the latter is chosen, $D_C = D_{no\_reac}$. The analytical MSDs are plotted for various systems with the dashed lines on Figure 3.19, where it is confronted to the MSDs obtained with the simulations (plain lines). The analytical MSDs do not

fit well the data. They fail to reproduce the different intermediate regimes. Anyway, the long-time slopes of the MSDs are correctly predicted by the analytical computations. Both indicate a diffusive regime, however, the analytical MSDs fail to predict the correct value of D_{eff}, as the intercepts are not the same. This observation holds also for the short times. The short-time approximations can be improved using the diffusion coefficient at infinite dilution in Eq. (3.11), $D_{\text{C}} = D^0_{\text{C}}$. The analytical MSDs using this value are represented on Fig. 3.19 by the dotted lines and predict well the short times, $t < 0.02$. Indeed, at short times, the movement of the colloid is free, as it has not yet encountered solute particles. The first linear regime described by Eq. (3.12) seems to last until $t \sim 2$ for all cases presented here. This regime is in fact composed of two first linear regimes. The first one for $t < 0.02$ where $D_{\text{C}} = D^0_{\text{C}}$ and the second one for $0.02 < t < 2$, where $D_{\text{C}} = D_{\text{no\_reac}}$. The crossover between the two first linear regimes can be observed on the figure.

Table III.5 sums up the characteristic times for each case. This table stresses that the timescales are not clearly separated, as suggested by Fig. 3.18. For example, for the first three cases presented in Table III.5, $t_2 > \tau_p$, therefore the second ballistic regime cannot be observed. Moreover, for all the cases, t_1 and t_0 are not clearly separated, which induces a ballistic regime with $\beta < 2$. The overlaps of timescales can explain the mismatch between the analytical MSD and results from simulation.

ε	r_{cut}	t_1	t_0	t_2	τ_p
2.5	6.5	9.7	10	154.6	16.4
2.5	7.5	8.3	25	196.8	43.6
2.5	9	8.0	10	99.1	88.7
2.5	10.5	8.5	15	129.7	142.9
3	7.5	7.0	20	87.4	48.0
3	9	7.1	10	59.4	99.6
3	10.5	7.8	15	82.5	161.9
5	7.5	5.8	10	34.6	60.8

Table III.5: Characteristic times: t_1, t_0, t_2 and τ_p, which separate the various regimes found in the MSD, computed from analytical expressions given in the paragraph 3.5.2. Only parameters of the investigated cases in this section appear in the table.

3.5.4 Reconstruction of the MSD from explicit simulations

The semi-analytical MSD fails to capture all the regimes emerging from simulations. Another approach in order to reconstruct the MSD obtained in the simulations is presented here. First, the idea is to use the simulation data to compute the terms of the

effective Langevin equation proposed in Eq. (3.7). Second, the assumptions made on the autocorrelation function of the noise (Eq. (3.9)) and on the contribution of cross-correlation function (Eq. (3.10)) can be verified. Last, the contributions identified in Eq. (3.8) are computed and are compared to the MSD computed in the simulation.

Method

In order to compute the different contributions of the MSD identified in Eq. (3.8), several steps are carried out and are presented here.

1. The different terms of the effective Langevin equation are computed. The polarization vector $\boldsymbol{p}$, which intervenes in the effective Langevin equation, is an output of the simulation. The noise vector $\boldsymbol{\xi}$ is constructed from the effective Langevin equation (3.7):

$$\boldsymbol{\xi}(t) \approx \frac{\Delta \boldsymbol{r}(t)}{\Delta t} + K\boldsymbol{p}(t). \tag{3.18}$$

In this approximation, the velocity is estimated for a time step Δt sufficiently small by: $\boldsymbol{v} \approx \frac{\Delta \boldsymbol{r}_C}{\Delta t}$. The propulsion coefficient, K is, in this approach, determined numerically. The hypothesis states that the ballistic motion of the colloid originates from the active force defined in Eq. (3.7), $-K\boldsymbol{p}$. According to the hypotheses made on the mechanism of propulsion, the velocity is proportional to the polarization vector during a time window τ_0. The propulsion coefficient is then also estimated from the computed data using the following equation:

$$K = -\left\langle \frac{\langle \boldsymbol{p}(t) \rangle_{\tau_0} \cdot \langle \boldsymbol{v}(t) \rangle_{\tau_0}}{|\langle \boldsymbol{p}(t) \rangle_{\tau_0}|^2} \right\rangle_t,$$

where $\langle . \rangle_t$ represents the average over time. The choice of τ_0 is detailed in the next paragraph. The characteristic time τ_0 corresponds to the time window where the velocity is proportional to the polarization vector. This implies that τ_0 must be smaller or comparable to τ_p, since the orientation of the polarization vector is randomized at long times. In addition, the average of the noise vector, which represents the fluctuations of the bath, should vanish on a large enough time window. Consequently, the choice of τ_0 must also be long enough to have $\langle \boldsymbol{\xi} \rangle_{\tau_0} = 0$. Under these conditions, one can write $\langle \boldsymbol{v}(t) \rangle_{\tau_0} = -K \langle \boldsymbol{p}(t) \rangle_{\tau_0}$, where $\langle . \rangle_{\tau_0}$ represents the average over a time of duration τ_0.

2. The autocorrelation functions: $\langle \boldsymbol{p}(t') \cdot \boldsymbol{p}(t'+t) \rangle_{t'}$, $\langle \boldsymbol{\xi}(t') \cdot \boldsymbol{\xi}(t'+t) \rangle_{t'}$, $\langle \boldsymbol{p}(t') \cdot \boldsymbol{\xi}(t'+t) \rangle_{t'}$, and $\langle \boldsymbol{\xi}(t') \cdot \boldsymbol{p}(t'+t) \rangle_{t'}$, are computed from the simulation data once $\boldsymbol{\xi}(t)$ is determined.

3. The contributions: $\Delta_{\boldsymbol{pp}}(t)$, $\Delta_{\boldsymbol{\xi\xi}}(t)$, $\Delta_{\boldsymbol{p\xi}}(t)$, and $\Delta_{\boldsymbol{\xi p}}(t)$ are computed from simulations. To do so, the autocorrelation functions are numerically integrated, transforming the double integral into a single one for convenience: $\int_0^t \mathrm{d}t' \int_0^t \mathrm{d}t'' \, \varphi(|t'-t''|) = 2\int_0^t \mathrm{d}u \, (t-u)\varphi(u)$. This can be done as the autocorrelation functions are in reality functions of the difference $|t'-t''|$. The transition from double to simple integral is given in Appendix B.

4. The different contributions are plotted, and are compared to the MSD.

Computation of τ_0

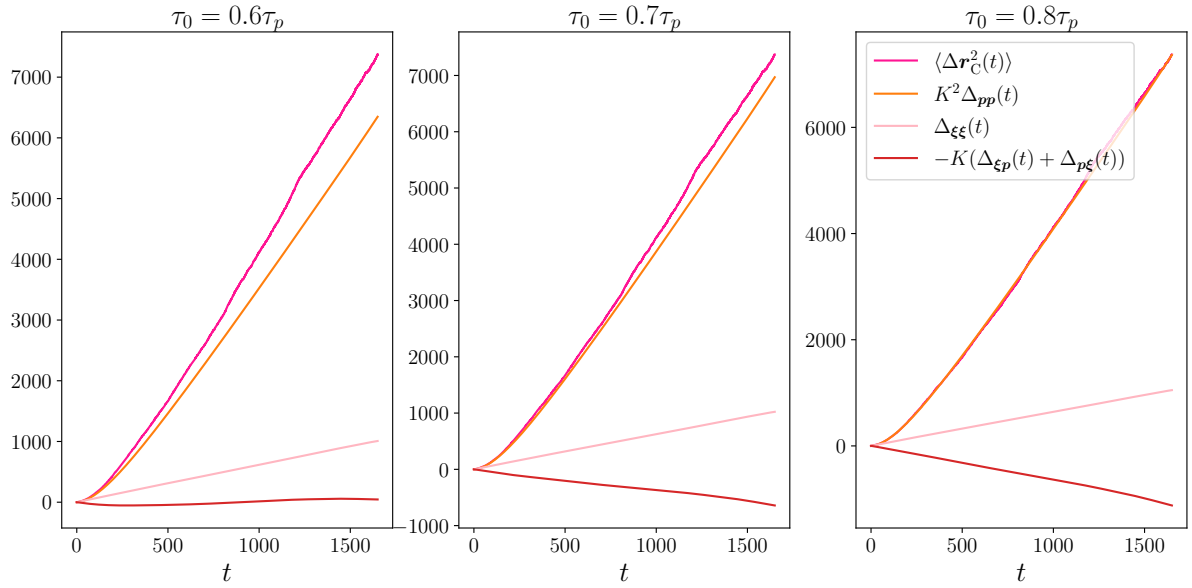

Figure 3.20: Example of several MSD reconstructions for various $\tau_0 = x\tau_p$ chosen which leads to various K_x values. The objective is for the cross correlation to be negligible in comparison to the other quantities. The set of the chosen parameters here is $(\rho, \varepsilon, r_{\mathrm{cut}}) = (0.1, 3, 10.5)$. The more suitable choice is $\tau_0 = 0.6\tau_p$.

The accuracy of the reconstruction depends on the choice of τ_0, since the validity of the assumptions rely on an appropriate choice of the time window. The method to find the appropriate τ_0 is empirical. Several values $\tau_0 = x\tau_p$, varying x, are tried. I have fixed $x \in [0.4, 0.8]$. The limits of this range correspond to the upper and lower values of the constraints imposed on τ_0. In order to reduce the number of trials, I have only considered values of x with a digit of precision. For each τ_0, K the propulsion coefficient is computed, from which the noise vector $\boldsymbol{\xi}$ is deduced using Eq. (3.18). Then, the contribution of the cross-correlation functions, $-K\left(\Delta_{\boldsymbol{\xi p}}(t) + \Delta_{\boldsymbol{p\xi}}(t)\right)$ is computed. The value of x is selected in order to have the best agreement with the assumptions made, i.e. to have $-K\left(\Delta_{\boldsymbol{\xi p}}(t) + \Delta_{\boldsymbol{p\xi}}(t)\right) \approx 0$, or at least negligible in front of the other quantities.

The computed contributions using different values of τ_0 are then plotted, and the most appropriate value is chosen graphically. An example for the parameters $(\rho, \varepsilon, r_{\text{cut}}) = (0.1, 3, 10.5)$ is shown on Figure 3.20. Only three out of the five tried values are shown: $x = 0.6$, $x = 0.7$ and $x = 0.8$. Graphically, the more suitable choice is $x = 0.6$, since for this value the contribution of the cross-correlation functions is negligible regarding the other quantities. The values of τ_0 and K for each investigated case, are summarized in Table III.6. Interestingly, the numerical values of K are of the same order of magnitude as the one computed from analytical considerations.

ε	r_{cut}	x	τ_0	K
2.5	7.5	0.8	34.9	0.0326
2.5	9	0.8	71	0.0419
2.5	10.5	0.8	114.23	0.0422
3	7.5	0.8	38.4	0.0425
3	9	0.7	69.7	0.0459
3	10.5	0.6	97.1	0.0431

Table III.6: Summary of the chosen values for x, τ_0, and the associated values for the proportionality coefficient K. This analysis was only done at $\rho = 0.1$.

Computation of the correlation functions

Once τ_0 is chosen, all the terms of the effective Langevin equation are known. The autocorrelation function $\langle \boldsymbol{\xi}(t') \cdot \boldsymbol{\xi}(t'+t) \rangle_{t'}$ is computed and plotted on Figure 3.21a for each system of interest in this section. The autocorrelation functions vary on timescales very small compared to the other timescale of the problem. This validates the approximation made considering it as a delta function. The cross-correlation functions are also computed and plotted on Figure 3.21b. The cross-correlation functions are almost zero at all times, as expected with the made choices.

Reconstruction of the MSD

Finally, the MSD can be reconstructed from the numerical computations. Figure 3.22 shows the reconstruction for the set of parameters $(\rho, \varepsilon, r_{\text{cut}}) = (0.1, 3, 10.5)$, in a log-log scale on Fig. 3.22a and in a linear-linear scale on Fig. 3.22b. Both representations underline that at short times, the contribution of the noise $\Delta_{\boldsymbol{\xi}\boldsymbol{\xi}}$ dominates. The contribution of the polarization vector $\Delta_{\boldsymbol{pp}}$ is responsible for the transient ballistic part and matches the long time diffusion. This confirms that the polarization vector is at the origin of the propulsion, and it validates the identified intuitive mechanism.

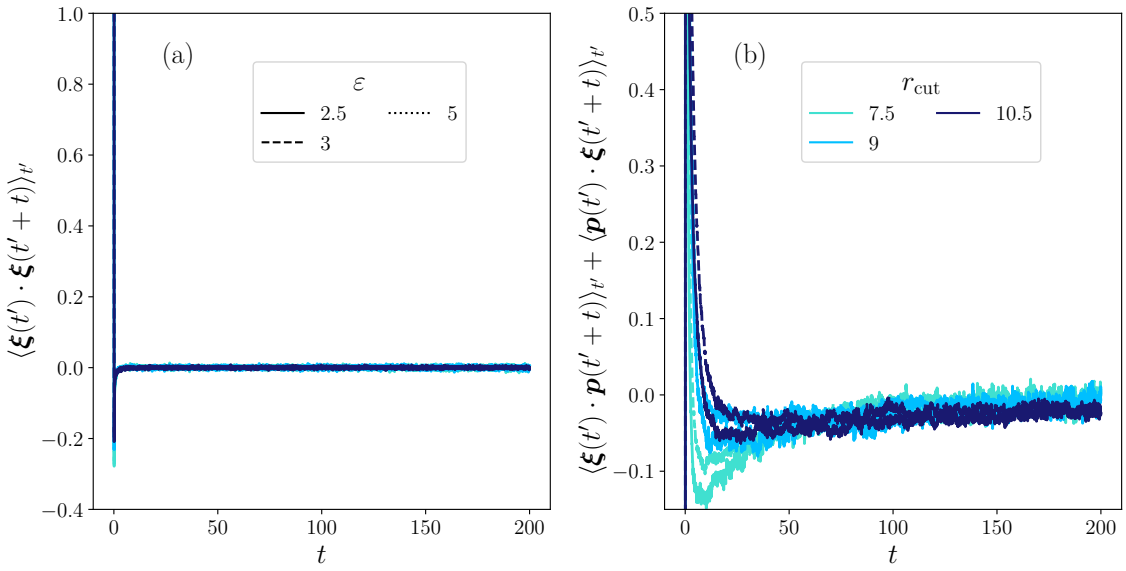

Figure 3.21: (a) Autocorrelation functions of the noise vector as a function of time $\langle \boldsymbol{\xi}(t') \cdot \boldsymbol{\xi}(t'+t) \rangle_{t'}$. (b) Cross-correlation functions of the noise and the polarization vector as a function of time $\langle \boldsymbol{p}(t') \cdot \boldsymbol{\xi}(t'+t) \rangle_{t'} + \langle \boldsymbol{\xi}(t') \cdot \boldsymbol{p}(t'+t) \rangle_{t'}$. Data correspond to systems discussed in this section. Data are shown for $t < 200$ to emphasize the interesting part.

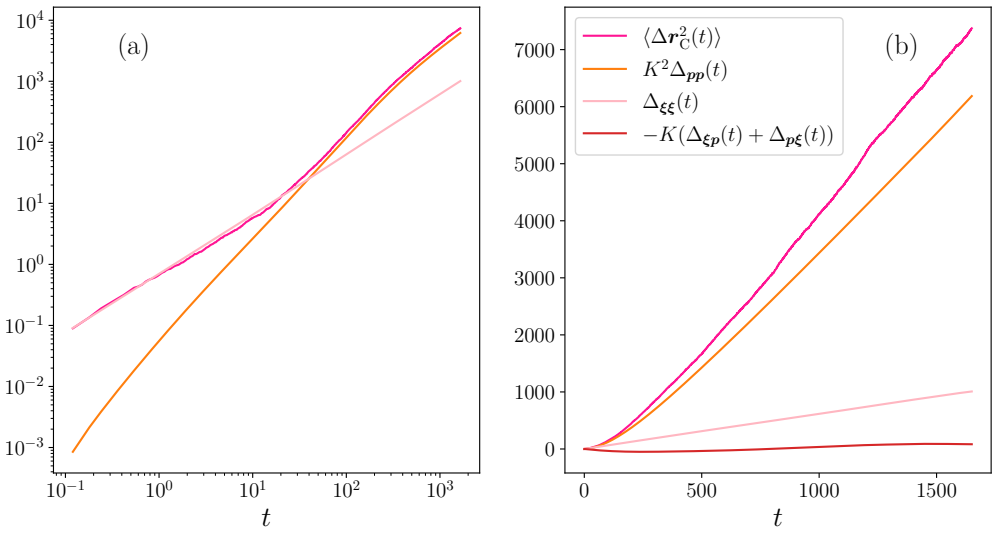

Figure 3.22: The MSD as a function of time $\langle \Delta \boldsymbol{r}_{\mathrm{C}}^2(t) \rangle$ is represented as well as the different contributions from Eq. (3.8) computed from the simulation data. (a) Log-log scale. (b) Linear-linear scale. The parameters represented here are $(\rho, \varepsilon, r_{\mathrm{cut}}) = (0.1, 3, 10.5)$.

3.6 Robustness of the model

A wide range of parameters have been studied, which have evidenced the range where a phase transition of solute particles for the particular geometry investigated here can occur, leading to a significant enhanced diffusion. The filling fraction of the reaction area at steady state, $N_{\mathrm{shell},\infty}/N_{\mathrm{max}}$, is a quantity which takes into account both the size of the reaction area r_{cut} and the attraction intensity ε, and is found to be relevant to collapse all the data together. This underlines that the presence of activity is strongly dependent on the geometry of the problem. The reaction area radius r_{cut}, as well as the diameter of the colloid σ_{C}, control the geometry of the reaction area. Besides, one may wonder how the mechanism is dependent on the relative solute-colloid size. The geometry of the reaction area also depends on the reverse reaction. If the reverse reaction is slowed or located elsewhere, the shape of the reaction area will be modified. In this section, parameters considered as fixed so far will be modified in order to challenge the robustness of the mechanism. Therefore, the following changes are made: the size of the colloid σ_{C} is increased, the reverse reaction rate τ_{BA} is slowed, and the location of the reverse reaction is displaced at the edge of the simulation box. When a parameter is modified, the other remain unchanged and keep the default value exposed in Section 3.2. Finally, simulations are carried out in three dimensions, showing that the mechanism is also valid.

3.6.1 Influence of the size of the colloid σ_{C}

The influence of the size of the colloid is investigated, increasing its diameter by a factor 2 ($\sigma_{\mathrm{C}} = 10$ instead of $\sigma_{\mathrm{C}} = 5$ previously). For each system presented in this paragraph, the average solute density is $\rho = 0.1$, and the attraction intensity is $\varepsilon = 3$ as the enhanced diffusion was strong for these parameters for a smaller colloid. Several values of r_{cut} are chosen, larger than in the previous section, to account for the larger size of the colloid. The values of r_{cut} vary between 8 and 13, these values corresponding to shells of about the same thickness as those obtained with $r_{\mathrm{cut}} = 5.5$ and $r_{\mathrm{cut}} = 10.5$ for a colloid twice smaller. A corresponding reference system has been simulated in order to compute the reference diffusion coefficient, which is found to be $D_{\mathrm{no\_reac}} = 0.05$ and the associated error $\delta D_{\mathrm{no\_reac}} = 0.001$.

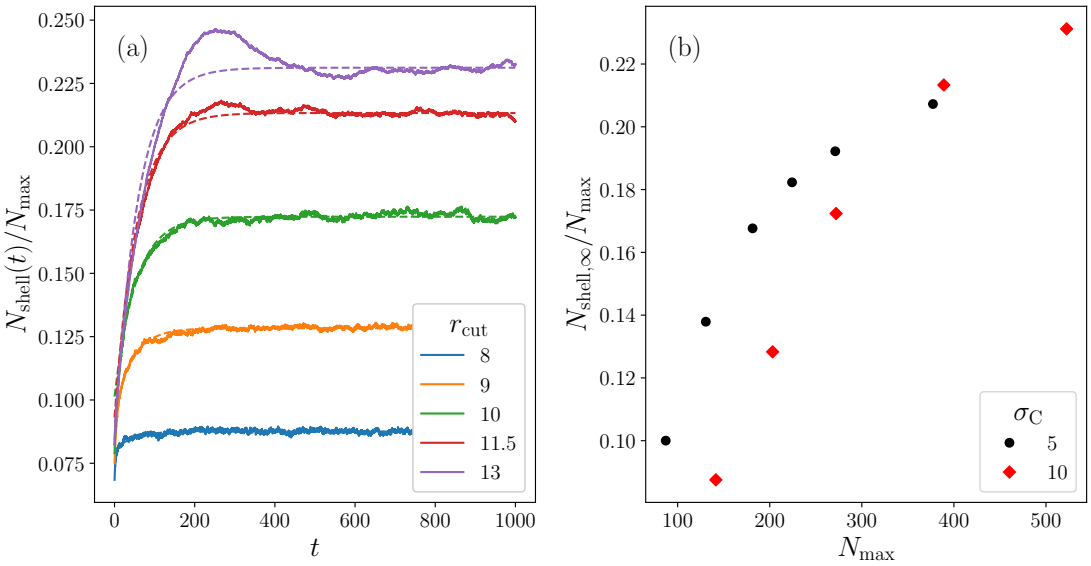

Figure 3.23: (a) $N_{\text{shell}}/N_{\text{max}}(t)$ for various r_{cut} at $\rho = 0.1$, $\varepsilon = 3$ and $\sigma_{\text{C}} = 10$. The dashed lines represent the fits using Eq. (3.2). (b) $N_{\text{shell},\infty}/N_{\text{max}}$ as function of N_{max} for $\sigma_{\text{C}} = 5$ (circles) and $\sigma_{\text{C}} = 10$ (diamonds).

The kinetics of the filling of the reaction area is plotted on Figure 3.23a for various r_{cut}. N_{shell} is normalized by the maximum number of particles that would fill the shell N_{max}, whose expression is given by Eq. (3.1). The dashed lines represent the fits using Equation (3.2) which are in good agreements with the simulation data. The filling fraction of the reaction area at steady state $N_{\text{shell},\infty}/N_{\text{max}}$ as a function of N_{max} is shown on Figure 3.23b for both σ_{C}. N_{max} is used as a measurement of the surface of the reaction area in order to compare results from the simulation where $\sigma_{\text{C}} = 5$ to the results for $\sigma_{\text{C}} = 10$. In both cases, $N_{\text{shell},\infty}/N_{\text{max}}$ increases before reaching a plateau value. This is due to an artifact of the model as discussed in Section 3.3, but as demonstrated before it does not change qualitatively the obtained results. The kinetics of the filling of the reaction area remains unchanged while increasing the size of the colloid by a factor 2. From the steady state, the time is rescaled so that $t_{\text{init}} = 3\tau_N$. Values of $N_{\text{shell},\infty}$ and t_{init} are reported in Table III.7.

Figure 3.24a represents the mean squared displacements of the colloid as a function of time in a log-log scale for various r_{cut}. As before, the MSDs have an intermediate ballistic regime, which indicates that the colloid is self-propelled. On longer timescales, the colloid displays an enhanced diffusion with a maximum ratio $D_{\text{eff}}/D_{\text{no\_reac}} = 20$. The intermediate ballistic regime is particularly visible for the highest reaction areas (red and

purple curves). Using the criterion whose definition is recalled by:

$$\begin{cases} \text{if } D_{\text{eff}} - \delta D_{\text{eff}} > D_{\text{no\_reac}} + \delta D_{\text{no\_reac}}, & \text{the system is active} \\ \text{otherwise,} & \text{the system is passive.} \end{cases}$$

All the systems are found to be active. Values of t_{lin} used to compute D_{eff}, as well as D_{eff} and its associated error δD_{eff} are shown in Table III.7.

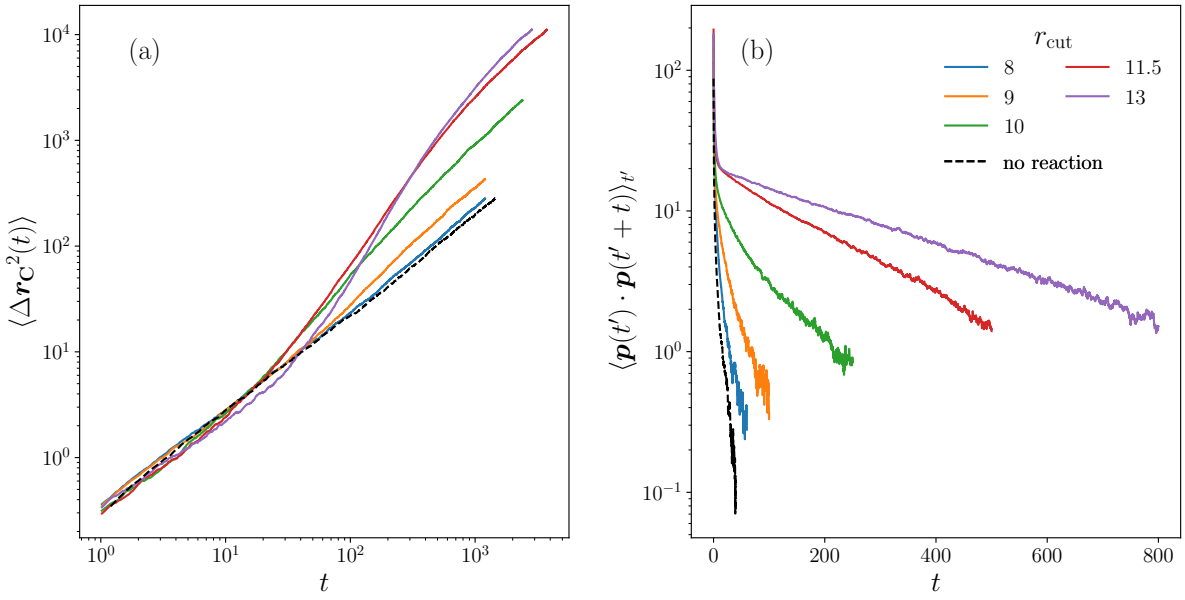

Figure 3.24: (a) Mean squared displacements of the colloid as a function of time in a log-log scale. Data are shown for $t > 10^0$ to emphasize the interesting part. (b) Autocorrelation functions of the polarization vector as a function of time in a semi-log scale. Data are shown for different value of r_{cut} at $\rho = 0.1$ and $\varepsilon = 3$. Here $\sigma_{\text{C}} = 10$.

The autocorrelation functions of the polarization vector are shown on Figure 3.24b as a function of time. An exponential tail is observed for the more active cases (red and purple curves) from which the persistence orientation time τ_p can be extracted, values are displayed in Table III.7.

The ratio $D_{\text{eff}}/D_{\text{no\_reac}}$, as well as τ_p are plotted as a function of the steady state filling rate of the reaction area $N_{\text{shell},\infty}/N_{\text{max}}$ on Figure 3.25. The green points correspond to $D_{\text{eff}}/D_{\text{no\_reac}}$ and the brown points to τ_p. The estimated errors on the diffusion coefficients are represented by the black error bars. The dashed line represents the limit between active and passive system. Data for $\sigma_{\text{C}} = 5$ at $\varepsilon = 3$ are represented by the circles while data at $\sigma_{\text{C}} = 10$ are represented by diamonds. The results obtained with both values of σ_{C} coincide very well. All systems present activity, as all the green points are above the dashed line. At this density, only two regimes are reachable and are visible on this figure. The first regime, which corresponds to systems where activity is limited, can be seen for

$N_{\text{shell},\infty}/N_{\text{max}} < 0.14$. Indeed, for all the points, except at ($N_{\text{shell},\infty}/N_{\text{max}} \approx 0.13$), there are no associated values of τ_p as the exponential regime is no present. In the second regime, for $N_{\text{shell},\infty}/N_{\text{max}} > 0.14$, τ_p and $D_{\text{eff}}/D_{\text{no\_reac}}$ are increasing functions of $N_{\text{shell},\infty}/N_{\text{max}}$. Data at $\sigma_{\text{C}} = 10$ follow the same trend as data at $\sigma_{\text{C}} = 5$. Again, this shows that the enhanced diffusion is mainly controlled by the filling rate of the reaction area.

Finally, no significant changes are observed while increasing the ratio $\sigma_{\text{C}}/\sigma_{\text{A}}$ by a factor two. The mechanism which causes an enhanced diffusion is thus a robust feature of the modeled system.

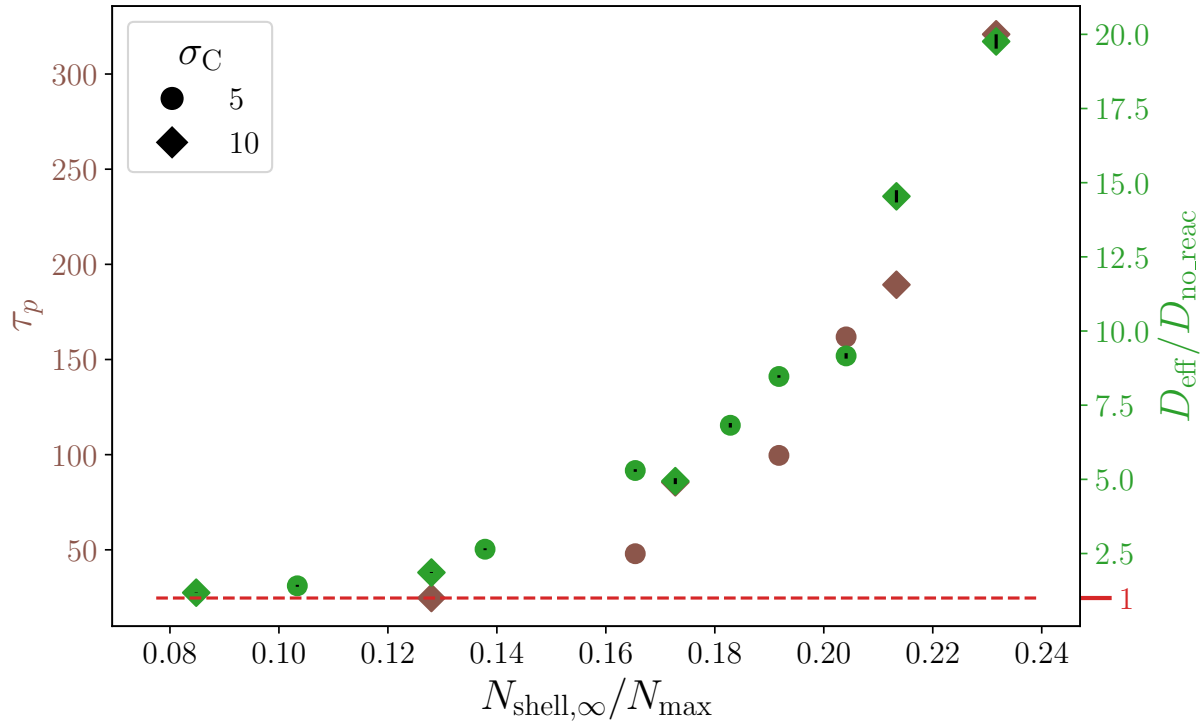

Figure 3.25: The persistence time of the polarization vector orientation, τ_p, as a function of the steady state filling rate of the reaction area, measured here by $N_{\text{shell},\infty}/N_{\text{max}}$ is represented by the brown points. The long-time diffusion coefficient of the colloid divided by its value without reaction, $D_{\text{eff}}/D_{\text{no\_reac}}$, as a function of $N_{\text{shell},\infty}/N_{\text{max}}$ is represented by the green points. The estimated error on the diffusion coefficients is represented by the black error bars which are smaller than the size of the symbols. The dashed red line marks the limit above which the colloid is considered as active. Results obtained for both ratio σ_{C} are displayed, for $\rho = 0.1$ and $\varepsilon = 3$.

3.6.2 Influence of the reverse reaction rate τ_{BA}

Another important parameter of the model is the one which controls the kinetics of the reaction B $\rightarrow$ A. One may wonder in particular if the activity still holds if this reaction is slowed, which is expected to create a cloud of B particles behind the colloid

$\rho = 0.1$, $\varepsilon = 3$, $\sigma_C = 10$						
r_{cut}	t_{init}	$N_{shell,\infty}$	t_{lin}	D_{eff}	δD_{eff}	τ_p
8	126	12	200	0.059	0.000	–
9	132	26	600	0.093	0.001	24.7
10	158	47	2000	0.247	0.005	85.5
11.5	165	83	2450	0.727	0.010	189.3
13	166	121	2150	0.988	0.010	320.9

Table III.7: Summary of the quantities of interest: t_{init} the initial simulation time from steady state, $N_{shell,\infty}$ the number of particles inside the reaction area at steady state, t_{lin} the time from which the last linear regime of the MSD is reached and from which D_{eff} can be computed, D_{eff} the effective diffusion coefficient, δD_{eff} the associated error, and τ_p the persistence time.

as it moves. To investigate this, the case $\rho = 0.1$, $\varepsilon = 3$ is considered, and the reverse reaction rate is changed in order to make the reverse reaction 100 times slower: $\tau_{BA} = 10$ instead of $\tau_{BA} = 0.1$. The study is restricted to only two reaction area radii: $r_{cut} = 7.5$ and $r_{cut} = 10.5$.

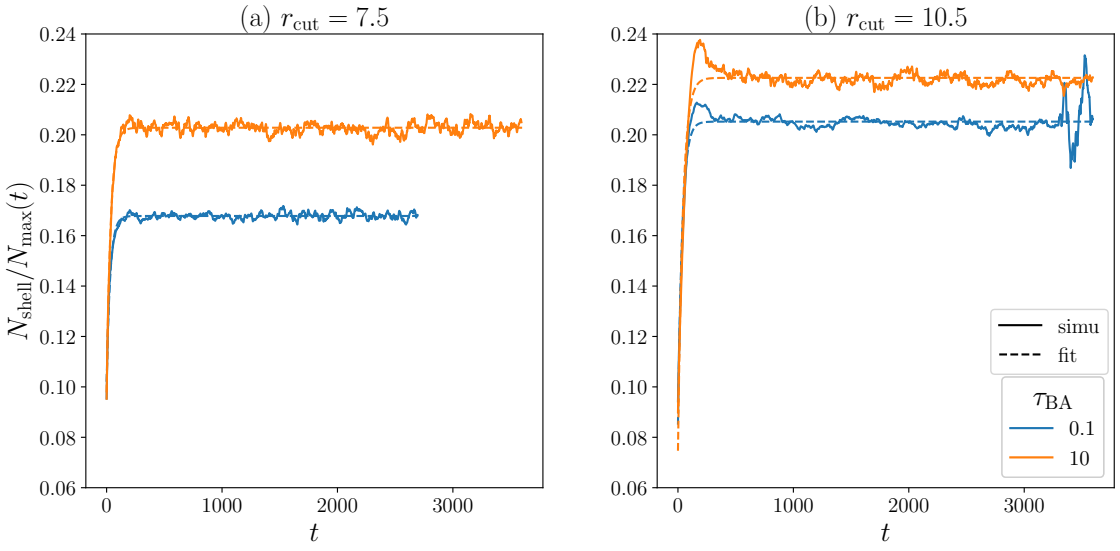

Figure 3.26: Number of particles in the reaction area divided by the maximum value, $N_{shell,\infty}/N_{max}$ as a function of time for different values of τ_{BA}. The dashed line is the fit using Equation (3.2). The parameters of the model are: $\rho = 0.1$, $\varepsilon = 3$, (a): $r_{cut} = 7.5$, (b): $r_{cut} = 10.5$.

First, the amount of particles in the reaction area is monitored as a function of time. Results are displayed on Figure 3.26a for $r_{cut} = 7.5$ and on Figure 3.26b for $r_{cut} = 10.5$. On these plots, N_{shell} is normalized by N_{max}. The systems where $\tau_{BA} = 0.1$ are represented by the blue curves, while systems where $\tau_{BA} = 10$ are in orange. For both values of r_{cut}, the

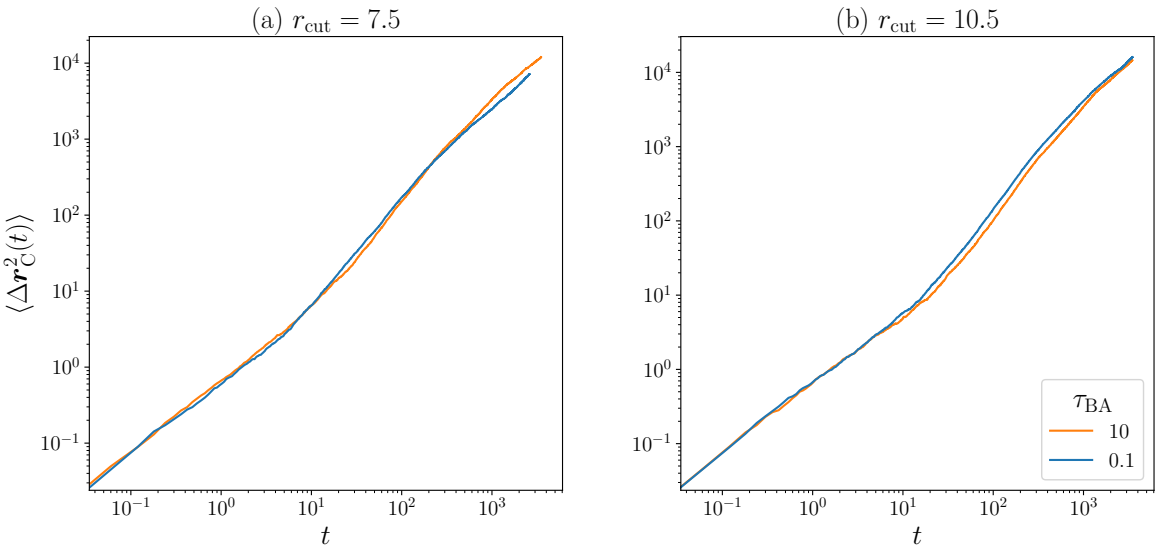

Figure 3.27: Mean squared displacements of the colloid as a function of time, in a log-log scale for the systems with $\rho = 0.1$, $\varepsilon = 3$, $\sigma_{\mathrm{C}} = 5$ and two different values of the characteristic time τ_{BA} of the reverse reaction B $\rightarrow$ A. (a): $r_{\mathrm{cut}} = 7.5$. (b): $r_{\mathrm{cut}} = 10.5$. Note that the initial time here corresponds to the steady state of the system.

filling rate of the reaction area increases when the kinetics of the reverse reaction is slowed. Exponential fits agree well with simulation data, and the characteristic timescale needed to reach the steady state, τ_{N}, is slightly increased when the reverse reaction is slowed. At $r_{\mathrm{cut}} = 7.5$, $\tau_{\mathrm{N}} = 35$ for $\tau_{\mathrm{BA}} = 10$, instead of $\tau_{\mathrm{N}} = 31$ for $\tau_{\mathrm{BA}} = 0.1$, and at $r_{\mathrm{cut}} = 10.5$, $\tau_{\mathrm{N}} = 41$, instead of $\tau_{\mathrm{N}} = 36$. Again, the time is rescaled, so that $t_{\mathrm{init}} = 3\tau_N$. From then the other quantities are computed. The reaction areas are more densely filled for $\tau_{\mathrm{BA}} = 10$ than for $\tau_{\mathrm{BA}} = 0.1$. Indeed, as the B particles are not immediately transformed back into A particles when outside the reaction area, the formed droplets go over the edge of the reaction area. At the border, there are particles, which was not the case before. Values of t_{init} and $N_{\mathrm{shell},\infty}$ for systems presented on Fig. 3.26 are shown in Table III.8.

Figure 3.27 compares the MSDs obtained with $\tau_{\mathrm{BA}} = 0.1$ and with $\tau_{\mathrm{BA}} = 10$ for $r_{\mathrm{cut}} = 7.5$ (Fig. 3.27a) and for $r_{\mathrm{cut}} = 10.5$ (Fig. 3.27b). The colloid again displays an intermediate ballistic regime, indicating activity. The effective diffusion coefficient, D_{eff}, computed from t_{lin}, its associated error δD_{eff}, as well as t_{lin} are reported in Table III.8. At $r_{\mathrm{cut}} = 7.5$, the colloid has an effective diffusion coefficient $D_{\mathrm{eff}} = 0.861$ at $\tau_{\mathrm{BA}} = 10$, which is higher than at $\tau_{\mathrm{BA}} = 0.1$ ($D_{\mathrm{eff}} = 0.657$). Conversely, at $r_{\mathrm{cut}} = 10.5$, the effective diffusion coefficient is slightly decreased at $\tau_{\mathrm{BA}} = 10$, $D_{\mathrm{eff}} = 1.038$ instead of $D_{\mathrm{eff}} = 1.136$ at $\tau_{\mathrm{BA}} = 0.1$.

Figure 3.28 shows the autocorrelation functions of the polarization vector $\boldsymbol{p}$ for the systems investigated here in a semi-log scale. In every case, there is an exponential decay

at long times, from which a characteristic time of correlation, τ_p, is extracted. The values are recorded in Table III.8. It appears clearly that this correlation time increases for both values of r_{cut}. When the reverse reaction rate is slowed, $\tau_p = 100$ and $\tau_p = 213$ instead of $\tau_p = 48$ and $\tau_p = 162$ at $r_{\text{cut}} = 7.5$ and $r_{\text{cut}} = 10.5$, respectively.

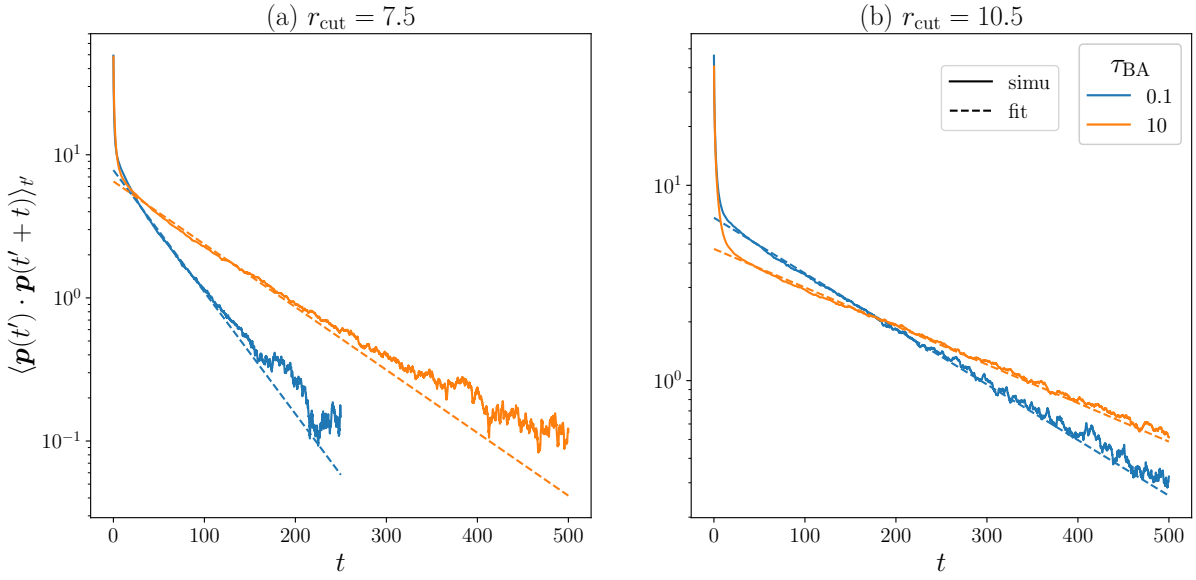

Figure 3.28: Autocorrelation functions of the polarization vector $\boldsymbol{p}$ as a function of time in a semi-log scale, for the systems with $\rho = 0.1$, $\varepsilon = 3$, $\sigma_{\text{C}} = 5$ and two different values of the characteristic time τ_{BA} of the reverse reaction B $\rightarrow$ A. (a): $r_{\text{cut}} = 7.5$. (b): $r_{\text{cut}} = 10.5$.

The filling fraction of the reaction area at steady state for $\tau_{\text{BA}} = 10$ is: $N_{\text{shell},\infty}/N_{\text{max}} = 0.203$ and $N_{\text{shell},\infty}/N_{\text{max}} = 0.222$ at $r_{\text{cut}} = 7.5$ and $r_{\text{cut}} = 10.5$, respectively. In this range, τ_p and D_{eff} are increasing functions of $N_{\text{shell},\infty}/N_{\text{max}}$. The results observed at $r_{\text{cut}} = 7.5$ follows this trend. In contrast, at $r_{\text{cut}} = 10.5$, τ_p increases while $D_{\text{eff}}/D_{\text{no\_reac}}$ decreases as a function of the filling fraction. This can be intuitively understood. When the reverse reaction is slowed, the total number of solutes B in the system is higher than N_{shell} and the LJ fluid goes over the edge of the reaction area. This yields the formation of a larger droplet of solutes B in the vicinity of the colloid, which acts as an effective r_{cut} higher than the real one. If the reaction area becomes too large, the droplet can detach from the colloid, decreasing the force induced by the polarization vector $\boldsymbol{p}$, thus the effective diffusion coefficient is not significantly increased.

3.6.3 Influence of the localization of the reverse reaction

Up to here, the system was partitioned in two: inside the reaction area delimited by r_{cut}, where the reaction A + C $\rightarrow$ B + C takes place, and outside the reaction area, where the reverse reaction B $\rightarrow$ A occurs. In this paragraph, a new parameter comes into play,

$\rho = 0.1$, $\varepsilon = 3$, $\tau_{\mathrm{BA}} = 10$						
r_{cut}	t_{init}	$N_{\mathrm{shell},\infty}$	t_{lin}	D_{eff}	δD_{eff}	τ_p
7.5	105	37	2500	0.861	0.013	100
10.5	124	84	2000	1.038	0.012	213

Table III.8: Summary of the quantities of interest: t_{init} the initial simulation time from steady state, $N_{\mathrm{shell},\infty}$ the number of particles inside the reaction area at steady state, t_{lin} the time from which the last linear regime of the MSD is reached and from which D_{eff} can be computed, D_{eff} the effective diffusion coefficient, δD_{eff} the associated error, and τ_p the persistence time.

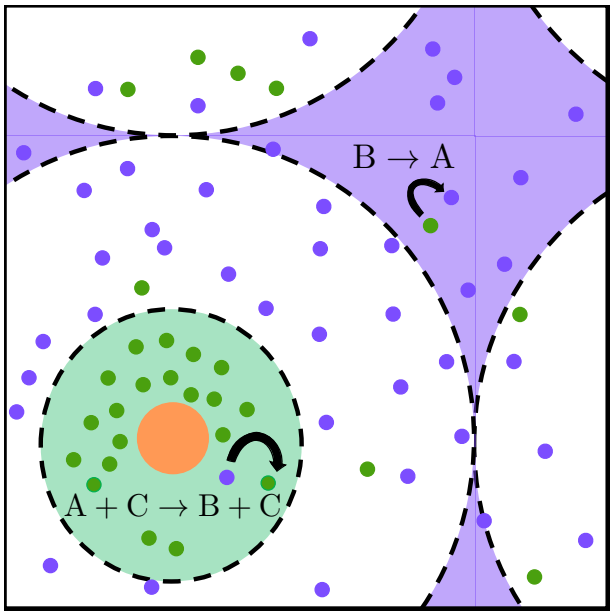

Figure 3.29: Drawing of the system, which illustrates the different reaction zones. Inside the green area, the reaction A + C → B + C occurs, while the reaction B → A occurs inside the purple area. No reaction occurs inside the blank area.

the reverse reaction cutoff, $r_{\mathrm{reverse\_cut}}$, which defines a third zone. Figure 3.29 represents schematically where the different reactions occur in the system. The reaction areas are:

- for $r < r_{\mathrm{cut}}$, the following reaction occurs: A + C → B + C, represented by the green area on Fig. 3.29.
- for $r_{\mathrm{cut}} < r < r_{\mathrm{reverse\_cut}}$, no reaction occurs, represented by the blank area on Fig. 3.29.
- for $r > r_{\mathrm{reverse\_cut}}$, the reverse reaction B → A takes place, represented by the purple area on Fig. 3.29.

The purpose is to investigate the influence of the location of the reverse reaction, in particular when it occurs far away from the colloid, thus in a restricted domain. Therefore,

the value $r_{\text{reverse\_cut}} = l_{\text{box}}/2 = 35$ is chosen. The reverse reaction only occurs at the edge of the simulation box (in the colloid reference frame). Two systems are studied at $\rho = 0.1$ and $\varepsilon = 3$: $r_{\text{cut}} = 7.5$ and $r_{\text{cut}} = 10.5$.

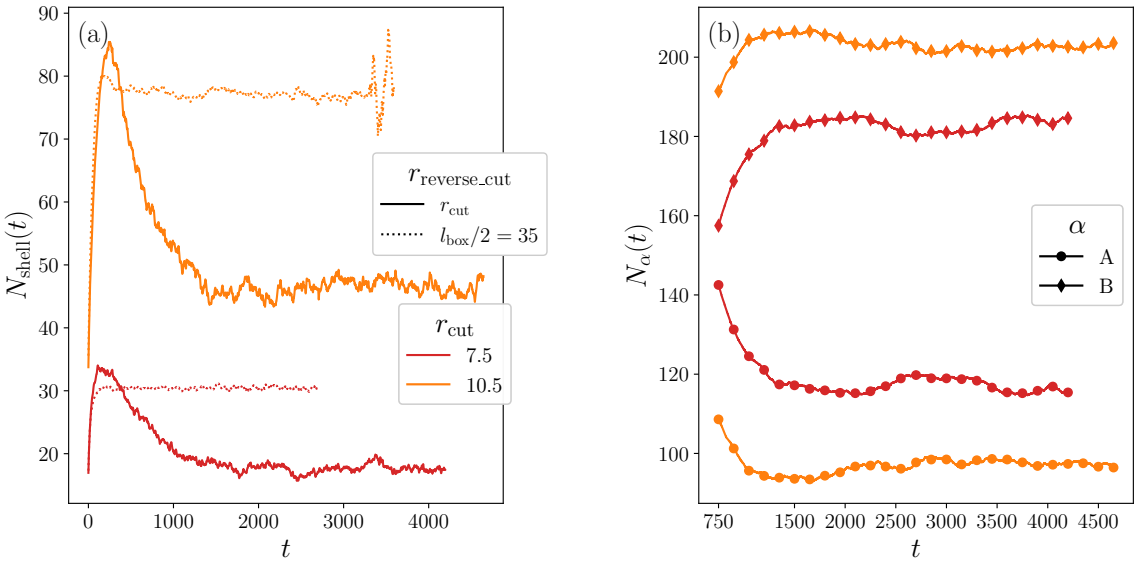

Figure 3.30: (a) Number of particles inside the system as a function of time, $N_{\text{shell}}(t)$. Comparison between systems where $r_{\text{reverse\_cut}} = r_{\text{cut}}$ (dotted lines) and where $r_{\text{reverse\_cut}} = 35$ (plain lines). (b) Number of solute particles of type $\alpha \in \{\text{A}, \text{B}\}$ in the system as a function of time $N_\alpha(t)$. Note that data on this plot start at $t = 750$. On both plots, the results are shown for $r_{\text{cut}} = 7.5$ in red and $r_{\text{cut}} = 10.5$ in orange.

Figure 3.30a shows the number of particles inside the reaction area as a function of time $N_{\text{shell}}(t)$ for the two reaction area radii studied: $r_{\text{cut}} = 7.5$ (red) and $r_{\text{cut}} = 10.5$ (orange). The results are compared to the reference situation: $r_{\text{reverse\_cut}} = r_{\text{cut}}$, represented on the figure by the dotted lines. The kinetics for both reaction area radii is clearly very different from their corresponding reference systems. First, the number of particles inside the reaction area increases, then, in contrast to the systems where $r_{\text{reverse\_cut}} = r_{\text{cut}}$, it decreases. The process can no longer be fitted by an exponential function (Eq. (3.2)). Nevertheless, $N_{\text{shell}}(t)$ reaches a plateau and can still be used as an indicator to define the steady state. In these systems, the initial simulation time t_{init} is defined graphically from the plot $N_{\text{shell}}(t)$: at $r_{\text{cut}} = 7.5$, $t_{\text{init}} = 1700$; at $r_{\text{cut}} = 10.5$, $t_{\text{init}} = 1430$. The time to reach the steady state is much longer than in the reference systems, which is $t_{\text{init}} = 92$ and $t_{\text{init}} = 108$ for $r_{\text{cut}} = 7.5$ and $r_{\text{cut}} = 10.5$, respectively. Values of the initial simulation time are recorded in Table III.9. This can be explained: it takes about $t \approx \left(\frac{l_{\text{box}}}{2}\right)^2 \frac{1}{D_{\text{A}}^0} = 1225$ for a solute particle to diffuse from the reaction area to the reverse reaction area when these two domains are separated by a distance about $\left(\frac{l_{\text{box}}}{2} - r_{\text{cut}}\right)$. On the contrary, the typical time needed for a solute particle to leave the reaction area is $t \approx \frac{r_{\text{cut}}^2}{D_{\text{A}}^0}$, which yields

$t = 56$ and $t = 110$ for $r_{\text{cut}} = 7.5$ and $r_{\text{cut}} = 10.5$, respectively.

Figure 3.30b shows the number of solute particles of type A (circles) and B (diamonds) inside the system as a function of time for $r_{\text{cut}} = 7.5$ (red) and $r_{\text{cut}} = 10.5$ (orange). This quantity was not monitored from the start, as its relevance appeared during the analysis of the first data of these systems. Therefore, note that the time starts at 750 on this plot. The amount of reactant (solute particles A), decreases with time as they are consumed during the reaction, whereas the amount of product (solute particles B) increases as they are created. The quantity of A and B stabilizes around $t_{\text{init}} = 1700$ and $t_{\text{init}} = 1430$, for $r_{\text{cut}} = 7.5$ and $r_{\text{cut}} = 10.5$, respectively. This corresponds to the steady state. In systems where $r_{\text{reverse\_cut}} = r_{\text{cut}}$, the number of B particles is equal to the number of particles inside the reaction area, i.e. $N_{\text{shell},\infty} = N_{\text{B}}$. Indeed, since the reverse reaction takes place outside the reaction area, a B particle is transformed back into an A particle as soon as it leaves the reaction area. This is not the case here, when a B particle leaves the reaction area it can diffuse freely until reaching $r = r_{\text{reverse\_cut}}$ where it is transformed back into A. The area where B particles can exist is larger than the reaction area which leads to $N_{\text{B}} > N_{\text{shell},\infty}$.

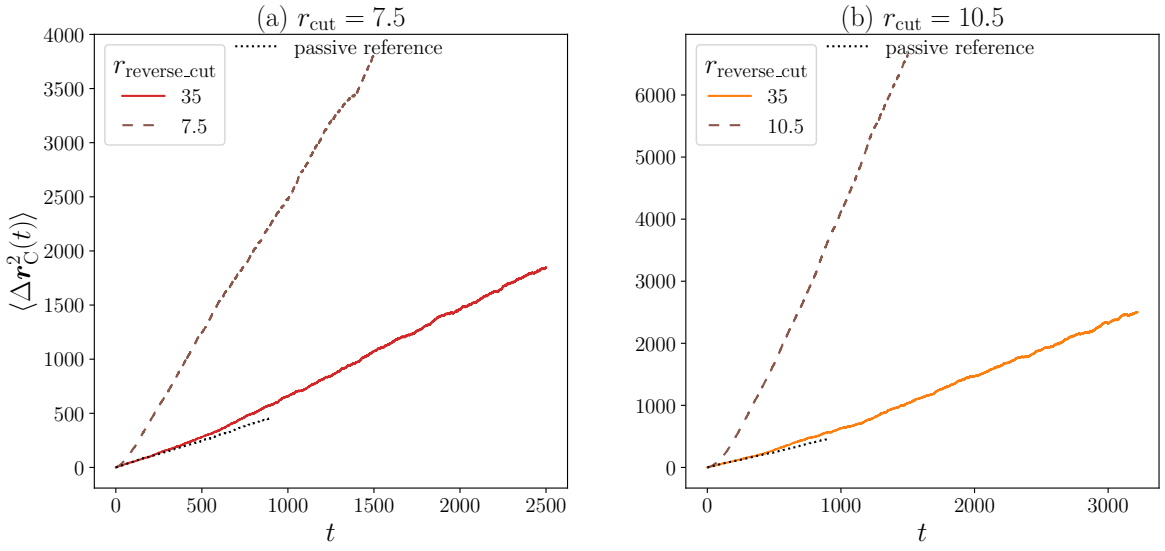

Figure 3.31: Mean squared displacements $\langle \Delta \boldsymbol{r}_{\text{C}}^2(t) \rangle$ as a function of time. Comparison between systems where $r_{\text{reverse\_cut}} = 35$ (plain lines) and the active reference systems for which $r_{\text{reverse\_cut}} = r_{\text{cut}}$ (dashed lines). Time for the active reference systems are shown until $t = 1500$ for clarity. The passive reference is indicated by the black dotted line. (a) $r_{\text{cut}} = 7.5$. (b) $r_{\text{cut}} = 10.5$.

The dynamics of the systems is shown on Figure 3.31. The MSDs are represented as a function of time for $r_{\text{cut}} = 7.5$ on Fig. 3.31a, and for $r_{\text{cut}} = 10.5$ on Fig. 3.31b. The reference systems where $r_{\text{reverse\_cut}} = r_{\text{cut}}$ are represented by the brown dashed line

on each plot. The passive reference is also indicated by the dotted black line. Both plots stress a drastic decrease of the activity for $r_{\text{reverse\_cut}} = 35$. Though, the long-time diffusion is slightly enhanced as the orange and red curves deviate from the black curves at the end. D_{eff} is measured in both systems, values are reported in Table III.9. The ballistic part of each MSD is very long, and despite the long simulations run, the MSDs have still not reached the final linear regime. Therefore, the computed values represent a lower bound for the real value of D_{eff}. In both cases, $D_{\text{eff}} = 0.162$ which is superior to $D_{\text{no\_reac}} = 0.124$, but smaller than D_{eff} of the cases where $r_{\text{reverse\_cut}} = r_{\text{cut}}$ which is $D_{\text{eff}} = 0.66$ and $D_{\text{eff}} = 1.14$ at $r_{\text{cut}} = 7.5$ and $r_{\text{cut}} = 10.5$, respectively.

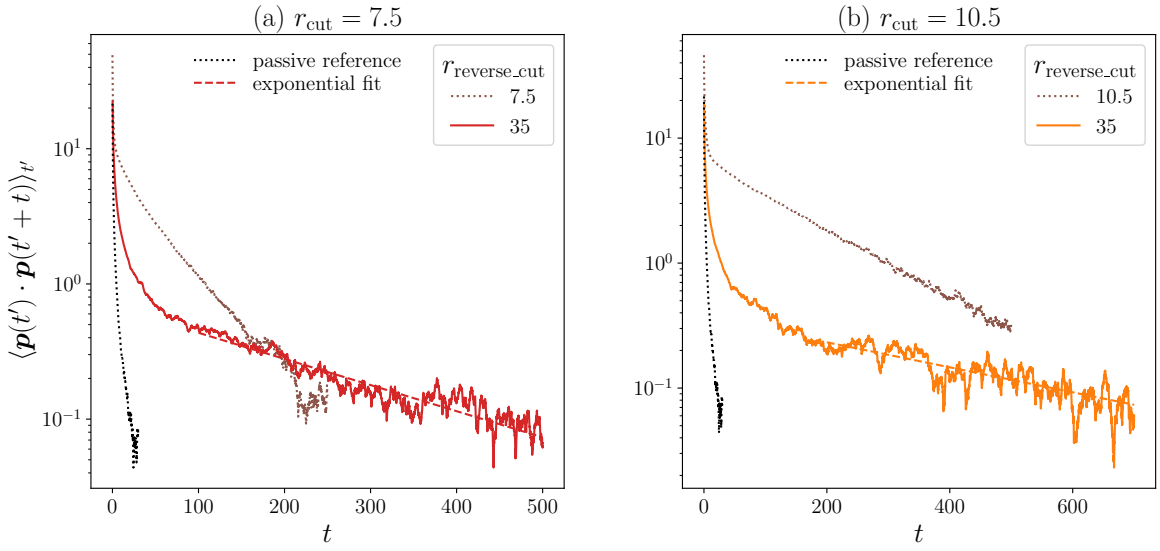

Figure 3.32: Autocorrelation functions of the polarization vector: $\langle \boldsymbol{p}(t') \cdot \boldsymbol{p}(t'+t) \rangle_{t'}$. Comparison between systems where $r_{\text{reverse\_cut}} = 35$ (plain lines) and the active reference systems for which $r_{\text{reverse\_cut}} = r_{\text{cut}}$ (dotted lines). The passive reference is indicated by the black dotted line. The exponential fits using Eq. (3.6) are represented by the dashed lines. (a) $r_{\text{cut}} = 7.5$. (b) $r_{\text{cut}} = 10.5$.

Figure 3.32 represents the autocorrelation functions of the polarization vector $\boldsymbol{p}$ as a function of time. $\langle \boldsymbol{p}(t') \cdot \boldsymbol{p}(t'+t) \rangle_{t'}$ is shown for the system at $r_{\text{cut}} = 7.5$ on Fig. 3.32a, and for the system at $r_{\text{cut}} = 10.5$ on Fig. 3.32b. The brown dashed line represents the results for the corresponding active reference systems in which $r_{\text{reverse\_cut}} = r_{\text{cut}}$. The case of the passive reference system is indicated by the black dotted line. An exponential tail is observed as well for systems with $r_{\text{reverse\_cut}} = 35$, which can be fitted using Eq. (3.6). The fit is represented by the dashed lines and is in good agreement with the data. The persistence time τ_p is extracted, whose values are recorded in Table III.9. The persistence times of systems where the reverse reaction is far away from the colloid are much larger than cases where the reverse reaction takes place outside the reaction area. $\tau_p = 225$

vs $\tau_p = 48$ at $r_{\text{cut}} = 7.5$, and $\tau_p = 434$ vs $\tau_p = 162$ at $r_{\text{cut}} = 10.5$. Similarly to the previous situation investigated, where τ_{BA} is increased, the droplet formed goes beyond the reaction area. The motion of such a large object is slow, hence a large value for τ_p.

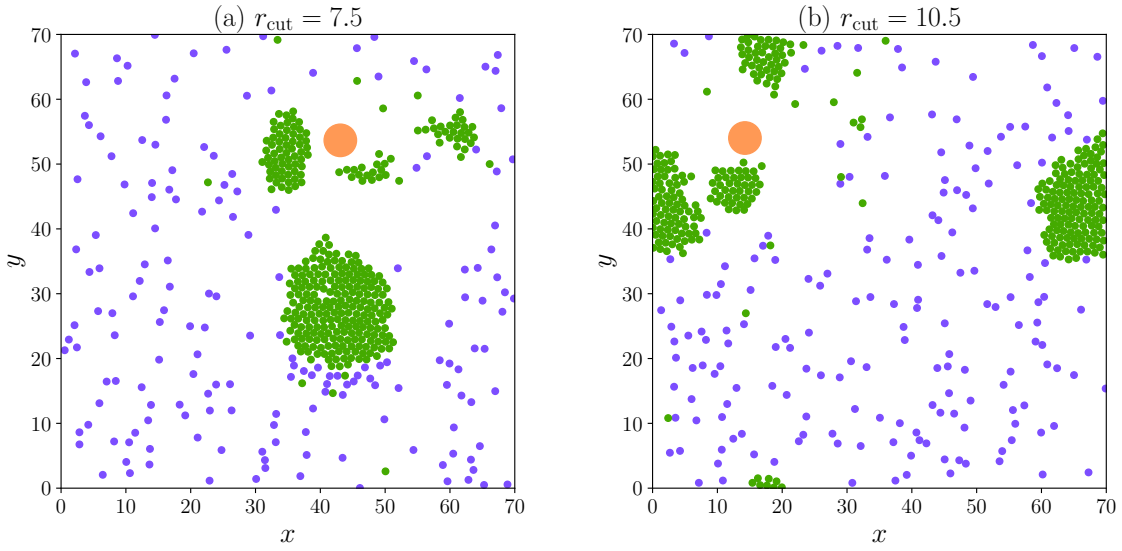

Figure 3.33: Snapshots of the system at $t = 2450$. (a) $r_{\text{cut}} = 7.5$. (b) $r_{\text{cut}} = 10.5$.

Snapshot of the system at $t = 2400$ are shown on Figure 3.33. This confirms the formation of a large droplet. It shows also that the droplet detaches from the surface of the colloid, which empties the reaction area. The filling fraction of the reaction area at steady state for $r_{\text{reverse\_cut}} = 25$ is: $N_{\text{shell},\infty}/N_{\text{max}} = 0.09$ and $N_{\text{shell},\infty}/N_{\text{max}} = 0.12$ at $r_{\text{cut}} = 7.5$ and $r_{\text{cut}} = 10.5$, respectively. This corresponds to a regime where the enhanced diffusion is limited, as the density fluctuations are not strong enough to generate ballistic motion.

Finally, in this paragraph, the changes made to the system modify the location of the reverse reaction, which is conceptually different from the changes made in the previous paragraph which has modified the characteristic time of the reverse reaction. Yet, the effects observed are similar. It is expected that the situation of $\tau_{\text{BA}} \to \infty$ tends towards the extreme case shown in this paragraph.

3.6.4 Propulsion in three dimensions

So far, all the presented results concern 2D simulations. As the mechanism of droplet formation and the persistence time of the droplet may depend on the dimension of the system, simulations for the same model in three dimensions were also performed. The simulation box is cubic, with $l_{\text{box}} = 22$. In 3D simulations, the solute density is $\rho = 0.05$,

$\rho = 0.1$, $\varepsilon = 3$, $r_{\text{reverse\_cut}} = 35$						
r_{cut}	t_{init}	$N_{\text{shell},\infty}$	t_{lin}	D_{eff}	δD_{eff}	τ_p
7.5	1700	17	2000	0.182	0.004	225
10.5	1430	45	2900	0.196	0.004	434

Table III.9: Summary of the quantities of interest: t_{init} the initial simulation time from steady state, $N_{\text{shell},\infty}$ the number of particles inside the reaction area at steady state, t_{lin} the time from which the last linear regime of the MSD is reached and from which D_{eff} can be computed, D_{eff} the effective diffusion coefficient, δD_{eff} the associated error, and τ_p the persistence time.

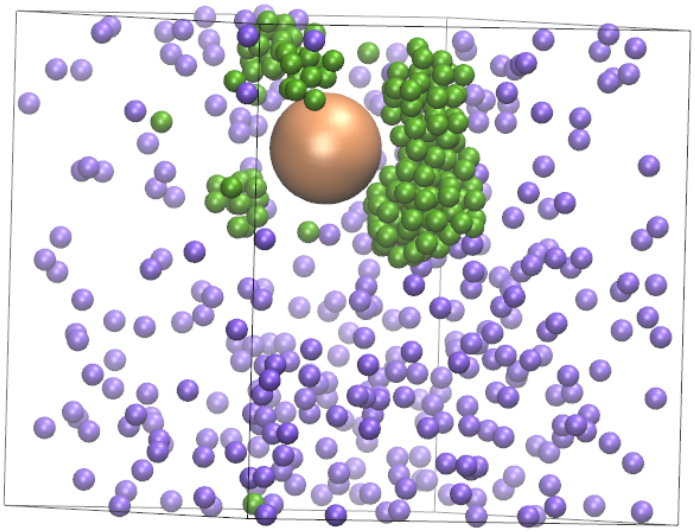

Figure 3.34: Snapshot of the studied system in three dimensions at steady state. The density of solute particles is $\rho = 0.05$, the intensity of the LJ attraction is $\varepsilon = 3$, and the size of the reaction area is $r_{\text{cut}} = 7.5$.

the strength of the attraction of the LJ potential is $\varepsilon = 3$ and the reaction area radius is $r_{\text{cut}} = 7.5$. A snapshot of the system at steady state is shown on Figure 3.34. Qualitatively, as it can be seen on the figure, droplets of B particles around the colloid are observed, as it was obtained in 2D. The kinetics of the filling of the reaction area can still be modeled using Equation (3.2) as shown on Figure 3.35. The number of particles inside the reaction area N_{shell} is normalized by N_{max} which is defined in 3D by Eq. (3.19) where ϕ_{max} is the maximum packing fraction. For hard spheres in 3D, $\phi_{\text{max}} = \frac{\pi}{3\sqrt{2}} \simeq 0.74$. The simulation data are well-fitted using Equation (3.2).

$$N_{\text{max}} = \phi_{\text{max}} \frac{r_{\text{cut}}^3 - (\sigma_{\text{C}}/2)^3}{(\sigma_{\text{A}}/2)^3}, \tag{3.19}$$

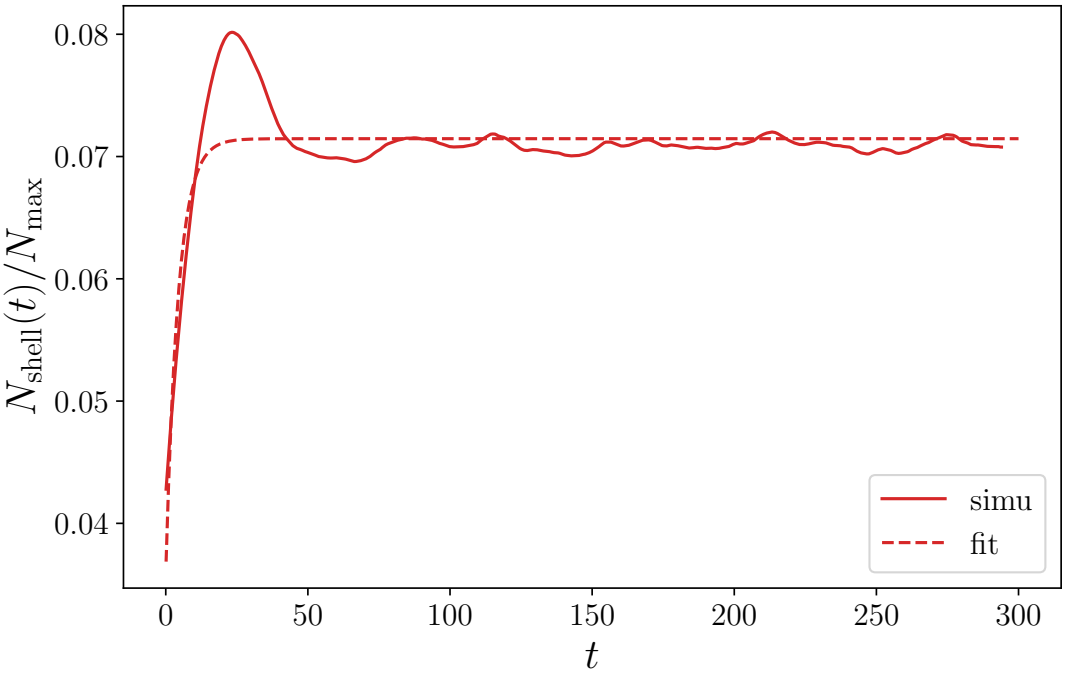

Figure 3.35: $N_{\text{shell}}(t)/N_{\text{max}}$ for a 3D simulation where $\rho = 0.05$, $\varepsilon = 3$, and $r_{\text{cut}} = 7.5$. The dashed line is the fit using Equation (3.2).

The mean squared displacement of the colloid as a function of time at steady state is given on Figure 3.36a. A behavior similar to 2D systems is observed. The MSD has a transiently ballistic behavior at intermediate times and becomes linear in time at long times. The colloid self-propels, with a long-time enhanced diffusion $D_{\text{eff}}/D_{\text{noreac}} \sim 11$ for the parameters used here. The autocorrelation function of the polarization vector $\boldsymbol{p}$ is shown on Figure 3.36b in a semi-log scale. It is linear at long times, and characterized by a persistence time $\tau_p = 33$ of the same order of magnitude as in 2D. It appears thus that all the essential features of the 2D propulsion mechanism still hold in 3D: droplets form in the reaction area, which push the colloid with a persistent orientation. All the values of the quantities of interest are summed up in Table III.10.

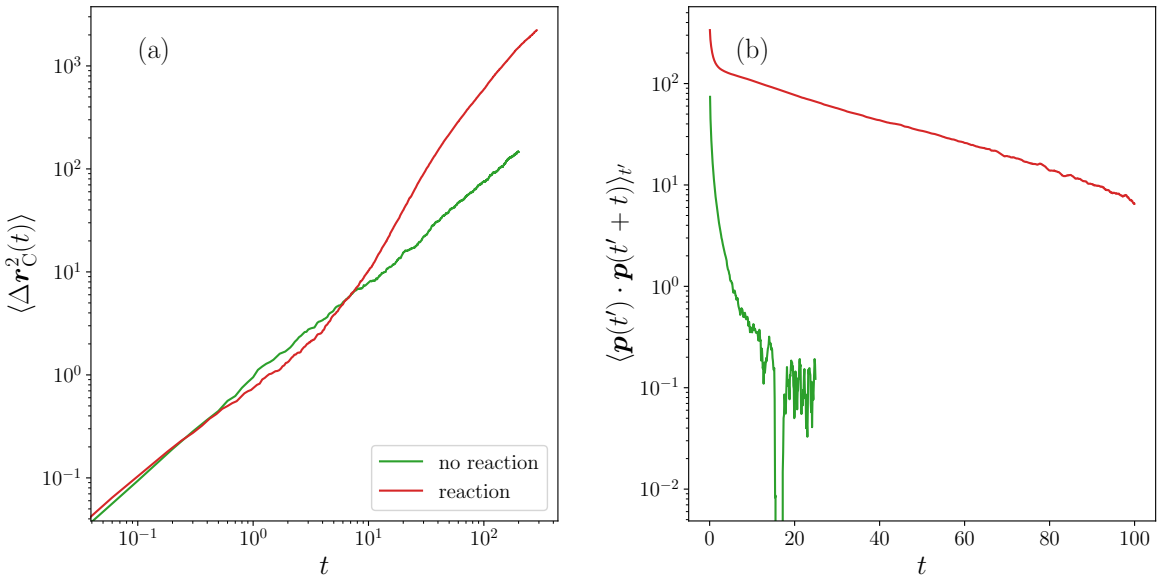

Figure 3.36: Dynamic quantities obtained at steady state for a 3D system with the solute density $\rho = 0.05$, the LJ attraction $\varepsilon = 3$, and the reaction area of radius $r_{\mathrm{cut}} = 7.5$. The case with reaction, which displays activity (in red) is compared to the case without reaction (in green). (a) Mean squared displacement of the colloid as a function of time in a log-log scale. (b) Autocorrelation function of the polarization vector $\boldsymbol{p}$ as a function of time for the system with reaction.

t_{init}	$N_{\mathrm{shell},\infty}$	t_{lin}	$D_{\mathrm{no\_reac}}$	$\delta D_{\mathrm{no\_reac}}$	D_{eff}	δD_{eff}	τ_p
12	172	225	0.125	0.001	1.283	0.004	33

Table III.10: Summary of the quantities of interest: t_{init} the initial simulation time from steady state, $N_{\mathrm{shell},\infty}$ the number of particles inside the reaction area at steady state, t_{lin} the time from which the last linear regime of the MSD is reached and from which D_{eff} can be computed, $D_{\mathrm{no\_reac}}$ the reference diffusion coefficient and $\delta D_{\mathrm{no\_reac}}$ the associated error, D_{eff} the effective diffusion coefficient and δD_{eff} the associated error, and τ_p the persistence time.

CHAPTER 4

Properties of suspensions of active colloids

Contents

Summary

In this chapter, collective effects of suspensions of active colloids are investigated. The key parameters for activity (the solute density ρ, the intensity of the attraction ε, and the reaction area r_{cut}) are fixed. First, simulations of several systems are performed, varying the surface fraction of colloids. The results are compared to those obtained for an assembly of passive colloids. The radial distribution functions reveal that in the active systems, an effective attraction at short distances exists, that is much stronger than in suspensions of passive colloids. A shoulder at larger distances indicates a structuration. A cluster analysis is performed, which shows that there is formation of small aggregates. The dynamics of the systems is also investigated. Although the colloids are still active at all the surface fractions studied, the long-time diffusion coefficients measured are strongly decreased in comparison to the case of a single colloid. In addition, implicit simulations (BD-APB) which do not describe explicitly the solute particles are performed. The parameters of the BD-ABP simulations are inferred from the explicit simulations. The procedure is presented in this chapter. Strong differences are observed between results obtained from BD and BD-ABP simulations. In the latter, the systems present less structuration. Only a small attraction peak at short distances on the radial distribution functions exists and the clusters are smaller. Finally, the influence of the radius of the reaction area is studied. This does not change much the structural and dynamical results obtained from explicit simulations, while implicit simulation results are affected. This indicates that implicit simulations overestimate the activity intensity since it does not take into account the blockage due to solute particles.

4.1 Introduction

The model I built exhibits activity and the mechanism of propulsion has been characterized in Chapter 3 for one colloid. In experimental works, the behavior of a collection of active particles is usually studied. The following step is thus to study an assembly of such colloids, which raises several questions. Will activity persist? How the mechanism that leads to self-propulsion will be affected? Which collective effects will emerge? To address these questions, simulations are run using the developed BD code, where the solute particles as well as their interactions are explicitly described. These BD simulations will be referred to as *explicit simulations*. As discussed in Chapter 1, the literature on active systems is rich, but coarse-grained descriptions, which ignore the microscopic details, are mainly used in theoretical works. Our approach is well suited to a rigorous attempt to link explicit and implicit models. In this end, simulations of a corresponding active Brownian particle (ABP) model are also performed and will be referred to as *BD-ABP simulations* or *implicit simulations*. The chapter is organized as follows: in Section 4.2 a new relevant parameter for the description of collective effects, namely the surface fraction, is introduced, and the numerical values of the chosen parameters are given. Section 4.3 describes the parameterization of the ABP model to map the dynamics as well as the interactions onto the explicit model. Section 4.4 is devoted to the definition of the steady state. Section 4.5 and 4.6 present structural and dynamical properties of the system. In Section 4.7, the influence of the size of the reaction area is investigated.

4.2 Numerical values of the parameters

In the previous chapter, the parameters favorable to self-propulsion have been identified. In this chapter, the key parameters for activity are fixed: the solute density ρ, the intensity of the attraction ε, and the reaction area r_{cut}. The chosen solute density is $\rho = 0.1$, the attraction intensity is $\varepsilon = 3$. Since the time step depends only on ρ and ε, its value is fixed to $\Delta t = 0.00006$. At $\varepsilon = 3$, the reaction area radius for which the diffusion is the most enhanced is about $r_{\text{cut}} = 12$. However, as several colloids are in the system, if the reaction areas are too large, they will cover all the simulation box, a situation that must be avoided. Therefore, the chosen reaction area radius is $r_{\text{cut}} = 7.5$. In Section 4.7, where the effect of the reaction area is investigated, this value will be modified. The other parameters remain fixed: the colloid diameter is $\sigma_{\text{C}} = 5$, the characteristic times of reactions are $\tau_{\text{AB}} = \tau_{\text{BA}} = 0.1$, and the reverse reaction takes place for $r > r_{\text{cut}}$.

The quantities of interest in this chapter involve timescales and length scales larger than in a system with one colloid. Moreover, in the coarse-grained model, it is not relevant

to use a unit system based on the solute particles since they are not explicitly described. Therefore, in this chapter, all the quantities will be in units related to the colloid as presented in Chapter 2. The lengths are expressed in terms of colloid diameter, and the time in terms of time needed for the colloid to explore an area about the size of its diameter. By denoting r^* and $\tilde{r}$, the distances in units relative to a solute particle and to the colloid, respectively, the two unit systems are related through:

$$\tilde{r} = r^* \frac{\sigma_\mathrm{A}}{\sigma_\mathrm{C}}.$$

Similarly, the time in units related to the solute particles is denoted t^* and $\tilde{t}$ in units related to the colloid. The two are linked through:

$$\tilde{t} = t^* \frac{\sigma_\mathrm{A}^2}{D_\mathrm{A}^0} \frac{D_\mathrm{t,C}}{\sigma_\mathrm{C}^2}.$$

In what follows, all the quantities are in units related to the colloid and $\tilde{}$ is removed for clarity. In this unit system, the colloid size is $\sigma_\mathrm{C} = 1$. The reaction radius area is then $r_\mathrm{cut} = 1.5$ and, in Section 4.7, $r_\mathrm{cut} = 1.3$. The time step of BD simulations is then $\Delta t = 2.4 \times 10^{-7}$. In BD-ABP simulations, since the solute particles are not described, a larger time step is acceptable, $\Delta t = 0.0001$.

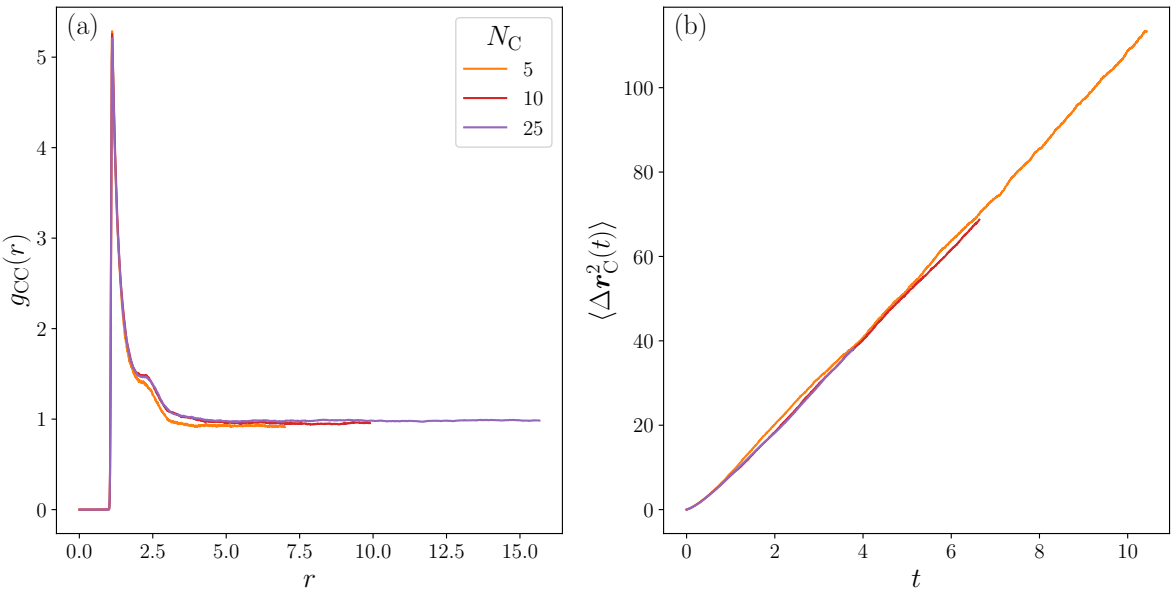

Figure 4.1: (a) Radial distribution functions g_CC between colloids. (b) MSDs as a function of time $\langle \Delta \boldsymbol{r}_\mathrm{C}^2(t) \rangle$. $\phi_\mathrm{C} = 0.02$, for different system sizes: $N_\mathrm{C} = 5$ and $l_\mathrm{box} = 14$, $N_\mathrm{C} = 10$ and $l_\mathrm{box} = 19.8$, and $n_\mathrm{c} = 25$ and $l_\mathrm{box} = 31.3$.

A new relevant parameter is introduced, namely the surface fraction of colloids ϕ_C which is defined by:

$$\phi_C = \frac{\pi \sigma_C^2 N_C}{4 l_{box}^2}.$$

The number of colloids N_C must be large enough, so it is meaningful to investigate collective effects, and the size of the simulation box large enough to avoid finite size effects. Nevertheless, at fixed ϕ_C, increasing N_C also increases the size of the box l_{box}. The number of solute particles N is then adjusted to have $\rho = 0.1$. Thus, the numerical cost is greatly enhanced when increasing N_C. A compromise must be found. Various system sizes were tried for each studied ϕ_C. To guide the choice, the radial distribution function g_{CC} between colloids and the mean squared displacement of the colloids $\langle \Delta \boldsymbol{r}_C^2(t) \rangle$ are computed. These quantities should be unaffected by the size of the system.

Figure 4.1 illustrates for $\phi_C = 0.02$ the reasoning behind each choice. The radial distribution functions g_{CC} between the colloids are displayed on Fig. 4.1a and the mean squared displacement of the colloid as a function of time $\langle \Delta \boldsymbol{r}_C^2(t) \rangle$ on Fig. 4.1b. Three sizes were tested: $N_C = 5$ and $l_{box} = 14$, $N_C = 10$ and $l_{box} = 19.8$, and $n_c = 25$ and $l_{box} = 31.3$. Differences are observed between the system with $N_C = 5$ and the others. This system is thus too small. For this case, $N_C = 10$ is chosen, as both g_{CC} and MSD are very close to those obtained with $N_C = 25$. The larger system with $N_C = 25$ requires too long simulations, therefore it is discarded. $N_C = 10$ colloids is sufficient for the purpose of the study.

Table IV.1 lists the various surface fractions of colloids ϕ_C that were investigated, and all the tested sizes of the systems: N_C, and l_{box}. The number of solute particles N is also indicated, as its value is adjusted in order to have $\rho = 0.1$. The systems for which results are presented in what follows are in bold.

ϕ_C	0.008			0.01	0.02			0.03		0.04		0.1	
N_C	2	4	**10**	**25**	5	**10**	25	8	**25**	10	**50**	**25**	100
l_{box}	14	19.8	**31.3**	**44.2**	14	**19.8**	31.3	14	**24.4**	14	**31.3**	**14**	44.2
N	500	980	**2455**	**4885**	500	**980**	2455	500	**1500**	500	**2455**	**500**	4885

Table IV.1: Size of the tested systems in terms of number of particles N_C for each surface fraction of colloids ϕ_C. The size of the simulation box l_{box} and the number of particles N are indicated for the corresponding ϕ_C.

4.3 Coarse-graining of active colloids: computation of effective parameters for non-equilibrium situations

4.3.1 Dynamical parameters

There are many routes to access parameters of a coarse-grained model for which a finer model is available. In colloidal sciences, one of the usual methods is to extract an effective interaction potential by computing the so-called potential of mean force between two colloids in an infinite bath [84, 85, 86]. A similar route is followed here to determine the effective parameters for the ABP model (see Eq. (2.11) and Eq. (2.12) in Chapter 2). Both rotational and translational diffusion coefficients, $D_{r,\mathrm{C}}$ and $D_{\mathrm{t,C}}$, as well as the propulsion velocity v_0 are obtained through the analysis of trajectories that were generated through BD simulations of one colloid. This defines an active colloid at infinite dilution. The translational diffusion coefficient at infinite dilution is denoted by $D^0_{t,\mathrm{C}}$ in what follows.

The rotational diffusion coefficient $D_{r,\mathrm{C}}$ is linked to the reorientation time, τ_{r}. In the explicit model, the orientation of the colloid has been shown to be determined by the polarization vector $\boldsymbol{p}$ which represents the droplets orientation (see Chapter 3). A characteristic persistence time τ_p emerges from the autocorrelation function of the polarization vector $\boldsymbol{p}$, analogous to τ_{r} of the ABP model. τ_p has been computed, therefore the rotational diffusion coefficient is set to $D_{r,\mathrm{C}} = 1/\tau_p$.

The inference procedure is based on the fitting of the mean squared displacement of a single active colloid in an infinite bath of solute particles. As discussed in Chapter 3, the obtained MSD differs from the one predicted by the ABP model. Particularly, the transient ballistic regime is shorter and less intense. Therefore, it is not possible to fit the MSD with Eq. (2.14) to extract the three dynamic parameters. Another possibility is to fit the different regimes independently. In Chapter 2, the asymptotic developments of the MSD at long times and at short times have evidenced three regimes:

- At short times, the MSD is linear in time:

$$\left\langle \Delta \boldsymbol{r}^2_{\mathrm{C}}(t) \right\rangle \sim 4 D^0_{t,\mathrm{C}} t. \tag{4.1}$$

  The dynamics is dominated by the translational diffusion coefficient of the colloids $D^0_{t,\mathrm{C}}$. The effects of activity are not yet detected. This translational diffusion coefficient is about the same as the reference diffusion coefficient, $D_{\mathrm{no\_reac}}$, introduced in Chapter 3. Yet, discrepancy is observed in systems where $\rho = 0.1$, $\varepsilon = 3$ due to a local increase of the solute density caused by the attractive interactions between

B solute particles as discussed in Chapter 3. For more precision, it will be fitted here, and the fitted value denoted by $D^0_{t,\mathrm{C}}$ will be used as an input of BD-ABP simulations.

- At intermediate times, the MSD is ballistic:

$$\left\langle \Delta \boldsymbol{r}^2_{\mathrm{C}}(t) \right\rangle \sim v_0^2 t^2. \tag{4.2}$$

The magnitude of the propulsion speed determines the ballistic behavior.

- At long times, the MSD is again diffusive:

$$\left\langle \Delta \boldsymbol{r}^2_{\mathrm{C}}(t) \right\rangle \sim \left(4D^0_{t,\mathrm{C}} + 2\frac{v_0^2}{D_{r,\mathrm{C}}} \right) t. \tag{4.3}$$

All the parameters are involved at this timescale.

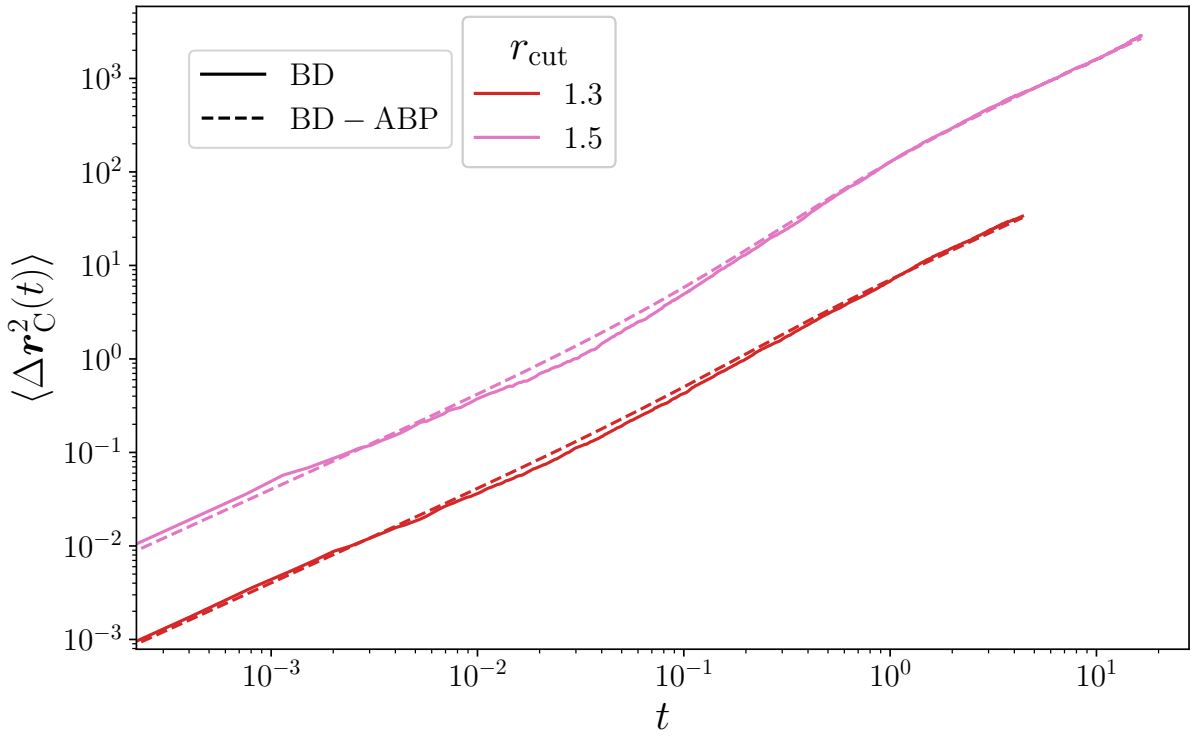

Figure 4.2: Comparison between MSDs from BD simulations (dashed lines) and Eq. (2.14) (plain lines). $N_{\mathrm{C}} = 1$, $\varepsilon = 3$, $r_{\mathrm{cut}} = 1.3$ (red) and $r_{\mathrm{cut}} = 1.5$ (pink). The curves are vertically shifted for more clarity.

The MSD of a single colloid exhibits long and short times that are both linear in time, similarly to the long and short times of the ABP model. Therefore, the dynamic parameters will be inferred from the fits of the first and of the last regimes. The translational

diffusion coefficient of the colloid $D^0_{t,\mathrm{C}}$ is extracted from the short-time fit, and the propulsion velocity v_0 is extracted by fitting the last linear regime of the MSD. These quantities are in units related to the solute particles and must be then converted in units related to the colloid, as described in Section 4.2. The procedure is done for both reaction radii $r_{\mathrm{cut}} = 1.3$ and $r_{\mathrm{cut}} = 1.5$ that are used in this chapter. The values found for the dynamic parameters are displayed in Table IV.2. Figure 4.2 represents the MSDs of the colloid from the explicit simulations compared to the MSDs computed with Eq. (2.14) using the fitted parameters v_0, $D^0_{t,\mathrm{C}}$, and $D_{r,\mathrm{C}}$. The two systems used in this chapter are shown, $r_{\mathrm{cut}} = 1.3$ and $r_{\mathrm{cut}} = 1.5$. There is a good agreement between the two MSDs at short times and at long times. The dynamics of the ABP model is thus perfectly mapped onto the explicit model.

r_{cut}	1.3	1.5
$D^0_{t,\mathrm{C}}$	1.0	1.0
$D_{r,\mathrm{C}}$	7.3	3.2
v_0	3.6	4.5

Table IV.2: Values of the parameters of the ABP model. They are fitted to reproduce the MSDs, which are obtained from explicit BD simulations at short and long times.

4.3.2 Depletion potential

In addition to effective dynamical parameters, the coarse-grained model also requires the effective interactions between the colloidal particles, which take into account the influence of small solute particles. Nevertheless, the exact definition of such interactions is not obvious for non-equilibrium systems, since activity affects their structural and thermodynamic properties. The implicit effective potential between colloids is then computed from equilibrium simulations of the explicit model, i.e. when the colloids do not catalyze a reaction and are in a purely repulsive bath of solute particles. Simulations are run at the various studied ϕ_{C} for the passive systems. The radial distribution functions g_{CC} between colloids are shown on Figure 4.3. At all surface fractions, a peak is observed close to the contact distance $r = 1$. This indicates an effective attraction between the colloids, which is an expected consequence of solute depletion, which occurs when colloids get close to each other [87]. The peak is increasingly high as the surface fraction of colloids rises. A shoulder even appears for $\phi_{\mathrm{C}} = 0.1$ at the distance $r = 1.3$, indicating a structuring of the system.

The idea is to have an effective potential that takes into account the effective attraction between colloids due to the solute depletion, so that both the ABP model and the explicit simulations have the same initial structural and dynamical parameters. For simplicity and

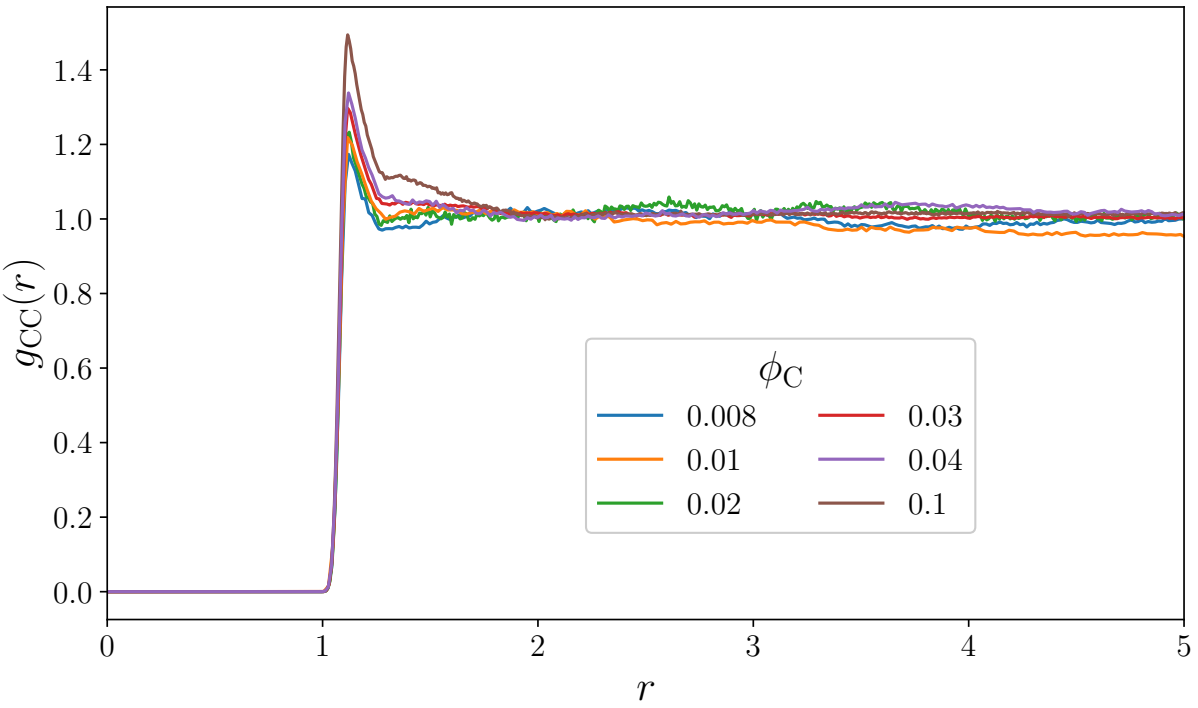

Figure 4.3: Radial distribution functions g_{CC} between colloids for different surface fractions ϕ_C. Data are from BD simulations of equilibrium systems, with colloids and solute particles. The colloids do not catalyze the reaction. Data are shown for $r < 5$ to emphasize the interesting part.

because the ABP model is only employed for comparison purposes, the effective potential will be modeled by a Lennard-Jones potential. The attraction intensity ε_{ABP} will be set in order to match the height of the peak of the g_{CC} function of explicit simulations. This is done empirically for the most dilute system studied, i.e. $\phi_C = 0.008$, and the same effective interaction potential is kept for all other surface fractions. The inference procedure to find ε_{ABP} is the following. Simulations using the BD-ABP code are run, fixing the activity term of Eq. (2.11), v_0, to 0, so the colloids are passive. There are only colloids, which interact through a LJ potential, whose expression has been given in Chapter 2 by Eq. (2.1). The attraction intensity ε_{ABP} is initially set with an arbitrary value. The simulation is run, then the radial distribution function is plotted and compared to the one from explicit simulations of the equilibrium system with solute particles. If the peak is too high, the attraction intensity is reduced, in contrast if it too small, the attraction intensity is increased. A new simulation is run and this goes on until the two peak heights match. Figure 4.4 represents the radial distribution functions between colloids from BD-ABP simulations for various ε_{ABP} (colored, plain lines) and the target g_{CC} from BD simulation (dashed, black line). It is found that the correct value for ε_{ABP}

to recover the same attraction peak is $\varepsilon_{\mathrm{ABP}} = 0.15$. This value is then used for the other studied surface fractions.

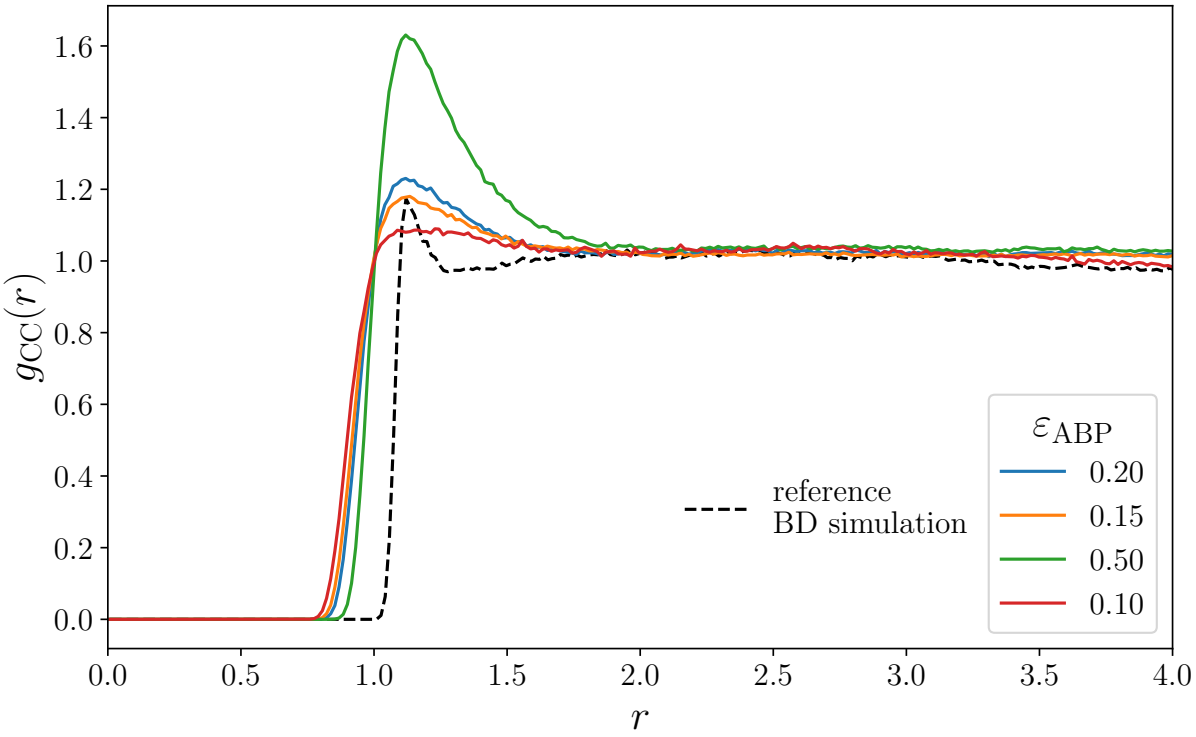

Figure 4.4: Radial distribution functions g_{CC} between colloids of passive systems at $\phi_{\mathrm{C}} = 0.008$. In BD simulations (plain lines), the colloids interact purely repulsively and are in a purely repulsive bath. In BD-ABP simulations, colloids interact with a LJ potential where the attraction intensity $\varepsilon_{\mathrm{ABP}}$ is varied.

4.4 Definition of a steady state

The filling of the reaction area for each colloid is monitored by computing the number of solute particles inside the reaction area N_{shell} of each colloid as a function of time. In this chapter, the quantity is averaged over noise realizations, and over the number of colloids, $N_{\mathrm{shell}} = \langle N_{\mathrm{shell}} \rangle_{N_{\mathrm{C}}, n_{\mathrm{realizations}}}$. Figure 4.5 displays $N_{\mathrm{shell}}(t)$ for the various ϕ_{C} investigated (plain colored lines). The system of reference, which contains a single active colloid, is represented by the black dashed line for comparison. Interestingly, $N_{\mathrm{shell},\infty}$ is a decreasing function of the surface fraction. Indeed, when ϕ_{C} increases, the space available for solute particles inside the reaction area is reduced because of exclusion zones that emerge due to the depletion. The kinetics of filling of the reaction area can still be fitted by an exponential function (Eq. (3.2)). The corresponding exponential fits are represented by the colored dashed lines on Fig. 4.5 and are in good agreement with

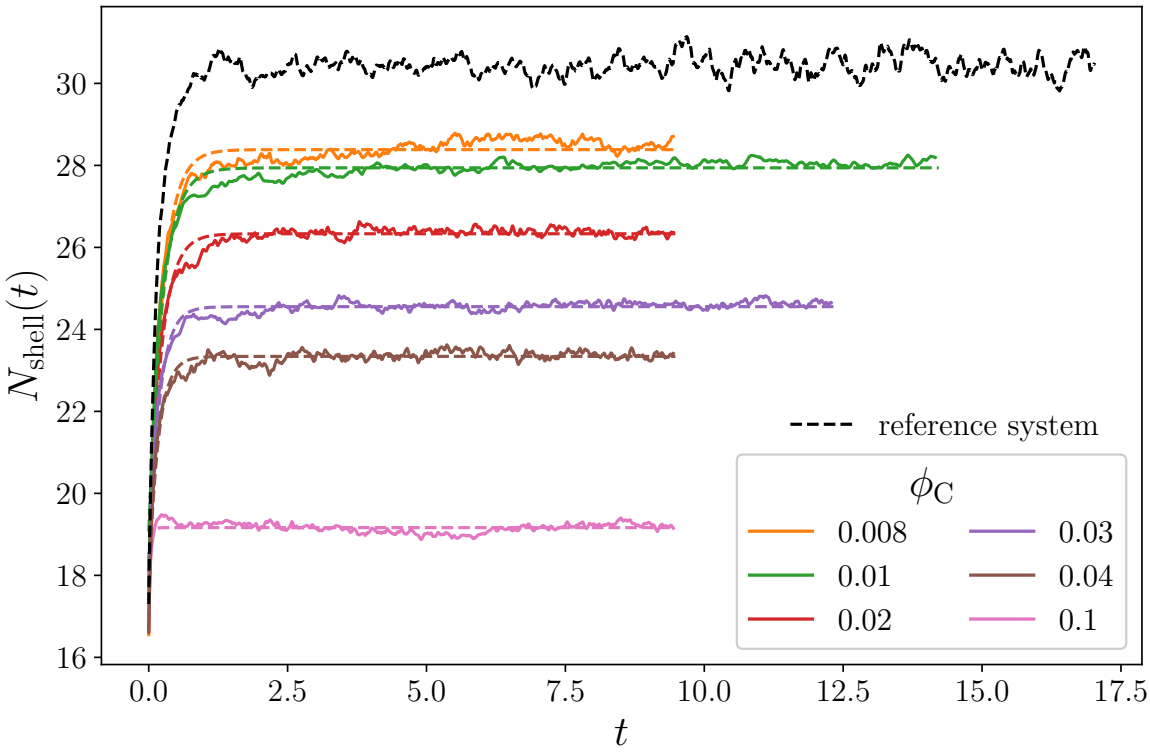

Figure 4.5: The number of solute particles inside the reaction area as a function of time, $N_{\text{shell}}(t)$. The figure shows various surface fractions ϕ_C, where each curve is averaged over noise realizations and over the colloids. The colored dashed lines show the exponential fits using Eq. (3.2). The black dashed line shows $N_{\text{shell}}(t)$ for the system containing a single colloid as a reference.

computed data. In particular, the number of particles inside the reaction area still reaches a steady state characterized by $N_{\text{shell},\infty}$. However, while N_{shell} converges, it is possible that more collective quantities, related to inter-colloidal interactions, are still time dependent. Therefore, $N_{\text{shell}}(t)$ might be insufficient to characterize the steady state of the systems, as it is the collective dynamics which is looked at.

There is an additional larger timescale involved in the many-body problem, because once the shell has formed around each colloid, colloids start moving due to activity. The radial distribution functions g_{CC} is measured on different time intervals, to evaluate if a steady state is reached. The collective steady state time, $t_{s,\text{col}}$, is determined graphically by plotting $g_{CC}(r)$ at different times for each system, and by looking at the time for which it becomes constant. The same procedure is carried out for BD-ABP simulations. An example for the system at $\phi = 0.1$ is depicted on Figure 4.6, which represents the radial distribution functions g_{CC} between colloids for different time intervals. Fig. 4.6a shows results from BD simulations. First, g_{CC} evolves in time, the peak at $r = 1$ and the shoulder at $r = 2.5$ becomes increasingly high. From $t = 1$, the function g_{CC} is constant over time.

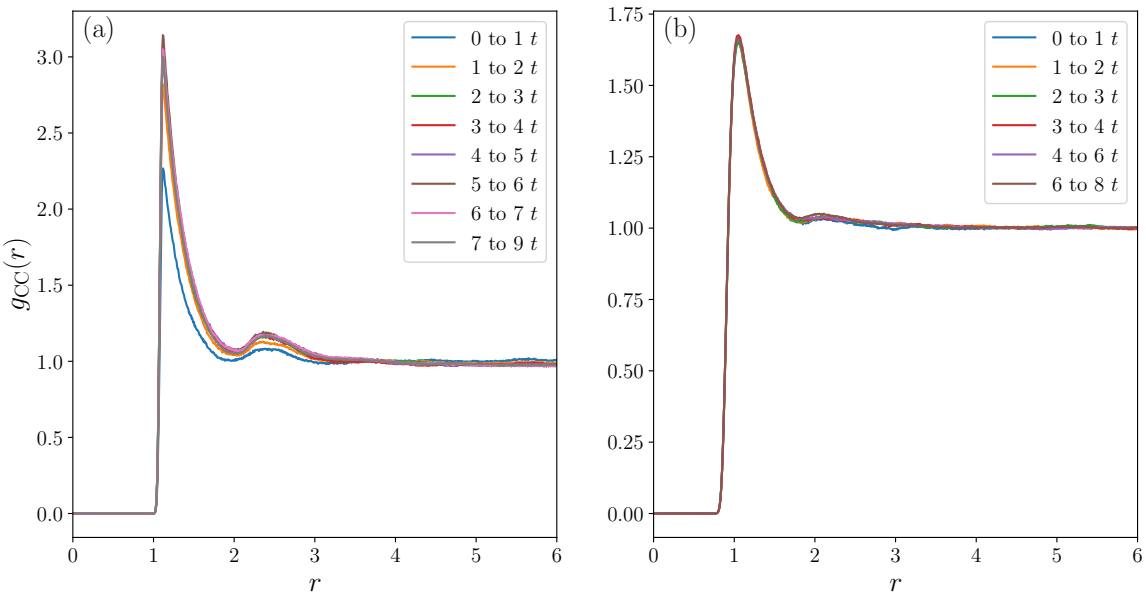

Figure 4.6: Radial distribution functions between colloids g_{CC} from different time intervals for the system $\phi_C = 0.1$. Only data for $r < 6$ are shown to emphasize the most interesting part.

Fig. 4.6b shows results from BD-ABP simulations. All the curves are superimposed, g_{CC} converges immediatly and $t_{s,col} = 0$. Thus, this quantity is a relevant indicator to define the collective steady state. Values of steady state times are summarized in Table IV.3. The time is rescaled in what follows so that the initial time $t_{init} = t_{s,col}$. The structural and dynamic properties of the system are studied for $t > t_{init}$. Therefore, from the steady state, the radial distribution functions are averaged over noise realizations and over time $g_{CC} = \langle g_{CC} \rangle_{n_{realizations},t}$.

Explicit simulations						
ϕ_C	0.008	0.01	0.02	0.03	0.04	0.1
t_{init}	2.4	3.0	1.8	1.8	1.2	1.2
Implicit simulations						
ϕ_C	0.008	0.01	0.02	0.03	0.04	0.1
t_{init}	0	0	2	0	0	0

Table IV.3: Values of the initial simulation time from which a steady state is reached for explicit and implicit simulations.

4.5 Structural properties

4.5.1 Comparison of radial distribution functions for both models at various surface fractions

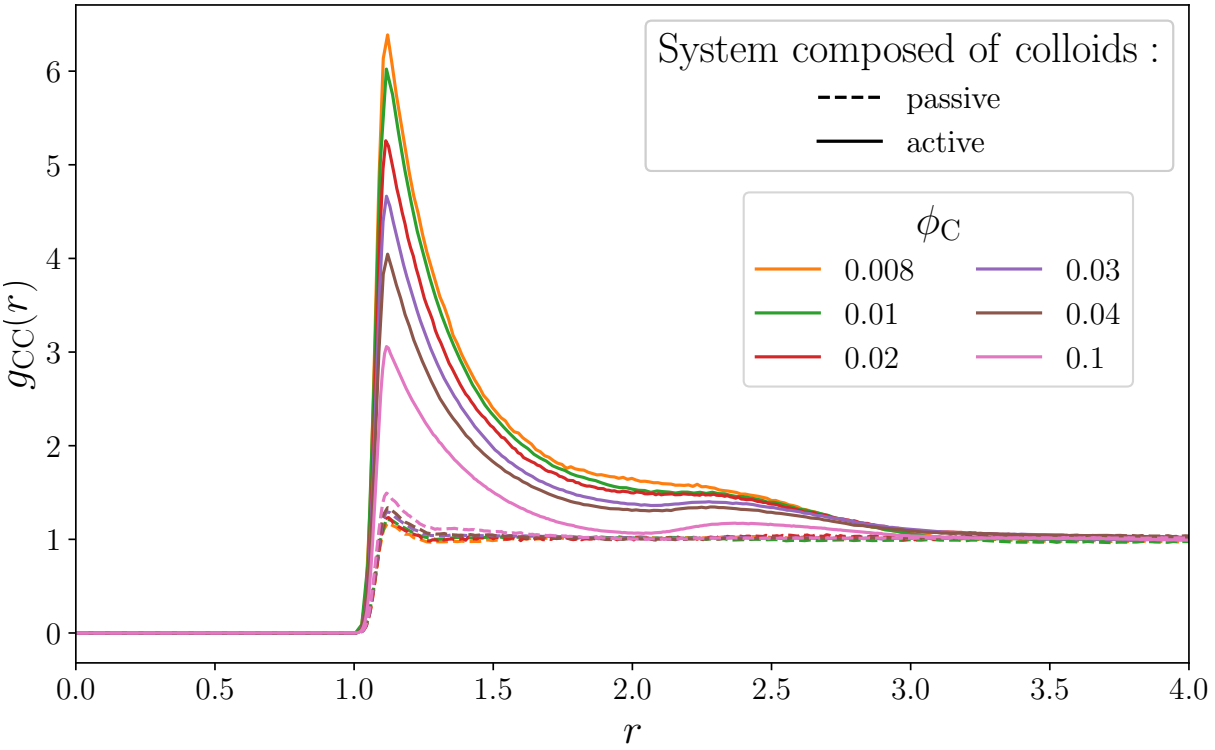

Figure 4.7: Radial distribution functions between colloids g_{CC} for various ϕ_C obtained with BD simulations. Data from systems where the colloids are active are represented by the plain lines, while systems where the colloids are passive are represented by the dashed lines.

Figure 4.7 compares the structure of passive systems and active systems for various ϕ_C, computed from explicit BD simulations. At short distances ($r = 1.12$), there is a peak, which is a signature of an effective attraction between colloids. The figure underlines that in active systems, at all packing fraction, the peak is much higher than that induced by depletion at equilibrium. The intensity of the peak is a decreasing function of the surface fraction, which is typical of a fluid of hard attractive spheres with pair additive potentials [88]. Moreover, the active systems are more structured, as a shoulder at long distances ($r \approx 2.3$) appears in all cases.

In order to interpret the role of propulsion in the appearance of density peaks, the results of explicit solute particles simulations (BD) are compared with implicit solute particles description (BD-ABP). BD-ABP simulations using a potential that takes into

account the depletion are performed. In addition to BD-ABP simulations using the depletion potential, simulations using purely repulsive potential (WCA) are also run, as a comparison. This is done in the perspective of decoupling the contribution of activity and the contribution of the depletion in the g_{CC} peaks. The results are shown on Figure 4.8, where the radial distribution functions g_{CC} between colloids are plotted for various ϕ_C and various types of simulations. A peak is also observed at short distances in the BD-ABP simulations. For all surface fractions, the peak is shifted and larger for simulations using the depletion potential because the LJ potential contains a rather wide well. The sharp increase begins at $r = 0.82$ and reaches a maximum at $r = 1.10$, whereas for the other cases, the increase starts at $r = 1.10$ and the maximum is at $r = 1.12$. This is due to the choice made for the fitting of the depletion potential, as the priority was to recover the first peak intensity. Both BD-ABP simulations fail to reproduce the behavior of the g_{CC} of explicit simulations. The intensity of the first peak is reduced, for instance, at $\phi_C = 0.02$, g_{CC} reaches a maximum intensity of 5.2 in explicit simulations, whereas both peaks of the BD-ABP simulations are around 1.6. Moreover, the shoulders do not appear. This indicates that implicit simulations yield less structured suspensions than explicit simulations. The radial distribution functions of the BD-ABP simulations using the depletion potential are similar to the one using the WCA potential. It was expected that the simulations that take into account the depletion potential, show an enhanced peak. The results demonstrate that the choice of the potential does not influence the structuration in BD-ABP simulations. In what follows, the results presented of BD-ABP simulations are obtained using the depletion potential.

4.5.2 Analysis of the structure of the suspensions in terms of clusters

In order to get a better insight on the structure that creates the correlation peak of the radial distribution function in explicit simulations, a cluster analysis was performed. Only systems where $N_C \geq 25$ are analyzed.

A simple definition of clusters following the example of [89, 72] is considered: a cluster is an assembly of two or more bounded particles. Two particles are considered as bounded when their interparticle distance r_{ij} is smaller than a cutoff distance d_c. The cutoff distance must be large enough to detect the neighbors, but not too large, otherwise all the particles would be considered to belong to the same cluster. Two values were tried: $d_c = 1.5$ and $d_c = 2$. At first, the analysis was made using both cutoff. It turned out that the cutoff $d_c = 2$ was too permissive. For a more visual explanation, two snapshots of the same configuration of the system at $\phi_C = 0.1$ are shown on Figure 4.9. The cluster cutoff

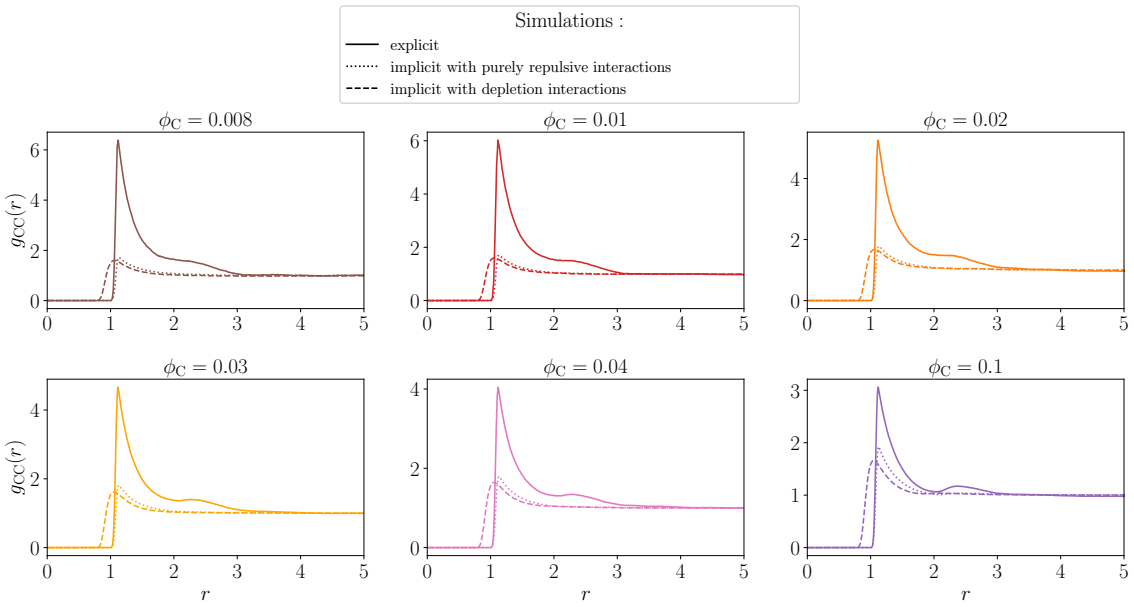

Figure 4.8: Radial distribution functions between colloids g_{CC} for various ϕ_C obtained with BD simulations (plain lines), confronted to BD-ABP simulations using depletion potential (dashed line) and WCA potential (dotted lines). Only data for $r < 5$ are shown to emphasize the most interesting part.

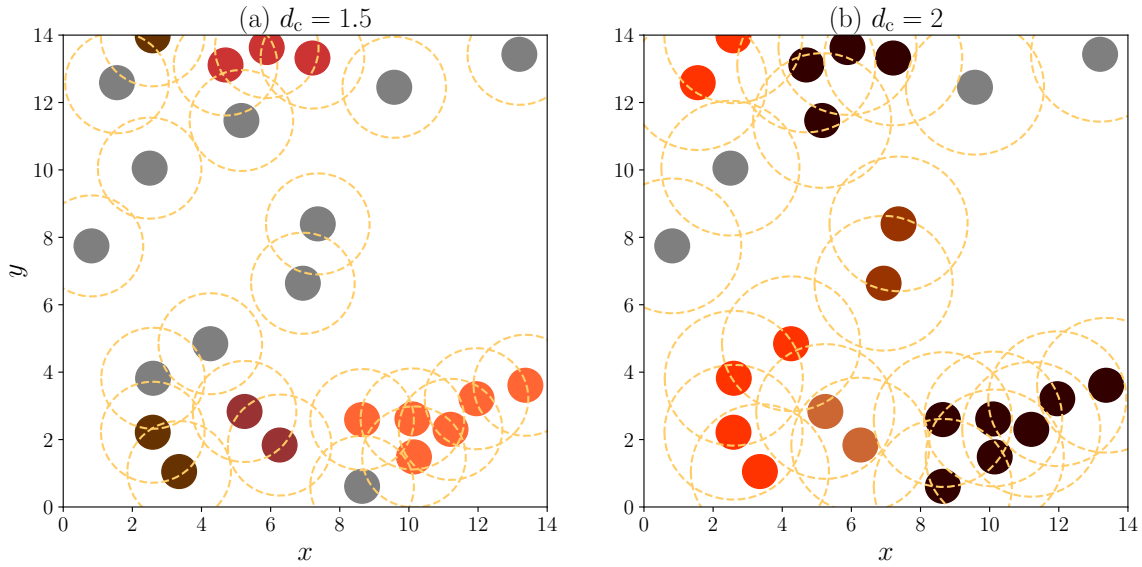

Figure 4.9: Snapshot of the system $\phi_C = 0.1$, for clarity solute particles are not represented. Colloids belonging to the same cluster are colored with the same color. The gray colloids do not belong to a cluster. The dashed orange circle represents the cluster cutoff distance d_c. (a) $d_c = 1.5$. (b) $d_c = 2$.

d_c is marked by the yellow dashed circles around each colloid, and the solute particles are not represented for clarity. The colloids which belong to the same cluster are colored evenly, whereas the isolated colloids are in gray. Fig. 4.9a shows the results of the cluster analysis for $d_c = 1.5$, and Fig. 4.9b, the results for $d_c = 2$. This example illustrates that the value $d_c = 2$ is too large.

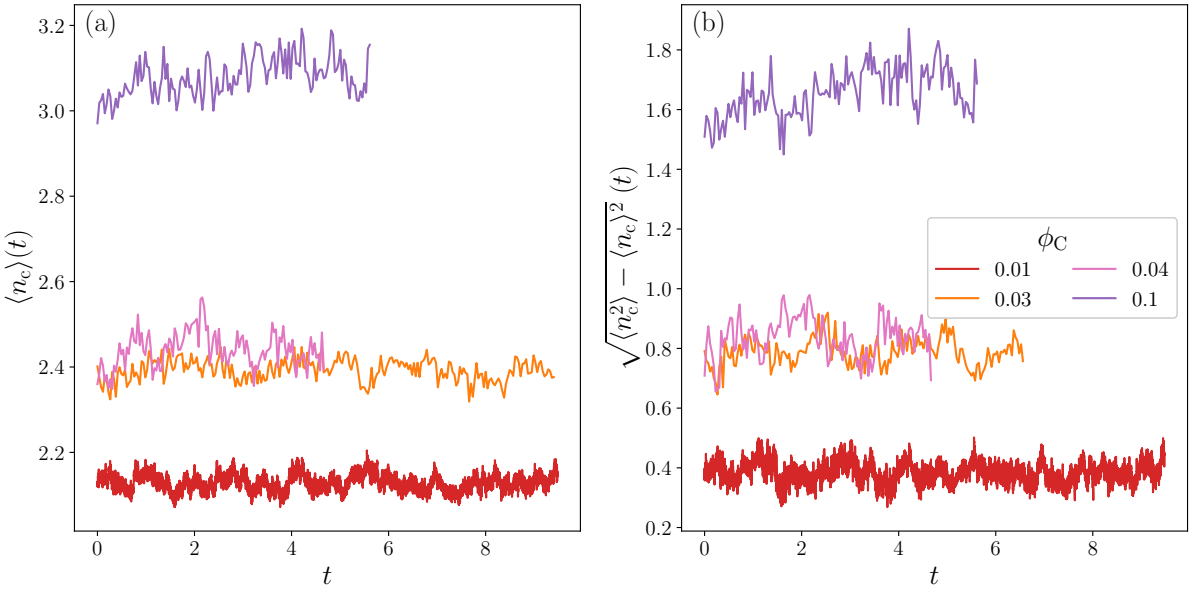

Figure 4.10: Statistic of clusters as a function of time for various ϕ_C. (a) $\langle n_c \rangle (t)$, with n_c being the number of colloids in a cluster. (b) $\sqrt{\langle n_c^2 \rangle - \langle n_c \rangle^2}\,(t)$.

The clusters are computed from the positions of colloids which are saved at a frequency large enough so that two configurations are independent (the time δt between two configurations is $\delta t = 0.04$ for BD simulations, and $\delta t = 0.1$ for BD-ABP simulations). The number of particles inside a cluster, which is denoted by n_c, is monitored during the simulation. n_c is averaged over noise realizations $\langle n_c \rangle = \langle n_c \rangle_{n_{\text{realizations}}}$. Figure 4.10 displays the evolution of the clusters size with time for various ϕ_C. Fig. 4.10a shows the mean size as a function of time $\langle nc \rangle (t)$ and Fig. 4.10b the standard deviation as a function of time $\sqrt{\langle n_c^2 \rangle - \langle n_c \rangle^2}\,(t)$. The number of particles inside the clusters is stationary, as it is expected at steady state. The quantities are then averaged over noise realizations and time from the steady state, so in what follows $\langle n_c \rangle = \langle n_c \rangle_{n_{\text{realizations}},t}$.

Figure 4.11 shows the cluster distribution, the mean size of clusters $\langle n_c \rangle$ and the standard deviation $\sqrt{\langle n_c^2 \rangle - \langle n_c \rangle^2}$ as a function ϕ_C. The active systems are compared to the passive systems, which serve as references. All the values are summed up in Appendix H. Figure 4.11a compares the cluster distribution $P(n_c)$ for various ϕ_C and simulations: explicit simulations of active systems (plain lines), explicit simulations of passive systems

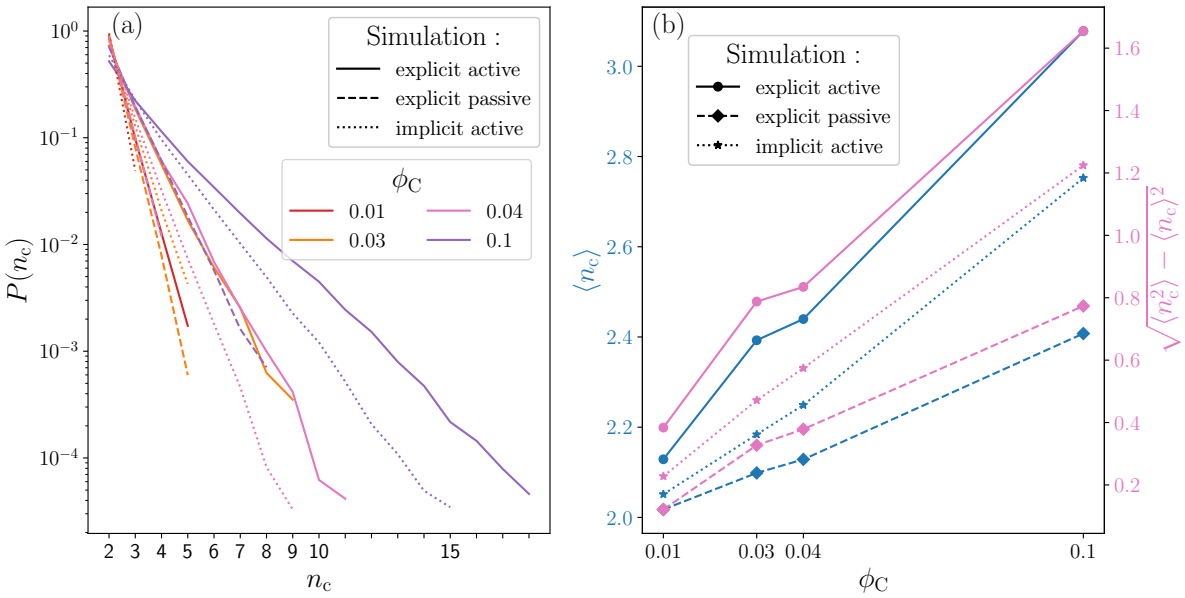

Figure 4.11: (a) Cluster sizes distribution $P(n_c)$, colors indicate the surface fraction. The plot compares results from explicit simulation of active colloids (plain lines), explicit simulation of passive colloids (dashed lines) and implicit simulations of active colloids (dotted lines). (b) Average cluster size $\langle n_c \rangle$ and standard deviation $\sqrt{\langle n_c^2 \rangle - \langle n_c \rangle^2}$ as a function of ϕ_C. Circles represent data from explicit simulations of active systems, diamonds data from explicit simulations of passive systems, and stars data from implicit simulations with activity.

(dashed lines), and implicit simulations of active systems (dotted lines). Figure 4.11b shows the mean size of clusters $\langle n_c \rangle$ and the standard deviation $\sqrt{\langle n_c^2 \rangle - \langle n_c \rangle^2}$ as a function of ϕ_C. Again, different types of simulations are compared. The clusters mean size is at all surface fractions larger in active systems than in passive systems. As it is usually observed in active systems, more clusters form than in their passive counterparts [58, 63]. The model with explicit solute description also presents this feature. The comparison between explicit and implicit simulations underline that on average, the number of particles inside a cluster $\langle n_c \rangle$ is higher for explicit solute models. A large majority of small clusters, with two or three particles, is observed. For explicit models though, the cluster size distribution differs by the presence of larger clusters. The standard deviation of the distribution is high, indicating a wider range of cluster sizes compared to the implicit solute model (ABP). These results lead to similar conclusions: the explicit solute model leads to more structuring. All in all, the explicit presence of solute particles seems to increase the size of colloidal particle aggregates, which may be the signature of an enhanced depletion.

4.6 Dynamics: influence of colloid density on activity

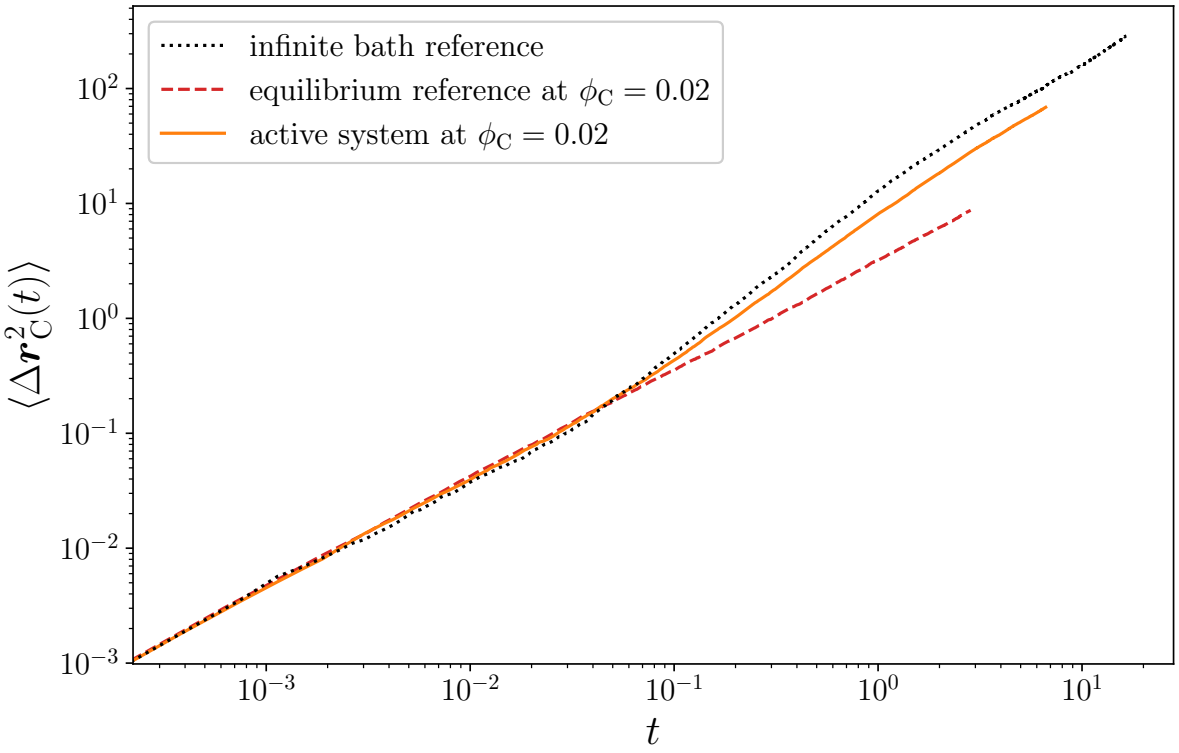

Figure 4.12: MSDs as a function of time $\langle \Delta \boldsymbol{r}_C^2(t) \rangle$ averaged over the noise realizations and over the colloids. On this plot, one active system at $\phi_C = 0.02$ (in orange, plain line) is compared to its corresponding references: at infinite dilution (in black, dotted line) and the corresponding equilibrium system (red, dashed line).

Using the same method as in Chapter 3, the dynamics of the colloids is characterized by computing the mean squared displacement $\langle \Delta \boldsymbol{r}_C^2(t) \rangle$. It is computed for each colloid and averaged over noise realizations and over the colloids, so $\langle \Delta \boldsymbol{r}_C^2(t) \rangle = \langle \Delta \boldsymbol{r}_C^2(t) \rangle_{n_{\text{realizations}}, N_C}$. For the dynamic properties, two references are considered:

- Equilibrium reference: an equilibrium situation at the same colloid density, where the colloids do not trigger a reaction.
- Infinite bath reference: a non-equilibrium situation with a single colloid (the situation for which the effective dynamic parameters of the ABP model have been determined).

Figure 4.12 represents the MSDs for a system where $\phi_C = 0.02$, as well as for the corresponding reference systems. The MSD of the equilibrium reference case is linear at all time, as expected. The value of diffusion coefficient $D_{\text{no\_reac,col}}$ is extracted from the slope using Eq (2.7). The reference value for the system at $\phi_C = 0.02$ is found to be

$D_{\text{no\_reac,col}} = 0.131$. When the reaction is triggered, the MSD displays a ballistic part at intermediate times (MSD $\propto t^2$), a signature that activity still exists in a suspension of active colloids. The enhanced diffusion on longer timescales is computed as explained in Chapter 3 and is denoted for the collective system as $D_{\text{eff,col}}$. The time t_{lin}, from which the last linear regime begins, used for each system to compute $D_{\text{eff,col}}$ is summarized in Appendix H. In this case, the effective diffusion coefficient is found to be $D_{\text{eff,col}} = 0.527$. The plot underlines that the activity is decreased compared to the case of one colloid in an infinite bath, i.e. $D_{\text{eff}} = 0.660$, and thus shows that the surface fraction ϕ_{C} has an effect on the dynamics.

The reference diffusion coefficient, $D_{\text{no\_reac,col}}$, as well as the effective diffusion coefficient $D_{\text{eff,col}}$ are computed for all the systems investigated. The effective diffusion coefficients of the BD-ABP simulations, denoted by $D_{\text{t,eff}}$, are also computed from the t_{lin}. The estimated errors on the diffusion coefficients are represented by the black error bars, which are smaller than the size of the symbols. All the values are plotted as a function of the surface fraction on Figure 4.13. These values can also be found in Appendix H. First, the systems investigated from explicit simulations present activity for all the surface fractions investigated, as $D_{\text{eff,col}} > D_{\text{no\_reac,col}}$, even for the larger surface fraction $\phi_{\text{C}} = 0.1$. Yet, activity progressively decreases with the surface fraction. This may originate from several factors. First, the overall increase of the density usually hinders diffusion in passive colloidal systems, and the observed effect might be a similar consequence of the reduction of space availability around moving active colloids. Secondly, in addition to the effect of the average density, the colloids may also be part of local clusters. In the latter case, the propelling velocity may point towards the center of the cluster, hence strongly reducing the propulsion. Last but not least, the increase of colloid density also leads to the superposition of the regions around colloids where the chemical reaction takes place. As a consequence, it may become more likely that the structure of the solute cloud around the colloid become less asymmetric as colloids get closer to each other. Therefore, the density fluctuations at the origin of activity may change in nature, and lead to less important pressure gradients at the surface of the colloids. The BD-ABP simulations also present enhanced diffusion, and the dynamics is characterized by an effective diffusion coefficient higher than for BD simulations. However, interestingly, the effect of the surface fraction ϕ_{C} is less dramatic in implicit simulations. In contrast to $D_{\text{eff,col}}$, $D_{\text{t,eff}}$ is less impacted by the surface fraction. This result stresses the limitation of implicit simulations that are widely used in the active matter community. It is interesting to have a model that takes into account the effect of the crowding induced by active colloids and their droplets in order to analyze biological systems, especially cells where crowding effects are important.

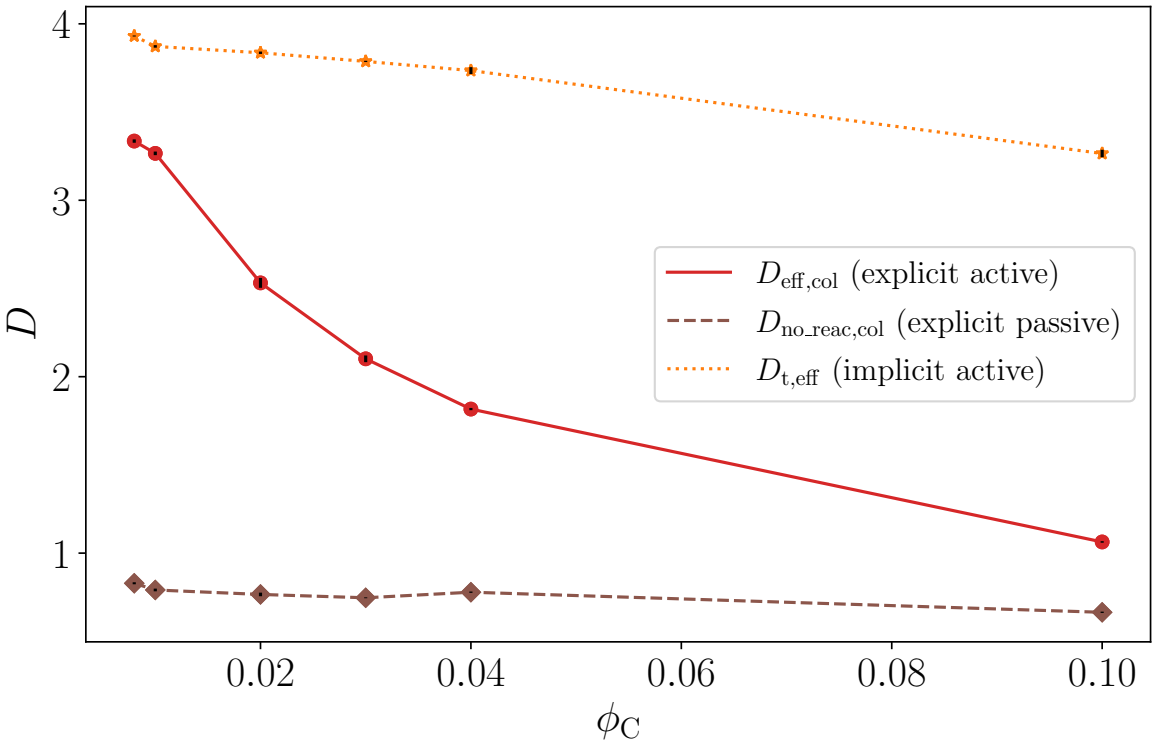

Figure 4.13: Long-time effective diffusion coefficient as a function of ϕ_C. The diffusion coefficients of the equilibrium references from explicit simulations $D_{no\_reac,col}$ are represented by the diamonds and are linked by the brown dashed line. The effective diffusion coefficients from explicit simulations $D_{eff,col}$ are represented by the circles and are linked by the red plain line. The effective diffusion coefficients from implicit simulations $D_{t,eff}$ are represented by the stars and are linked by the orange dotted line. The estimated errors on the diffusion coefficients are represented by the black error bars, which are smaller than the size of the symbols.

4.7 Influence of the reaction area size

Figure 4.14 shows the radial distribution functions g_{CC} at $\phi_C = 0.1$, $r_{cut} = 1.3$ (red) and $r_{cut} = 1.5$ (brown). Fig. 4.14a presents the results from BD simulations. The influence of r_{cut} is limited: the intensity of the peak is unaffected, and a slight difference is observed on the shoulder, which is wider for $r_{cut} = 1.5$. Fig. 4.14b presents the results from BD-ABP simulations. On the contrary, there is a significant change of the behavior of g_{CC}. The intensity of the peak at short distances is stronger at $r_{cut} = 1.5$ than $r_{cut} = 1.3$. Moreover, a shoulder is observed at $r_{cut} = 1.5$ at a distance $r = 2.1$ which is not observed at $r_{cut} = 1.3$.

Figure 4.15 shows the distribution of the cluster size n_c for $r_{cut} = 1.3$ (red) and $r_{cut} = 1.5$ (brown). Results from explicit simulation are shown by the plain lines and are confronted to the implicit simulations results, represented by the dotted lines. The

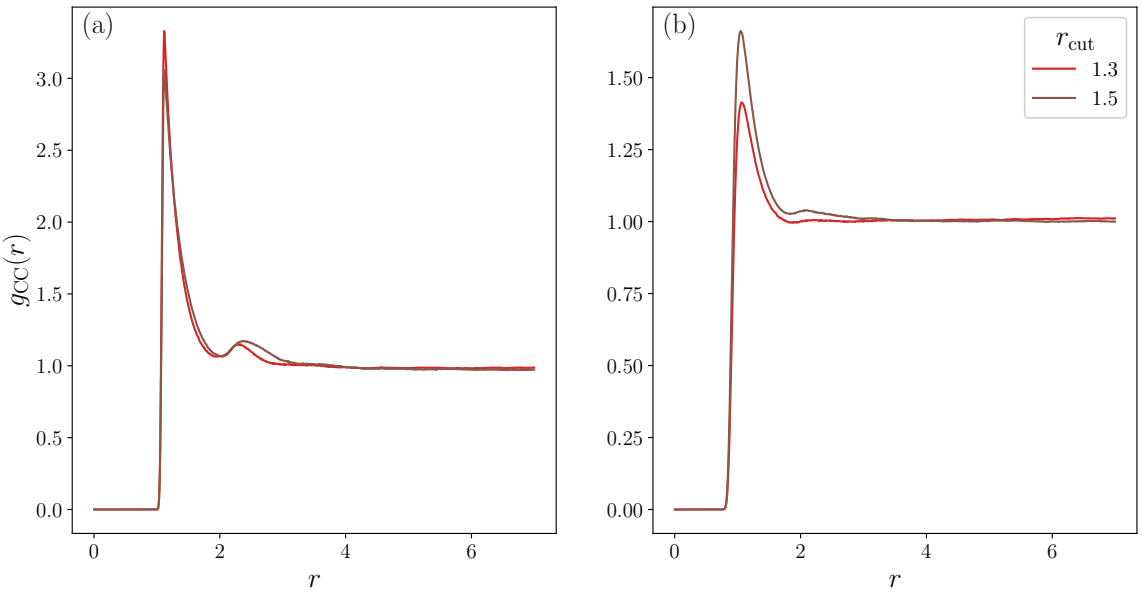

Figure 4.14: Radial distribution functions g_{CC} at $\phi_C = 0.1$, $r_{cut} = 1.3$ (red) and $r_{cut} = 1.5$ (brown). (a) Explicit simulation results. (b) Implicit simulation results.

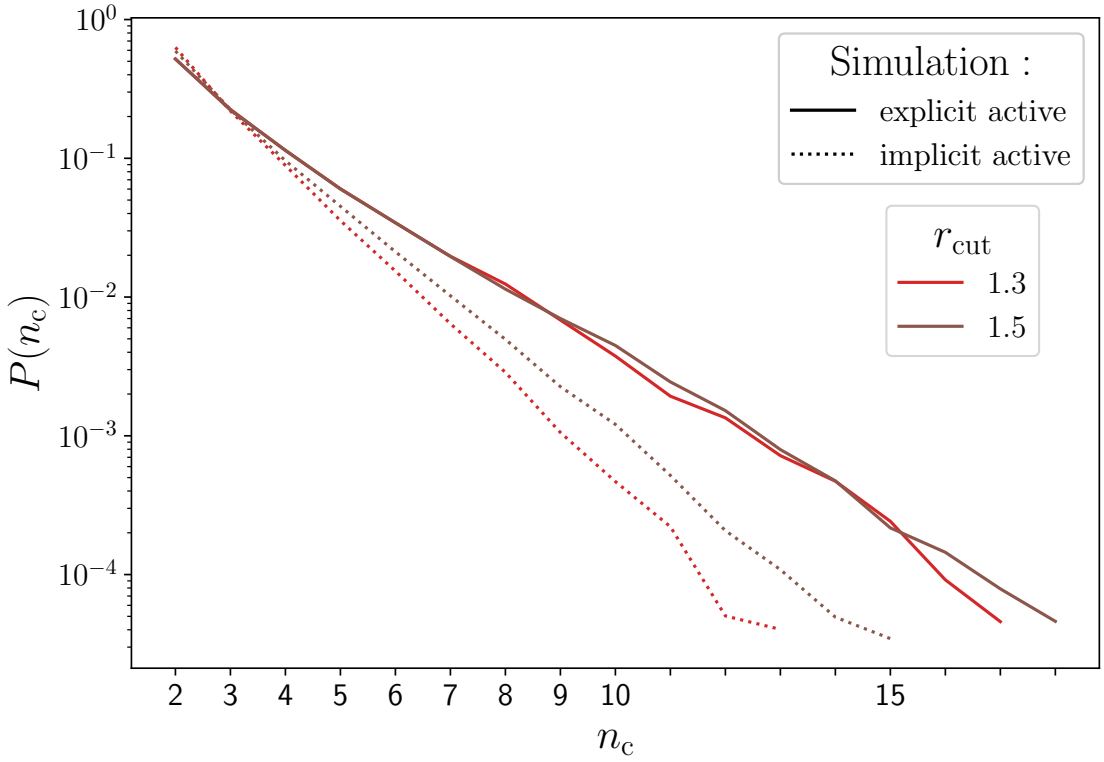

Figure 4.15: Distribution of the cluster sizes $P(n_c)$ at $\phi_C = 0.1$, $r_{cut} = 1.3$ (red) and $r_{cut} = 1.5$ (brown). Comparison between explicit simulation results (plain lines) and implicit simulation results (dotted lines).

cluster distribution is the same regarding the reaction area radius for explicit simulations. The mean size is $\langle n_c \rangle = 3.07$ for $r_{cut} = 1.3$ and $\langle n_c \rangle = 3.08$ at $r_{cut} = 1.5$. In contrast, for implicit simulations, the clusters are smaller in BD-ABP simulations. The mean size is $\langle n_c \rangle = 2.63$ for $r_{cut} = 1.3$ and $\langle n_c \rangle = 2.75$ at $r_{cut} = 1.5$. Indeed, it has been shown that the clusters size is a increasing function of the propulsion velocity v_0. Here, $v_0 = 4.5$ at $r_{cut} = 1.5$ which is higher than the one at $r_{cut} = 1.3$, $v_0 = 3.6$. The results displayed on this figure are consistent with the radial distribution functions.

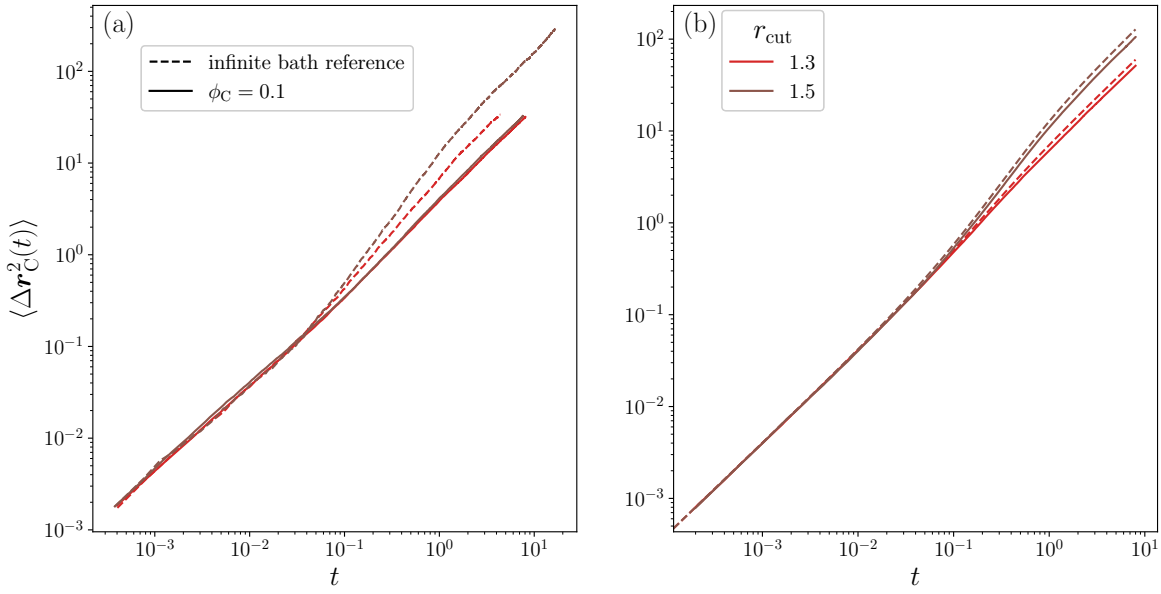

Figure 4.16: Mean squared displacements as a function of time $\langle \Delta \boldsymbol{r}_C^2(t) \rangle$ at $\phi_C = 0.1$, $r_{cut} = 1.3$ (red) and $r_{cut} = 1.5$ (brown). (a) Explicit simulation results. (b) Implicit simulation results.

Figure 4.16 shows the MSDs $\langle \Delta \boldsymbol{r}_C^2(t) \rangle$ at $\phi_C = 0.1$, $r_{cut} = 1.3$ (red) and $r_{cut} = 1.5$ (brown). Fig. 4.16a presents the results from BD simulations, and Fig. 4.16b results from BD-ABP simulations. For BD simulations, at this surface fraction, similarly to $r_{cut} = 1.5$, the activity in the system at $r_{cut} = 1.3$ is reduced. There is a discrepancy at infinite dilution, i.e. when the colloid is alone, that disappear when studying collective effects. At $\phi_C = 0.1$, the measured effective diffusion coefficients are $D_{eff,col} = 0.994$ and $D_{eff,col} = 1.063$ at $r_{cut} = 1.3$ and $r_{cut} = 1.5$, respectively. Conversely, in BD-ABP simulations, there is a difference in both cases. The self-propulsion is slightly slowed down due to the effect of the high surface fraction. However, as it has been discussed, activity in implicit simulations is not drastically affected by the increase of the surface fraction. Since the propulsion input in the ABP model is higher for $r_{cut} = 1.5$ than $r_{cut} = 1.3$, at $\phi_C = 0.1$ the difference still holds. All the values can be found in Appendix H.

CHAPTER 5

Preliminary work on a mixture of colloids

Contents

Summary

This chapter presents the preliminary results of an extension of the model containing a mixture of colloids. There are two types of colloids in the system: C_{AB} colloids, around which the reaction $A + C \rightarrow B + C$ is more probable, and C_{BA} colloids, around which the reverse reaction $B + C \rightarrow A + C$ is more probable. Only one colloid of type C_{AB} is modeled, and N_{BA}, the number of colloids of type C_{BA}, varies. The colloid of type C_{AB} is expected to be active. The objective is to investigate the effect of N_{BA} on the active colloid dynamics. The preliminary work exposed in this chapter indicates that an optimal value for N_{BA} exists. Indeed, for low values of N_{BA}, the B species is predominant, droplets form but detached from the colloid surface. The density fluctuations are not confined to the vicinity of the colloid, which suppresses the propulsion. Conversely, for large value of N_{BA}, the crowding induced by the colloids hinders the active colloid motion, reducing its activity.

5.1 Introduction

In this chapter, an extension of the model of active colloids is presented, that is inspired by biological systems, in particular intracellular life. In a cell, many particles are active: one component may self-propel by catalyzing a reaction, while another takes its energy for self-propulsion by catalyzing the reverse reaction. This ensues a continuous activity. In the model studied in previous chapters, all the colloids were of the same nature, catalyzing the reaction $A + C \rightarrow B + C$, which implies that B is more stable than A. The reverse reaction that occurred in the bulk was implemented to mimic the diffusion of the product particles in an infinite bath of reactants. This could also describe the situation inside a cell, where the reverse reaction would be catalyzed from another component. This model has been well characterized in this PhD work. Here, we propose to extend this model to a more complex situation, which is also closer to reality. The properties of a mixture of two types of colloids that catalyze inverse chemical reactions is investigated. One species of colloids, denoted by C_{AB} catalyzes the reaction $A+C \rightarrow B+C$. In a real out-of-equilibrium system, a source of energy, such as the hydrolysis of ATP, coupled to a catalyst maintains the species B predominant. Far from the C_{AB} catalysts, which are coupled to the energy source, no energy is consumed and the A species may be predominant. To model this situation, another kind of catalyst is introduced. These colloids, denoted by C_{BA}, are independent of the energy source. For simplicity, as the reaction shall effectively lead to the predominance of A species close to C_{BA} catalysts, this type of colloids only catalyzes the reverse reaction $B+C \rightarrow A+C$. Only the C_{AB} species is expected to be active, as the other type will be surrounded only by purely repulsive solute particles, by construction. Preliminary results on this system are presented in this chapter. The results obtained can be intuitively understood and analyzed based on the knowledge of the mechanism. However, the study of this case should be continued after my PhD to assert the hypothesis stated in this section. The work presented in this section gather data from simulations run by both myself and Sophie Devos, a second year intern who spent one month in the laboratory (June 22) under the supervision of Vincent Dahirel. The chapter is organized as follows: the model is described in Section 5.2, a steady state is defined in Section 5.3 and the dynamics of the C_{AB} colloid is investigated in Section 5.4. Finally, conclusion and perspectives on this preliminary work are presented in Section 5.5.

5.2 Description of the model

Figure 5.1 illustrates where the different reactions occur in the system. There are two species of colloids: the colloid of type C_{AB} which catalyzes the reaction $A + C \rightarrow$

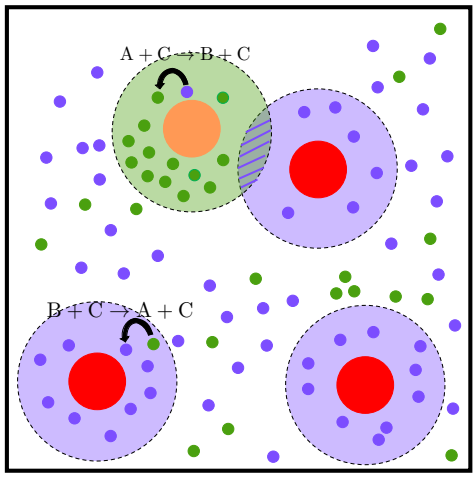

Figure 5.1: Illustration of where the different reactions occur. The colloid of type C_{AB} is represented in orange and catalyzes the reaction A+C → B+C in the green reaction area. The colloids of type C_{BA} are represented in red and catalyze the reaction B + C → A + C in the purple reaction areas. When two reaction areas overlap, the reaction B+C → A+C is done.

B+C, represented in orange on the snapshot, and the colloids of type C_{BA} which catalyze B + C → A + B, represented in red. Both reactions occur in a reaction area delimited by r_{cut} centered around a colloid. $r_{cut} = 7.5$ is fixed and is the same for both reactions. Both reaction rates are equal and remain unchanged: $\tau_{AB} = \tau_{BA} = 0.1$. In the situation where two colloids of different type are close enough so that their reaction area overlap, the reaction B+C → A+C has the priority. This choice was made arbitrary and the influence of the prior reaction can be investigated in a future work. There are $N_C = N_{AB} + N_{BA}$ colloids. The number of solute particles N is fixed in order to have the solute density $\rho = 0.1$. $N_{AB} = 1$ remains constant, and the number of C_{BA} colloids varies. The following values were investigated: $N_{BA} = 1$, $N_{BA} = 9$, $N_{BA} = 14$ and $N_{BA} = 24$. The size of the simulation box remains constant ($l_{box} = 70$), consequently the surface fraction of colloids ϕ_C varies. Table V.1 summarizes the systems investigated and the corresponding surface fraction. The attraction intensity of the LJ potential between B solute particles is fixed to $\varepsilon = 3$ and the time step of simulations to $\Delta t = 0.0006$.

The goal is to have a glimpse of the behavior of the colloid C_{AB}, which is expected to be active. Indeed, as seen before, the propulsion relies on density fluctuations that must be confined in its vicinity. However, in Chapter 3, it has been shown that the location of the reverse reaction dramatically affects the activity. The purpose here is to investigate how the behavior of one active colloid is influenced by the passive colloids.

5.3 Understanding of the steady state

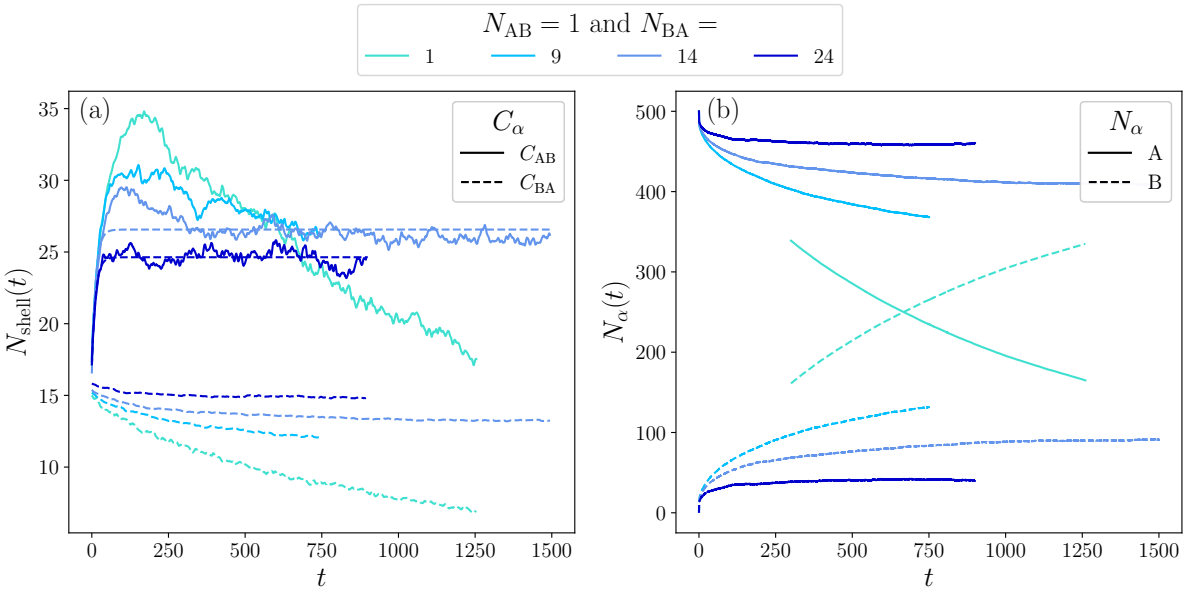

Figure 5.2: (a) Number of solute particles (A or B) inside the reaction area, averaged over noise realizations for C_{AB} colloids and over noise realizations and colloids for C_{BA} colloids, as a function of time $N_{shell}(t)$. Dotted lines represent the exponential fits using Eq. (3.2) when applicable. (b) Number of solute particles of type α as a function of time. Plain lines represent $N_A(t)$, dashed line $N_B(t)$. In both plots, $N_{AB} = 1$ and N_{BA} varies.

The steady state in systems with one colloid is reached when the flux of A particles going inside the reaction area and being transformed into B particles is equal to the flux of B particles leaving the reaction area and being transformed into A particles. It leads to a steady state value of the number of particles inside the reaction area, $N_{shell,\infty}$. Here, the situation is different, as the reverse reaction depends on the number of colloids of type C_{BA} and is coupled to their dynamics. In order to understand how the system evolves towards a steady state, the number of solute particles (A or B) inside the reaction area N_{shell}, as well as the number of particles of type A and of type B inside the system, N_A and N_B, respectively, are monitored. These quantities are averaged over noise realizations for the C_{AB} colloid, and over noise realizations and the colloids for the C_{BA} colloids. The kinetics of the filling of the reaction area is represented on Figure 5.2a. The data show the number of particles inside the reaction area around the colloid C_{AB} (plain lines) and around the colloids C_{BA} (dashed lines). According to the catalyzed reaction, the reaction area will be filled with A particles for the C_{BA} colloids, or with B particles for the C_{AB} colloids. The evolution of the number of solute particles of type A, N_A (plain lines), and B, N_B (dashed lines), is shown on Figure 5.2b for the various systems. Note that for

$N_{\mathrm{BA}} = 1$, the data are only available for $t > 300$. On both plots, the colors indicate which system is considered, which corresponds to the number of colloids of type $\mathrm{C_{BA}}$ it contains. Snapshot of the systems were also analyzed in order to interpret the results. Figure 5.3 displays snapshots of the system for different values of N_{BA}. The active colloid is represented in orange and the passive colloids are in red. Solute particles A are in purple and B are in green. The figure only displays one noise realization, but it is chosen in order to represent the typical situation that is found on a majority of snapshots. Fig. 5.2 and Fig. 5.1, point out a similar behavior of the systems $N_{\mathrm{BA}} = 9, 14, 21$, whereas the case $N_{\mathrm{BA}} = 1$ is different.

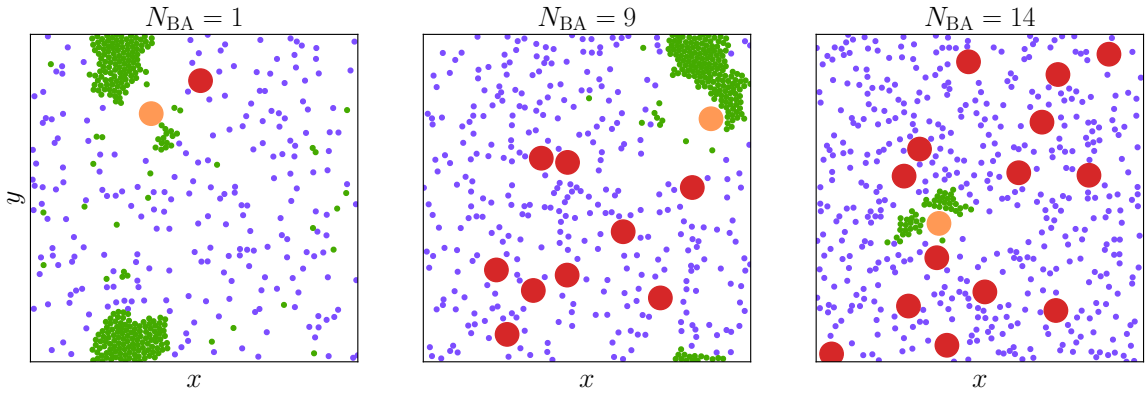

Figure 5.3: Snaphots of the system for $N_{\mathrm{AB}} = 1$ in orange, and $N_{\mathrm{BA}} = 1, 9, 14$ in red.

First, the discussion concerns the cases $N_{\mathrm{BA}} = 9, 14, 24$. Fig 5.2a shows that N_{shell} is almost a constant for the passive colloids (dashed lines). This is expected, as the colloids $\mathrm{C_{BA}}$ is only surrounded by repulsive solute particles. The kinetics of the filling of the reaction area of the active colloid (plain lines), is similar to what was obtained with one active colloid. It increases due to the attractive interactions between the B particles, before reaching a steady state. All the systems start with $N_{\mathrm{A}} = 500$. Fig 5.2b shows that N_{A} decays as a function of time whereas N_{B} increases, until both quantities stabilize. Indeed, B particles are created in the reaction area of the colloid $\mathrm{C_{AB}}$, the $\mathrm{C_{BA}}$ colloids maintain the systems out of equilibrium by transforming the B particles into A. The steady state is reached when there is a balance between the $\mathrm{A} \rightarrow \mathrm{B}$ and $\mathrm{B} \rightarrow \mathrm{A}$ transformations. The plateaux observed for the systems $N_{\mathrm{BA}} = 24$ and $N_{\mathrm{BA}} = 14$ on both plots indicate that the simulation has already converged towards steady state. These curves can be fitted by an exponential using Eq. (3.2), from which the steady state time τ_N is extracted. The corresponding fits are indicated by the dotted lines on Fig. 5.2.

These results suggest that the system with $N_{\mathrm{BA}} = 9$ is about to also reach a plateau, but simulation was not run long enough. The time needed to reach steady state is larger for systems with less $\mathrm{C_{BA}}$ colloids. Indeed, τ_N is linked to the time needed for all the passive colloids to explore the space, which is shorter when the surface fraction increases. For these cases, snapshots reveal that the B particles are confined near the colloid, as there are enough passive colloids to perform the reverse reaction homogeneously in the bulk.

The case $N_{\mathrm{BA}} = 1$ is particular. The steady state is far from being reached, as on both plots the curves have not yet converged. Fig. 5.2a shows that the number of B particles inside the reaction area is a decreasing function of time, while Fig. 5.2b shows that there is an increasing number of B particles inside the system. This indicates that a LJ droplet grows until detaching and displacing inside the system, as shown on the snapshot on Figure 5.3.

5.4 A glimpse at the dynamics of the active colloid

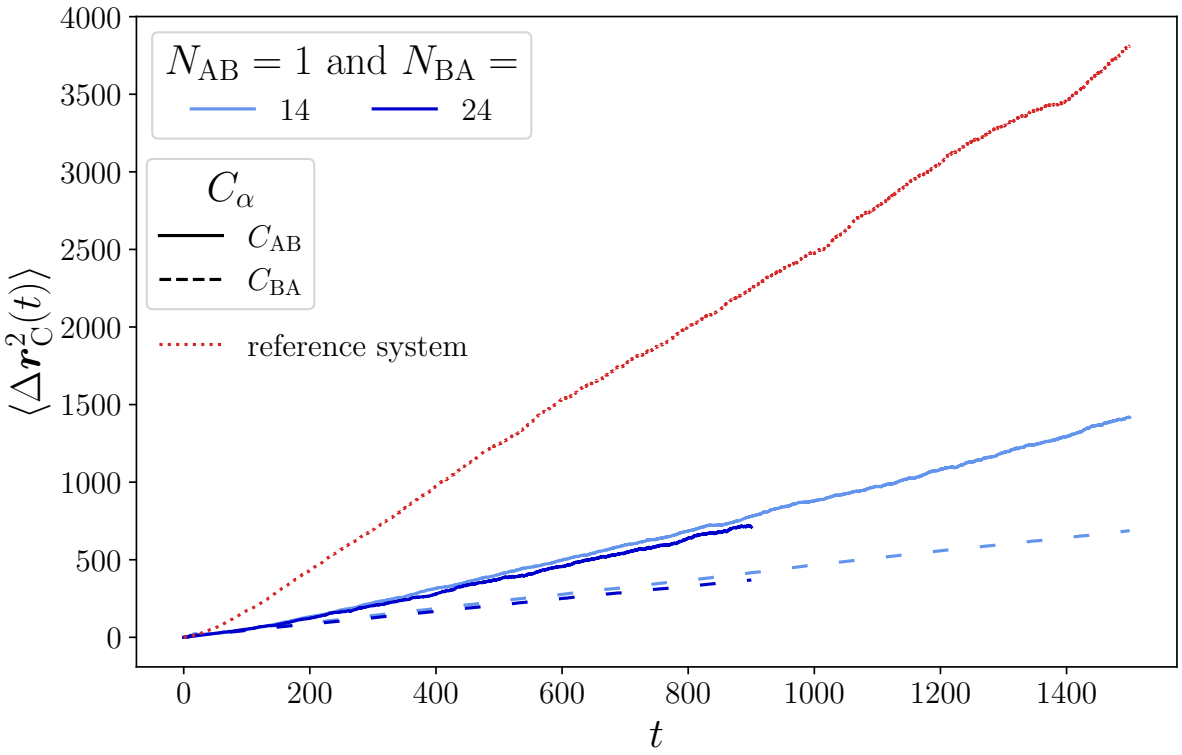

Figure 5.4: Mean squared displacements as a function of time, $\langle \Delta \boldsymbol{r}_{\mathrm{C}}^2(t) \rangle$, from the steady state. The time is rescaled so that $t_{\mathrm{init}} = 3\tau_N$. Results are shown for $N_{\mathrm{BA}} = 14$, and $N_{\mathrm{BA}} = 24$.

First, the dynamics of the $\mathrm{C_{AB}}$ colloid is investigated for systems where a steady state

has been defined, i.e. for $N_{\mathrm{BA}} = 14$ and $N_{\mathrm{BA}} = 24$. The MSD, $\langle \Delta \boldsymbol{r}_{\mathrm{C}}^2(t) \rangle$, is computed, where $\langle . \rangle$ denotes the average over noise realizations for the $\mathrm{C_{AB}}$ colloid, and over noise realizations and the colloids for the $\mathrm{C_{BA}}$ colloids. For these cases, the time is rescaled so that the initial simulation time t_{init} is $3\tau_N$, where τ_N is the time needed by the system to reach steady state. For these cases, values of t_{init} are reported in Table V.1. Figure 5.4 shows the MSDs of these systems for both types of colloids, $\mathrm{C_{AB}}$ (plain lines) and $\mathrm{C_{BA}}$ (dashed lines). The MSD of an active colloid alone at the same set of parameters ($\rho = 0.1$, $\varepsilon = 3$ and $r_{\mathrm{cut}} = 7.5$) is displayed for comparison (dotted line).

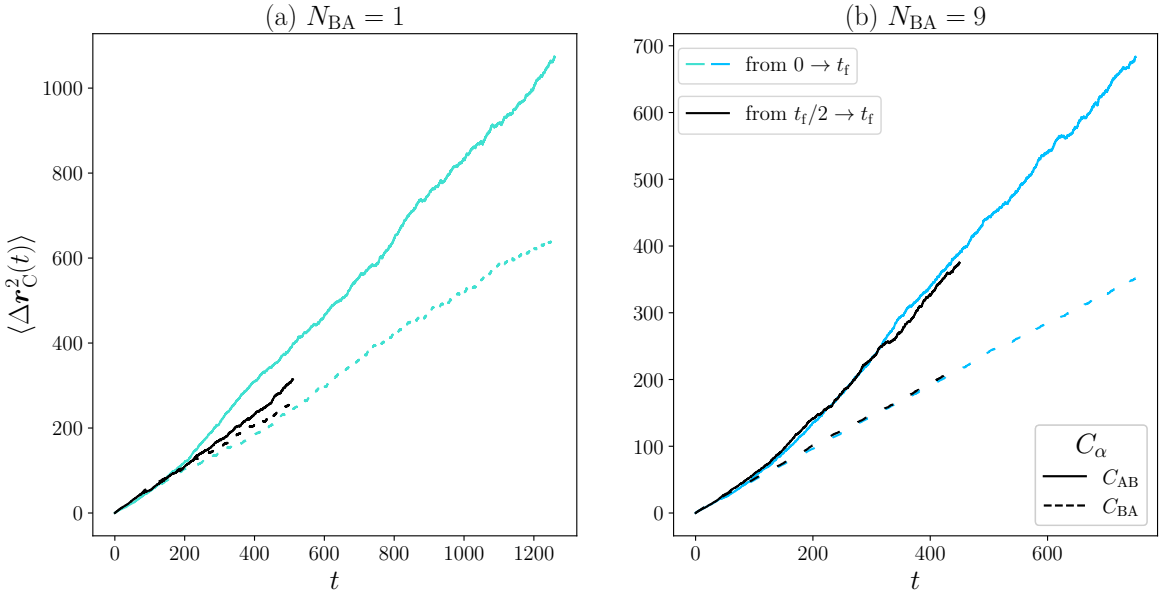

Figure 5.5: Mean squared displacements as a function of time, $\langle \Delta \boldsymbol{r}_{\mathrm{C}}^2(t) \rangle$. The MSD is either computed from the beginning of the simulation to the final time t_{f} (colored lines), or from a threshold time $t_{\mathrm{f}/2}$ to t_{f} (black lines). The plain lines represent the MSD of the active colloid, the dashed lines of the passive colloids. Results are shown for: (a) $N_{\mathrm{BA}} = 1$, (b) $N_{\mathrm{BA}} = 9$, and (c) $N_{\mathrm{BA}} = 14$.

Second, the cases $N_{\mathrm{BA}} = 9$ and $N_{\mathrm{BA}} = 1$ are discussed. A steady state has not been clearly defined for these systems. Nevertheless, the mean squared displacements are computed as a function of time for the various systems in order to see briefly if activity subsists and how it is influenced by the number of $\mathrm{C_{BA}}$ colloids. The MSDs are computed both for the entire simulation time available, from $t = 0$ to $t = t_{\mathrm{f}}$ (colored lines on Fig. 5.6), and from a threshold time, which has been chosen arbitrarily as $t_{\mathrm{f}}/2$, to the end t_{f} (black lines on Fig. 5.6). The plain lines represent the MSDs of active colloids, the dashed lines of passive colloids. The figure shows results for the system $N_{\mathrm{BA}} = 1$ (Fig. 5.5a), and $N_{\mathrm{BA}} = 9$ (Fig. 5.5b). The figure emphasizes that for the system at $N_{\mathrm{BA}} = 1$, the behavior of the colloid evolves in time. Thus, it confirms that the steady state is not reached for

$N_{\mathrm{BA}} = 1$, as for this case, the MSD computed at all times is very different from the MSD computed at the end of the simulation.

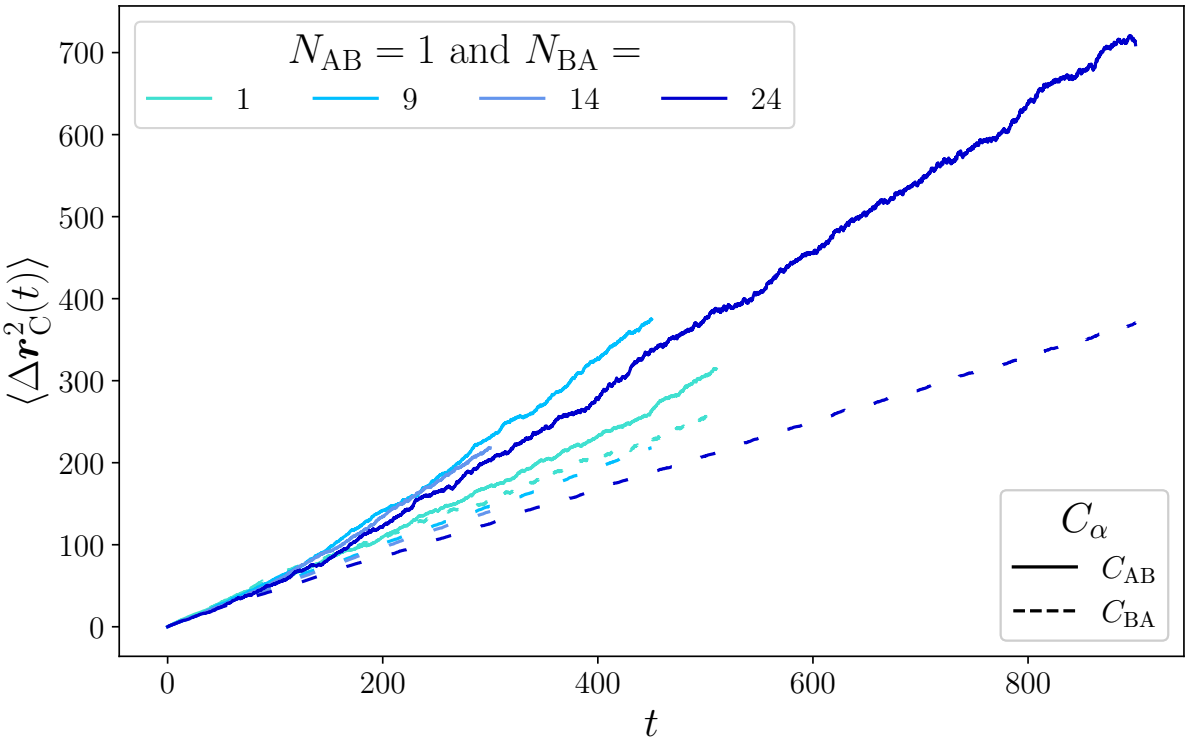

Figure 5.6: Mean squared displacements as a function of time, $\langle \Delta \boldsymbol{r}_{\mathrm{C}}^2(t) \rangle$, of various systems. The MSD is computed from a threshold time $t_{\mathrm{f}}/2$ to t_{f}. The plain lines represent the MSD of the active colloid, the dashed lines of the passive colloids.

Figure 5.6 represents the MSDs of the active colloid (plain lines) and of the passive colloids (dashed lines) computed from the threshold time $t_{\mathrm{f}}/2$. The results cannot be rigorously analyzed, as the steady state is not reached for all the systems presented in this section. However, several interesting features can be commented on:

- The MSDs of passive colloids are linear in time, as it is expected, characterized by a diffusion coefficient D_{BA}. Table V.1 sums up the values found by fitting the MSDs using Eq. (2.7). Table V.1 also presents the diffusion coefficient of the corresponding passive systems, $D_{\mathrm{no\_reac,col}}$, if available. The latter are composed of the same number of colloids $N_{\mathrm{C}} = N_{\mathrm{AB}} + N_{\mathrm{BA}}$ at the same surface fraction ϕ_{C}, where the colloids do not trigger a reaction. The diffusion coefficients of the passive systems, $D_{\mathrm{no\_reac,col}}$, are computed as a reference. The values are similar, which confirms the passive nature of the $\mathrm{C_{BA}}$ colloids.

- The $\mathrm{C_{AB}}$ colloid in the system $N_{\mathrm{BA}} = 1$ has a transient active behavior, but is passive on longer timescales (see Fig. 5.5a). The transient behavior corresponds

to the filling of the reaction area, characterized by the first increasing regime of $N_{\text{shell}}(t)$. During this time window, conditions are favorable for propulsion. Then, when the droplet detaches, the colloid activity reduces.

- Fig. 5.6 seems to indicate a non-monotonic behavior of the activity with N_{BA}. Effective diffusion coefficients of the active colloids D_{AB} are computed on the last $100t$ of each MSD. These values are purely indicative as the MSDs are not linear in time. Nevertheless, the effective diffusion coefficient of $N_{\text{BA}} = 1$ and $N_{\text{BA}} = 24$ are smaller than for the systems $N_{\text{BA}} = 9$ and $N_{\text{BA}} = 14$. For $N_{\text{BA}} = 1$, D_{AB} is expected to decrease as activity disappear on longer timescales. For $N_{\text{BA}} = 24$, D_{AB} is expected to be unchanged, as the steady state seems to be reached. However, $N_{\text{BA}} = 9$ and $N_{\text{BA}} = 14$ are still in a transient ballistic behavior, thus the effective diffusion coefficients are expected to be increased. Therefore, the non-monotonic behavior is expected to be robust. The interpretation is not clear at this stage of the study. In particular, ϕ_{C} is not constant and can maybe explain the decrease of the activity at $N_{\text{BA}} = 24$.

N_{BA}	1	9	14	24
ϕ_{C}	0.008	0.04	0.06	0.1
t_{init}	–	–	108	108
D_{AB}	0.149	0.204	0.177	0.2
D_{BA}	0.130	0.122	0.120	0.104
$D_{\text{no\_reac,col}}$	0.127	0.120	–	0.105

Table V.1: Summary of the computed quantities in this chapter for the studied systems. Values are indicated if available.

5.5 Conclusion

To conclude, in this chapter, the reverse reaction process is modified, as the reverse reaction is restricted to the vicinity of C_{BA} colloids. This preliminary work indicates an optimal value for the number of colloids performing the reverse reaction. This suggests that the surface fraction is expected to play an important role on the obtained results. Indeed, for low surface fractions, the distances between colloids are larger and the space available for B solute particles to exist is wider. This is exemplified by the situation studied in this chapter at $N_{\text{BA}} = 1$, which corresponds to a surface fraction $\phi_{\text{C}} = 0.008$. The number of B particles measured in this case is about $N_{\text{B}} = 300$ and is still increasing. This represents the 60 percent of the total of solute particles, whereas at $N_{\text{BA}} = 24$

($\phi_C = 0.1$) B particles represent only 5 percent of the total solute particles. From this ensues the formation of large droplets that eventually detach from the surface of the C_{AB} colloid. This affects the propulsion of the colloid since the density fluctuations are not confined in its vicinity, thus the activity is reduced. Interestingly, although the way the reverse reaction is modified is different from in Section 3.6, the emerging behaviors are very similar. In the end, it leads to the same situation: B particles are free to move outside the reaction area, they agglomerate in a droplet that goes beyond the reaction area. For critical values of the parameters involved for each situation: low ϕ_C, high τ_{BA}, or high $r_{reverse\_cut}$, it leads to a drastic reduction of activity.

The results from this chapter are obtained on the basis of the knowledge of the mechanism and are expected to be confirmed by a more extensive study. The mixture of C_{AB} and C_{BA} colloids paves the way to new possibilities. As an example of future possible studies, Sophie Devos, the second year intern, has started to investigate other combinations by varying N_{AB}. She has also started to look deeper into the importance of the prior reaction when two reaction areas overlap.

Conclusion

The first objective of this PhD work was to build a minimal model for an isotropic active colloid, whose activity would emerge from interactions within the bath of solute particles. Inspired by the literature on Janus particles in a binary mixture that demixes [15], the simplest route was considered: density fluctuations would appear from a phase separation in the vicinity of the colloid. To do so, the constructed model describes explicitly the interactions between the solute particles. The colloid is initially immersed in a bath of purely repulsive particles. It catalyzes isotropically a reaction around itself, which changes the nature of the interactions between solute particles by adding attractions. The solute particles near the colloid are then forming a Lennard-Jones fluid. Several key parameters are identified and varied, the solute density ρ, the attraction intensity ε and the reaction area size r_{cut}. For suitable parameters, the LJ fluid phase separates and the system exhibits activity as required.

Secondly, the mechanism of propulsion of this model has been well characterized in this manuscript using a variety of parameters. It has been shown that the propulsion relies on fluctuations of the solute density that must be localized in the vicinity of the colloid. In the studied model, the density fluctuations arise due to the formation of droplets inside the reaction area. The orientation of the droplet is characterized by a polarization vector. A characteristic persistence time can be extracted from the autocorrelation function of the polarization vector, which stresses the link between the propulsion and the droplets. The filling fraction of the reaction area has been found to be a relevant indicator for the prediction of activity. The droplets must fulfill some conditions in order to trigger self-propulsion, which are characterized by intermediate filling fractions of the reaction area. The conditions have been fully understood and are the following:

- The droplet must stay in contact with the colloid. By varying the place of the

reverse reaction in Section 3.6 of Chap. 3 or in the preliminary work presented in Chap. 5, it has been demonstrated that if the droplets are no longer confined in the reaction area, activity decreases or disappears. In such situations, the droplets grow and eventually detach from the colloid, so that the colloid is not self-propelled. The same behavior is expected when increasing the reverse reaction rate τ_{BA} as discussed in Sect. 3.6 in Chapter 3. All of these situations are characterized by a low filling fraction of the reaction area.

- The droplets must be large enough to push the colloid. The state diagram presented in Sect 3.3. in Chap. 3, as well as the behavior of the effective diffusion coefficient as a function of the filling fraction, underline that when ε and/or r_{cut} are small, the filling fraction area is also very low. Moreover, for this set of parameters, the persistence time of the droplet orientation is also small. Therefore, such conditions are not favorable to form persistent droplets, thus there is no propulsion.

- Yet, the droplets must not be too large. Indeed, a critical value for the filling fraction has been evidenced: if the droplet fills the entire reaction area, it hinders the colloid motion, hence the propulsion is suppressed.

After that, suspensions of active colloids have been studied. The solute density and the attraction intensity between solute particles have been fixed. Several surface fractions of colloids has been studied. The system still exhibits activity, which is unexpectedly sensitive to surface fraction increase. Implicit simulations in which the solute particles are not explicitly described have been run for comparison. The parameters used in those simulations have been calibrated so that a single colloid exhibit the same dynamic behavior and so that the interaction potential takes into account the solute depletion at equilibrium. Nevertheless, strong discrepancies are observed, which indicates the importance of the role played by the solute particles. This underlines the limitation of implicit simulations that are widely used in the active matter community.

Finally, a preliminary work has been presented on a mixture of colloids composed of two types of catalytic colloids. One creates solute particles that will form the LJ fluid, whereas the others are catalyzing the opposite reaction. Interestingly, this complex situation shares similarities with simpler systems studied in Chapter 3, which shows that by tuning the different parameters of the simple model, more complex situations can be reproduced. The results seem to indicate an optimum surface fraction for enhanced diffusion.

The last chapter of the manuscript actually constitutes an introduction to the perspectives offered by the model designed during my PhD. By considering a mixture of colloids with different properties, other combinations can be tested. The case of only

one colloid performing the direct reaction (repulsive towards LJ fluid) has been investigated, the study can be extended to several colloids of this type. Moreover, the current results are preliminary as only the dynamics of the active colloid has been investigated. Larger systems can be analyzed as interesting features can emerge from collective effects [90, 91, 92]. It would be interesting to see if the predicted behavior is observed when explicitly describing the solute particles. The model can be then made more complex by considering linked colloids, to form a dimer or a polymer [32, 93, 94]. Another aspect that has been left out of this work could be looked at. Indeed, for the study of collective effects and of a mixture, the parameters defining activity were chosen in order to maximize it. However, it can be possible for a suspension of passive isotropic colloids to form active clusters, [49]. Another aspect that could be deepened is the link with biological systems. In the cells, liquid-liquid phase separations have recently aroused the interest of the scientific community, since it is an important mechanism for the intracellular organization [95]. Links between experimental observations of long-range directed motion due to the formation of droplets [96] and this model can be made.

APPENDIX A

Publications from this work

- J. Decayeux, V. Dahirel, M. Jardat, and P. Illien. Spontaneous propulsion of an isotropic colloid in a phase-separating environment. *Physical Review E*, 104:034602 (2021)
- J. Decayeux, M. Jardat, P. Illien, and V. Dahirel. Conditions for the propulsion of a colloid surrounded by a mesoscale phase separation. *The European Physical Journal E*, **45**,96 (2022).
- J. Decayeux, V. Dahirel, M. Jardat, and P. Illien. Collective effects of colloid self-propelled by the interactions between solute particles. *In preparation.*

APPENDIX B

Technical computation details

B.1 Details about the integration of a delta function $\delta(x)$

The noise correlation function is represented by a delta function: $\langle \mathcal{R}(t_1)\mathcal{R}(t_2)\rangle = \delta(t_1 - t_2)$. Numerous computations involve the integration of a noise correlation function. Here, the principle is presented, based on an example. The following function is considered:

$$F(t_1, t_2) = \int_0^{t_1} \mathrm{d}t_1' \int_0^{t_2} \mathrm{d}t_2' \delta(t_1' - t_2').$$

First, the limits of the integral are modified by making a Heaviside function to appear.

$$F(t_1, t_2) = \int_0^{\infty} \mathrm{d}t_1' \int_0^{\infty} \mathrm{d}t_2' \delta(t_1' - t_2')\Theta(t_1 - t_1')\Theta(t_2 - t_2')$$

- If $t_1 > t_2$, and defining $G(t_1') = \theta(t_1 - t_1')$, from the definition of the delta function: $\int_0^{\infty} G(t_1')\delta(t_1' - t_2')\,\mathrm{d}t_1' = G(t_2')$. Therefore, F becomes:

$$F(t_1, t_2) = \int_0^{\infty} \mathrm{d}t_2' \Theta(t_1 - t_2')\Theta(t_2 - t_2').$$

$\Theta(t_1 - t'_2) = 1$ since $t_1 > t_2$, and the second Heaviside function is removed by modifying again the limits of the integral.

$$F(t_1, t_2) = \int_0^{t_2} \mathrm{d}t'_2$$

Finally the function can be easily integrated, yielding:

$$F(t_1, t_2) = t_2.$$

- If $t_2 > t_1$, and defining $G(t'_2) = \theta(t_2 - t'_2)$, the first integration made is on t'_2: $\int_0^\infty G(t'_2)\delta(t'_1 - t'_2)\,\mathrm{d}t'_2 = G(t'_1)$, consequently F becomes:

$$\begin{aligned} F(t_1, t_2) &= \int_0^\infty \mathrm{d}t'_1 \Theta(t_1 - t'_1)\Theta(t_2 - t'_1) \\ F(t_1, t_2) &= \int_0^{t_1} \mathrm{d}t'_1 \\ F(t_1, t_2) &= t_1. \end{aligned}$$

To conclude:

$$F(t_1, t_2) = \min(t_1, t_2).$$

B.2 From a double integral to a simple

Let I be the double integral of a function of a difference between two variables $\varphi(|t' - t''|)$, $I = \int_0^t \mathrm{d}t' \int_0^t \mathrm{d}t''\ \varphi(|t' - t''|)$. The double integral can be reduced to a single integral $I = 2\int_0^t \mathrm{d}u(t-u)\varphi(u)$ as shown in this paragraph. First, the following change of variable is made:

- $u = t' - t''$
- $\mathrm{d}u = -\mathrm{d}t''$

The integral becomes $I = -\int_0^t \mathrm{d}t' \int_{t'}^{t'-t} \mathrm{d}u\ \varphi(|u|) = \int_0^t \mathrm{d}t' \int_{t'-t}^{t'} \mathrm{d}u\ \varphi(|u|)$. The absolute value of u can be split:

$$I = \int_0^t \mathrm{d}t' \left[\int_{t'-t}^0 \mathrm{d}u\ \varphi(-u) + \int_0^{t'} \mathrm{d}u\ \varphi(u) \right]$$

The area represented by the first and the second double integral can be delimited choosing other bounds for the ingrals:

$$\begin{aligned} I &= \int_{-t}^{0} \mathrm{d}u \int_{0}^{u+t} \mathrm{d}t' \; \varphi(-u) + \int_{0}^{t} \mathrm{d}u \int_{u}^{t} \mathrm{d}t' \; \varphi(u) \\ &= \int_{-t}^{0} \mathrm{d}u \; (u+t)\varphi(-u) + \int_{0}^{t} \mathrm{d}u \; (t-u)\varphi(u) \end{aligned}$$

For the first member of I, the following change of variable is made:

- $v = -u$
- $\mathrm{d}v = -\mathrm{d}u$

Using this the first part becomes $\int_{-t}^{0} \mathrm{d}u(u+t)\varphi(-u) = \int_{0}^{t}(t-v)\varphi(v)$. Consequently :

$$I = 2\int_{0}^{t} \mathrm{d}u \; (t-u)\varphi(u) \tag{B.1}$$

APPENDIX C

Mean squared displacement of the Langevin equation

The Langevin equation in one dimension for a single particle subjected to no external force is:

$$m\dot{v}(t) + m\gamma v(t) = \mathcal{R}(t). \tag{C.1}$$

$\mathcal{R}(t)$ is a Gaussian white noise with the following properties:

- $\langle \mathcal{R}(t) \rangle = 0$, where $\langle . \rangle$ denotes the average over noise realizations.
- $\langle \mathcal{R}(t')\mathcal{R}(t'') \rangle = 2m\gamma k_{\mathrm{B}} T \delta(t' - t'')$

Integrating Eq. (C.1) with the initial condition $v(t = 0) = v_0$ yields:

$$v(t) = v_0 \, \mathrm{e}^{-\gamma t} + \frac{1}{m} \int_0^t \mathrm{e}^{-\gamma(t-t')} \, \mathcal{R}(t') \, \mathrm{d}t' \tag{C.2}$$

The initial conditions are the following:

- The initial position $x(0)$ is unknown.
- The initial velocity $v_0 = v(t = 0)$ is supposed to have a Maxwellian distribution $P(v_0) = \left(\frac{m}{2\pi k_{\mathrm{B}} T} \right)^2 \mathrm{e}^{\frac{-m v_0^2}{2 k_{\mathrm{B}} T}}$, centered around zero, whose mean is $\langle v_0 \rangle = 0$ and $\langle v_0^2 \rangle = \frac{k_{\mathrm{B}} T}{m}$.

Using the initial conditions, the mean velocity is $\langle v(t) \rangle = 0$, and the variance is $\sigma_v^2 = \langle v^2(t) \rangle - \langle v(t) \rangle^2 = \langle v^2(t) \rangle$. The mean squared velocity $\langle v^2(t) \rangle$ is found by first

computing the correlation function:

$$\begin{aligned}
\langle v(t_1)v(t_2)\rangle &= \langle v_0^2\,\mathrm{e}^{-\gamma(t_1+t_2)} + v_0\,\mathrm{e}^{-\gamma t_1}\,\frac{1}{m}\int_0^{t_1}\mathrm{e}^{-\gamma(t_1-t_1')}\,\mathcal{R}(t_1')\,\mathrm{d}t_1' \\
&\quad + v_0\,\mathrm{e}^{-\gamma t_2}\,\frac{1}{m}\int_0^{t_2}\mathrm{e}^{-\gamma(t_2-t_2')}\,\mathcal{R}(t_2')\,\mathrm{d}t_2' + \frac{1}{m^2}\int_0^{t_1}\mathrm{e}^{-\gamma(t_1-t_1')}\,\mathcal{R}(t_1')\,\mathrm{d}t_1'\int_0^{t_2}\mathrm{e}^{-\gamma(t_2-t_2')}\,\mathcal{R}(t_2')\,\mathrm{d}t_2'\rangle \\
\langle v(t_1)v(t_2)\rangle &= \langle v_0^2\rangle\,\mathrm{e}^{-\gamma(t_1+t_2)} + \frac{1}{m^2}\int_0^{t_1}\mathrm{d}t_1'\int_0^{t_2}\mathrm{d}t_2'\,\mathrm{e}^{-\gamma(t_1-t_1')}\,\mathrm{e}^{-\gamma(t_2-t_2')}\,\langle\mathcal{R}(t_1')\mathcal{R}(t_2')\rangle \\
\langle v(t_1)v(t_2)\rangle &= \frac{k_\mathrm{B}T}{m}\,\mathrm{e}^{-\gamma(t_1+t_2)} + \frac{2\gamma k_\mathrm{B}T}{m}\int_0^{t_1}\mathrm{d}t_1'\int_0^{t_2}\mathrm{d}t_2'\,\mathrm{e}^{-\gamma(t_1-t_1')}\,\mathrm{e}^{-\gamma(t_2-t_2')}\,\delta(t_1'-t_2') \\
\langle v(t_1)v(t_2)\rangle &= \frac{k_\mathrm{B}T}{m}\,\mathrm{e}^{-\gamma(t_1+t_2)} + \frac{2\gamma k_\mathrm{B}T}{m}\,\mathrm{e}^{-\gamma(t_1+t_2)}\int_0^{t_1}\mathrm{d}t_1'\int_0^{t_2}\mathrm{d}t_2'\,\mathrm{e}^{\gamma(t_1'+t_2')}\,\delta(t_1'-t_2') \\
\langle v(t_1)v(t_2)\rangle &= \frac{k_\mathrm{B}T}{m}\,\mathrm{e}^{-\gamma(t_1+t_2)} + \frac{k_\mathrm{B}T}{m}\,\mathrm{e}^{-\gamma(t_1+t_2)}\left(\mathrm{e}^{2\gamma\min(t_1,t_2)}-1\right) \\
\langle v(t_1)v(t_2)\rangle &= \frac{k_\mathrm{B}T}{m}\,\mathrm{e}^{-\gamma|t_1-t_2|}
\end{aligned}$$

Details about the integration of the delta function are given in Appendix B. From the correlation function, taking $t_1 = t_2 = t$, $\langle v^2(t)\rangle$ can be deduced:

$$\langle v^2(t)\rangle = \frac{k_\mathrm{B}T}{m} \tag{C.3}$$

The position is obtained by integrating Eq. (C.2):

$$x(t) = \frac{v_0}{\gamma}(1-\mathrm{e}^{-\gamma t}) + \frac{1}{m}\int_0^t\mathrm{d}t'\int_0^{t'}\mathrm{d}t''\,\mathrm{e}^{-\gamma(t'-t'')}\,\mathcal{R}(t'') + x(0) \tag{C.4}$$

The displacement is then:

$$x(t) - x(0) = \frac{v_0}{\gamma}(1-\mathrm{e}^{-\gamma t}) + \frac{1}{m}\int_0^t\mathrm{d}t'\int_0^{t'}\mathrm{d}t''\,\mathrm{e}^{-\gamma(t'-t'')}\,\mathcal{R}(t'') \tag{C.5}$$

The mean displacement is zero, $\langle x(t)-x(0)\rangle = 0$, therefore the mean squared displacement is $\mathrm{MSD}(t) = \langle (x(t)-x(0))^2\rangle - \langle x(t)-x(0)\rangle^2 = \langle (x(t)-x(0))^2\rangle$. Using the correla-

tion function of the velocity, $\langle (x(t)-x(0))^2 \rangle = \int_0^t \mathrm{d}t_1 \int_0^t \mathrm{d}t_2 \langle v(t_1)v(t_2)\rangle$:

$$\begin{aligned}
\left\langle x^2(t)\right\rangle &= \int_0^t \mathrm{d}t_1 \int_0^t \mathrm{d}t_2 \frac{k_\mathrm{B}T}{m}\, \mathrm{e}^{-\gamma|t_1-t_2|} \\
\left\langle (x(t)-x(0))^2\right\rangle &= \frac{k_\mathrm{B}T}{m}\left[\int_0^t \mathrm{d}t_1 \int_0^{t_1} \mathrm{d}t_2\, \mathrm{e}^{-\gamma(t_1-t_2)} + \int_0^t \mathrm{d}t_1 \int_{t_1}^t \mathrm{d}t_2\, \mathrm{e}^{-\gamma(t_2-t_1)}\right] \\
&= \frac{k_\mathrm{B}T}{\gamma m}\left[\int_0^t \left[\mathrm{e}^{-\gamma(t_1-t_2)}\right]_0^{t_1} \mathrm{d}t_1 - \int_0^t \left[\mathrm{e}^{-\gamma(t_2-t_1)}\right]_{t_1}^{t} \mathrm{d}t_1\right] \\
&= \frac{k_\mathrm{B}T}{\gamma m}\int_0^t 2 - \mathrm{e}^{-\gamma t_1} - \mathrm{e}^{-\gamma(t-t_1)}\, \mathrm{d}t_1 \\
&= \frac{k_\mathrm{B}T}{\gamma m}\left[2t_1 + \frac{1}{\gamma}\mathrm{e}^{-\gamma t_1} - \frac{1}{\gamma}\mathrm{e}^{-\gamma(t-t_1)}\right]_0^t \\
&= \frac{k_\mathrm{B}T}{\gamma m}\left(2t + \frac{1}{\gamma}\mathrm{e}^{-\gamma t} - \frac{1}{\gamma} - \frac{1}{\gamma} + \frac{1}{\gamma}\mathrm{e}^{-\gamma t}\right) \\
&= \frac{2k_\mathrm{B}T}{\gamma^2 m}\left(t\gamma + \mathrm{e}^{-\gamma t} - 1\right)
\end{aligned}$$

The mean squared displacement displays two regimes. At short times $t \ll \gamma^{-1}$:

$$\begin{aligned}
\left\langle (x(t)-x(0))^2\right\rangle &\sim \frac{2k_\mathrm{B}T}{\gamma^2 m}\left(t\gamma + 1 - t\gamma + \gamma^2\frac{t^2}{2} - 1\right) \\
\left\langle (x(t)-x(0))^2\right\rangle &\sim \frac{k_\mathrm{B}T}{m}t^2
\end{aligned}$$

At long times $t \to \infty$:

$$\left\langle (x(t)-x(0))^2\right\rangle \sim \frac{2k_\mathrm{B}T}{\gamma m}t$$

The results can be generalized in d dimensions. Each element of the velocity vector satisfies Eq. (C.2), therefore $\langle v_x(t_1)v_x(t_2)\rangle = \langle v_y(t_1)v_y(t_2)\rangle = \langle v_z(t_1)v_z(t_2)\rangle$. In three dimensions, $d=3$, the correlation function yields: $\langle \boldsymbol{v}(t_1)\cdot\boldsymbol{v}(t_2)\rangle = \langle v_x(t_1)v_x(t_2)\rangle + \langle v_y(t_1)v_y(t_2)\rangle + \langle v_z(t_1)v_z(t_2)\rangle = 3\langle v_x(t_1)v_x(t_2)\rangle = 3\frac{k_\mathrm{B}T}{m}$. In two dimensions, $\langle \boldsymbol{v}(t_1)\cdot\boldsymbol{v}(t_2)\rangle = 2\frac{k_\mathrm{B}T}{m}$. Similarly, in d dimensions:

$$\mathrm{MSD}(t) = \left\langle (\boldsymbol{r}(t)-\boldsymbol{r}(0))^2\right\rangle = \frac{2dk_\mathrm{B}T}{\gamma^2 m}\left(t\gamma + \mathrm{e}^{-\gamma t} - 1\right).$$

APPENDIX D

Mean squared displacement of the overdamped Langevin equation

The overdamped Langevin equation in one dimension, for one particle subjected to no external force is:

$$v(t) = \frac{D}{k_{\mathrm{B}}T}\mathcal{R}(t). \tag{D.1}$$

It can easily be integrated to obtain the position of the particle:

$$x(t) = \frac{D}{k_{\mathrm{B}}T}\int_0^t \mathcal{R}(t')\mathrm{d}t' + x(0). \tag{D.2}$$

The displacement of the particle is:

$$\Delta x(t) = x(t) - x(0) = \frac{D}{k_{\mathrm{B}}T}\int_0^t \mathcal{R}(t')\mathrm{d}t' \tag{D.3}$$

$\mathcal{R}(t)$ is a Gaussian white noise with the following properties:

- $\langle \mathcal{R}(t) \rangle = 0$,
- $\langle \mathcal{R}(t')\mathcal{R}(t'') \rangle = 2\frac{(k_{\mathrm{B}}T)^2}{D}\delta(t' - t'')$.

The mean displacement of the particle is given by:

$$\langle \Delta x(t) \rangle = \left\langle \frac{D}{k_{\mathrm{B}}T}\int_0^t \mathcal{R}(t')\mathrm{d}t' \right\rangle = \frac{D}{k_{\mathrm{B}}T}\int_0^t \langle \mathcal{R}(t') \rangle \, \mathrm{d}t' = 0.$$

The correlation function of the displacement is given by:

$$\begin{aligned}\langle \Delta x(t_1)\Delta x(t_2)\rangle &= \left(\frac{D}{k_{\mathrm{B}}T}\right)^2 \int_0^{t_1} \mathrm{d}t_1' \int_0^{t_2} \mathrm{d}t_2' \,\langle \mathcal{R}(t_1')\mathcal{R}(t_2')\rangle \\ &= 2D \int_0^{t_1} \mathrm{d}t_1' \int_0^{t_2} \mathrm{d}t_2' \delta(t_1' - t_2') \\ &= 2D\mathrm{min}(t_1, t_2)\end{aligned}$$

The mean squared displacement of the particle can be deduced from the previous calculations taking $t = t_1 = t_2$.

$$\mathrm{MSD}(t) = \left\langle \Delta x^2(t)\right\rangle - \langle \Delta x(t)\rangle^2 = \left\langle \Delta x^2(t)\right\rangle = 2Dt \tag{D.4}$$

In d-dimensions the mean squared displacement becomes: $\langle \Delta \boldsymbol{r}^2(t)\rangle = 2dDt$.

APPENDIX E

Numerical integration of the Gaussian white noise

The overdamped Langevin equation is discretized using the Euler scheme yielding:

$$x_i(t+\Delta t) = x_i(t) + \Delta t \frac{D_\alpha}{k_\mathrm{B}T} \sum_{i \neq j} F_{x,j\to i}(t) + \frac{D_\alpha}{k_\mathrm{B}T} \underbrace{\int_t^{t+\Delta t} \mathcal{R}_{x,i}(t')\mathrm{d}t'(\Delta t)}_{\mathcal{B}}.$$

The integration of $\mathcal{R}_{x,i}$ can be seen as a sum of random variables, therefore, according to the central limit theorem $\mathcal{B}(\Delta t)$ follows a Gaussian distribution. The mean is:

$$\langle \mathcal{B} \rangle = \int_t^{t+\Delta t} \langle \mathcal{R}_{x,i}(t') \rangle \, \mathrm{d}t' = 0.$$

The variance is:

$$\begin{aligned}
\langle \mathcal{B}(t_1)\mathcal{B}(t_2) \rangle &= \int_{t_1}^{t_1+\Delta t_1} \mathrm{d}t_1' \int_{t_2}^{t_2+\Delta t_2} \mathrm{d}t_2' \langle \mathcal{R}_{x,i}(t_1')\mathcal{R}_{x,i}(t_2') \rangle \\
&= \frac{2(k_\mathrm{B}T)^2}{D_\alpha} \int_{t_1}^{t_1+\Delta t_1} \mathrm{d}t_1' \int_{t_2}^{t_2+\Delta t_2} \mathrm{d}t_2' \delta(t_1' - t_2') \\
&= \frac{2(k_\mathrm{B}T)^2}{D_\alpha} \min(\Delta t_1, \Delta t_2) \\
\left\langle \mathcal{B}^2(t) \right\rangle &= \frac{2(k_\mathrm{B}T)^2}{D_\alpha} \Delta t
\end{aligned}$$

The standard deviation : $\sqrt{\langle \mathcal{B}^2(t) \rangle} = \frac{(k_\mathrm{B}T)}{D_\alpha} \sqrt{2 D_i \alpha \Delta t}$.

APPENDIX F

Computation of the concentration profiles

A colloid, of diameter σ_{C}, is in a bath of solute particles of type A or B. Both species are of diameter σ_{A}. The solute particles diffuse with a diffusion coefficient D_{A}^0. The colloid catalyzes isotropically the reaction $\mathrm{A}+\mathrm{C} \rightarrow \mathrm{B}+\mathrm{C}$ in a circular reaction area of radius r_{cut} centered around itself. This domain is labelled in what follows 1. The reaction occurs at a rate k_{AB}. Outside the reaction area, in the domain label 2, the reverse reaction $\mathrm{B} \rightarrow \mathrm{A}$ occurs at a rate k_{BA}. The interactions between particles are not taken into account, but the solute particles cannot interpenetrate with the colloid. Under these conditions, the concentration profiles of the solute particles A and B can be estimated analytically. The concentration profile of solute particles A (resp. B) in domain 1 is denoted by $c_{\mathrm{A}}^{(1)}$ (resp. $c_{\mathrm{B}}^{(1)}$) and in domain 2 by $c_{\mathrm{A}}^{(2)}$ (resp. $c_{\mathrm{A}}^{(2)}$). The concentrations obey the following reaction-diffusion equations in domain 1:

$$\left\{ \begin{array}{ll} \frac{\partial}{\partial t} c_{\mathrm{A}}^{(1)}(\boldsymbol{r},t) & = D_{\mathrm{A}}^0 \nabla^2 c_{\mathrm{A}}^{(1)} - k_{\mathrm{AB}} c_{\mathrm{A}}^{(1)} \\ \frac{\partial}{\partial t} c_{\mathrm{B}}^{(1)}(\boldsymbol{r},t) & = D_{\mathrm{A}}^0 \nabla^2 c_{\mathrm{B}}^{(1)} + k_{\mathrm{AB}} c_{\mathrm{A}}^{(1)} \end{array} \right. ,$$

and in domain 2:

$$\left\{ \begin{array}{ll} \frac{\partial}{\partial t} c_{\mathrm{A}}^{(2)}(\boldsymbol{r},t) & = D_{\mathrm{A}}^0 \nabla^2 c_{\mathrm{A}}^{(2)} + k_{\mathrm{BA}} c_{\mathrm{B}}^{(2)} \\ \frac{\partial}{\partial t} c_{\mathrm{B}}^{(2)}(\boldsymbol{r},t) & = D_{\mathrm{A}}^0 \nabla^2 c_{\mathrm{B}}^{(2)} - k_{\mathrm{BA}} c_{\mathrm{B}}^{(2)} \end{array} \right.$$

We consider the steady state, and suppose that the concentration profile is axially symmetric. In polar coordinates, the system of equations becomes:

$$\begin{cases} D_{\mathrm{A}}^0 \frac{\partial^2}{\partial r^2} c_{\mathrm{A}}^{(1)} + 2\frac{D_{\mathrm{A}}^0}{r}\frac{\partial}{\partial r} c_{\mathrm{A}}^{(1)} - k_{\mathrm{AB}} c_{\mathrm{A}}^{(1)} = 0 \\ D_{\mathrm{A}}^0 \frac{\partial^2}{\partial r^2} c_{\mathrm{B}}^{(1)} + 2\frac{D_{\mathrm{A}}^0}{r}\frac{\partial}{\partial r} c_{\mathrm{B}}^{(1)} + k_{\mathrm{AB}} c_{\mathrm{A}}^{(1)} = 0 \\ D_{\mathrm{A}}^0 \frac{\partial^2}{\partial r^2} c_{\mathrm{A}}^{(2)} + 2\frac{D_{\mathrm{A}}^0}{r}\frac{\partial}{\partial r} c_{\mathrm{A}}^{(2)} + k_{\mathrm{BA}} c_{\mathrm{B}}^{(2)} = 0 \\ D_{\mathrm{A}}^0 \frac{\partial^2}{\partial r^2} c_{\mathrm{B}}^{(2)} + 2\frac{D_{\mathrm{A}}^0}{r}\frac{\partial}{\partial r} c_{\mathrm{B}}^{(2)} - k_{\mathrm{BA}} c_{\mathrm{B}}^{(2)} = 0 \end{cases}$$

We assume the following boundary conditions:

- No normal flux at the colloid surface:

$$\left.\frac{\partial c_{\mathrm{A}}^{(1)}}{\partial r}\right|_{r=\sigma_{\mathrm{C}}} = \left.\frac{\partial c_{\mathrm{B}}^{(1)}}{\partial r}\right|_{r=\sigma_{\mathrm{C}}} = 0$$

- The concentration profiles, as well as their derivative, are continuous at the boundary between the two domains:

$$\begin{aligned} c_{\mathrm{A}}^{(1)}(r = r_{\mathrm{cut}}) &= c_{\mathrm{A}}^{(2)}(r = r_{\mathrm{cut}}) \\ c_{\mathrm{B}}^{(1)}(r = r_{\mathrm{cut}}) &= c_{\mathrm{B}}^{(2)}(r = r_{\mathrm{cut}}) \\ \left.\frac{\partial c_{\mathrm{A}}^{(1)}}{\partial r}\right|_{r=r_{\mathrm{cut}}} &= \left.\frac{\partial c_{\mathrm{A}}^{(2)}}{\partial r}\right|_{r=r_{\mathrm{cut}}} \\ \left.\frac{\partial c_{\mathrm{B}}^{(1)}}{\partial r}\right|_{r=r_{\mathrm{cut}}} &= \left.\frac{\partial c_{\mathrm{B}}^{(2)}}{\partial r}\right|_{r=r_{\mathrm{cut}}} \end{aligned}$$

- At $r \to \infty$, the concentration profiles are finite:

$$\begin{aligned} \lim_{r\to\infty} c_{\mathrm{A}}^{(2)}(r) &= c_{\mathrm{A},\infty} \\ \lim_{r\to\infty} c_{\mathrm{B}}^{(2)}(r) &= c_{\mathrm{B},\infty} \end{aligned}$$

The solutions are:

$$
\begin{aligned}
c_{\mathrm{A}}^{(1)} &= \frac{1}{r}\left(C_3 \sinh(r/\lambda) + C_4 \cosh(r/\lambda)\right) \\
c_{\mathrm{B}}^{(1)} &= \frac{1}{r}\left(-C_1 + C_2 r - C_3 \sinh(r/\lambda) - C_4 \cosh(r/\lambda)\right) \\
c_{\mathrm{A}}^{(2)} &= \frac{1}{r}\left(-B_1 + B_2 r - B_3 \sinh(r/L) - B_4 \cosh(r/L)\right) \\
c_{\mathrm{B}}^{(2)} &= \frac{1}{r}\left(B_3 \sinh(r/L) + B_4 \cosh(r/L)\right),
\end{aligned}
$$

where $\lambda = \sqrt{D_{\mathrm{A}}^0/k_{\mathrm{AB}}}$, $L = \sqrt{D_{\mathrm{A}}^0/k_{\mathrm{BA}}}$, and B_1, B_2, B_3, B_4, C_1, C_2, C_3, C_4 are constant. Using the boundary conditions, the constant are found to be:

- $B_1 = 0$
- $B_2 = c_0$
- $B_3 = \frac{c_0 \lambda^2 k_{\mathrm{AB}}}{l^2 L k_{\mathrm{BA}}}\, \mathrm{e}^{-r_{\mathrm{cut}}\frac{2L-\lambda}{L\lambda}} \left[(r_{\mathrm{cut}} - \lambda)(\sigma_{\mathrm{C}} + \lambda)\, \mathrm{e}^{2r_{\mathrm{cut}}/\lambda} - (r_{\mathrm{cut}} + \lambda)(\sigma_{\mathrm{C}} - \lambda)\, \mathrm{e}^{2\sigma_{\mathrm{C}}/\lambda}\right]$
- $B_4 = -B_3$
- $C_1 = 0$
- $C_2 = c_0$
- $C_3 = \frac{1}{l^2}(r_{\mathrm{cut}} + L) c_0 \left[(\sigma_{\mathrm{C}} - \lambda)\, \mathrm{e}^{2\sigma_{\mathrm{C}}/\lambda} - \sigma_{\mathrm{C}} - \lambda\right] \lambda\, \mathrm{e}^{-r_{\mathrm{cut}}/\lambda}$
- $C_4 = -\frac{1}{l^2}(r_{\mathrm{cut}} + L) c_0 \left[(\sigma_{\mathrm{C}} - \lambda)\, \mathrm{e}^{2\sigma_{\mathrm{C}}/\lambda} + \sigma_{\mathrm{C}} + \lambda\right] \lambda\, \mathrm{e}^{-r_{\mathrm{cut}}/\lambda}$

with $l^2 = (\sigma_{\mathrm{C}} - \lambda)(L - \lambda)\, \mathrm{e}^{\frac{2\sigma_{\mathrm{C}} - 2rcut}{\lambda}} - (\sigma_{\mathrm{C}} + \lambda)(L + \lambda)$

APPENDIX G

Analysis of the mean squared displacement of the effective Langevin equation

In the main text, the MSD is shown to be the sum of three contributions:

$$\left\langle \Delta \boldsymbol{r}_{\mathrm{C}}^2(t) \right\rangle = K^2 \Delta_{\boldsymbol{pp}}(t) + \Delta_{\boldsymbol{\xi\xi}}(t) - K \left(\Delta_{\boldsymbol{p\xi}}(t) + \Delta_{\boldsymbol{\xi p}}(t) \right), \tag{G.1}$$

where $\Delta_{\boldsymbol{ab}}(t) \equiv \int_0^t \mathrm{d}t' \int_0^t \mathrm{d}t'' \left\langle \boldsymbol{a}(t') \cdot \boldsymbol{b}(t'') \right\rangle$. The computation of each contribution is detailed in this chapter. Then, asymptotic developments at short times and at long times are performed to analyze the different regimes of the MSD.

G.1 Computation of the contribution of the polarization vector

The vector $\boldsymbol{p}$ is defined as:

$$\langle \boldsymbol{p}(t') \cdot \boldsymbol{p}(t'+t) \rangle_{t'} = \begin{cases} \frac{A}{(t+c)^\alpha} & \text{if } t \leq t_0, \\ \frac{A}{(t_0+c)^\alpha} \exp\left(\frac{-(t-t_0)}{\tau_p} \right) & \text{else.} \end{cases} \tag{G.2}$$

The contribution of the polarization vector is then:

$$\begin{aligned}
\Delta_{\boldsymbol{pp}}(t) &= \int_0^t \mathrm{d}t' \int_0^t \mathrm{d}t'' \, \langle \boldsymbol{p}(t') \cdot \boldsymbol{p}(t'') \rangle \\
&= 2 \int_0^t (t-u)\varphi(u) \, \mathrm{d}u \\
&= \begin{cases} 2\int_0^t (t-u)\frac{A}{(u+c)^\alpha} \, \mathrm{d}u & \text{if } t \leq t_0 \\ 2\int_0^{t_0} (t-u)\frac{A}{(u+c)^\alpha} \, \mathrm{d}u + 2\int_{t_0}^t (t-u)\frac{A}{(t_0+c)^\alpha} \, \mathrm{e}^{-(u-t_0)/\tau_p} \, \mathrm{d}u & \text{else.} \end{cases}
\end{aligned}$$

If $t \leq t_0$:

$$\begin{aligned}
\Delta_{\boldsymbol{pp}}(t) &= 2 \int_0^t (t-u) \frac{A}{(u+c)^\alpha} \, \mathrm{d}u \\
&= 2 \int_0^t \frac{tA}{(u+c)^\alpha} \, \mathrm{d}u - 2 \int_0^t \frac{uA}{(u+c)^\alpha} \, \mathrm{d}u \\
&= \frac{2At}{1-\alpha} \left[(u+c)^{1-\alpha} \right]_0^t - \frac{2A}{1-\alpha} \left[u(u+c)^{1-\alpha} \right]_0^t + \frac{2A}{1-\alpha} \int_0^t (u+c)^{1-\alpha} \, \mathrm{d}u \\
&= \frac{2At}{1-\alpha} \left((t+c)^{1-\alpha} - c^{1-\alpha} \right) - \frac{2At(t+c)^{1-\alpha}}{1-\alpha} + \frac{2A}{(1-\alpha)(2-\alpha)} \left[(u+c)^{2-\alpha} \right]_0^t \\
&= -\frac{2Atc^{1-\alpha}}{1-\alpha} + \frac{2A}{(1-\alpha)(2-\alpha)} \left((t+c)^{2-\alpha} - c^{2-\alpha} \right) \\
&= \frac{2A}{(1-\alpha)(2-\alpha)} \left((t+c)^{2-\alpha} - t(2-\alpha)c^{1-\alpha} - c^{2-\alpha} \right)
\end{aligned}$$

If $t > t_0$, then the first integral yields:

$$\begin{aligned}
2\int_0^{t_0}(t-u)\frac{A}{(u+c)^\alpha}\,\mathrm{d}u &= 2At\int_0^{t_0}(u+c)^{-\alpha}\,\mathrm{d}u - 2A\int_0^{t_0}u(u+c)^{-\alpha}\,\mathrm{d}u \\
&= \frac{2At}{1-\alpha}\left[(u+c)^{1-\alpha}\right]_0^{t_0} - \frac{2A}{1-\alpha}\left[u(u+c)^{1-\alpha}\right]_0^{t_0} + \frac{2A}{1-\alpha}\int_0^{t_0}(u+c)^{1-\alpha}\,\mathrm{d}u \\
&= \frac{2At}{1-\alpha}\left((t_0+c)^{1-\alpha} - c^{1-\alpha}\right) - \frac{2At_0(t_0+c)^{1-\alpha}}{1-\alpha} \\
&+ \frac{2A}{(1-\alpha)(2-\alpha)}\left[(u+c)^{2-\alpha}\right]_0^{t_0} \\
&= \frac{2At}{1-\alpha}\left((t_0+c)^{1-\alpha} - c^{1-\alpha}\right) - \frac{2At_0(t_0+c)^{1-\alpha}}{1-\alpha} \\
&+ \frac{2A}{(1-\alpha)(2-\alpha)}\left((t_0+c)^{2-\alpha} - c^{2-\alpha}\right) \\
&= \frac{2A}{1-\alpha}\left((t-t_0)(t_0+c)^{1-\alpha} - tc^{1-\alpha}\right) + \frac{2A}{(1-\alpha)(2-\alpha)}\left((t_0+c)^{2-\alpha} - c^{2-\alpha}\right)
\end{aligned}$$

And the second integral yields:

$$\begin{aligned}
2\int_{t_0}^{t}(t-u)\frac{A}{(t_0+c)^\alpha}\,\mathrm{e}^{-(u-t_0)/\tau_p}\,\mathrm{d}u &= \frac{2At}{(t_0+c)^\alpha}\int_{t_0}^{t}\mathrm{e}^{-u/\tau_p}\,\mathrm{d}u - \frac{2A}{(t_0+c)^\alpha}\int_{t_0}^{t}u\,\mathrm{e}^{-(u-t_0)/\tau_p}\,\mathrm{d}u \\
&= \frac{2At}{(t_0+c)^\alpha}\left[-\tau_p\,\mathrm{e}^{-(u-t_0)/\tau_p}\right]_{t_0}^{t} + \frac{2A\tau_p}{(t_0+c)^\alpha}\left[u\,\mathrm{e}^{-(u-t_0)/\tau_p}\right]_{t_0}^{t} \\
&- \frac{2A\tau_p}{(t_0+c)^\alpha}\int_{t_0}^{t}\mathrm{e}^{-(u-t_0)/\tau_p}\,\mathrm{d}u \\
&= \frac{-2At\tau_p}{(t_0+c)^\alpha}\left(\mathrm{e}^{-(t-t_0)/\tau_p} - 1\right) + \frac{2A\tau_p}{(t_0+c)^\alpha}\left(t\,\mathrm{e}^{-(t-t_0)/\tau_p} - t_0\right) \\
&+ \frac{2A\tau_p^2}{(t_0+c)^\alpha}\left[\mathrm{e}^{-(u-t_0)/\tau_p}\right]_{t_0}^{t} \\
&= \frac{2At\tau_p}{(t_0+c)^\alpha}(t-t_0) + \frac{2A\tau_p^2}{(t_0+c)^\alpha}\left(\mathrm{e}^{-(t-t_0)/\tau_p} - 1\right) \\
&= \frac{2A\tau_p}{(t_0+c)^\alpha}(t-t_0) + \frac{2A\tau_p^2}{(t_0+c)^\alpha}\left[\mathrm{e}^{-(t-t_0)/\tau_p} - 1\right] \\
&= \frac{2A\tau_p}{(t_0+c)^\alpha}\left((t-t_0) + \tau_p\left(\mathrm{e}^{-(t-t_0)/\tau_p} - 1\right)\right)
\end{aligned}$$

In conclusion:

$$\Delta_{\boldsymbol{pp}}(t) = \begin{cases} \frac{2A}{(1-\alpha)(2-\alpha)}\left[(t+c)^{2-\alpha} - t(2-\alpha)c^{1-\alpha} - c^{2-\alpha}\right] & \text{if } t < t_0 \\ \frac{2A}{1-\alpha}\left((t-t_0)(t_0+c)^{1-\alpha} - tc^{1-\alpha}\right) + \frac{2A}{(1-\alpha)(2-\alpha)}\left((t_0+c)^{2-\alpha} - c^{2-\alpha}\right) & \\ +\frac{2A\tau_p}{(t_0+c)^{\alpha}}\left((t-t_0) + \tau_p\left(\mathrm{e}^{-(t-t_0)/\tau_p} - 1\right)\right) & \text{else.} \end{cases}$$

G.2 Contribution of the noise vector

The Gaussian white noise $\boldsymbol{\xi}(t)$ is defined by:

$$\begin{cases} \langle \boldsymbol{\xi}(t) \rangle = 0 \\ \langle \boldsymbol{\xi}(t') \cdot \boldsymbol{\xi}(t'') \rangle = 2D_{\mathrm{C}}\delta(t'-t'') \end{cases}$$

Therefore the contribution of the noise is:

$$\begin{aligned} \Delta_{\boldsymbol{\xi\xi}}(t) &= \int_0^t \mathrm{d}t' \int_0^t \mathrm{d}t'' \, \langle \boldsymbol{\xi}(t') \cdot \boldsymbol{\xi}(t'') \rangle \\ &= \int_0^t \mathrm{d}t' \int_0^t \mathrm{d}t'' \left(\langle \xi_x(t') \cdot \xi_x(t'') \rangle + \langle \xi_y(t') \cdot \xi_y(t'') \rangle \right) \\ &= 2\int_0^t \mathrm{d}t' \int_0^t \mathrm{d}t'' 2D_{\mathrm{C}}\delta(t'-t'') \\ &= 4D_{\mathrm{C}}t \end{aligned}$$

G.3 Contribution of the cross term between the noise and the polarization vector

The cross-correlation functions are supposed to be $\langle \boldsymbol{p}(t') \cdot \boldsymbol{\xi}(t'') \rangle = 0$ and $\langle \boldsymbol{\xi}(t') \cdot \boldsymbol{p}(t'') \rangle = 0$, therefore $\Delta_{\boldsymbol{p\xi}}(t) = \Delta_{\boldsymbol{\xi p}}(t) = 0$

G.4 Sum of all the contributions

All in all, the mean squared displacement is:

$$\left\langle \Delta \boldsymbol{r}_{\mathrm{C}}^2(t) \right\rangle = \begin{cases} 4D_{\mathrm{C}}t + \frac{2AK^2}{(1-\alpha)(2-\alpha)}\left[(t+c)^{2-\alpha} - t(2-\alpha)c^{1-\alpha} - c^{2-\alpha}\right] & \text{if } t \leq t_0, \\ 4D_{\mathrm{C}}t & \\ +\frac{2AK^2}{1-\alpha}\left[(t-t_0)(t_0+c)^{1-\alpha} - tc^{1-\alpha}\right] + \frac{2AK^2}{(1-\alpha)(2-\alpha)}\left[(t_0+c)^{2-\alpha} - c^{2-\alpha}\right] & \\ +\frac{2AK^2\tau_p}{(t_0+c)^{\alpha}}\left[(t-t_0) + \tau_p\left(\mathrm{e}^{-(t-t_0)/\tau_p} - 1\right)\right] & \text{else.} \end{cases}$$

G.5 Analysis of the different regimes

if $t < t_0$:

The case $t \to 0$ is considered. The term $(t+c)^{2-\alpha}$ can be developed using the Taylor expansion:

$$(t+c)^{2-\alpha} \sim c^{2-\alpha} + (2-\alpha)tc^{1-\alpha} + (2-\alpha)(1-\alpha)c^{-\alpha}\frac{t^2}{2}.$$

As a consequence:

$$\left\langle \Delta \boldsymbol{r}_{\mathrm{C}}^2(t) \right\rangle \sim AK^2 c^{-\alpha} t^2 + 4D_{\mathrm{C}} t.$$

There is a crossover between t and t^2 in $t_1 = \frac{4D_{\mathrm{C}}c^{\alpha}}{K^2 A}$.

if $t > t_0$:

- First, at intermediate times, for τ_p large: $t \ll \tau_p$ and $t_0 \ll \tau_p$. Therefore, the Taylor expansion of $\mathrm{e}^{-(t-t_0)/\tau_p}$ yields:

$$\mathrm{e}^{-(t-t_0)/\tau_p} \sim 1 - \frac{t-t_0}{\tau_p} + \frac{(t-t_0)^2}{2\tau_p^2},$$

and the last term of the MSD becomes:

$$\begin{aligned}(t-t_0) + \tau_p\left(\mathrm{e}^{-(t-t_0)/\tau_p} - 1\right) &\sim (t-t_0) + \tau_p\left(1 - \frac{t-t_0}{\tau_p} + \frac{(t-t_0)^2}{2\tau_p^2} - 1\right) \\ &\sim \frac{(t-t_0)^2}{2\tau_p}.\end{aligned}$$

Consequently, at intermediate times, the MSD becomes:

$$\left\langle \Delta \boldsymbol{r}_{\mathrm{C}}^2(t) \right\rangle \sim \left(4D_{\mathrm{C}} + \frac{2AK^2}{1-\alpha}\left((t_0+c)^{1-\alpha} - c^{1-\alpha}\right) - \frac{2t_0 AK^2}{(t_0+c)^{\alpha}}\right)t + \frac{AK^2}{(t_0+c)^{\alpha}}t^2$$

A crossover occurs between t and t^2 in $t_2 = \frac{4D_{\mathrm{C}}(t_0+c)^{\alpha}}{AK^2} + \frac{2(t_0+c)}{1-\alpha}\left[1 - \left(\frac{t_0+c}{c}\right)^{\alpha-1}\right] - 2t_0$.

- Second, at long times, $t \gg \tau_p$: $(t-t_0) \sim t$ and $\mathrm{e}^{-(t-t_0)/\tau_p} \sim 0$, the MSD becomes:

$$\begin{aligned}\left\langle \Delta \boldsymbol{r}_{\mathrm{C}}^2(t) \right\rangle &\sim 4D_{\mathrm{C}}t + \frac{2AK^2}{1-\alpha}t\left[(t_0+c)^{1-\alpha} - c^{1-\alpha}\right] + \frac{2AK^2\tau_p}{(t_0+c)^{1-\alpha}}t \\ &\sim \left(4D_{\mathrm{C}} + \frac{2AK^2}{1-\alpha}\left[(t_0+c)^{1-\alpha} - c^{1-\alpha}\right] + \frac{2AK^2\tau_p}{(t_0+c)^{\alpha}}\right)t\end{aligned}$$

Conclusion

To conclude there are five regimes separated by four characteristic times: t_1,t_0,t_2, and τ_p.

- At $t < t_1$, the MSD is linear, indicating a diffusive motion:

$$\left\langle \Delta \boldsymbol{r}_{\mathrm{C}}^2(t) \right\rangle \sim 4D_{\mathrm{C}}t \tag{G.3}$$

- At $t_1 < t < t_0$, the MSD is proportional to t^2, indicating a ballistic motion:

$$\left\langle \Delta \boldsymbol{r}_{\mathrm{C}}^2(t) \right\rangle \sim AK^2c^{-\alpha}t^2 \tag{G.4}$$

- At $t_0 < t < t_2$, the MSD is linear again, indicating a diffusive motion:

$$\left\langle \Delta \boldsymbol{r}_{\mathrm{C}}^2(t) \right\rangle \sim \left[4D_{\mathrm{C}} + \frac{2AK^2}{1-\alpha}\left((t_0+c)^{1-\alpha} - c^{1-\alpha}\right) - \frac{2t_0AK^2}{(t_0+c)^{\alpha}}\right]t \tag{G.5}$$

- At $t_2 < t < \tau_p$, the MSD is proportional again to t^2, indicating a ballistic motion:

$$\left\langle \Delta \boldsymbol{r}_{\mathrm{C}}^2(t) \right\rangle \sim \frac{AK^2}{(t_0+c)^{\alpha}}t^2 \tag{G.6}$$

- At $t > \tau_p$, the MSD is linear again, indicating a diffusive motion:

$$\left\langle \Delta \boldsymbol{r}_{\mathrm{C}}^2(t) \right\rangle \sim \left(4D_{\mathrm{C}} + \frac{2AK^2}{1-\alpha}\left[(t_0+c)^{1-\alpha} - c^{1-\alpha}\right] + \frac{2AK^2\tau_p}{(t_0+c)^{\alpha}}\right)t \tag{G.7}$$

APPENDIX H

Summary of simulation data

$\rho = 0.1$						
ε	r_{cut}	t_{init}	$N_{\text{shell},\infty}$	t_{lin}	D_{eff}	δD_{eff}
1	5.5	24	7	300	0.129	0.003
	7.5	117	17	100	0.136	0.001
	10.5	136	37	100	0.138	0.002
1.5	7.5	170	19	600	0.145	0.006
1.75	7.5	122	21	600	0.149	0.003
2	5.5	110	8	100	0.145	0.003
	6.5	112	14	200	0.162	0.004
	7.5	140	23	900	0.190	0.002
	8.25	173	31	800	0.202	0.002
	9	188	39	1000	0.232	0.003
	10.5	245	59	1000	0.249	0.004
2.25	5.5	50	8	300	0.146	0.002
	6.5	97	15	300	0.177	0.002
	7.5	134	25	600	0.235	0.006
	8.25	198	35	900	0.302	0.003
	10.5	213	67	1950	0.497	0.004
2.5	5.5	60	8	100	0.152	0.002
	6.5	120	16	1100	0.225	0.007
	7.5	115	28	800	0.367	0.003
	8.25	138	38	800	0.493	0.014
	9	147	49	1000	0.648	0.002
	10.5	143	72	2000	0.870	0.015
3	5.5	67	9	300	0.175	0.004
	6.5	98	18	500	0.328	0.004
	7.5	92	30	1000	0.657	0.006
	8.25	94	41	1000	0.846	0.010
	9	94	52	2000	1.05	0.005
	10.5	108	77	1500	1.136	0.011
	12	136	99	2400	1.153	0.021
	15	191	135	3000	0.927	0.015
5	7.5	79	36	800	0.888	0.011

Table H.1: Summary of the quantities of interest of Chapter 3 at $\rho = 0.1$, t_{init} the initial steady state simulation time, $N_{\text{shell},\infty}$ the number of particles inside the reaction area at steady state, t_{lin} the time from which the last linear regime of the MSD is reached and from which D_{eff} can be computed, D_{eff} the effective diffusion coefficient, and δD_{eff} the associated error.

$\rho = 0.3$						
ε	r_{cut}	t_{init}	$N_{\text{shell},\infty}$	t_{lin}	D_{eff}	δD_{eff}
1	5.5	22	26	300	0.080	0.002
	7.5	28	63	200	0.082	0.001
	10.5	36	131	200	0.087	0.001
2	5.5	49	31	400	0.107	0.001
	7.5	28	83	150	0.106	0.002
	10.5	41	180	150	0.098	0.002
2.5	5.5	20	33	150	0.152	0.001
	6.5	23	61	150	0.122	0.002
	7.5	26	93	150	0.098	0.002
	9	31	146	150	0.084	0.001
	10.5	40	202	150	0.078	0.001
3	5.5	23	36	200	0.224	0.005
	6.5	25	67	100	0.104	0.001
	7.5	26	100	100	0.062	0.001
	9	33	160	70	0.039	0.001
	10.5	45	230	30	0.022	0.000
5	5.5	44	40	500	2.110	0.010
	6.5	30	80	40	0.024	0.001
	7.5	46	118	10	0.007	0.000
	9	42	183	5	0.005	0.000
	10.5	56	246	15	0.004	0.000

Table H.2: Summary of the quantities of interest of Chapter 3 at $\rho = 0.3$, t_{init} the initial steady state simulation time, $N_{\text{shell},\infty}$ the number of particles inside the reaction area at steady state, t_{lin} the time from which the last linear regime of the MSD is reached and from which D_{eff} can be computed, D_{eff} the effective diffusion coefficient, and δD_{eff} the associated error.

	Passive explicit simulations					
ϕ_{C}	0.008	0.01	0.02	0.03	0.04	0.1
$\langle n_{\text{c}} \rangle$	–	2.02	–	2.10	2.13	2.41
$\sqrt{\langle n_{\text{c}}^2 \rangle - \langle n_{\text{c}} \rangle^2}$	–	0.12	–	0.33	0.38	0.77
$D_{\text{no\_reac,col}}$	0.829	0.791	0.766	0.747	0.778	0.665
$\delta D_{\text{no\_reac,col}}$	0.006	0.006	0.013	0.000	0.006	0.006

Table H.3: Summary of the quantities of interest of Chapter 4 for passive explicit simulations: $\langle n_{\text{c}} \rangle$ the mean clusters size and the standard deviation $\sqrt{\langle n_{\text{c}}^2 \rangle - \langle n_{\text{c}} \rangle^2}$, the equilibrium diffusion coefficient $D_{\text{no\_reac,col}}$, and $\delta D_{\text{no\_reac,col}}$ the associated error.

	Active explicit simulations $r_{\text{cut}} = 1.5$					
ϕ_{C}	0.008	0.01	0.02	0.03	0.04	0.1
$\langle n_{\text{c}} \rangle$	–	2.13	–	2.39	2.46	3.08
$\sqrt{\langle n_{\text{c}}^2 \rangle - \langle n_{\text{c}} \rangle^2}$	–	0.38	–	0.78	0.86	1.65
t_{lin}	5.2	7.8	4.6	7.8	3.8	2.5
$D_{\text{eff,col}}$	3.335	3.266	2.532	2.101	1.816	1.063
$\delta D_{\text{eff,col}}$	0.013	0.013	0.025	0.019	0.006	0.006

Table H.4: Summary of the quantities of interest of Chapter 4 for active explicit simulations at $r_{\text{cut}} = 1.5$: $\langle n_{\text{c}} \rangle$ the mean clusters size and the standard deviation $\sqrt{\langle n_{\text{c}}^2 \rangle - \langle n_{\text{c}} \rangle^2}$, t_{lin} the time from which the last linear regime of the MSD is reached and from which $D_{\text{eff,col}}$ is computed, the effective diffusion coefficient $D_{\text{eff,col}}$, and $\delta D_{\text{eff,col}}$ the associated error.

Active explicit simulations $\phi_{\text{C}} = 0.1$ and $r_{\text{cut}} = 1.3$				
$\langle n_{\text{c}} \rangle$	$\sqrt{\langle n_{\text{c}}^2 \rangle - \langle n_{\text{c}} \rangle^2}$	t_{lin}	$D_{\text{eff,col}}$	$\delta D_{\text{eff,col}}$
3.07	1.63	3.2	0.994	0.006

Table H.5: Summary of the quantities of interest of Chapter 4 for explicit simulations at $\phi_{\text{C}} = 0.1$ and $r_{\text{cut}} = 1.3$: $\langle n_{\text{c}} \rangle$ the mean clusters size and the standard deviation $\sqrt{\langle n_{\text{c}}^2 \rangle - \langle n_{\text{c}} \rangle^2}$, t_{lin} the time from which the last linear regime of the MSD is reached and from which $D_{\text{eff,col}}$ is computed, the effective diffusion coefficient $D_{\text{eff,col}}$, and $\delta D_{\text{eff,col}}$ the associated error.

	Implicit simulations $r_{\text{cut}} = 1.5$					
ϕ_{C}	0.008	0.01	0.02	0.03	0.04	0.1
$\langle n_{\text{c}} \rangle$	–	02.05	–	2.18	2.25	2.75
$\sqrt{\langle n_{\text{c}}^2 \rangle - \langle n_{\text{c}} \rangle^2}$	–	0.23	–	0.47	0.57	1.22
t_{lin}	5.3	5.5	4.3	6	6.3	4.4
$D_{\text{t,eff}}$	3.931	3.872	3.836	3.787	3.735	3.265
$\delta D_{\text{t,eff}}$	0.003	0.007	0.007	0.004	0.020	0.021

Table H.6: Summary of the quantities of interest of Chapter 4 for implicit simulations at $r_{\text{cut}} = 1.5$: $\langle n_{\text{c}} \rangle$ the mean clusters size and the standard deviation $\sqrt{\langle n_{\text{c}}^2 \rangle - \langle n_{\text{c}} \rangle^2}$, t_{lin} the time from which the last linear regime of the MSD is reached and from which $D_{\text{t,eff}}$ is computed, the effective diffusion coefficient $D_{\text{t,eff}}$, and $\delta D_{\text{t,eff}}$ the associated error.

Implicit simulations $\phi_C = 0.1$ and $r_{cut} = 1.3$				
$\langle n_c \rangle$	$\sqrt{\langle n_c^2 \rangle - \langle n_c \rangle^2}$	t_{lin}	$D_{t,eff}$	$\delta D_{t,eff}$
2.63	1.05	3	1.605	0.005

Table H.7: Summary of the quantities of interest of Chapter 4 for implicit simulations at $\phi_C = 0.1$ and $r_{cut} = 1.3$: $\langle n_c \rangle$ the mean clusters size and the standard deviation $\sqrt{\langle n_c^2 \rangle - \langle n_c \rangle^2}$, t_{lin} the time from which the last linear regime of the MSD is reached and from which $D_{t,eff}$ is computed, the effective diffusion coefficient $D_{t,eff}$, and $\delta D_{t,eff}$ the associated error.

Bibliography

[1] Jean Perrin. Mouvement Brownien et Molécules. *Journal de Physique théorique et appliquée*, 9:5, 1910.

[2] Jonathan R. Howse, Richard A L Jones, Anthony J. Ryan, Tim Gough, Reza Vafabakhsh, and Ramin Golestanian. Self-motile colloidal particles: from directed propulsion to random walk. *Phys. Rev. Lett.*, 99:048102, 2007.

[3] C. Mavroidis, A. Dubey, and M. L. Yarmush. Molecular machines. *Annual Review of Biomedical Engineering*, 6:363, 2004.

[4] Eric Lauga and Thomas R. Powers. The hydrodynamics of swimming microorganisms. *Reports on Progress in Physics*, 72:096601, 2009.

[5] SongSong Tang, Fangyu Zhang, Hua Gong, Fanan Wei, Jia Zhuang, Emil Karshalev, Berta Esteban-Fernandez De Avila, Chuynig Huang, Zhidong Zhou, Zhengwing Li, Lu Yin, Haifeng Dong, Ronnie H. Fang, Xueji Zhang, Liangfang Zhang, and Joseph Wang. Enzyme-powered Janus platelet cell robots for active and targeted drug delivery. *Science Robotics*, 5:6137, 2020.

[6] Jemish Parmar, Diana Vilela, Katherine Villa, Joseph Wang, and Samuel Sánchez. Micro- and Nanomotors as Active Environmental Microcleaners and Sensors. *Journal of the American Chemical Society*, 140:9317, 2018.

[7] Stephen J. Ebbens and Jonathan R. Howse. In pursuit of propulsion at the nanoscale. *Soft Matter*, 6:726, 2010.

[8] Shakuntala Sundararajan, Paul E. Lammert, Andrew W. Zudans, Vincent H. Crespi, and Ayusman Sen. Catalytic motors for transport of colloidal cargo. *Nano Letters*, 8:1271, 2008.

[9] Clemens Bechinger, Roberto Di Leonardo, Hartmut Löwen, Charles Reichhardt, Giorgio Volpe, and Giovanni Volpe. Active Brownian Particles in Complex and Crowded Environments. *Rev. Mod. Phys.*, 88:045006, 2016.

[10] J. Anderson. Colloid Transport By Interfacial Forces. *Annual Review of Fluid Mechanics*, 21:61, 1989.

[11] Ramin Golestanian. Phoretic active matter. *http://arxiv.org/abs/1909.03747*, 2019.

[12] Walter F. Paxton, Paul T. Baker, Timothy R. Kline, Yang Wang, Thomas E. Mallouk, and Ayusman Sen. Catalytically induced electrokinetics for motors and micropumps. *Journal of the American Chemical Society*, 128:14881, 2006.

[13] Hong Ren Jiang, Natsuhiko Yoshinaga, and Masaki Sano. Active motion of a Janus particle by self-thermophoresis in a defocused laser beam. *Physical Review Letters*, 105:268302, 2010.

[14] Pierre Illien, Ramin Golestanian, and Ayusman Sen. 'Fuelled' motion: Phoretic motility and collective behaviour of active colloids. *Chemical Society Reviews*, 46:5508, 2017.

[15] Ivo Buttinoni, Giovanni Volpe, Felix Kümmel, Giorgio Volpe, and Clemens Bechinger. Active Brownian motion tunable by light. *Journal of Physics Condensed Matter*, 24:284129, 2012.

[16] Giovanni Volpe, Ivo Buttinoni, Dominik Vogt, Hans Jürgen Kümmerer, and Clemens Bechinger. Microswimmers in patterned environments. *Soft Matter*, 7:8810, 2011.

[17] Rajeev Dattani, Enrico F. Semeraro, and Theyencheri Narayanan. Phoretic motion of colloids in a phase separating medium. *Soft Matter*, 13:2817, 2017.

[18] Thomas Zinn, Lewis Sharpnack, and Theyencheri Narayanan. Phoretic dynamics of colloids in a phase separating critical liquid mixture. *Physical Review Research*, 2:033177, 2020.

[19] Enrico F. Semeraro, Rajeev Dattani, and Theyencheri Narayanan. Microstructure and dynamics of Janus particles in a phase separating medium. *Journal of Chemical Physics*, 148:014904, 2018.

[20] Ramin Golestanian, Tanniemola B. Liverpool, and Armand Ajdari. Propulsion of a molecular machine by asymmetric distribution of reaction products. *Phys. Rev. Lett.*, 94:220801, 2005.

[21] R. Golestanian, T. B. Liverpool, and A. Ajdari. Designing phoretic micro- and nano-swimmers. *New Journal of Physics*, 9:126, 2007.

[22] M. N. Popescu, S. Dietrich, and G. Oshanin. Confinement effects on diffusiophoretic self-propellers. *Journal of Chemical Physics*, 130:194702, 2009.

[23] Edward J Banigan and John F Marko. Self-propulsion and interactions of catalytic particles in a chemically active medium. *Phys. Rev. E*, 93:012611, 2016.

[24] Sébastien Michelin and Eric Lauga. Optimal feeding is optimal swimming for all Péclet numbers. *Physics of Fluids*, 23:101901, oct 2011.

[25] Sébastien Michelin and Eric Lauga. Phoretic self-propulsion at finite Péclet numbers. *Journal of Fluid Mechanics*, 747:572, 2014.

[26] Thomas Bickel, Arghya Majee, and Alois Würger. Flow pattern in the vicinity of self-propelling hot Janus particles. *Physical Review E*, 88:012301, 2013.

[27] Alois Würger. Self-Diffusiophoresis of Janus Particles in Near-Critical Mixtures. *Physical Review Letters*, 115:188304, 2015.

[28] Sela Samin and René Van Roij. Self-Propulsion Mechanism of Active Janus Particles in Near-Critical Binary Mixtures. *Physical Review Letters*, 115:188305, 2015.

[29] Thomas Speck. Thermodynamic approach to the self-diffusiophoresis of colloidal Janus particles. *Physical Review E*, 99:060602, 2019.

[30] Pierre De Buyl and Raymond Kapral. Phoretic self-propulsion: a mesoscopic description of reaction dynamics that power motion. *Nanoscale*, 5:1337, 2013.

[31] Gunnar Rückner and Raymond Kapral. Chemically powered nanodimers. *Physical Review Letters*, 98:150603, 2007.

[32] Yu Guo Tao and Raymond Kapral. Design of chemically propelled nanodimer motors. *Journal of Chemical Physics*, 128:164518, 2008.

[33] Snigdha Thakur and Raymond Kapral. Dynamics of self-propelled nanomotors in chemically active media. *Journal of Chemical Physics*, 135:024509, 2011.

[34] Snigdha Thakur, Jiang-Xing Chen, and Raymond Kapral. Interaction of a Chemically Propelled Nanomotor with a Chemical Wave. *Angewandte Chemie*, 123:10347, 2011.

[35] Ramin Golestanian. Anomalous diffusion of symmetric and asymmetric active colloids. *Phys. Rev. Lett.*, 102:188305, 2009.

[36] R. J. Allen C. Valeriani and D. Marenduzzo. Non-equilibrium dynamics of an active colloidal " chucker ". *Journal of Chemical Physics*, 132:204904, 2010.

[37] Ziane Izri, Marjolein N. Van Der Linden, Sébastien Michelin, and Olivier Dauchot. Self-propulsion of pure water droplets by spontaneous marangoni-stress-driven motion. *Phys. Rev. Lett.*, 113:248302, 2014.

[38] Marco De Corato, Ignacio Pagonabarraga, Loai K. E. A. Abdelmohsen, Samuel Sánchez, and Marino Arroyo. Spontaneous polarization and locomotion of an active particle with surface-mobile enzymes. *Physical Review Fluids*, 5:122001, 2020.

[39] Sébastien Michelin, Eric Lauga, and Denis Bartolo. Spontaneous autophoretic motion of isotropic particles. *Physics of Fluids*, 25:061701, 2013.

[40] Pierre De Buyl, Alexander S. Mikhailov, and Raymond Kapral. Self-propulsion through symmetry breaking. *Epl*, 103:60009, 2013.

[41] Dolachai Boniface, Cécile Cottin-Bizonne, Ronan Kervil, Christophe Ybert, and François Detcheverry. Self-propulsion of symmetric chemically active particles: Point-source model and experiments on camphor disks. *Physical Review E*, 99:062605, 2019.

[42] Shashi Thutupalli, Ralf Seemann, and Stephan Herminghaus. Swarming behavior of simple model squirmers. *New Journal of Physics*, 13:073021, 2011.

[43] Sebastien Michelin. Self-propulsion of chemically-active droplets. *http://arxiv.org/abs/2204.08953*, 2022.

[44] M. Reza Shaebani, Adam Wysocki, Roland G. Winkler, Gerhard Gompper, and Heiko Rieger. Computational models for active matter. *Nature Reviews Physics*, 2:181, 2020.

[45] J. Tailleur and M. E. Cates. Statistical mechanics of interacting run-and-tumble bacteria. *Physical Review Letters*, 100:218103, 2008.

[46] P. Romanczuk, M. Bär, W. Ebeling, B. Lindner, and L. Schimansky-Geier. Active Brownian particles: From individual to collective stochastic dynamics. *European Physical Journal: Special Topics*, 202:1, 2012.

[47] Grzegorz Szamel. Theory for the dynamics of dense systems of athermal self-propelled particles. *Physical Review E*, 93:012603, 2016.

[48] David Martin, Jérémy O'Byrne, Michael E. Cates, Étienne Fodor, Cesare Nardini, Julien Tailleur, and Frédéric Van Wijland. Statistical mechanics of active Ornstein-Uhlenbeck particles. *Physical Review E*, 103:032607, 2021.

[49] Akhil Varma, Thomas D Montenegro-Johnson, and Sébastien Michelin. Clustering-induced self-propulsion of isotropic autophoretic particles. *Soft Matter*, 14:7155, 2018.

[50] Stephen Ebbens, Richard A.L. Jones, Anthony J. Ryan, Ramin Golestanian, and Jonathan R. Howse. Self-assembled autonomous runners and tumblers. *Physical Review E*, 82:015304, 2010.

[51] Henricus H. Wensink, Jörn Dunkel, Sebastian Heidenreich, Knut Drescher, Raymond E. Goldstein, Hartmut Löwen, and Julia M. Yeomans. Meso-scale turbulence in living fluids. *Proceedings of the National Academy of Sciences*, 109:14308, 2012.

[52] Volker Schaller, Christoph Weber, Christine Semmrich, Erwin Frey, and Andreas R. Bausch. Polar patterns of driven filaments. *Nature*, 467:73, 2010.

[53] Fernando Peruani, Jörn Starruß, Vladimir Jakovljevic, Lotte Søgaard-Andersen, Andreas Deutsch, and Markus Bär. Collective motion and nonequilibrium cluster formation in colonies of gliding bacteria. *Physical Review Letters*, 108:098102, 2012.

[54] Hanumantha Rao Vutukuri, Maciej Lisicki, Eric Lauga, and Jan Vermant. Light-switchable propulsion of active particles with reversible interactions. *Nature Communications*, 11:2628, 2020.

[55] Ramin Golestanian. Collective behavior of thermally active colloids. *Physical Review Letters*, 108:038303, 2012.

[56] F. Ginot, I. Theurkauff, F. Detcheverry, C. Ybert, and C. Cottin-Bizonne. Aggregation-fragmentation and individual dynamics of active clusters. *Nature Communications*, 9:696, 2018.

[57] Julian Bialké, Thomas Speck, and Hartmut Löwen. Active colloidal suspensions: Clustering and phase behavior. *Journal of Non-Crystalline Solids*, 407:367, 2015.

[58] I. Theurkauff, C. Cottin-Bizonne, J. Palacci, C. Ybert, and L. Bocquet. Dynamic clustering in active colloidal suspensions with chemical signaling. *Physical Review Letters*, 108(26):1–5, 2012.

[59] Michael E. Cates and Julien Tailleur. Motility-induced phase separation. *Annual Review of Condensed Matter Physics*, 6:219, 2015.

[60] M. E. Cates and J. Tailleur. When are active Brownian particles and run-and-tumble particles equivalent? Consequences for motility-induced phase separation. *Epl*, 101:20010, 2013.

[61] Julian Bialké, Hartmut Löwen, and Thomas Speck. Microscopic theory for the phase separation of self-propelled repulsive disks. *Epl*, 103:30008, 2013.

[62] Julian Bialké, Thomas Speck, and Hartmut Löwen. Crystallization in a dense suspension of self-propelled particles. *Physical Review Letters*, 108:168301, 2012.

[63] Yaouen Fily and M. Cristina Marchetti. Athermal phase separation of self-propelled particles with no alignment. *Physical Review Letters*, 108:235702, 2012.

[64] Gabriel S. Redner, Michael F. Hagan, and Aparna Baskaran. Structure and dynamics of a phase-separating active colloidal fluid. *Physical Review Letters*, 110:055701, 2013.

[65] Ivo Buttinoni, Julian Bialké, Felix Kümmel, Hartmut Löwen, Clemens Bechinger, and Thomas Speck. Dynamical clustering and phase separation in suspensions of self-propelled colloidal particles. *Physical Review Letters*, 110:238301, 2013.

[66] B. M. Mognetti, A. Šarić, S. Angioletti-Uberti, A. Cacciuto, C. Valeriani, and D. Frenkel. Living clusters and crystals from low-density suspensions of active colloids. *Physical Review Letters*, 111:245702, 2013.

[67] Adam Wysocki, Roland G. Winkler, and Gerhard Gompper. Cooperative motion of active Brownian spheres in three-dimensional dense suspensions. *Epl*, 105:48004, 2014.

[68] Andreas Zöttl and Holger Stark. Hydrodynamics determines collective motion and phase behavior of active colloids in quasi-two-dimensional confinement. *Phys. Rev. Lett.*, 112:118101, 2014.

[69] Snigdha Thakur and Raymond Kapral. Self-propelled nanodimer bound state pairs. *Journal of Chemical Physics*, 133:204505, 2010.

[70] Andreas Zöttl and Holger Stark. Emergent behavior in active colloids. *J. Phys. Condens. Matter*, 28:253001, 2016.

[71] Supropriya Saha, Ramin Golestanian, and Sriram Ramaswamy. Clusters, asters, and collective oscillations in chemotactic colloids. *Phys. Rev. E*, 89:062316, jun 2014.

[72] Oliver Pohl and Holger Stark. Dynamic clustering and chemotactic collapse of self-phoretic active particles. *Physical Review Letters*, 112:238303, 2014.

[73] Oliver Pohl and Holger Stark. Self-phoretic active particles interacting by diffusiophoresis: A numerical study of the collapsed state and dynamic clustering. *European Physical Journal E*, 38:93, 2015.

[74] Snigdha Thakur and Raymond Kapral. Collective dynamics of self-propelled sphere-dimer motors. *Physical Review E*, 85:026121, 2012.

[75] Peter H. Colberg and Raymond Kapral. Many-body dynamics of chemically propelled nanomotors. *Journal of Chemical Physics*, 147:064910, 2017.

[76] Alexis Torres-Carbajal, Salvador Herrera-Velarde, and Ramón Castañeda-Priego. Brownian motion of a nano-colloidal particle: the role of the solvent. *Physical Chemistry Chemical Physics*, 17:19557, 2015.

[77] Alexis Torres-Carbajal and Ramón Castañeda-Priego. Friction and diffusion of a nano-colloidal disk in a two-dimensional solvent with a liquid-liquid transition. *Physical Chemistry Chemical Physics*, 20:6917, 2018.

[78] John D. Weeks, David Chandler, and Hans C. Andersen. Role of repulsive forces in determining the equilibrium structure of simple liquids. *The Journal of Chemical Physics*, 54:5237, 1971.

[79] Daan Frenkel and Berend Smit. *Understanding Molecular Simulation: From Algorithms to Simulations*. Academic Press, 2nd edition, 2002.

[80] Giorgio Volpe, Sylvain Gigan, and Giovanni Volpe. Simulation of the active Brownian motion of a microswimmer. *American Journal of Physics*, 82:659, 2014.

[81] N. W. Ashcroft and J. Lekner. Structure and resistivity of liquid metals. *Physical Review*, 145:83, 1966.

[82] Alice L. Thorneywork, Roberto E. Rozas, Roel P.A. Dullens, and Jürgen Horbach. Effect of Hydrodynamic Interactions on Self-Diffusion of Quasi-Two-Dimensional Colloidal Hard Spheres. *Physical Review Letters*, 115:268301, 2015.

[83] B Smit and D Frenkel. Vapor – liquid equilibria of the two- dimensional Lennard-Jones fluid (s). *J.Chem.Phys.*, 94:5663, 1991.

[84] Jean-Pierre Hansen and Hartmut Löwen. Effective interactions between electric double layers. *Annual Review of Physical Chemistry*, 51:209, 2000.

[85] Christos N. Likos. *Effective interactions in soft condensed matter physics*, volume 348. 2001.

[86] Vincent Dahirel and Jean Pierre Hansen. Ion-mediated interactions in suspensions of oppositely charged nanoparticles. *Journal of Chemical Physics*, 131:084902, 2009.

[87] Sho Asakura and Fumio Oosawa. Interaction between particles suspended in solutions of macromolecules. *Journal of Polymer Science*, 33:183, 1958.

[88] Jean-Pierre Hansen. *Theory of simple liquids*. Academic Press, 2nd edition, 1986.

[89] Demian Levis and Ludovic Berthier. Clustering and heterogeneous dynamics in a kinetic Monte Carlo model of self-propelled hard disks. *Physical Review E - Statistical, Nonlinear, and Soft Matter Physics*, 89:062301, 2014.

[90] Rodrigo Soto and Ramin Golestanian. Self-Assembly of Catalytically Active Colloidal Molecules: Tailoring Activity Through Surface Chemistry. *Physical Review Letters*, 112:068301, 2014.

[91] Rodrigo Soto and Ramin Golestanian. Self-assembly of active colloidal molecules with dynamic function. *Physical Review E*, 91:052304, 2015.

[92] Jaime Agudo-Canalejo and Ramin Golestanian. Active Phase Separation in Mixtures of Chemically Interacting Particles. *Physical Review Letters*, 123:018101, 2019.

[93] Yu Guo Tao and Raymond Kapral. Self-propelled polymer nanomotors. *ChemPhysChem*, 10:770, 2009.

[94] Thomas Eisenstecken, Gerhard Gompper, and Roland G Winkler. Conformational properties of active semiflexible polymers. *Polymers*, 8:304, 2016.

[95] Anthony A. Hyman, Christoph A. Weber, and Frank Jülicher. Liquid-Liquid Phase Separation in Biology. *Annual Review of Cell and Developmental Biology*, 30(1):39–58, 2014.

[96] Jiah Kim, Kyu Young Han, Nimish Khanna, Taekjip Ha, and Andrew S. Belmont. Nuclear speckle fusion via long-range directional motion regulates speckle morphology after transcriptional inhibition. *Journal of Cell Science*, 132(8), 2019.